ENGINEERING HIGH-EFFICIENCY ADSORPTION CONTACTORS VIA 3D PRINTING OF MICROPOROUS POLYMERS

A Dissertation
Presented to
The Academic Faculty

by

Fengyi Zhang

In Partial Fulfillment
of the Requirements for the Degree
Doctor of Philosophy in the
School of Chemical & Biomolecular Engineering

Georgia Institute of Technology
May 2020

ENGINEERING HIGH-EFFICIENCY ADSORPTION CONTACTORS VIA 3D PRINTING OF MICROPOROUS POLYMERS

Approved by:

Dr. Ryan P. Lively, Advisor
School of Chemical & Biomolecular Engineering
Georgia Institute of Technology

Dr. Victor Breedveld, Advisor
School of Chemical & Biomolecular Engineering
Georgia Institute of Technology

Dr. Christopher W. Jones
School of Chemical & Biomolecular Engineering
Georgia Institute of Technology

Dr. Krista S. Walton
School of Chemical & Biomolecular Engineering
Georgia Institute of Technology

Dr. Martin Maldovan
School of Chemical & Biomolecular Engineering
Georgia Institute of Technology

Dr. H. Jerry Qi
School of Mechanical Engineering
Georgia Institute of Technology

Dr. Mark D. Losego
School of Materials Science and Engineering
Georgia Institute of Technology

Date Approved: December 02, 2019

To my loving parents, Xiurong Tian and Xinguo Zhang.

To my supportive wife, Yao Ma

ACKNOWLEDGEMENTS

There are many people I would like to thank for supporting me through the journey to obtain my Ph.D. degree. I want to thank my mother, Xiurong Tian, who fostered my curiosity and encouraged me to become a scientist since my childhood. My father, Xinguo Zhang, who is a diligent chemical engineer, inspired me to devote my life to chemical engineering. Thanks to my grandmother, Yumei Zhang, who raised me and emotionally supports me all my life.

I would like to thank my advisors, Professor Ryan P. Lively and Professor Victor Breedveld, who provide me guidance on research and support me to try new ideas, which consumes them a huge amount of money and resources. Besides the technical support and professional education, they also helped me to grow up as a persistent, honest, and curious researcher. I also appreciate the professional advice from my committee members, Professor Christopher Jones, Professor Krista Walton, Professor Martin Maldovan, Professor H. Jerry Qi, and Professor Mark Losego.

I also enjoyed the 4.5 years spent with the Lively group and Breedveld group members. In the first few years when I am still an inexperienced researcher, Dr. Melinda Jue, Dr. Brian Pimentel, Dr. Simon Pang, Dr. Dong-Yeun Koh, Dr. Guanghui Zhu, Dr. Lu Jiang, Dr. Zhenguan Tang, and Erkang Zhou provided me with continuous technical and nontechnical guidance. Besides, I also appreciate the helpful discussion with Dr. Richelle Lyndon, Dr. Achintya Sujan, Yao Ma, Stephen DeWitt, Leo Chiang, Hye Youn Jang, Ronita Mathias, Matt Rivera, and Conrad Roos.

I want to acknowledge the funding from Georgia Institute of Technology, Simmons Bedding Company, and ExxonMobil Research and Engineering Company. Without their financial support, my research could not have been finished. I also appreciate the helpful discussion with ExxonMobil scientists: Dr. Simon C Weston, Dr. Carter W. Abney, Dr. David C. Calabro, Dr. Lisa S. Baugh, and Dr. Neel D. Rangnekar. Besides, I would like to acknowledge the Institute for Electronics and Nanotechnology of the Georgia Institute of Technology for the characterization equipment.

This thesis was completed with extensive collaboration. Chapter 3 was finished with the help of Yao Ma and Yuzuki Kondo. Yao Ma conducted the material synthesis and characterization, and Yuzuki Kondo determined the ternary phase diagrams. Chapter 4 was finished with the help of Jianshan Liao, Yao Ma, and Yadong Chiang. Jianshan Liao conducted the rheology characterization of the polymer solutions, Yao Ma assisted with the material synthesis and characterization, and Yadong Chiang assisted with the toluene vapor breakthrough experiments. Chapter 6 was finished with the help of Emily McGuinness and Yao Ma. Emily McGuinness conducted the vapor phase infiltration, and Yao Ma assisted with characterization. Chapter 7 was finished with the help of Stephen DeWitt, who conducted the MIL-101 synthesis.

Especially, I want to thank my wife, Yao Ma, who makes my life colorful, provides me technical assistance, and helps me survive the dark days when my experiments fail again and again.

TABLE OF CONTENTS

LIST OF TABLES

LIST OF FIGURES

LIST OF SYMBOLS AND ABBREVIATIONS

a	Characteristic Length of Diffusion
δ	Phase Lag between Shear Stress and Shear Strain
BET	Brunauer-Emmett-Teller
c	Concentration
CCUS	Carbon Capture, Utilization, and Storage
DEZ	Diethyl Zinc
DFT	Density Function Theory
DIW	Direct Ink Writing
DMAc	Dimethylacetamide
DMF	Dimethylformamide
EDX	Energy Dispersive X-Ray Analysis
FDM	Fused Deposition Modeling
FTIR	Fourier Transform Infrared Spectroscopy
G	Gibbs Free Energy
G^*	Complex Modulus
G'	Shear Modulus
G''	Loss Modulus
GC	Gas Chromatography
HPLC	High Performance Liquid Chromatography
IPCC	Intergovernmental Panel on Climate Change
μ	Viscosity
m	Adsorption Mass Uptake

M_w	Weight Average Molecular Weight
M_n	Number Average Molecular Weight
MOF	Metal Organic Frameworks
MSMPR	Mixed Product Mixed Suspension Removal
MTZ	Mass Transfer Zone
MWCO	Molecular Weight Cut-Off
NMP	N-Methyl-2-Pyrrolidone
OSN	Organic Solvent Nanofiltration
OSRO	Organic Solvent Reverse Osmosis
p	Pressure
p^{sat}	Saturation Pressure
PDI	Polydispersity Index
PEI	Polyethylenimine
PIM-1	Polymer of Intrinsic Microporosity 1
q	Adsorption Capacity
Q	Flow Rate
R	Radius
SEM	Scanning Electron Microscopy
SLA	Stereolithography
τ	Shear Stress
t	Time
T	Temperature
TFTPN	Tetrafluoroterephthalonitrile
THF	Tetrahydrofuran
$TiCl_4$	Titanium Chloride

TMA	Trimethylaluminum
TTSBI	5,5′,6,6′-Tetrahydroxy-3,3,3′,3′-Tetramethyl-1,1′-Spirobisindane
v	Velocity
V	Volume
γ	Shear Strain

SUMMARY

Adsorption is a promising energy-efficient separation process, which selectively removes one or several components from a mixture by transporting a fluid through a mass transfer contactor. The most traditional mass transfer contactor design is a packed bed of adsorbent pellets, which suffers from high pressure drop, low mass transfer rate, difficulty in heat integration, etc. State-of-the-art structured mass transfer contactors have been developed to address these problems. For instance, hollow fiber sorbents can achieve rapid temperature manipulation by flowing heat-exchange media through the bore channels, and monoliths provide uniform fluid channels to minimize pressure drop. However, limited by manufacturing techniques, existing structured mass transfer contactors struggle to address all of the aforementioned problems with one structural design. 3D printing techniques can fabricate complex architectures without molding-based approaches, which is suitable for rapid prototyping of novel mass transfer contactor designs.

The overarching goal of this thesis is to engineer high-efficiency adsorption contactors via 3D printing of microporous polymers. To achieve this goal, three objectives were established: (1) develop 3D printing techniques that can process adsorptive materials and generate hierarchical porosity, (2) prototype scalable mass transfer contactors with optimized energy efficiency, (3) perform proof-of-concept adsorption experiments to demonstrate the advantages of 3D printing in mass transfer contactor fabrication.

In Chapter 3, a novel 3D printing technique is developed. Current 3D printing methods have strong limitations in the classes of compatible polymers. Many polymers of significant technological interest cannot currently be 3D printed. Here, a generalizable

Solution-based Additive Manufacturing (SBAM) method for viscous polymer solutions was developed for solution-processable polymers. SBAM fabricates polymeric objects by depositing ternary polymeric inks (e.g., solutions comprising polymer, volatile solvent, and nonvolatile nonsolvent), which undergo rapid phase inversion upon evaporation of a relatively small fraction of the volatile components, resulting in hierarchically porous filaments (e.g., pores of diameters ranging from 2 nm to 10 μm). In addition to the architecture of the printed object, its internal porosity can be manipulated for different applications. Compared with typical direct ink writing of binary polymeric inks, which typically only contain the polymer and a volatile solvent, SBAM is capable of (i) eliminating evaporation-induced shrinkage, and (ii) creating nanopores without the need for templating additives or nanoscale nozzles. Successful ternary ink formulations require a balancing of solution thermodynamics (phase separation), mass transfer (solvent evaporation), and rheology. SBAM is conceptually compatible with any solution-processable polymer with or without functional particles (e.g., zeolites), which significantly extends the 3D-printable polymeric material spectrum. Our research provides a practical guide towards the development of ternary polymeric inks, the design of 3D printer hardware for SBAM, and the post-treatment of printed objects for desired porosity. It also discusses solutions to common challenges encountered during this new polymer processing technology via case studies (e.g., polymer of intrinsic microporosity 1, cellulose acetate, Matrimid® 5218, etc.).

In Chapter 4, a microporous polymer (PIM-1) - incompatible with current additive manufacturing technologies - is 3D printed into a high-efficiency mass transfer contactor containing sub-nanometer to millimeter pores. Short contactors can fully purify gases

loaded with concentrated toluene vapor for six times longer than PIM-1 in traditional structures, and more than 4000 times the residence time of gas in the contactor. This demonstration strongly suggests that 3D printing could produce ultra-short adsorbers with precisely designed fluid distribution system without gas bypass.

In Chapter 5, the scalable, modular design of adsorption contactors was developed by taking advantage of the SBAM process. Such modular contactors possess high freedom in the engineering of characteristic lengths of diffusion, fluid distribution systems, fluid channel sizes, adsorbent loadings, etc. A systematic study in the structure design was conducted to maximize the breakthrough capacity while minimizing the pressure drop across the contactor. As a demonstration, PIM-1 is 3D printed into adsorption modules with hierarchical porosity. These adsorption modules serve as "molecular baskets" for branched polyethyleneimine (PEI). The PEI/PIM-1 composite adsorption modules are used for CO_2 capture from simulated flue gas. It is shown that by optimizing the adsorption module assembly strategy, the breakthrough capacity can be improved by nearly half without sacrificing pressure drop.

In Chapter 6, the "molecular basket", PIM-1, is reinforced with oxide nanostrands via vapor phase infiltration of the oxide material's precursors. The infiltrated oxide strands intertwine with the PIM-1 network, resulting in a robust hierarchical porous support for functional materials. PEI oligomers were loaded into the organic-inorganic hybrid. The infiltrated oxide constituent significantly improved the microstructural stability. Compared with PEI/PIM-1 composites, oxide/PEI/PIM-1 composites exhibit significantly improved CO_2 capacity and amine efficiency at the same PEI loading. The improvement of the CO2

capacity and amine efficiency is hypothetically contributed by the reinforced PIM-1 support and abundant hydroxyl groups provided by the oxide strands.

In Chapter 7, the processable material spectrum of SBAM is expanded from solution-processable polymers to nanoparticles, such as zeolites and metal-organic frameworks (MOFs). These adsorptive nanoparticles are dispersed in multicomponent polymer solutions to form a 3D printable slurry. Similar to SBAM of the polymer solution, the slurry filaments deposited by the 3D printer undergo evaporation-induced phase inversion, which results in hierarchical pores throughout the composite. Besides the creation of hierarchical porosity, SBAM of nanoparticles provides protection to water-unstable MOFs, such as HKUST-1. After SBAM, the MOF particles dispersed in the polymer retain their surface areas. The SBAM process does not negatively impact the MOF structure or block the micropores.

CHAPTER 1. INTRODUCTION

1.1 Sustainable Development

1.1.1 Sustainable Development Goals

Sustainable development refers to meeting the living standards of human beings without depleting natural resources or damaging the ecosystem. The sustainable development of human society is necessary so that the future of the next generation will not be sacrificed. In 2015, the United Nations proposed 17 Sustainable Development Goals (SDGs): (1) *No Poverty*, (2) *Zero Hunger*, (3) *Good Health and Well-being*, (4) *Quality Education*, (5) *Gender Equality*, (6) *Clean Water and Sanitation*, (7) *Affordable and Clean Energy*, (8) *Decent Work and Economic Growth*, (9) *Industry, Innovation, and Infrastructure*, (10) *Reducing Inequality*, (11) *Sustainable Cities and Communities*, (12) *Responsible Consumption and Production*, (13) *Climate Action*, (14) *Life Below Water*, (15) *Life On Land*, (16) *Peace, Justice, and Strong Institutions*, (17) *Partnerships for the Goals*. The accomplishment of these SDGs requires a joint effort from different experts, organizations, and countries all over the world. Among the 17 SDGs, 4 of them are directly related to chemical industries: *Clean Water and Sanitation*, *Affordable and Clean Energy*, *Responsible Consumption and Production*, and *Climate Action*.

Modern technologies consume energy to convert natural resources into products, transport humans and goods all over the world, and support the lives of human beings. Technologies are developed and improved to foster higher population, improve living standards, and provide longer life expectancy, which in turn results in a continuously

increasing energy demand[1] As shown in Figure 1.1, the world energy consumption has grown by 2 orders of magnitude since 1820.[2] To meet the high energy consumption, the last 50 years have witnessed a tremendous boost in the utilization of fossil fuels (coal, natural gases, and oil). While various alternative energy sources (e.g., hydroelectricity, solar energy, nuclear power, etc.) have been explored during the 20th century, the utilization of fossil fuels grows continuously. Especially in less developed regions, fossil fuels are expected to play important roles for a long time owing to easy utilization, convenient transportation, and reliability.[2]

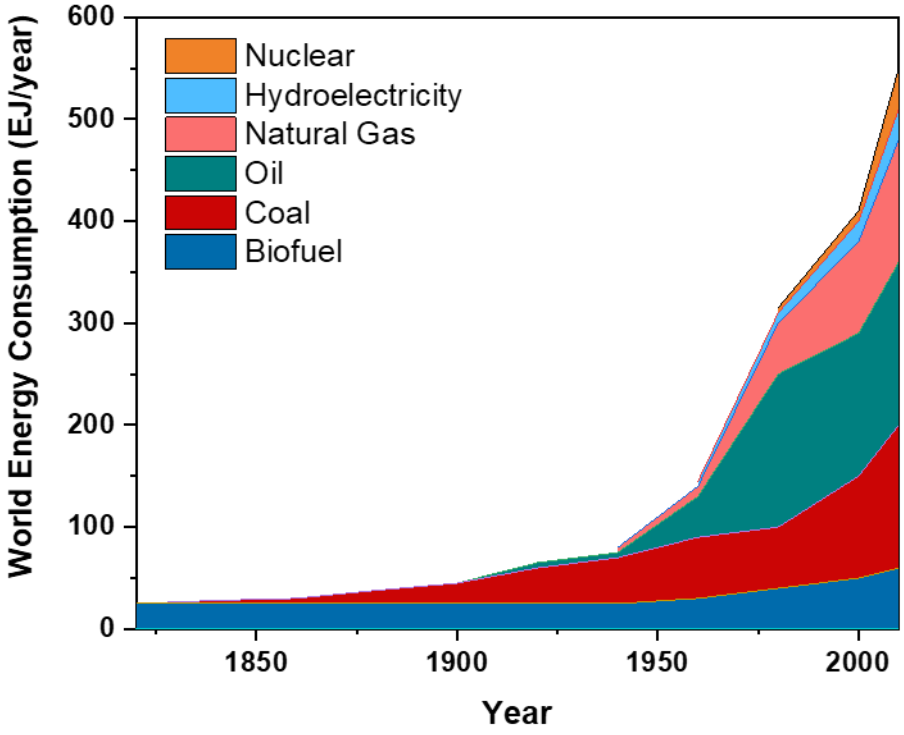

Figure 1.1. The evolution of world energy portfolio since the Industrial Revolution.[2]

The heavy dependence on fossil fuel for the global energy system challenges the sustainable development of human society. First, the direct combustion of fossil fuels generates a huge amount of greenhouse gases (e.g., CO_2, N_2O, CH_4), which are major

contributors to global warming. Second, increasing energy demand leads to intensified exploitation of fossil fuels, which accelerates the depletion of fuel reservoirs and threatens sustainable energy utilization.[3]

1.1.2 CO_2 Capture

Human activities, especially industrial activities, consume a huge amount of energy, which is associated with tremendous emission of greenhouse gases. Emission of greenhouse gases is known to contribute to global warming, which refers to the long-term temperature increase of the global climate system. Global warming threatens ecosystems, raises sea levels, and leads to extreme weather, which must be addressed to enable sustainable development.[4] While global warming has attracted the attention of all human societies, the increase of atmospheric CO_2 concentration has not stopped. Since 2000, the atmospheric CO_2 concentration increases around 20 ppm per decade and is approaching 410 ppm in 2019.[5] Compared with pre-industrial ages (before the late 19th century), human activities have induced approximately 1 °C global warming.[6] Moreover, 20%-40% of the globe's population has already experienced 1.5 °C regional temperature increase during 2018.[6] According to Intergovernmental Panel on Climate Change (IPCC), global warming must be limited to 1.5 °C to reduce the risks of global heavy precipitation, intense cyclones, increasing drought frequency, etc.

Researchers all over the world are tackling the global warming issue. One important strategy to limit the global warming is carbon capture, followed by carbon utilization and storage (Carbon Capture, Utilization, and Storage, CCUS).[7] Carbon capture from point sources (e.g., power plants) and the atmosphere requires energy-efficient CO_2 capture

techniques. While amine-based CO_2 absorption is the most mature technique for CO_2 capture, it suffers from a high energy penalty.[8] Alternative techniques should be developed to process emissions from different point sources and capture CO_2 from the air at lower costs.[9,10]

1.1.3 Energy Efficiency of Industrial Separation Processes

The modern industry consists of various energy-intensive processes. According to the Department of Energy, the US consumes 98 Quads energy every year, among which 32% is contributed by the industrial sector.[11] Of this, 45% to 55% is contributed by thermal-driven separation techniques. This large energy footprint provides enormous opportunities for energy savings.

Thermally-driven separation technologies refer to processes that separate components via the phase change of the materials in the process stream. Thermally-driven separation techniques are well developed and widely applied in the modern industry, but they do have disadvantages. First, thermal techniques rely on the phase change of the materials, which often results in low energy efficiency. Take desalination as an example: the heat associated with the evaporation of water is around 640 kWh/m^3 while the thermodynamic limitation of desalination, $\Delta G_{demixing}$, is only 1 kWh/m^3.[12-14] With advanced heat integration and process optimization, state-of-the-art multistage flash systems could reduce the desalination energy consumption to 50 kWh/m^3, which is still significantly higher than the thermodynamic limit. Second, the separation of isomers and azeotropes requires alternative separation routes. Moreover, typical thermal separation

techniques have large footprints, which inhibits their application in space-limited conditions (e.g., off-shore oil processing).

A sustainable development focus motivates the creation of energy-efficient alternatives to mainstream thermally-driven separation techniques. Energy-efficient separation techniques not only reduce the unnecessary energy consumption of human society but can also be applied to CO_2 capture, which will be discussed below.

1.2 Mainstream Energy-Intensive Separation Technologies

In this section, the following classical thermally-driven techniques will be covered: absorption, distillation, and crystallization. Unit operation principles, advantages, disadvantages, and example applications will be introduced briefly for each technique.

1.2.1 Absorption

Absorption is used to separate a component from a gas mixture via contact with a liquid, which is also referred to as stripping. Gas molecules can be separated owing to the different affinities of gas components with the absorbing liquid phase. Absorption is usually conducted in a packed tower, as shown in Figure 1.2a.[15] The gas enters the absorber from the bottom and leaves the absorber from the top. The fluid contact with the gas as a countercurrent flow: fresh absorbing liquid is distributed on the top of the absorber and the used liquid is drained from the bottom.

Absorption is widely applied in acid gas removal,[16] carbonyl compound removal from hydrocarbons,[17] carbon capture,[18] etc. Figure 1.2b is an example flow diagram of a conventional post-combustion carbon capture process.[19] For the ease of observation,

reboiler, condenser, and other supplementary equipment are not present in this simplified diagram. The whole carbon capture process includes two parts: (1) CO_2 absorption and (2) solution regeneration. Flue gas contacts with fresh solution counter-currently (e.g., aqueous solution of monoethanolamine, ammonia, piperazine, etc.) in the absorber, within which CO_2 is captured by the solution via reversible chemical reactions. The CO_2-rich amine solution is then pumped into the regenerator, where the amine solution is heated by the reboiler (100~120 °C). Vaporized amine solution is condensed at the top of the regenerator, and gas-phase CO_2 is recovered.

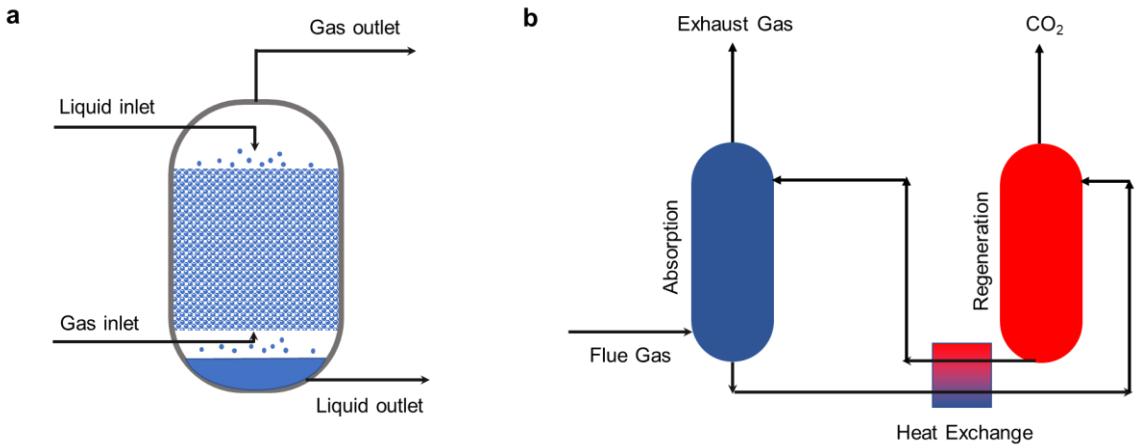

Figure 1.2 (a) A typical design of a packed tower for absorption. (b) Example flow diagram of an absorption-based post-combustion carbon capture process.[18]

Most of the energy consumption of absorption is associated with the regeneration process. Since the absorbent solution is regenerated by boiling the entire solution, the latent heat of the solvent contributes to a high regeneration energy penalty. For instance, monoethanolamine (MEA) is one of the most popular CO_2 absorbents that bonds with CO_2 forming carbamate.[18,20] During regeneration, heat is applied to break the bonds and release CO_2, which requires 1900 kJ/kg CO_2.[20] Due to the latent heat consumed by dilution water,

the typical regeneration heat requirement is around 4000 kJ/kg CO_2, which is 2-3 times higher than the heat of reaction.

1.2.2 Distillation

Distillation separates molecules based on their relative volatility, which is their vapor-liquid distribution ratio at equilibrium. The liquid mixture is boiled to generate vapor. If different components have different vapor pressure, the composition of the vapor phase is different from the liquid phase. Generally, there exist three classical distillation operations: (a) flash distillation, (b) rectification, and (c) batch distillation.

Flash distillation is achieved by partial evaporation of the liquid. Figure 1.3a shows the scheme for a single-stage flash distillation apparatus. The liquid fluid is preheated and pumped into the vapor-liquid separator. In the vapor-liquid separator, the liquid is drained from the bottom and the vapor phase in equilibrium with the liquid phase is separated from the system. The separated vapor phase can then be condensed and collected. As a result, the components with different volatility can be separated. A typical application of flash distillation is desalination. State-of-the-art desalination is achieved by multistage flash distillation, which recovers the heat via the contacting of the fresh brine water and the water vapor.[13,14]

While flash distillation is effective for the separation of components with distinct boiling points (e.g., seawater), the separation of components with similar volatility requires successive distillation to produce components with high purity. Rectification refers to continuous distillation with reflux. As shown in Figure 1.3b, a classical distillation column with reflux consists of a series of plates, at which liquid and vapor phases are in

equilibrium. By boiling liquid mixture, components can be enriched in different phases (either liquid or vapor). Liquid phases flow down driven by gravity, and vapor phases rise driven by buoyancy, which avoids the capital cost and energy cost for fluid delivery between plates. The volatile components are enriched in the vapor phase at the top plate, and the nonvolatile components are enriched in the liquid of the bottom plate. Rectification is one of the most widely applied separation techniques. Atmospheric and vacuum distillation are used to fractionate crude oil into different products, which counts for 32 % petroleum industry energy consumption.[21] Cryogenic distillation is widely used for the separation of gas mixtures, such as air,[22] light hydrocarbons,[23] etc.

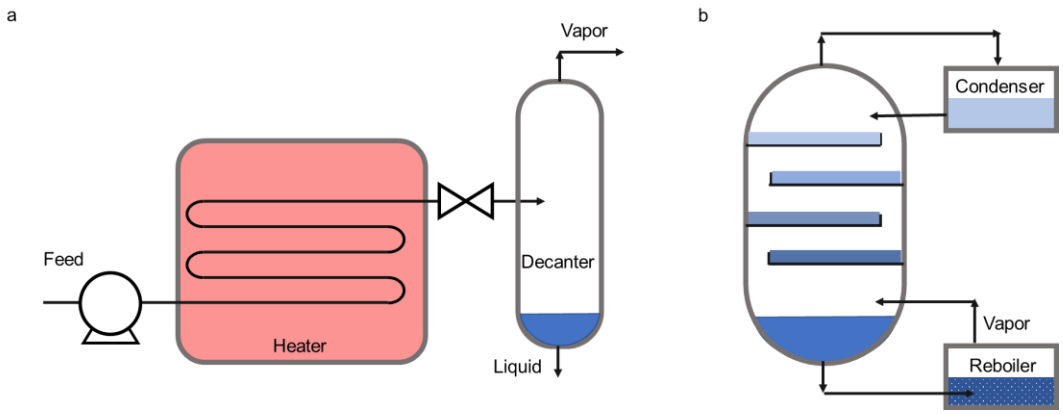

Figure 1.3. Schemes for (a) flash distillation and (b) rectification.

For plants where chemicals are produced at small scales or with diverse composition, batch distillation is usually utilized to recover volatile compounds from the liquid mixtures. Batch distillation could operate in a flash distillation mode (without reflux) or rectification mode (with reflux) depending on the relative volatility of components.

Distillation is suitable for the production of chemicals with high purity and high yield. The separation performance is determined by the process optimization and

distillation column design. Distillation-based separation processes can be easily designed and fabricated at large scale. Such merits enable the wide application of distillation in the modern industry. However, distillation separation is inefficient for the separation of isomers, azeotropes, and heat-sensitive compounds.

1.2.3 Crystallization

In industry, crystallization usually refers to the unit operations that form solid particles from a liquid solution, such as crystallization of solute from a saturated solution and crystallization of a solvent from a solvent mixture. Figure 1.4 shows a typical scheme for Mixed Product Mixed Suspension Removal (MSMPR) crystallizer, which resembles a continuous stirred tank reactor.[24,25] The feed mixture is continuously delivered into the crystallizers. Crystallization within the crystallizer is usually driven by (1) solution cooling, (2) solvent evaporation, or (3) combination of cooling and evaporation. Crystals nucleate and grow within the crystallizer, converting the supersaturated solution into suspensions. After crystallization, the suspension containing crystal particles are delivered into sequential separation equipment, such as filtration and centrifuge.

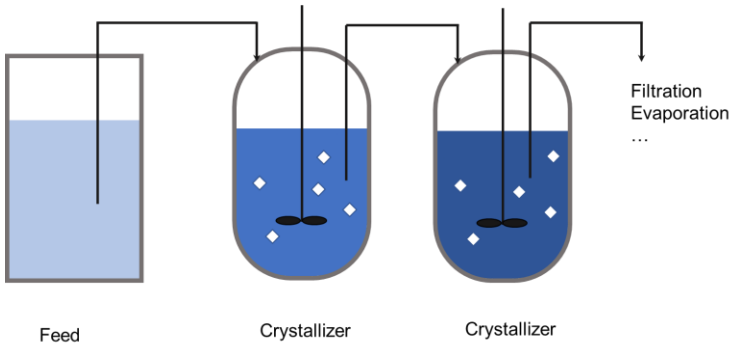

Figure 1.4. Scheme of continuous crystallization processes.

Crystallization is a widely applied separation process that has been employed for centuries in the commodity chemical industry, fine chemical industry, and pharmaceutical industries.[25] Around 70% of solid materials for chemical industries are produced via crystallization.[26] To improve the energy efficiency of industries involving crystallization processes, two strategies can be applied: (1) separate crystals from mother liquid via non-thermal separation techniques, and (2) replacing crystallization with membrane separation or adsorption processes (section 1.3).

1.3 Alternative Energy-Efficient Separation Techniques

1.3.1 Membrane Separation

Membrane-based molecular separation is a promising technique to debottleneck or replace traditional separation techniques. Within the membrane, different molecules exhibit different diffusivities and different affinities with the membrane material, which contributes to selective transmembrane transportation. When dealing with azeotropes, chemicals with similar boiling points, or heat-sensitive materials, membrane separation can be employed as a pre-treatment process to debottleneck distillation processes.[12] To date,

there exist two membrane separation processes that directly process organic liquid streams: organic solvent nanofiltration (OSN) and organic solvent reverse osmosis (OSRO).

Organic solvent nanofiltration (OSN) refers to the membrane separation that selectively transports organic solvents while rejects bulky solutes. The performance of the organic solvent nanofiltration membrane is quantified by permeance and molecular weight cut-off (MWCO), which influence the process of productivity and product purity correspondingly. Ideally, an OSN membrane selectively transports molecules based on their molecule size. Since the molecule size is directly related to the molecular weight, engineers quantify the performance of OSN membranes by correlating the rejection rate with the molecular weight. Molecular weight cut-off is defined as the smallest molecular weight that the membrane can reject with 90 % efficiency.[27] In literature, MWCOs of membranes are usually determined using marker solutes such as polystyrene oligomers. However, since different solutes possess different shapes in solvents and different interactions with the membrane material, the real MWCO for the target mixture may deviate from the expected ones. Membrane-based organic solvent nanofiltration is a promising alternative to crystallization.[27] Bulky solute molecules (e.g., pharmaceutical compounds) can be separated from the mother solution based on their molecular weights. By applying OSN membranes with different MWCOs, the target molecules can be separated from the other solutes.

Organic solvent reverse osmosis (OSRO) directly process organic solvent in liquid phases.[28-31] The liquid mixture is pressurized at the feed side of the membrane while the permeate side is maintained at a lower pressure (e.g., atmospheric pressure). The transmembrane pressure difference induces fugacity difference, which drives molecular

transportation across the membrane. OSRO utilizes microporous membrane, the micropores of which are designed to differentiate guest molecules. OSRO has demonstrated potential in isomer separation and organic solvent fractionation.[30,31] As OSRO directly processes liquid organic solvent without phase change, it is more attractive than the pervaporation. However, organic solvent reverse osmosis is far from industrial application. First, both inorganic materials and organic materials have an inherent limitation: it is difficult to fabricate crystalline materials into membranes at industrial scale, and direct processing of high-pressure organic solvent liquid requires high organic solvent stability, which is challenging for polymeric materials.[31] Second, it is not trivial to create "mid-range" micropores to precisely differentiate organic solvent molecules.[29] Extensive researches are needed to investigate membrane design, process optimization, and contactor design for OSRO.

1.3.2 Adsorption

Adsorption is a promising energy-efficient separation process, which selectively removes one or several components from a mixture by transporting a fluid through a solid mass transfer contactor. The separation of different molecules is contributed by their different affinities with the adsorbent materials. Contrary to absorption processes that selectively capture molecules from gas phases into the liquid phase, adsorption captures molecules from the liquid phase or gas phase into the solid adsorbent phase. In absorption systems, the active absorptive molecules (e.g., amines) are dispersed or dissolved into solvents (e.g., water). On the other hand, adsorption systems utilize solid materials to disperse the adsorptive functional groups or molecules. Switching from an absorptive

solution to an adsorptive solid effectively reduces the energy penalty related to regeneration.

Absorption processes designed for new factories can be replaced with adsorption processes. The knowledge developed for absorption chemistry can be readily transferred. For example, amine molecules developed for CO_2 absorption can be dispersed in microporous supports and be used as CO_2 adsorbent. However, it might be expensive to retrofit existing absorption processes since absorption and adsorption relies on distinct equipment. Advanced heat integration and absorption materials might be the best solution for old factory retrofit.

Based on the regeneration method, adsorption processes fall into two main categories: (1) temperature-swing adsorption (TSA), and (2) pressure-swing adsorption (PSA). TSA and PSA can also be combined.

1.3.2.1 Temperature Swing Adsorption

The principle for TSA is illustrated in Figure 1.5. Owing to the exothermic nature of adsorption, adsorbents have higher capacity at low temperature compared with high temperature given the same adsorbate partial pressure. For instance, an adsorbent could capture adsorbates at low temperatures from dilute sources (denoted by the blue dot in Figure 1.5a) and partially release the adsorbate at elevated temperature (denoted by the red dot in Figure 1.5a). During the adsorption process, the fresh adsorber contacts with the gas mixture at low temperature (Figure 1.5b). After adsorption, the saturated adsorber is heated via contacting with hot purge gas. The hot purge gas should be carefully selected so that the adsorbate can be easily separated from the purge gas. For instance, hot steam can be

used for the CO_2 capture process. The hot steam can be condensed from the concentrated CO_2 stream, generating high-purity CO_2 products.[32]

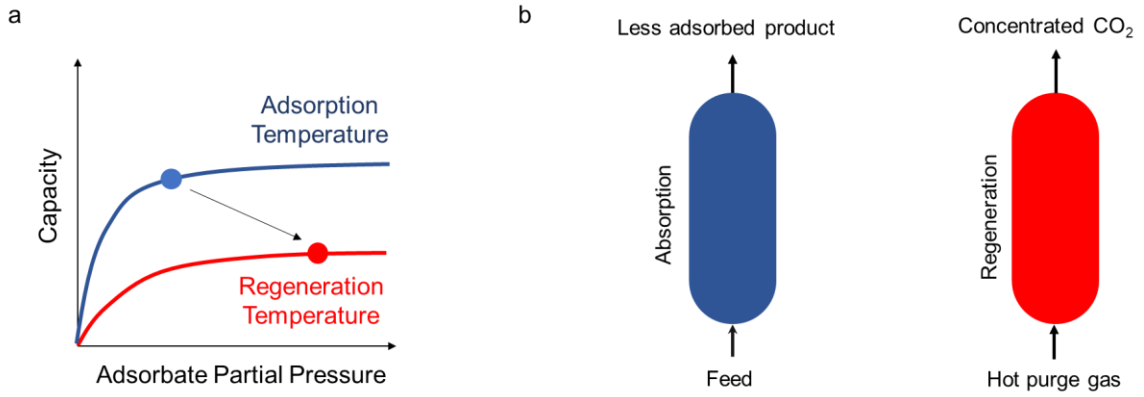

Figure 1.5 Temperature swing adsorption. (a) Capacity change during temperature swing. (b) Simplified scheme for temperature swing adsorption.

While both TSA and absorption requires heat for regeneration, TSA is often more energy efficient. First, the specific heat capacities of solid adsorbents (e.g., the specific heat capacity of active carbon is around 0.7 J/g ºC) are much lower than those of liquid solvents (e.g., the specific heat capacity of H_2O is 4.2 J/g ºC). Second, the thermal loss due to solvent evaporation of the solvent is avoided.

1.3.2.2 Pressure Swing Adsorption

Pressure-swing adsorption is illustrated in Figure 1.6. As illustrated by the adsorption isotherms (Figure 1.6a and Figure 1.6b), the adsorbent capture more adsorbate at high adsorbate partial pressures than at low adsorbate partial pressures. The fresh adsorber firstly is contacted with the pressurized gas mixture. After adsorption, the pressure within the saturated adsorber is lowered abruptly (Figure 1.6c). When regeneration is achieved via the use of vacuum, it is also referred to as vacuum swing adsorption (VSA). The low

adsorbate pressure triggers the release of captured molecules. Pressure swing adsorption is a promising separation technique for CO_2 capture, biogas upgrading, air separation, and others.[33] Pressure swing adsorption is especially effective for adsorbents with step-shaped adsorption isotherms (Figure 1.6b), which is commonly observed for amine-loaded MOFs.[34]

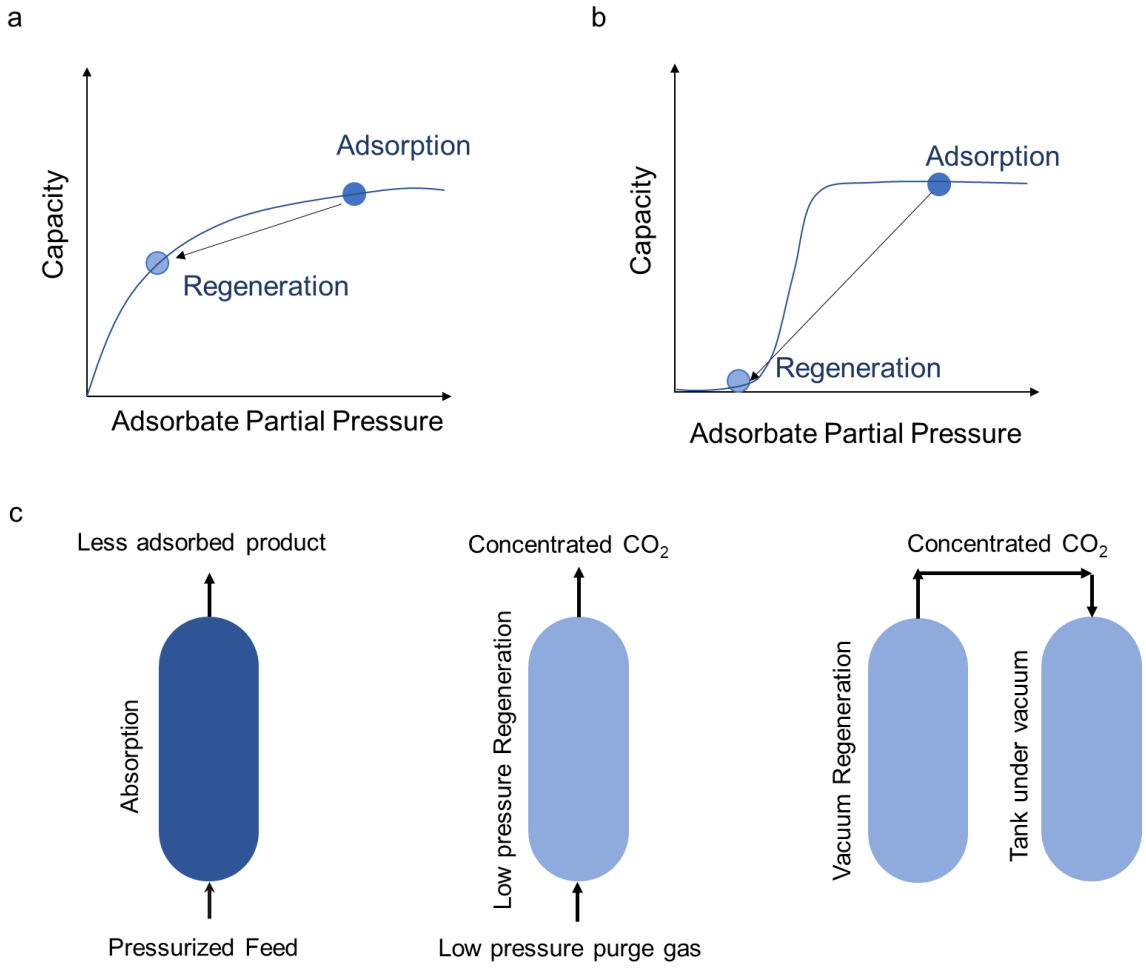

Figure 1.6 Pressure swing adsorption. Capacity change during pressure swing for (a) an ordinary Type-I isotherm and (b) a step isotherm. (c) Simplified scheme for temperature swing adsorption.

1.4 Mass Transfer Contactors for Molecular Separation

The key challenge for the widespread application of nonthermal separation techniques is the translation of advanced materials into mass transfer contactors.[35] Different from thermal-driven techniques, the performance of non-thermal driven separation techniques is strongly determined by the design and quality of the mass transfer contactors.[9,36] While significant progress has been made in the development of advanced materials, limited research has been conducted in the development of a cost-effective scalable fabrication method for high-performance mass transfer contactors.

Mass transfer contactors play critical roles in non-thermal separation techniques. The quality and functionality of the contactor directly influence the performance, stability, and cost of the separation technique.[9] While extensive researches about nonthermal separation materials has been conducted, limited innovation has been done in the design and fabrication of mass transfer contactors. In this chapter, popular mass transfer contactors for adsorption and membrane separation are introduced.

1.4.1 Membrane Mass Transfer Contactor

State-of-the-art membrane mass transfer contactor designs are spiral wound membranes and hollow fiber membranes. Based on the application and membrane material, engineers should properly choose the membrane contactor design.

1.4.1.1 Spiral Wound Membrane Contactor

The spiral wound membrane is a common contactor design for polymeric membranes. In the modern industry, the membranes used in spiral-wound membrane

contactors are usually fabricated by roll-to-roll membrane casting or its derivatives. Figure 1.7a illustrates a simplified roll-to-roll membrane casting setup for thin-film composite membrane fabrication. Support membranes are delivered from the feeding roller to a roller attached to a coating bath, which contains a polymer solution. After contact with the coating solution, a thin layer of polymer solution liquid film is coated onto the support membrane. Optionally, the liquid polymer film can be delivered into a quench bath, undergoes nonsolvent-induced phase inversion, and result in a highly porous membrane structure.[37] The coated membrane travels through the dryers, where the liquid polymer solution is completely solidified into a thin polymer membrane.

Depending on the fabrication condition, two membrane morphologies (Figure 1.7b) are commonly observed in the industry: (1) integrally skinned asymmetric membrane, and (2) thin-film composite membrane. The integrally skinned asymmetric membrane is coated directly onto fabric supports (e.g., polyethylene nonwoven fabrics). The asymmetric polymer membrane formed by nonsolvent induced phase separation possesses a mesoporous support layer and an integral selective skin layer. For expensive polymer materials, the thin composite membrane is preferred. A prefabricated composite film consisting of mesoporous support membrane and fabric reinforcement is used as the substrate. The substrate is then coated with a thin polymer layer. For the commercialized membrane, the thickness of the selective layer is controlled below 100 nm to achieve high permeance.

Figure 1.7c and Figure 1.7d illustrate the assembly of the spiral wound membrane contactor. Membranes are assembled into sandwich-like membrane elements. As shown in Figure 1.7c, two membranes are glued on their edges. Permeate-side spacers are placed

between the membranes to create flow channels for the permeate. Feed-side spacers are placed on the other sides to create flow channels for the feed. The glued membrane packets are attached to a tubular permeate collector. As shown in Figure 1.7d, the membrane packets are wrapped around the permeate collector and sealed in a membrane housing. Feed fluid is delivered through the feed flow channels. Molecules are transferred across the membrane into the permeate channels sealed in the membrane packets. The permeates are collected by the center permeable tube and transferred out of the module.

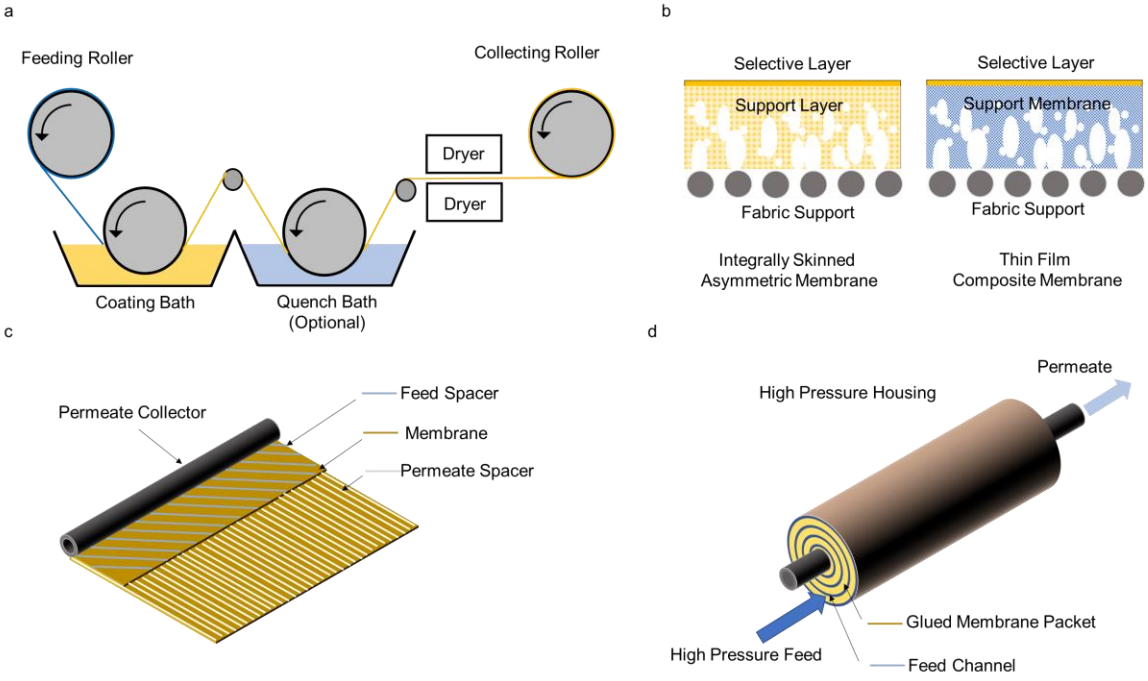

Figure 1.7 Spiral wound membrane contactor. (a) Roll-to-roll membrane casting. (b) The structures of the integrally skinned asymmetric membrane and the thin-film composite membrane. (c) Flatten spiral wound membrane module elements. (d) Assembly of spiral wound membrane contactor.

Spiral wound membrane contactors provide a high surface area per unit volume of the module. Given a membrane of 62.5 μm thickness and a spacer of 700 μm thickness, a spiral wound membrane contactor could provide up to 1300 m^2 membrane area per 1 m^3

of module volume, which is sufficient for a variety of industrial applications (e.g., desalination, wastewater treatment, organic solvent nanofiltration). Besides, spiral wound membrane contactors have advantages such as good fouling control, low capital cost, ease of operation, etc.[38]

1.4.1.2 Hollow Fiber Membrane Contactor

For polymeric materials, hollow fiber membranes can be fabricated via dry-wet spinning as illustrated in Figure 1.8a. Dry-wet spinning processes multicomponent polymer solution containing polymer, solvent, and nonsolvent. The multicomponent polymer solution is delivered through the core dope channel of the spinneret. A neutral solution that does not precipitate the polymer solution is delivered through the bore fluid channel. The optional sheath fluid channel can be used to deliver additional polymer solution or sheath solvent. The composite filament coming out of the spinneret travels through an air gap and a nonsolvent quench bath and finally is collected onto a rotating take-up drum. In the air gap, evaporation of volatile solvent induces the formation of a dense skin layer on the outer surface of the polymer filament. In the quench bath, the entire filament undergoes nonsolvent-induced phase separation and forms hierarchically porous support layers beneath the skin layer (Figure 1.8b).

While pure inorganic materials (e.g., zeolites, MOFs, etc.) cannot be directly solution-processed into hollow fiber membranes, they can be fabricated onto hollow fiber membrane supports. Fabrication methods of inorganic selective layers on hollow fiber membrane supports can be categorized into two strategies: *in situ* growth and secondary growth.[39] *In situ* growth means directly immersing a bare substrate (without MOF crystal

attached) into the synthesis solution containing metal sources, ligands, additives and solvents. During the reaction, MOFs will nucleate and grow on the substrate spontaneously. By contrast, secondary growth utilizes a substrate with nanosized pre-synthesized MOF or metal oxide seeds. During the reaction, growth and intergrowth of the seed crystals ideally result in the formation of a defect-free membrane.

After fabrication and post-treatment, hollow fiber membranes can be assembled into a membrane module, the design of which resembles a tubular heat exchanger (Figure 1.8b). Hollow fiber membranes are fixed in a cylinder housing. Feed fluid is delivered into the shell side and the retentate flows out of the housing through the outlet. Permeates (e.g., liquids, vapors, or gases) are collected from the bore side.

Compared with spiral wound membrane contactors, state-of-the-art hollow fiber membrane contactors provide much higher membrane area density and pressure resistance. Given hollow fiber membranes with a 250 μm diameter and 125 μm diameter provide up to 8000 m^2 surface area per 1 m^3 of hollow fiber membrane module volume. The circular cross-section of the hollow fiber membrane could effectively withstand high transmembrane pressure. For example, carbon molecular sieve membranes are so brittle that freestanding carbon membranes cannot process pressurized fluid. On the contrast, carbon molecular sieve hollow fiber membranes can withstand hydraulic pressure >100 bar without failure.[28] Owing to these properties, the hollow fiber membrane is ideal contactor design for low-permeability precise molecular sieving (e.g., organic solvent reverse osmosis).

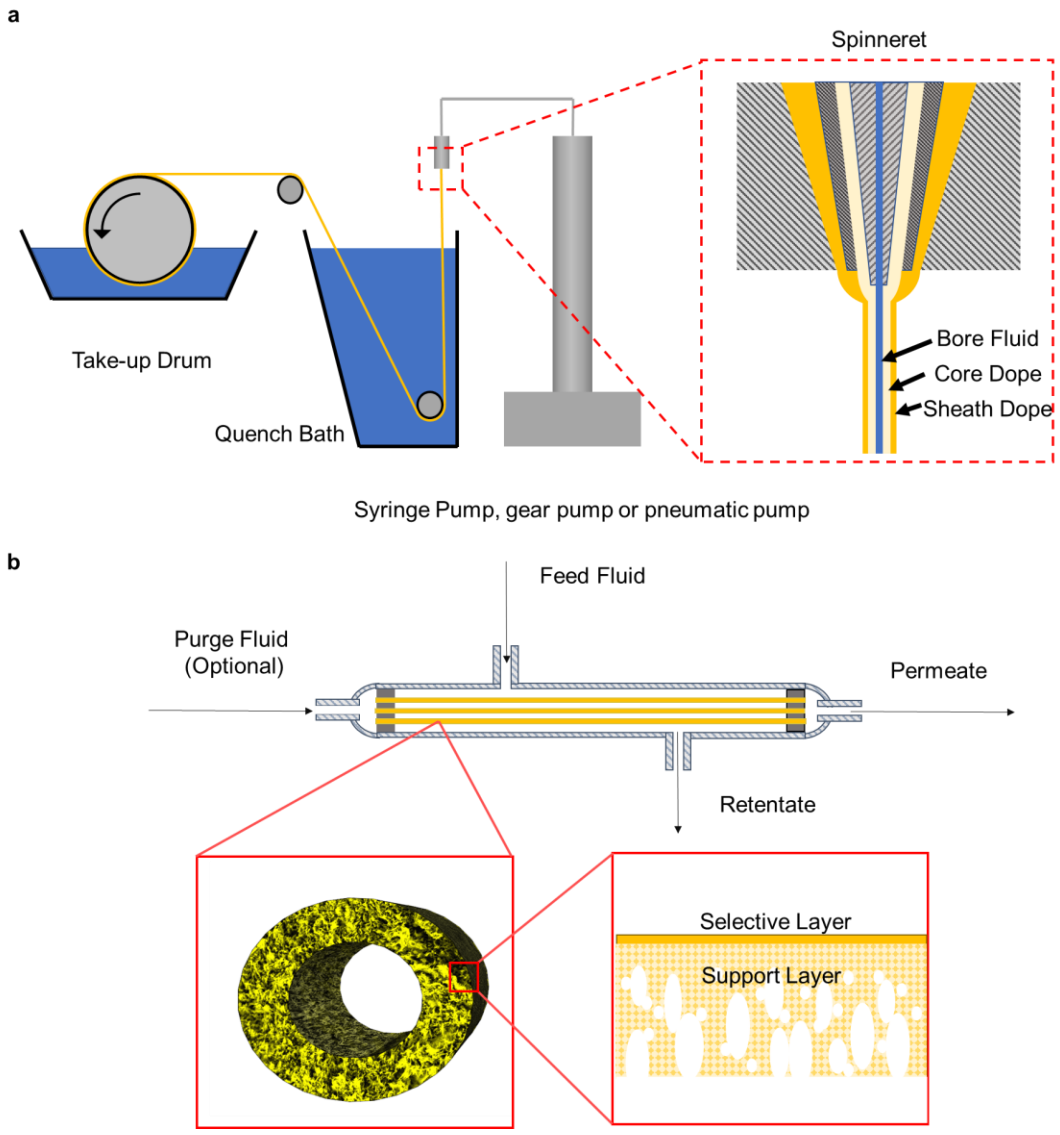

Figure 1.8 Hollow fiber membrane contactor. (a) Hollow fiber spinning system. (b) Hollow fiber membrane assembly.

1.4.2 Adsorption Mass Transfer Contactor

1.4.2.1 Packed Bed Adsorption Contactor

Packed bed adsorption contractors are tubes or vessels randomly filled with adsorptive packing materials. The packing materials are usually fabricated into spheres or cylinders with the equivalent diameters (the diameter of a sphere with the same apparent

volume) ranging from 1 mm to 4 mm. The individual packing elements can also be fabricated into specific structures (e.g., short monolith) to provide more surface area per unit volume.

Owing to the ease of fabrication, packed bed adsorption contactors are widely utilized in the modern industry. However, the tortuous fluid distribution system formed by random packing could result in high pressure drop, which results in high operational cost.

1.4.2.2 Monolithic Adsorption Contactor

A monolithic structure is one of the most popular mass-transfer contactor designs. It has been widely used in various applications, such as three-way catalytic converters and adsorption columns.[40-42] Monolithic structures possess macropores and thin honeycomb-like channels, which significantly reduce pressure drop across the adsorber while providing high surface areas for mass transfer with processing fluids (e.g., gas mixtures). State-of-art monoliths with high mechanical strength minimize the influence of fluid-induced abrasion, which can be a severe issue in pellet-based packed beds.[9,41] By tuning porosity, channel sizes, and material types, monolithic adsorbents can be optimized for different operation conditions.[43] Generally, monolithic adsorbents can be fabricated via two approaches: (i) direct fabrication, in which pastes containing *in situ* synthesized adsorbents are extruded through a nozzle with specific opening and (ii) post-fabrication synthesis, in which secondary growth of adsorbent materials is conducted on seeded monolithic substrates.[44]

Direct fabrication of monolithic adsorbents involves the extrusion of a paste-like mixture of nanoporous particles, binders, additives, and solvents into a specific monolithic structure. Post-treatments like drying are also required for the enhanced mechanical

strength of the adsorbents. For example, Kaskel et al. fabricated HKUST-1 monolith by extruding HKUST-1 particles with silicone resin as binder and methyl hydroxyl propyl cellulose as the plasticizer.[41] In their approach, the partly cross-linked liquid silicone was chosen on purpose to create a viscoelastic suspension. The following microwave-assisted heating fully crosslinked the silicone resin and generated a robust monolith. Besides HKUST-1, a variety of MOFs monoliths, such as MIL-101(Cr), have also been fabricated through direct extrusion method.[41,45-50]

Monolith fabrication by direct extrusion typically results in higher adsorbent loading than those fabricated via post-treatment methods but requires suitable binders, additives, and post-treatments.[44] By contrast, secondary growth utilizes pre-fabricated or commercially available ceramic monoliths and requires less modification to existing synthesis procedures. Ceramic monolith with high mechanical strength and high stability can be fabricated via extrusion of cordierite, water and agglomerating agents.[51] For instance, Gascon et al. immobilized MIL-101(Cr) onto a commercially available cordierite monolith.[52] Their approach consists of three steps: first, the monolith is activated by NaOH and α-alumina particles; second, the resulting alumina-coated monolith is dip-coated with MIL-101(Cr) seeds; third, secondary growth of uniform MOF layer is achieved by subjecting seeded monolith to synthesis solution under rotation.

1.4.2.3 Fiber Sorbent

Besides the monolith structure, the fiber adsorbent is another promising mass transfer contactor design featuring easy fabrication, low pressure drop, high surface area to volume ratio and heat integration.[9,53-55] A typical fiber adsorbent consists of

macroporous polymeric matrix and adsorbent particles distributed throughout the wall of the fiber. Fabrication of fiber adsorbents is mainly accomplished by dry-wet fiber spinning, which is widely applied in the fabrication of hollow fiber membranes.

Polymer, adsorbent particles (or seeding materials), solvent, nonsolvent, and other additives are first mixed. The resulting mixture, which is also referred to as ‘dope’ in literature, is then extruded through a spinneret as shown in Figure 1.8a. Drawn by a rolling drum, the extruded viscoelastic filaments go through an air gap into a nonsolvent bath (typically water). Complicated mass transfer during this process triggers the phase inversion of polymer, which turns into a hierarchical porous matrix that supports adsorbent particles.[53,55] After complete solvent exchange and drying, the composite fibers are ready for use (*in situ* synthesis) or further treatments (secondary growth).

Although fiber adsorbent spinning is inspired by hollow fiber membrane spinning, they have different fabrication strategies due to their distinct requirements for target morphologies. First, fiber adsorbent spinning utilizes inhomogeneous suspensions of solid particles instead of a homogenous polymer solution for membrane spinning. A primary dope containing solid particles and a small amount of polymer is first produced to ensure uniform distribution of particles within the mixture, and then the remaining materials are subsequently added. Repeated sonication, stirring and shear mixing are also critical for the distribution of the particles. The resulting dopes for fiber adsorbent spinning should be handled as soon as possible to avoid sedimentation while dopes for membrane spinning undergo additional treatments such as degassing. Second, fiber adsorbents should be free of skin layers that significantly retard mass transfer. By contrast, the skin layer is the most critical feature of separation membranes. Therefore, dopes for adsorbent fibers seldom

contain volatile solvents and the air gap for adsorbent fiber spinning is minimized to avoid vitrification at the fiber surface.

Depending on the formation methods of adsorbent particles, the fabrication of fiber adsorbents can be categorized into *in situ* synthesis and secondary growth. Straightforward *in situ* synthesis is applicable for adsorbents that remain active after immersion in solvents (e.g., water), sonication, and post-treatment (e.g., drying, oxidation in ambient condition). Until now, fiber adsorbents containing zeolite LiX, NaX, NaY, and UIO-66 have been reported with adsorbent loadings as high as 75 wt%.[55-58] Secondary growth after fabrication of porous polymer fibers is utilized to process nanoporous materials incompatible with the dry-wet spinning process. For instance, Pimentel et al. converted cellulose acetate/ZnO fibers into HKUST-1 fibers with 85 wt% loading of the MOF.[59] This type of secondary growth strategy was firstly described by Zhao et al.[60] In both cases, the ZnO was transferred into a hydroxyl double salt (HDS) intermediate containing Zn and Cu, which was then rapidly converted into HKUST-1. Such HDS intermediate approaches can also be used to synthesize other MOFs, such as ZIF-8 and IRMOF-3. The secondary growth process can be conducted inside the adsorber shell and isolated from moisture, which is a promising fabrication strategy for water-sensitive nanoporous materials.

1.5 Microporous Materials for Molecular Separation

According to the pore size classification provided by International Union of Pure and Applied Chemistry (IUPAC), micropores are pores with widths equal to or smaller than 2 nm.[61] The last two decades have witnessed a rapid development of microporous materials, which refers to materials containing permanent micropores.[62] Microporous

materials possess high surface areas, which provide abundant adsorption sites, and molecular sieving pores, which differentiate guest molecules. Such features make microporous materials great candidates for adsorption and membrane separation.

1.5.1 Zeolites

Zeolites are crystals formed by hydrated aluminosilicates. The crystal structures of zeolites provide periodically arranged 3-dimensional nanopores with widths ranging from 4 Å to 13 Å. The uniform pore size distribution and rigid micropores provide zeolite with the capability of differentiating molecules with minor size (e.g., ~ 1 Å) difference and shape difference (e.g., C_2H_4/C_2H_6). The microporous structures of zeolite provide high surface areas (up to 1000 m^2/g has been reported) with diverse sorption sites (e.g., Lewis acid/base, Brønsted acid/base, etc.), which is attractive for catalysis and adsorption applications. The strong Al-O-Si bonding provide zeolites superior stability in high temperature and harsh chemical conditions, owing to which zeolites have been widely applied in catalysis, adsorption, membrane separation, etc.[63-66]

As inorganic crystalline materials, it is challenging to fabricate zeolites into complex mass transfer contactors. In most commercialized adsorption and catalysis processes, zeolites are utilized in the form of porous pellets, which can be made into packed beds. By dispersing zeolites in polymer solutions, modern industries can fabricate zeolite adsorption contactors via solution-processing. However, the incorporation of polymer matrix limits the application of zeolites in high temperature and harsh chemical conditions. In the membrane industry, zeolite membranes are usually fabricated on expensive ceramic supports via *in-situ* growth or secondary growth. While zeolite membranes exhibit

excellent separation performance at the lab scale, it is challenging to fabricate defect-free zeolite membranes with a preferred orientation at a large scale.[63]

1.5.2 Metal-Organic Frameworks

Metal-Organic Frameworks (MOFs) are crystalline porous materials formed by metal ions and coordinatively connected organic ligands.[67] The versatile combination of metal nodes and organic linkers provides nearly unlimited engineering potential to design MOFs for the specific applications. To date, over 40,000 MOFs have been experimentally reported. Adsorption sites of MOFs can be engineered via metal node manipulation, organic ligand functionalization, defects engineering, etc. The pore size distribution of MOFs is determined by the crystal structure and ligand size.[68]

MOFs have a variety of tailorable structural characteristics that translate into tunable performance properties. For instance, MOF apertures can be varied from a few angstroms to several nanometers while maintaining uniform pore size distribution. The resulting molecular sieving effect has been applied for size-selective sensing in luminescent Zn_3btc_2 and Cd_2^+-based MOFs.[69,70] This feature suggests that MOFs may be useful for separating molecules with similar size.[39,67,71,72] Beyond changes in topology, MOF apertures can be further tuned by mixing linkers of different lengths; it is possible to do this while retaining the topology of the MOF comprised of the starting linker.[73,74] Indeed, the immense number of possible metal-ligand combinations provide a rich design space with access to a variety of topologies and customized functionality. MOF functionality can derive from the organic linkers, the metal nodes/clusters, or both.[75] For example, by changing the metal centers of MOF-74, the CO_2 capacity can be increased by

50% owing to the enhanced interaction with CO_2.[76] Via changing linkers with different functional groups, BET surface areas of UIO-66 derivates can be tuned from 540 m^2/g to 1580 m^2/g.[77] Mixed-linker hybrid zeolitic imidazolate frameworks were also developed with a tunable gate-opening effect for target separation processes.[68] Besides engineering metal nodes of MOFs, organic linkers can also be tuned via either pre-synthesis or post-synthesis modification.[72]

Mesoporous MOFs is an emerging area of nanoporous materials research. The vast majority of existing MOFs exhibit cavities and channels with diameters smaller than 2 nm. Although micropores (< 2 nm) provide large surface areas, mesopores (according to IUPAC definition, pores with a diameter ranging from 2 nm to 50 nm) are attractive for energy-efficient separations and advanced catalysis. Mesoporous MOFs can be categorized into three types: (1) cage-type mesoporous MOFs, in which mesopores are connected via microporous channels, (2) channel-type mesoporous MOFs, in which mesopores are accessible as channels, and (3) mesoporous particles of MOFs, in which mesopores are formed via surfactant templating.[78] For instance, Férey and coworkers noted that MIL-100 exhibits mesopores with a diameter ranging from 2.5 nm to 3 nm and high surface area of 3100 m^2/g, and these fall within the Type 1 categorization of mesoporous MOFs.[79] Subsequent efforts resulted in the creation of MIL-101 with mesopores (2.9 nm to 3.4 nm), which resulted in even higher surface areas (5900 m^2/g).[80] One typical Type 2 channel-type mesoporous MOF is NU-1000 featuring pores with diameters ranging from 1 nm to 3 nm and versatile functionalization;[81] moreover, a variety of other Type 2 mesoporous MOFs (e.g., mesoMOF-1, JUC-48, UMCM-1, etc.) were also developed.[82-84] The Type 3 mesoporous MOFs are created via a surfactant-templated strategy, which results in the

formation of mesopores via surfactant micelles within microporous MOFs. After template removal, MOFs with hierarchical meso-/micro-pores are synthesized. Such strategies have been successfully applied to MOFs such as HKUST-1.[85-87] Mesopores MOFs are also excellent support materials for bulky functional materials. For example, mesoporous Mg_2(dobpdc) are excellent supports for amine molecules for CO_2 capture.[34,88]

Compared with zeolites, MOFs have better compatibility with polymers. It is a common approach to disperse MOFs into a polymer solution and then process the suspension into structured mass transfer contactors.[9] Fiber sorbents containing MOFs have demonstrated great potential for CO_2 adsorption from flue gases.[9,89] 3D printing of MOFs adsorption contractors have also been reported.[90]

1.5.3 Microporous Polymers

Organic microporous materials are formed from covalently bonded nonmetal atoms. Since covalent bonds usually possess higher binding energy than coordinate bonds, organic microporous materials often exhibit superior thermal stability and chemical stability without sacrificing the versatility in chemistry and structure. Crystalline organic nanoporous materials include covalent organic frameworks (COFs),[91] porous aromatic frameworks (PAFs),[92] porous organic cages (POCs),[93] etc. Amorphous microporous materials consist of hypercrosslinked polymers (HCPs),[94] conjugated microporous polymers (CMPs),[95] elemental organic frameworks,[96] and polymers of intrinsic microporosity (PIMs),[97] etc.

Among all the microporous polymers, linear PIMs are the most attractive materials for mass transfer contactor fabrication. Semi-permanent nanopores within linear polymers

can also be induced via spatially frustrated packing of the polymer backbones, which is the design principle for polymers of intrinsic microporosity. PIMs were firstly reported by Budd and McKeown in 2004.[98] The rigid backbones of PIMs hinder efficient packing of adjacent polymer chains thus providing semi-permanent nanoscopic voids within the polymer matrix. These materials are different from traditional glassy polymers that contain small amounts of isolated voids (free volumes): the contortion centers of PIMs effectively support micropores that are interconnected over several nanometer length scales. It is worth noting that debates still exist over the nature of the voids within PIMs. These voids provide useful molecular transport channels for selective adsorption and membrane separation. The prototypical PIM, PIM-1 (Figure 1.9a), is synthesized via the polycondensation of tetrafluoroterephthalonitrile (TFTPN) and 5,5′,6,6′-Tetrahydroxy- 3,3,3′,3′-tetramethyl-1,1′-spirobisindane (TTSBI). PIM-1 possesses a highly conjugated polymer backbone with repeated spiral carbon centers in each repeating unit. The rigid twisted polymer chain cannot pack efficiently, resulting in abundant interconnected micropores. Owing to the unique polymer structure, PIM-1 possesses a high BET surface area (~700 m^2/g), which makes is ideal adsorption materials (Figure 1.9b). The nitrile groups of PIM-1 can also be converted into different functional groups for different separation targets.[99] The micropores of PIM-1 range from 4 Å to 8 Å (Figure 1.9c), which is useful for membrane separation. Since PIM-1 possesses a linear polymer structure, it can be dissolved by organic solvents and processed into different structures via solution processing.[29-31,100,101] Owing to these properties, this research utilizes PIM-1 as the adsorption material for mass transfer contactor prototyping.

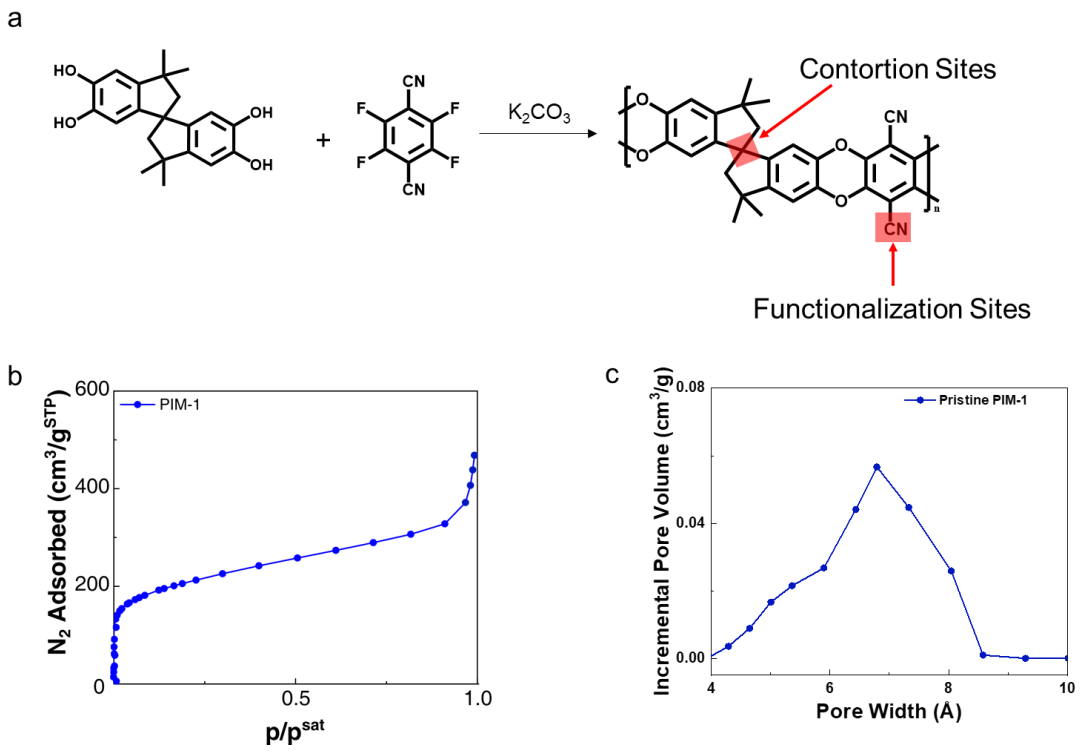

Figure 1.9 Polymer of intrinsic microporosity 1 (PIM-1). (a) Synthesis of PIM-1. (b) 77K nitrogen physisorption of PIM-1. (c) The pore size distribution of PIM-1 calculated by the DFT model.

1.6 3D Printing of Polymers

3D printing, which is the most well-known additive manufacturing technique, translates a computer-aided design (CAD) model into a physical object via directly adding materials to the object. The main advantage of 3D printing is the ability to fabricate complex structures without significant increase of the fabrication cost, which makes 3D printing an ideal tool to prototype new products.[102] State-of-the-art 3D printing techniques include fused deposition modeling (FDM), stereolithography (SLA), powder bed fusion, and direct ink writing (DIW).

1.6.1 Fused Deposition Modelling

FDM fabricates polymeric objects by successively depositing polymer melts layer by layer. A thermoplastic polymer filament is delivered to the 3D printer nozzle, where the filament is heated and semi-liquified. The polymer melts are then deposited on the substrate or on the top of the existing objects. After cooling, the deposited polymer melts fuse together and solidify.

FDM is simple and cost-effective, which makes it one of the most popular 3D printing techniques on the market.[103] Limited by the working principle, FDM can only be applied to thermoplastic-polymer-based filaments or composites. Since most microporous polymers possess a rigid polymer backbone, which usually results in a high melting point, FDM is not a convenient tool for adsorption contactor fabrication. Researchers have tried to disperse PIM-1 in thermoplastic polymers (e.g., polycaprolactone and polylactic acid) and then translate the composite materials into specific structures.[104] However, the thermoplastic polymer matrix blocks the micropores of microporous polymer and results in low accessible surface areas.

1.6.2 Stereolithography

SLA fabricates polymer objects via localized photopolymerization, which was firstly invented in 1986.[102] Patterned UV light is applied to the surface of the photoreactive monomer resin bath. Upon the UV radiation, a chain reaction is initiated, and the UV-exposed monomer resin is converted into the designed polymer structure. The cured layer is then moved away from the resin-gas interface so that the next layer can be 3D printed on fresh monomer resins. SLA could achieve high 3D printing resolution but suffers from

a limited spectrum of processable materials and complex reaction kinetics.[102,105] Since the microporosity of microporous polymers is related to the polymer structure, it is not trivial to develop or modify microporous polymers with photoreactivity.

1.6.3 Powder Bed Fusion

Powder bed fusion is conducted on thin layers of fine powders. The powder is locally fused according to CAD models via laser beam heating or binder deposition. After the patterned fusion of the existing powder layer, subsequent layers of powders are delivered to cover the powder bed surface for the 3D printing of the next layers. After the 3D printing of the entire object, excessive unfused powders are removed.

The 3D printing technique utilizing laser beams is referred to as selective laser sintering (SLS) or selective laser melting (SLM). SLS applies to polymers, metals, and alloys that possess low melting temperatures. During SLS, the surface layers of the powder particles are melted and fused. SLM applies to certain metal powders (e.g., such as steel and aluminum) and fully melts the powder, which results in a more robust structure than SLS. For materials with high melting points, liquid binders can be deposited onto the target position to bind particles instead of sintering or melting them.

1.6.4 Direct Ink Writing

DIW fabricates 3D structures via deposition of colloidal-based inks, nanoparticle-based inks, or polymer-based inks.[106,107] Based on the rheology of the DIW inks, two 3D printing strategies can be applied: droplet ink jetting and continuous filament writing. The ink design principle for droplet ink-jetting resembles conventional reprographic: materials

are dispersed in low-viscosity fluids or wax-based matrixes.[107] Typical inks for continuous filament writing are colloidal particulate gels, hydrogels, and nanoparticle suspensions.[108-111] DIW provides a plausible strategy to process polymers based on their solution processability. Researchers have 3D printing polymers (e.g., polylactide, cellulose acetate, acetoxypropy, etc.) in the form of viscous solution.[112-116] However, there exist various technical challenges associated with solution-based DIW, such as structure shrinking, high viscosity, dewetting of adjacent layers, etc.

1.7 Research Objectives

While extensive research has focused on the development of microporous materials for separation problems, fabrication difficulties inhibit their widespread application in the modern industry.[9,101] The overarching goal of this thesis is to prototype energy-efficient mass transfer contactors via 3D printing of microporous polymers. To achieve this goal, three objectives were established:

1. Developing 3D printing techniques for adsorptive materials

Current additive manufacturing methods have strong limitations with regards to the classes of compatible polymers. Many polymers of significant technological interest cannot currently be 3D printed. Here, a generalizable Solution-based Additive Manufacturing (SBAM) of viscous polymer solutions is developed for solution-processable polymers. With SBAM, microporous materials (e.g., zeolites, MOFs, microporous polymers) can be fabricated into mass transfer contactors with controllable hierarchical porosity.

2. Prototyping energy-efficient mass transfer contactors

It is well known that the separation performance of an adsorption contactor is strongly influenced by the contactor design. However, little research has been conducted to optimize the mass transfer contactor design due to the fabrication difficulties of well-controlled complex geometries. With the assistance of SBAM, mass transfer contactors with complex design can be fabricated without additional cost. The objective is to optimize mass transfer contactors made of microporous materials (e.g., PIM-1) to achieve high energy efficiency (e.g., better pressure drop efficiency). The influence of different packing patterns on adsorption performance is investigated.

3. Breakthrough experiments of prototypical adsorption contactors.

The prototypical energy-efficient adsorption contractors are used for volatile organic compounds (VOCs) removal and CO_2 capture. The contactor structures are designed for specific separation tasks. These experiments demonstrate the potential of 3D printing in the area of mass transfer contactor design and manufacturing.

1.8 Thesis Organization

This thesis focusses on *Engineering High-Efficiency Adsorption Contactors via 3D printing of Microporous Polymers*. After the introduction in Chapter 1, Chapter 2 will provide background knowledge about porous materials, adsorption isotherms, adsorption chromatography, and fluid rheology. In Chapter 3, a thorough guide to solution-based additive manufacturing of polymeric structures is provided. The strategies of polymer ink design, porosity manipulation, and printing condition are discussed in detail. Chapter 4

provides an example of solution-based additive manufacturing of PIM-1, which proved the concept of 3D printing high-efficiency adsorption contactors. The ultra-short adsorption contactor proposed in Chapter 4 exhibits lower pressure drop and more efficient VOC removal performance than traditional contactors. In Chapter 5, the influence of ultra-short contactor design and assembly on the adsorption performance is investigated. The optimized PEI/PIM-1 adsorption assembly exhibits significantly improved CO2 breakthrough capacity and reduced pressure drop compared with PEI/PIM-1 packed beds. To further improve the performance of the 3D printed adsorption contactors, Chapter 6 is devoted to developing an amine-loaded organic-inorganic nanoporous material for CO_2 capture, as well as investigating the fundamental mechanism about the interaction between CO_2, amine, and a metal hydroxide. Chapter 7 translates the knowledge about 3D printing of polymeric adsorber into crystalline adsorptive materials. An example procedure for 3D printing of MOFs is provided. CO_2 capture performance of the resulting hierarchical porous MOF adsorption contactors is evaluated. Finally, Chapter 8 provides conclusions for this thesis and future research directions regarding 3D printing of energy-efficient mass transfer contactors.

1.9 References

1. J. D. Sachs. *The age of sustainable development*: Columbia University Press; **2015**.

2. G. Tverberg. World energy consumption since 1820 in charts. *Our Finite World* **2012**.

3. S. Sorrell, J. Speirs, R. Bentley, A. Brandt, R. Miller. Global oil depletion: A review of the evidence. *Energy Policy* **2010**;38(9):5290-5295.

4. R. R. Bhandary. The IPCC's Fifth Assessment Report and Its Implications for Nepal. **2014**.

5. B. Bereiter, S. Eggleston, J. Schmitt, C. Nehrbass‐Ahles, T. F. Stocker, H. Fischer, S. Kipfstuhl, J. Chappellaz. Revision of the EPICA Dome C CO_2 record from 800 to 600 kyr before present. *Geophysical Research Letters* **2015**;42(2):542-549.

6. M. Allen, P. Antwi-Agyei, F. Aragon-Durand, M. Babiker, P. Bertoldi, M. Bind, S. Brown, M. Buckeridge, I. Camilloni, A. Cartwright. Technical Summary: Global warming of 1.5°C. An IPCC Special Report on the impacts of global warming of 1.5°C above pre-industrial levels and related global greenhouse gas emission pathways, in the context of strengthening the global response to the threat of climate change, sustainable development, and efforts to eradicate poverty. **2019**.

7. J. Rogelj, D. Shindell, K. Jiang, S. Fifita, P. Forster, V. Ginzburg, C. Handa, H. Kheshgi, S. Kobayashi, E. Kriegler. Mitigation pathways compatible with 1.5 °C in the context of sustainable development. **2018**.

8. C.-H. Yu, C.-H. Huang, C.-S. Tan. A review of CO2 capture by absorption and adsorption. *Aerosol Air Qual. Res* **2012**;12(5):745-769.

9. S. J. DeWitt, A. Sinha, J. Kalyanaraman, F. Zhang, M. J. Realff, R. P. Lively. Critical Comparison of Structured Contactors for Adsorption-Based Gas Separations. *Annual review of chemical and biomolecular engineering* **2018**;9:129-152.

10. R. P. Lively. *Hollow fiber sorbents for post-combustion CO_2 capture*, Georgia Institute of Technology; 2011.

11. D. S. Sholl, R. P. Lively. Seven chemical separations: to change the world: purifying mixtures without using heat would lower global energy use, emissions and pollution--and open up new routes to resources. *Nature* **2016**;532(7600):435-438.

12. W. J. Koros, R. P. Lively. Water and beyond: Expanding the spectrum of large‐scale energy efficient separation processes. *AIChE Journal* **2012**;58(9):2624-2633.

13. N. M. Wade. Distillation plant development and cost update. *Desalination* **2001**;136(1-3):3-12.

14. S. Avlonitis, K. Kouroumbas, N. Vlachakis. Energy consumption and membrane replacement cost for seawater RO desalination plants. *Desalination* **2003**;157(1-3):151-158.

15. W. L. McCabe, J. C. Smith, P. Harriott. *Unit operations of chemical engineering.* Vol 1130: McGraw-hill New York; **1993**.

16. C. Grossman, N. Asprion, Inventors. Absorbing agent and method for eliminating acid gases from fluids. US patent 7,374,734 2008.

17. S. A. Kurukchi, J. M. Gondolfe, Inventors. Removal of carbonyls from gaseous hydrocarbon streams. US patent 9,834,498 2018.

18. M. Wang, A. Lawal, P. Stephenson, J. Sidders, C. Ramshaw. Post-combustion CO2 capture with chemical absorption: a state-of-the-art review. *Chemical Engineering Research and Design* **2011**;89(9):1609-1624.

19. R. Watson, I. Noble, B. Bolin, N. Ravindranath, D. Verardo, D. Dokken. Intergovernmental Panel on Climate Change (IPCC) special report on land use, land use change and forestry: Cambridge, UK: Cambridge University Press; **2000**.

20. A. B. Rao, E. S. Rubin, M. B. Berkenpas. *An integrated modeling framework for carbon management technologies*, Carnegie Mellon University (US); 2004.

21. W. R. Morrow III, J. Marano, A. Hasanbeigi, E. Masanet, J. Sathaye. Efficiency improvement and CO_2 emission reduction potentials in the United States petroleum refining industry. *Energy* **2015**;93:95-105.

22. R. Cornelissen, G. Hirs. Exergy analysis of cryogenic air separation. *Energy Conversion and Management* **1998**;39(16-18):1821-1826.

23. K. Hoyer, C. Hulteberg, M. Svensson, J. Jernberg, Ö. Nörregård. Biogas upgrading-technical Review. **2016**.

24. G. Power, G. Hou, V. K. Kamaraju, G. Morris, Y. Zhao, B. Glennon. Design and optimization of a multistage continuous cooling mixed suspension, mixed product removal crystallizer. *Chemical Engineering Science* **2015**;133:125-139.

25. C. Darmali, S. Mansouri, N. Yazdanpanah, M. W. Woo. Mechanisms and Control of Impurities in Continuous Crystallization: A Review. *Industrial & Engineering Chemistry Research* **2018**;58(4):1463-1479.

26. M. Giulietti, M. Seckler, S. Derenzo, M. Ré, E. Cekinski. Industrial crystallization and precipitation from solutions: state of the technique. *Brazilian Journal of Chemical Engineering* **2001**;18(4):423-440.

27. P. Marchetti, M. F. Jimenez Solomon, G. Szekely, A. G. Livingston. Molecular separation with organic solvent nanofiltration: a critical review. *Chemical Reviews* **2014**;114(21):10735-10806.

28. D.-Y. Koh, B. A. McCool, H. W. Deckman, R. P. Lively. Reverse osmosis molecular differentiation of organic liquids using carbon molecular sieve membranes. *Science* **2016**;353(6301):804-807.

29. Y. Ma, M. L. Jue, F. Zhang, R. Mathias, H. Y. Jang, R. Lively. Creation of well‐defined “mid‐sized” micropores in carbon molecular sieve membranes. *Angewandte Chemie* **2019**;131(38):13393-13399.

30. Y. Ma, F. Zhang, S. Yang, R. P. Lively. Evidence for entropic diffusion selection of xylene isomers in carbon molecular sieve membranes. *Journal of Membrane Science* **2018**;564:404-414.

31. E. K. McGuinness, F. Zhang, Y. Ma, R. P. Lively, M. D. Losego. Vapor Phase Infiltration of Metal Oxides into Nanoporous Polymers for Organic Solvent Separation Membranes. *Chemistry of Materials* **2019**;31(15):5509-5518.

32. W. Li, S. Choi, J. H. Drese, M. Hornbostel, G. Krishnan, P. M. Eisenberger, C. W. Jones. Steam‐stripping for regeneration of supported amine‐based CO2 adsorbents. *ChemSusChem* **2010**;3(8):899-903.

33. C. A. Grande. Advances in pressure swing adsorption for gas separation. *ISRN Chemical Engineering* **2012**;2012.

34. R. L. Siegelman, P. J. Milner, E. J. Kim, S. C. Weston, J. R. Long. Challenges and opportunities for adsorption-based CO_2 capture from natural gas combined cycle emissions. *Energy & Environmental Science* **2019**;12:2161-2173.

35. Y. Ma, F. Zhang, R. P. Lively. Manufacturing Nanoporous Materials for Energy-Efficient Separations: Application and Challenges. *Sustainable Nanoscale Engineering*: Elsevier; **2020**:33-81.

36. M. L. Jue, D.-Y. Koh, B. A. McCool, R. P. Lively. Enabling widespread use of microporous materials for challenging organic solvent separations. *Chemistry of Materials* **2017**;29(23):9863-9876.

37. G. R. Guillen, Y. Pan, M. Li, E. M. Hoek. Preparation and characterization of membranes formed by nonsolvent induced phase separation: a review. *Industrial & Engineering Chemistry Research* **2011**;50(7):3798-3817.

38. J. Schwinge, P. Neal, D. Wiley, D. Fletcher, A. Fane. Spiral wound modules and spacers: review and analysis. *Journal of Membrane Science* **2004**;242(1-2):129-153.

39. S. Qiu, M. Xue, G. Zhu. Metal–organic framework membranes: from synthesis to separation application. *Chemical Society Reviews* **2014**;43(16):6116-6140.

40. T. Tian, J. Velazquez-Garcia, T. D. Bennett, D. Fairen-Jimenez. Mechanically and chemically robust ZIF-8 monoliths with high volumetric adsorption capacity. *Journal of Materials Chemistry A* **2015**;3(6):2999-3005.

41. P. Küsgens, A. Zgaverdea, H. G. Fritz, S. Siegle, S. Kaskel. Metal‐Organic Frameworks in Monolithic Structures. *Journal of the American Ceramic Society* **2010**;93(9):2476-2479.

42. A. Cybulski, J. A. Moulijn. *Structured catalysts and reactors*: CRC press; **2005**.

43. F. Rezaei, P. Webley. Optimum structured adsorbents for gas separation processes. *Chemical Engineering Science* **2009**;64(24):5182-5191.

44. F. Akhtar, L. Andersson, S. Ogunwumi, N. Hedin, L. Bergström. Structuring adsorbents and catalysts by processing of porous powders. *Journal of the European Ceramic Society* **2014**;34(7):1643-1666.

45. W. Y. Hong, S. P. Perera, A. D. Burrows. Manufacturing of metal-organic framework monoliths and their application in CO2 adsorption. *Microporous and Mesoporous Materials* **2015**;214:149-155.

46. Y. Li, S. Perera, B. Crittenden, J. Bridgwater. The effect of the binder on the manufacture of a 5A zeolite monolith. *Powder Technology* **2001**;116(1):85-96.

47. Z. Chen, S. Deng, H. Wei, B. Wang, J. Huang, G. Yu. Activated carbons and amine-modified materials for carbon dioxide capture—a review. *Frontiers of Environmental Science & Engineering* **2013**;7(3):326-340.

48. G.-P. Hao, W.-C. Li, D. Qian, G.-H. Wang, W.-P. Zhang, T. Zhang, A.-Q. Wang, F. Schüth, H.-J. Bongard, A.-H. Lu. Structurally designed synthesis of mechanically stable poly (benzoxazine-co-resol)-based porous carbon monoliths and their application as high-performance CO2 capture sorbents. *Journal of the American Chemical Society* **2011**;133(29):11378-11388.

49. T. Jordan, Z.-L. Yu, S.-H. Yu, M. Antonietti, N. Fechler. Porous nitrogen-doped carbon monoliths derived from biopolymer-structured liquid precursors. *Microporous and Mesoporous Materials* **2018**;255:53-60.

50. L. Liu, Z. Liu, J. Yang, Z. Huang, Z. Liu. Effect of preparation conditions on the properties of a coal-derived activated carbon honeycomb monolith. *Carbon* **2007**;45(14):2836-2842.

51. P. Avila, M. Montes, E. E. Miró. Monolithic reactors for environmental applications: A review on preparation technologies. *Chemical Engineering Journal* **2005**;109(1-3):11-36.

52. E. V. Ramos-Fernandez, M. Garcia-Domingos, J. Juan-Alcañiz, J. Gascon, F. Kapteijn. MOFs meet monoliths: Hierarchical structuring metal organic framework catalysts. *Applied Catalysis A: General* **2011**;391(1-2):261-267.

53. R. Lively, R. R. Chance, W. J. Koros, H. W. Deckman, B. T. Kelley, Inventors. Sorbent fiber compositions and methods of temperature swing adsorption. US patent 8,133,308 2012.

54. R. Lively, R. R. Chance, W. J. Koros, H. W. Deckman, B. T. Kelley. Sorbent fiber compositions and methods of temperature swing adsorption: Google Patents; **2013**.

55. R. P. Lively, R. R. Chance, B. Kelley, H. W. Deckman, J. H. Drese, C. W. Jones, W. J. Koros. Hollow fiber adsorbents for CO_2 removal from flue gas. *Industrial & Engineering Chemistry Research* **2009**;48(15):7314-7324.

56. D. A. Bhandari, N. Bessho, W. J. Koros. Hollow fiber sorbents for desulfurization of natural gas. *Industrial & Engineering Chemistry Research* **2010**;49(23):12038-12050.

57. G. Chen, W. J. Koros, C. W. Jones. Hybrid Polymer/UiO-66 (Zr) and Polymer/NaY Fiber Sorbents for Mercaptan Removal from Natural Gas. *ACS Applied Materials & Interfaces* **2016**;8(15):9700-9709.

58. A. R. Sujan, D.-Y. Koh, G. Zhu, V. P. Babu, N. Stephenson, A. Rosinski, H. Du, Y. Luo, W. J. Koros, R. P. Lively. High Temperature Activation of Zeolite-Loaded Fiber Sorbents. *Industrial & Engineering Chemistry Research* **2018**.

59. B. R. Pimentel, A. W. Fultz, K. V. Presnell, R. P. Lively. Synthesis of water-sensitive metal–organic frameworks within fiber sorbent modules. *Industrial & Engineering Chemistry Research* **2017**;56(17):5070-5077.

60. J. Zhao, W. T. Nunn, P. C. Lemaire, Y. Lin, M. D. Dickey, C. J. Oldham, H. J. Walls, G. W. Peterson, M. D. Losego, G. N. Parsons. Facile conversion of hydroxy double salts to metal–organic frameworks using metal oxide particles and atomic layer deposition thin-film templates. *Journal of the American Chemical Society* **2015**;137(43):13756-13759.

61. M. Thommes, K. Kaneko, A. V. Neimark, J. P. Olivier, F. Rodriguez-Reinoso, J. Rouquerol, K. S. Sing. Physisorption of gases, with special reference to the evaluation of surface area and pore size distribution (IUPAC Technical Report). *Pure and Applied Chemistry* **2015**;87(9-10):1051-1069.

62. G. Szekely, A. G. Livingston. *Sustainable Nanoscale Engineering: From Materials Design to Chemical Processing*: Elsevier; **2019**.

63. J. Caro, M. Noack, P. Kölsch, R. Schäfer. Zeolite membranes–state of their development and perspective. *Microporous and Mesoporous Materials* **2000**;38(1):3-24.

64. A. Corma. Inorganic solid acids and their use in acid-catalyzed hydrocarbon reactions. *Chemical Reviews* **1995**;95(3):559-614.

65. M. E. Davis. Zeolites from a materials chemistry perspective. *Chemistry of Materials* **2013**;26(1):239-245.

66. N. Rangnekar, N. Mittal, B. Elyassi, J. Caro, M. Tsapatsis. Zeolite membranes–a review and comparison with MOFs. *Chemical Society Reviews* **2015**;44(20):7128-7154.

67. X. Zhao, Y. Wang, D. S. Li, X. Bu, P. Feng. Metal–Organic Frameworks for Separation. *Advanced Materials* **2018**;30(37):1705189.

68. J. A. Thompson, C. R. Blad, N. A. Brunelli, M. E. Lydon, R. P. Lively, C. W. Jones, S. Nair. Hybrid zeolitic imidazolate frameworks: controlling framework porosity and functionality by mixed-linker synthesis. *Chemistry of Materials* **2012**;24(10):1930-1936.

69. L.-G. Qiu, Z.-Q. Li, Y. Wu, W. Wang, T. Xu, X. Jiang. Facile synthesis of nanocrystals of a microporous metal–organic framework by an ultrasonic method and selective sensing of organoamines. *Chemical Communications* **2008**(31):3642-3644.

70. X. Zou, G. Zhu, I. J. Hewitt, F. Sun, S. Qiu. Synthesis of a metal–organic framework film by direct conversion technique for VOCs sensing. *Dalton Transactions* **2009**(16):3009-3013.

71. J.-R. Li, J. Sculley, H.-C. Zhou. Metal–organic frameworks for separations. *Chemical Reviews* **2011**;112(2):869-932.

72. S. Kitagawa. Metal–organic frameworks (MOFs). *Chemical Society Reviews* **2014**;43(16):5415-5418.

73. W. Kleist, F. Jutz, M. Maciejewski, A. Baiker. Mixed‐Linker Metal‐Organic Frameworks as Catalysts for the Synthesis of Propylene Carbonate from Propylene Oxide and CO2. *European Journal of Inorganic Chemistry* **2009**;2009(24):3552-3561.

74. H. Deng, C. J. Doonan, H. Furukawa, R. B. Ferreira, J. Towne, C. B. Knobler, B. Wang, O. M. Yaghi. Multiple functional groups of varying ratios in metal-organic frameworks. *Science* **2010**;327(5967):846-850.

75. P. Deria, J. E. Mondloch, O. Karagiaridi, W. Bury, J. T. Hupp, O. K. Farha. Beyond post-synthesis modification: evolution of metal–organic frameworks via building block replacement. *Chemical Society Reviews* **2014**;43(16):5896-5912.

76. S. R. Caskey, A. G. Wong-Foy, A. J. Matzger. Dramatic tuning of carbon dioxide uptake via metal substitution in a coordination polymer with cylindrical pores. *Journal of the American Chemical Society* **2008**;130(33):10870-10871.

77. M. J. Katz, Z. J. Brown, Y. J. Colón, P. W. Siu, K. A. Scheidt, R. Q. Snurr, J. T. Hupp, O. K. Farha. A facile synthesis of UiO-66, UiO-67 and their derivatives. *Chemical Communications* **2013**;49(82):9449-9451.

78. W. Xuan, C. Zhu, Y. Liu, Y. Cui. Mesoporous metal–organic framework materials. *Chemical Society Reviews* **2012**;41(5):1677-1695.

79. G. Férey, C. Serre, C. Mellot‐Draznieks, F. Millange, S. Surblé, J. Dutour, I. Margiolaki. A hybrid solid with giant pores prepared by a combination of targeted chemistry, simulation, and powder diffraction. *Angewandte Chemie* **2004**;116(46):6456-6461.

80. G. Férey, C. Mellot-Draznieks, C. Serre, F. Millange, J. Dutour, S. Surblé, I. Margiolaki. A chromium terephthalate-based solid with unusually large pore volumes and surface area. *Science* **2005**;309(5743):2040-2042.

81. J. E. Mondloch, W. Bury, D. Fairen-Jimenez, S. Kwon, E. J. DeMarco, M. H. Weston, A. A. Sarjeant, S. T. Nguyen, P. C. Stair, R. Q. Snurr. Vapor-phase metalation by atomic layer deposition in a metal–organic framework. *Journal of the American Chemical Society* **2013**;135(28):10294-10297.

82. X.-S. Wang, S. Ma, D. Sun, S. Parkin, H.-C. Zhou. A Mesoporous Metal− Organic Framework with Permanent Porosity. *Journal of the American Chemical Society* **2006**;128(51):16474-16475.

83. Q. R. Fang, G. S. Zhu, Z. Jin, Y. Y. Ji, J. W. Ye, M. Xue, H. Yang, Y. Wang, S. L. Qiu. Mesoporous metal–organic framework with rare etb topology for hydrogen storage and dye assembly. *Angewandte Chemie* **2007**;119(35):6758-6762.

84. K. Koh, A. G. Wong‐Foy, A. J. Matzger. A crystalline mesoporous coordination copolymer with high microporosity. *Angewandte Chemie International Edition* **2008**;47(4):677-680.

85. L. G. Qiu, T. Xu, Z. Q. Li, W. Wang, Y. Wu, X. Jiang, X. Y. Tian, L. D. Zhang. Hierarchically Micro‐and Mesoporous Metal‐Organic Frameworks with Tunable Porosity. *Angewandte Chemie International Edition* **2008**;47(49):9487-9491.

86. X. Roy, L. K. Thompson, N. Coombs, M. J. MacLachlan. Mesostructured Prussian blue analogues. *Angewandte Chemie International Edition* **2008**;47(3):511-514.

87. Y. Zhao, J. Zhang, B. Han, J. Song, J. Li, Q. Wang. Metal–Organic Framework Nanospheres with Well‐Ordered Mesopores Synthesized in an Ionic Liquid/CO2/Surfactant System. *Angewandte Chemie International Edition* **2011**;50(3):636-639.

88. R. L. Siegelman, T. M. McDonald, M. I. Gonzalez, J. D. Martell, P. J. Milner, J. A. Mason, A. H. Berger, A. S. Bhown, J. R. Long. Controlling cooperative CO_2 adsorption in diamine-appended Mg2 (dobpdc) metal–organic frameworks. *Journal of the American Chemical Society* **2017**;139(30):10526-10538.

89. S. J. DeWitt, H. c. O. Rubiera Landa, Y. Kawajiri, M. Realff, R. P. Lively. Development of Phase-Change-Based Thermally Modulated Fiber Sorbents. *Industrial & Engineering Chemistry Research* **2018**.

90. H. Thakkar, S. Eastman, Q. Al-Naddaf, A. A. Rownaghi, F. Rezaei. 3D-Printed Metal–Organic Framework Monoliths for Gas Adsorption Processes. *ACS Applied Materials & Interfaces* **2017**;9(41):35908-35916.

91. X. Feng, X. Ding, D. Jiang. Covalent organic frameworks. *Chemical Society Reviews* **2012**;41(18):6010-6022.

92. T. Ben, H. Ren, S. Ma, D. Cao, J. Lan, X. Jing, W. Wang, J. Xu, F. Deng, J. M. Simmons. Targeted synthesis of a porous aromatic framework with high stability and exceptionally high surface area. *Angewandte Chemie* **2009**;121(50):9621-9624.

93. T. Hasell, A. I. Cooper. Porous organic cages: soluble, modular and molecular pores. *Nature Reviews Materials* **2016**;1(9):16053.

94. M. Tsyurupa, V. Davankov. Hypercrosslinked polymers: basic principle of preparing the new class of polymeric materials. *Reactive and Functional Polymers* **2002**;53(2-3):193-203.

95. Y. Xu, S. Jin, H. Xu, A. Nagai, D. Jiang. Conjugated microporous polymers: design, synthesis and application. *Chemical Society Reviews* **2013**;42(20):8012-8031.

96. M. Rose, W. Böhlmann, M. Sabo, S. Kaskel. Element–organic frameworks with high permanent porosity. *Chemical Communications* **2008**(21):2462-2464.

97. N. B. McKeown, P. M. Budd. Polymers of intrinsic microporosity (PIMs): organic materials for membrane separations, heterogeneous catalysis and hydrogen storage. *Chemical Society Reviews* **2006**;35(8):675-683.

98. P. M. Budd, E. S. Elabas, B. S. Ghanem, S. Makhseed, N. B. McKeown, K. J. Msayib, C. E. Tattershall, D. Wang. Solution‐processed, organophilic membrane derived from a polymer of intrinsic microporosity. *Advanced Materials* **2004**;16(5):456-459.

99. V. M. Suresh, S. Bonakala, H. S. Atreya, S. Balasubramanian, T. K. Maji. Amide functionalized microporous organic polymer (Am-MOP) for selective CO2 sorption and catalysis. *ACS Applied Materials & Interfaces* **2014**;6(7):4630-4637.

100. F. Zhang, Y. Ma, Y. Kondo, V. Breedveld, R. P. Lively. A Guide to Solution‐based Additive Manufacturing of Polymeric Structures: Ink Design, Porosity Manipulation, and Printing Strategy. *Journal of Advanced Manufacturing and Processing* **2019**:e10026.

101. F. Zhang, Y. Ma, J. Liao, V. Breedveld, R. P. Lively. Solution‐Based 3D Printing of Polymers of Intrinsic Microporosity. *Macromolecular Rapid Communications* **2018**:1800274.

102. T. D. Ngo, A. Kashani, G. Imbalzano, K. T. Nguyen, D. Hui. Additive manufacturing (3D printing): A review of materials, methods, applications and challenges. *Composites Part B: Engineering* **2018**;143:172-196.

103. K. V. Wong, A. Hernandez. A review of additive manufacturing. *ISRN Mechanical Engineering* **2012**;2012.

104. Z. C. Kennedy, J. F. Christ, B. W. Arey, L. Zhong, C. A. Barrett. Tunable Porosity in Fused Filament 3D-Printed Blends of Intrinsically Porous Polymer and Thermoplastic Aliphatic Polyesters Polycaprolactone and Polylactic Acid. *ACS Applied Polymer Materials* **2019**;1(3):482-492.

105. J. R. Tumbleston, D. Shirvanyants, N. Ermoshkin, R. Janusziewicz, A. R. Johnson, D. Kelly, K. Chen, R. Pinschmidt, J. P. Rolland, A. Ermoshkin. Continuous liquid interface production of 3D objects. *Science* **2015**;347(6228):1349-1352.

106. J. A. Lewis. Direct ink writing of 3D functional materials. *Advanced Functional Materials* **2006**;16(17):2193-2204.

107. J. A. Lewis, J. E. Smay, J. Stuecker, J. Cesarano. Direct ink writing of three‐dimensional ceramic structures. *Journal of the American Ceramic Society* **2006**;89(12):3599-3609.

108. R. A. Barry, R. F. Shepherd, J. N. Hanson, R. G. Nuzzo, P. Wiltzius, J. A. Lewis. Direct‐Write Assembly of 3D Hydrogel Scaffolds for Guided Cell Growth. *Advanced Materials* **2009**;21(23):2407-2410.

109. E. B. Duoss, M. Twardowski, J. A. Lewis. Sol‐Gel Inks for Direct‐Write Assembly of Functional Oxides. *Advanced Materials* **2007**;19(21):3485-3489.

110. V. C.-F. Li, C. K. Dunn, Z. Zhang, Y. Deng, H. J. Qi. Direct Ink Write (DIW) 3D Printed Cellulose Nanocrystal Aerogel Structures. *Scientific Reports* **2017**;7(1):8018.

111. S. W. Pattinson, A. J. Hart. Additive manufacturing of cellulosic materials with robust mechanics and antimicrobial functionality. *Advanced Materials Technologies* **2017**;2(4):1600084.

112. S. Z. Guo, F. Gosselin, N. Guerin, A. M. Lanouette, M. C. Heuzey, D. Therriault. Solvent‐cast three‐dimensional printing of multifunctional microsystems. *Small* **2013**;9(24):4118-4122.

113. S.-Z. Guo, M.-C. Heuzey, D. Therriault. Properties of polylactide inks for solvent-cast printing of three-dimensional freeform microstructures. *Langmuir* **2014**;30(4):1142-1150.

114. R. Passieux, L. Guthrie, S. H. Rad, M. Lévesque, D. Therriault, F. P. Gosselin. Instability - Assisted Direct Writing of Microstructured Fibers Featuring Sacrificial Bonds. *Advanced Materials* **2015**;27(24):3676-3680.

115. H. Yuk, X. Zhao. A New 3D Printing Strategy by Harnessing Deformation, Instability, and Fracture of Viscoelastic Inks. *Advanced Materials* **2017**;30(6):1704028

116. F. Zhang, C. Tuck, R. Hague, Y. He, E. Saleh, Y. Li, C. Sturgess, R. Wildman. Inkjet printing of polyimide insulators for the 3D printing of dielectric materials for microelectronic applications. *Journal of Applied Polymer Science* **2016**;133(18):43361.

CHAPTER 2. BACKGROUND & THEORY

2.1 Porosity and Porosimetry

Efficient adsorption processes require rapid adsorption kinetics. In a porous material, the rate of adsorption (and desorption) is usually limited by the mass transportation in the pores instead of the intrinsic adsorption at the surfaces of the porous materials.[1] In this thesis, the pores of materials are defined according to the IUPAC definition: micropores refer to pores with widths equal to or smaller than 2 nm; mesopores refer to pores with widths between 2 nm and 50 nm; macropores refer to pores with widths larger than 50 nm.[2] .

2.1.1 Micropores

Microporosity is a critical property of adsorbent materials. First, microporous materials are usually associated with high surface areas. The walls confining micropores geometrically contribute to high surface areas for adsorption and enormous anchor sites for functional groups. Second, micropores, especially the interconnected ones, provide adsorbates with easy access to adsorption sites. For instance, pristine PEI liquid has negligible CO_2 capacity since the amine groups inside the PEI droplets are inaccessible to CO_2 molecules. However, when PEI is dispersed in microporous materials (e.g., zeolites, PIM-1, etc.), CO_2 could diffuse into the composite and interact with more amine groups.[3]

Cryogenic nitrogen physisorption at 77 K is the standard method to evaluate the pore size distribution and the surface area of the micromaterial. Prior to the measurement, the material is activated under high temperature and vacuum to remove the residual solvent

trapped in the micropores. The activated sample is contained in air-tight sample chambers, which are immersed in liquid nitrogen (77 K). A known amount of nitrogen is introduced into the sample chamber until the nitrogen reaches a target pressure. The nitrogen capacity of the material at each pressure is typically calculated based on the pressure change of the sealed sample chamber. The resulting nitrogen adsorption isotherms are then analyzed with the Brunauer-Emmett-Teller (BET) model to calculate BET surface areas and density function theory (DFT) models to provide estimates of pore size distributions. The BET model is ideal for Type I isotherm. When the BET model is applied to other isotherms, the BET surface area should be carefully analyzed.[4] For instance, PIM-1 exhibits a dual-mode nitrogen sorption isotherm, which is contributed by both Langmuir adsorption and polymer swelling.[5] To get a reliable BET surface area for PIM-1, only the Langmuir-dominated region of the isotherm should be utilized. Various DFT models have been developed for different pore geometries, surface homogeneities, and force field assumptions.[6] One must choose the DFT models accordingly so that the calculated pore size distribution is reliable. For instance, the pore size distribution of PIM-1 can be analyzed by HS-2D-NLDFT model, which is developed based on carbon with consideration of surface heterogeneity and nonlinear force field.[6] It is worth noting that nitrogen physisorption can theoretically only probe the features larger than the nitrogen diameter (~ 3.64 Å). However, for micropores with diameters similar to the kinetic diameter of nitrogen (~ 3.64 Å), the diffusion of nitrogen inside the micropores can be too slow to effectively probe the micropores.[7,8] In this case, the materials should be analyzed with alternative techniques, such as X-ray diffraction, positron annihilation lifetime spectroscopy, etc.[9] However, these unconventional porosimetry techniques are out of the scope of this thesis.

2.1.2 Mesopores

Mesopores can originate from either the molecular (or crystal) structure of the material or inefficient packing of the materials. Mesoporous materials are excellent supports for functional compounds. For example, amines can be supported by mesoporous zeolites at loadings as high as 39.9 wt% without completely occupying the mesopores.[10] In contrast, PIM-1 loaded with 36 wt% PEI exhibits no interconnected micropores that are accessible to nitrogen at 77K, which results in slow adsorption kinetics.[3] Mesopores are often created intentionally in adsorbent materials to create rapid mass transfer channels. For instance, the polymer solution used for hollow fiber adsorbent spinning may consist of nonsolvent, hydrophilic additive, and sacrificial pore formers to enhance the formation of mesopores that enable rapid adsorption kinetics.[11-16]

Mesopores can be characterized by both cryogenic physisorption and mercury porosimetry. Figure 2.1a exhibits a nitrogen physisorption isotherm for a mesoporous alumina fiber obtained by sintering an AlO_x/PIM-1 fiber. The hysteresis of the isotherm is a qualitative indication of the existence of mesopores. When the nitrogen pressure is increased, nitrogen molecules accumulate on the mesopore surface. Since the mesopores provide enough space for molecules to interact with each other, nitrogen molecules will fill the mesopores and behave like liquids, which is also referred to as capillary condensation. When the nitrogen pressure is decreased, the desorption of nitrogen has to overcome the surface tension, which results in higher nitrogen adsorption quantity at the same nitrogen pressure. With the help of the HS-2D-NLDFT model, the pore size distribution can also be obtained (Figure 2.1b).

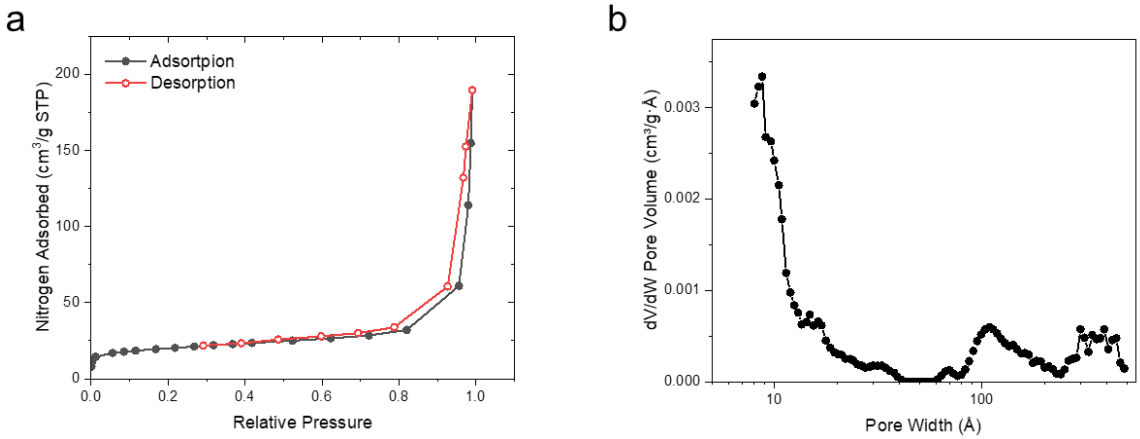

Figure 2.1 Nitrogen physisorption of mesoporous alumina fibers. (a) Nitrogen isotherm at 77 K. (b) The pore size distribution obtained by HS-2D-NLDFT model.

2.1.3 Macropores

The macropores of the material are usually generated during the device fabrication process. As shown in Figure 2.2, the PIM-1 fibers fabricated via different mechanisms possess distinct porosities: the PIM-1 fiber fabricated by drying a PIM-1/THF solution possesses a dense structure without macropores, while the fiber fabricated via phase inversion possesses interconnected macropores. Macropores of the adsorbent materials provide rapid mass transfer with the external fluids. Mercury porosimetry is the most standard method to determine the macropore size and distributions.

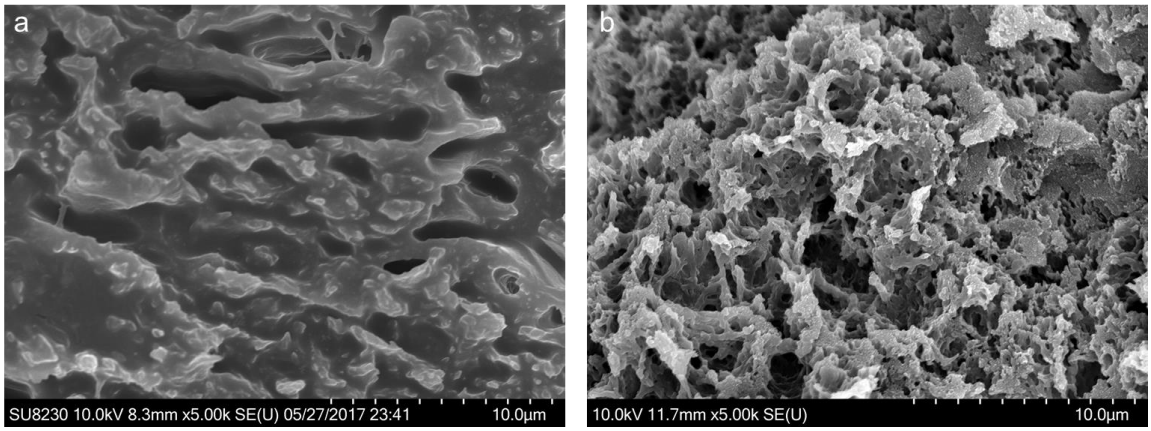

Figure 2.2 Macropores of different PIM-1 fibers revealed by SEM images. (a) Dense PIM-1 fibers fabricated by drying a PIM-1 solution. (b) Porous PIM-1 fibers fabricated by phase inversion of a PIM-1 solution.

2.2 Adsorption Isotherm

The adsorption isotherm is one of the most fundamental guides for adsorption process design and engineering. The adsorption isotherm of material records the amounts of adsorbate captured by the adsorbent at equilibrium with the adsorbate at specific relative pressures and temperature. Typical adsorption isotherm measurement techniques are the gravimetric method and the volumetric method. The gravimetric method records the weight change of the adsorbent during the exposure to adsorbate gases at specific partial pressures. Multiple strategies can be employed to control the partial pressure of adsorbate. Equipment such as VTI-SA+ (TA Instruments) keeps purging the sample chamber with a gas mixture containing adsorbate gas and inert balance gas. Equipment such as DVS (Surface Measurement Systems) can also expose the adsorbent to pure adsorbate gas with controlled pressure. Equipment such as ASAP (Micromeritics) is designed based on the volumetric method, which precisely records the volume of adsorbate gas dosed into the sample chamber, ultimately enabling the calculation of the adsorption amount.

According to the IUPAC classification, there exist six classical types of adsorption isotherms (Figure 2.3). Type I isotherms can be found in microporous adsorbent materials (e.g., microporous MOFs) with a limited external surface area. The limit of type I isotherms is determined by the micropore volume of the adsorbent material. Type II isotherms exhibit an apparent unlimited increase in uptake, which indicates multilayer adsorption without confinement from the pore structure. The turning point (A) of a type II isotherm indicates the complete monolayer adsorbate coverage and the starting of multilayer adsorption. Polymeric adsorbents (e.g., PIM-1) and macroporous materials usually exhibit type II isotherms, although the physics of adsorption may not be identical to the multilayer case just described. Type III isotherms exhibit no apparent adsorption limitation, which is relatively rare (e.g., nitrogen adsorption by polyethylene).[17] Type IV isotherms are similar to Type II isotherms. The adsorption amount keeps increasing after point B, which indicates the start of multilayer formation. However, different from Type II isotherms, Type IV isotherms exhibit a rapid adsorption amount increasing due to the complete filling of mesopores. Type IV isotherms also exhibit hysteresis. A type V isotherm is a variant of Type III isotherm. Capillary condensation in mesopores results in rapid adsorption amount increase and hysteresis. Type VI isotherms refer to step-wise adsorption isotherms. They correspond to multilayer adsorption on nonporous surfaces.

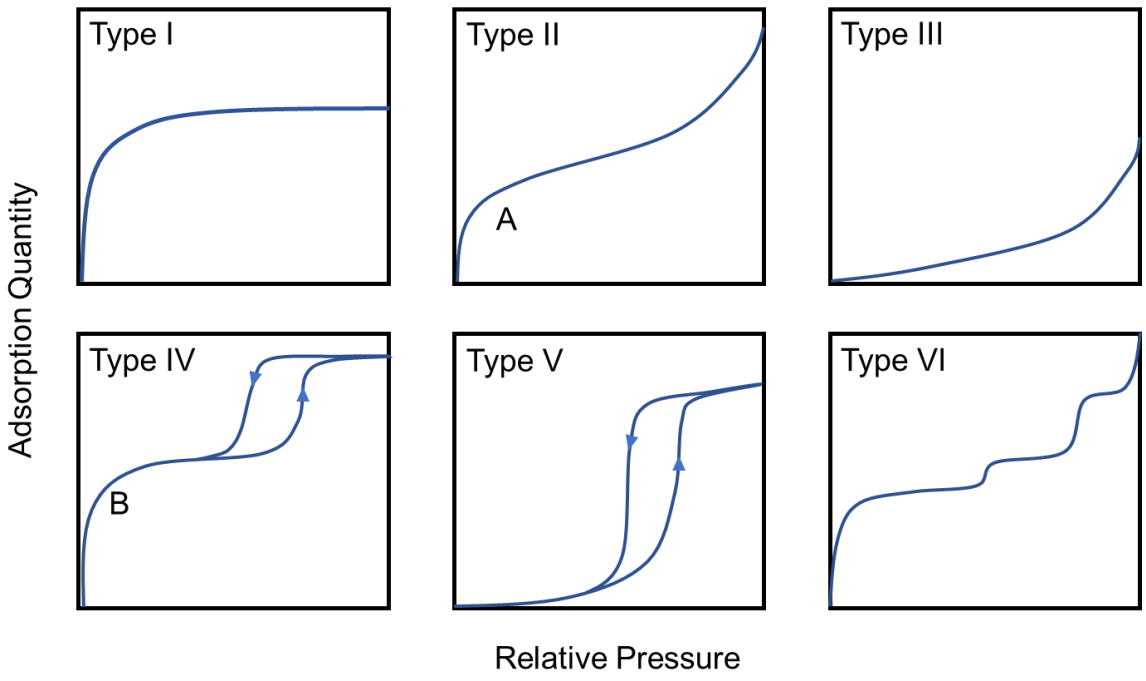

Figure 2.3 The classification of adsorption isotherms according to IUPAC definition.[17]

2.3 Adsorption Chromatography

2.3.1 Dynamic Adsorption

Kinetic adsorption performance of an adsorption contactor is evaluated via the breakthrough experiment. Figure 2.4 illustrates a classical breakthrough experiment setup.[18,19] Multiple gases are mixed as feed gas to simulate specific applications. The concentration of different components can be controlled by mass flow controllers. The premixed gas mixture can be used to eliminate the error induced by mass flow controllers. The feed gas mixture is delivered to the adsorption contactor being tested. The outlet of the adsorption contactor is attached to a union tee, which connects a mass spectrometer and a tubing coil with > 4 ft in length. The mass spectrometer samples the outlet gas every

second, and the long tubing coil prevents the back diffusion of atmospheric gases into the mass spectrometer.

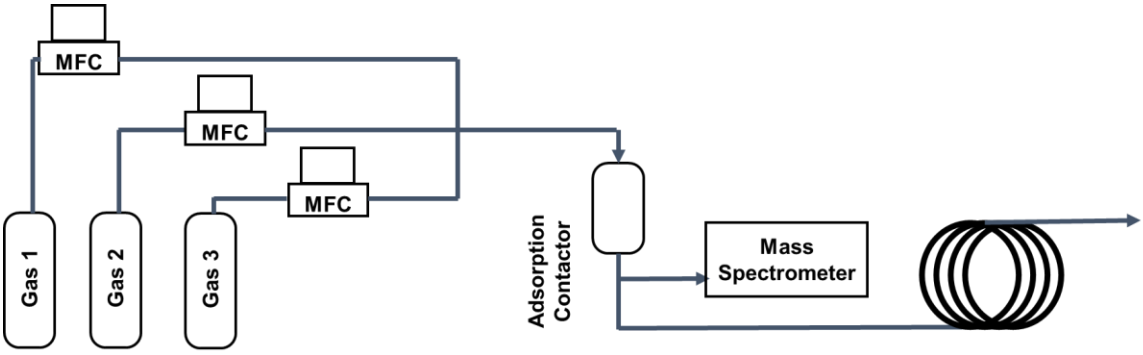

Figure 2.4 The scheme of a typical breakthrough system.

To simulate the flue gas carbon capture process, the feed gas consists of CO_2 (12.5%), He (12.5%), and N_2 (75%). CO_2 is the adsorbate, the compound that will be captured by the adsorbent materials. He is the tracer gas that indicates the flow of gases. Tracer gas and the adsorbate gas often have the same feed concentration, although this is not required. N_2 is typically the balance gas. A prototypical breakthrough curve is shown in Figure 2.5a. The concentration evolution of He indicates the theoretical concentration evolution of CO_2, assuming that there is no adsorption, which thusly captures the mean residence time of a nonadsorbing gas in the bed. The area enclosed by the breakthrough curves of He and CO_2 indicates the total adsorption capacity of the adsorption contactor. The adsorption process stops when the CO_2 emission reaches a certain threshold value (e.g., 5% of the feed concentration) to ensure low CO_2 emission and a high CO_2 recovery rate. The amount of adsorbed adsorbate before regeneration is defined as breakthrough capacity. As a result, the actual adsorption capacity can be only a small portion of the total

adsorption capacity (Figure 2.5b), although the goal of this thesis is to have the breakthrough capacity match the equilibrium capacity as closely as possible.

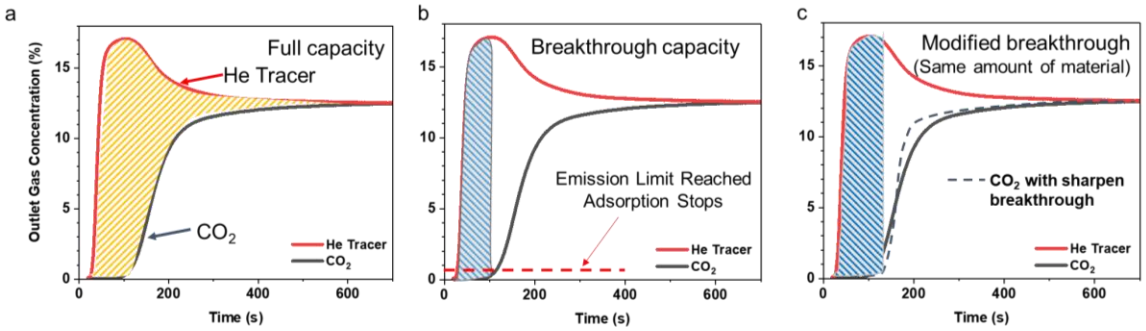

Figure 2.5 A typical breakthrough curve. (a) Total capacity. (b) Breakthrough capacity. (c) The increased breakthrough capacity of a sharpened breakthrough curve.

Such a waste of adsorption capacity will result in frequent adsorption contactor regeneration and low efficiency in operation time, material, and energy. An energy-efficient adsorption contactor is expected to increase the ratio between breakthrough and total adsorption capacity. A sharp breakthrough curve exhibits delayed adsorbate breakthrough (being detected in the outlet gas) and rapid adsorbate concentration increases. As shown in Figure 2.5c, the sharpened breakthrough curve effectively increases the breakthrough capacity.

For traditional packed-bed adsorption contactors, breakthrough curve sharpening is achieved by reducing packing pellets sizes. However, such a strategy significantly increases the pressure drop and result in higher operational costs.

2.3.2 Linear Driving Force Model

The breakthrough behavior of an adsorption contactor is usually described mathematically via the linear driving force model (LDF), which is expressed in Equation 2.1.[20] The linear driving force model can be applied to an adsorption contactor with simple material packing patterns (e.g., without variation in the fluid flow direction). Two phases exist in the adsorption contactor: the fluid phase (denoted with subscript flu), and the adsorbent phase (denoted with subscript ads).

$$\frac{\partial C_{i,flu}}{\partial t} = -v_{flu}\frac{\left(\partial C_{i,flu}\right)}{\partial z} - C_{i,flu}\frac{\left(\partial v_{flu}\right)}{\partial z} + D_{i,flu}\frac{\partial^2 C_i}{\partial z^2} - \rho_{ad}\frac{V_{ads}}{V_{flu}}K_{ov}(q^*_{i,ads} - q_{i,ads}) \qquad (2.1)$$

As shown in Figure 2.6, the fluid flowing direction is defined as z. In Equation 2.1, $C_{i,flu}$ is the adsorbate concentration in the fluid phase, which is a function of z. v_{flu} is the fluid velocity at corresponding z, which is influenced by the amount of adsorbate left in the fluid phase. V_{ads} is the volume of the adsorbent phase per contactor volume at corresponding z. Similarly, V_{flu} is the volume of the fluid phase per contactor volume at corresponding z. The LDF model assumes that the driving force for adsorption, the mass transfer of adsorbate from the fluid phase into the adsorbent phase, is the difference between equilibrium capacity, $q^*_{i,ads}$, and current capacity, $q_{i,ads}$. K_{ov} is the overall mass transfer coefficient used to describe the adsorption process. This lumped mass transfer coefficient is used to describe the mass transfer resistance contributed by the boundary layer and hierarchical pores.

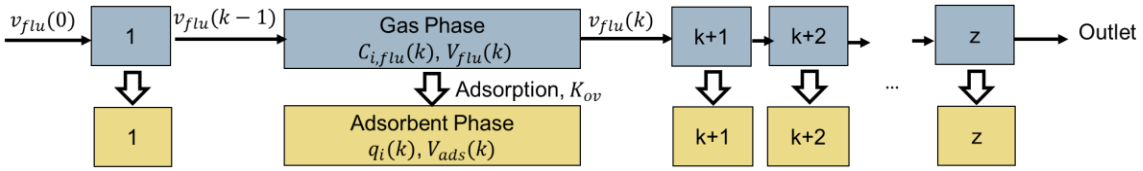

Figure 2.6 A general finite element mesh of an adsorption contactor used for the linear driving model.

According to the LDF model, adsorption contactor designs influence the breakthrough behavior by manipulating the local linear velocity, $v_{flu}(z)$, the local adsorbent/void fraction, $\frac{V_{ads}}{V_{flu}}(z)$, and interfacial mass transfer coefficient, K_{ov}. By optimizing the mass transfer contactor design, the breakthrough capacity can be improved without significantly sacrificing the pressure drop.

2.3.3 Mass Transfer Zone

During the adsorption process, different sections of the adsorption contactor have a different degree of saturation (Figure 2.7a). As shown in Figure 2.7b, when a fresh (regenerated) adsorption contactor is switched to the feed gas, the entrance region contacts with the feed gas and starts to capture adsorbate from the fluid phase. The feed gas flows through the adsorption contactor, where all of the adsorbate molecules are captured before the gas reaches the end of the adsorption contactor. As the operation time increases, the adsorbent in the front of the contactor is gradually saturated. It is important to note that within the adsorption contactor, the mass transfer only happens within a small region, which is defined as the mass transfer zone (MTZ). During the adsorption process, the mass transfer zone moves from the entrance to the outlet of the contactor (Figure 2.7b).

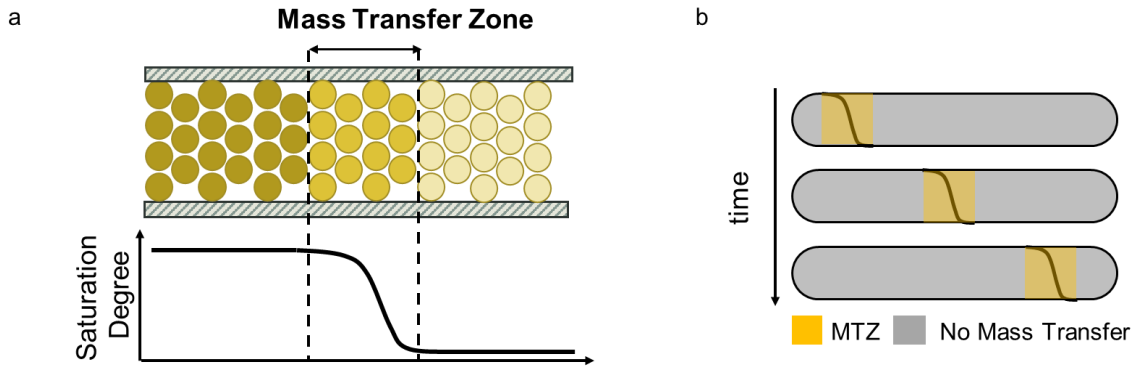

Figure 2.7 Mass transfer zone in the adsorption contactor. (a) Illustration of a mass transfer zone in the adsorption contactor at a specific moment during the adsorption process. (b) The movement of the mass transfer zone during the adsorption operation.

During this process, the adsorbent before the mass transfer zone is fully saturated, and the adsorbent after the mass transfer zone is fresh. The adsorbent out of the mass transfer zone does not contribute to the adsorption at every moment in time; however, all the materials packed in the contactor contribute to the pressure drop required for fluid delivery. Given the sample packing density, adsorbent material, and adsorption condition, the longer the adsorption contactor is, the longer the "idle" adsorbent sections (without contribution to adsorption) are.

Conceptually, short adsorption contactors have higher efficiency in material and energy usage. Compared with long adsorption contactors, short adsorption contractors require lower pressure drop, generate individual adsorbent element more frequently, and increase the efficiency in material and energy usage. However, traditional packed-bed adsorption contactors are designed with a length to diameter ratio over ten.[21] One disadvantage that limits the utilization of short packed bed adsorption contactor is a so-called bypass issue (Figure 2.8). In ideal cases, the pellets in a packed bed adsorption contactor are packed in well-organized patterns with the same porosity throughout the

contactor (Figure 2.8a). However, random packing generates regions with distinct packing densities. The regions with low density result in lower resistance to fluids, which can be considered as bypass channels. In the long contactor, these bypass channels are isolated (Figure 2.8b). However, in the case of short beds, the bypass channels could penetrate the entire contactor and result in immediate breakthrough (Figure 2.8c).

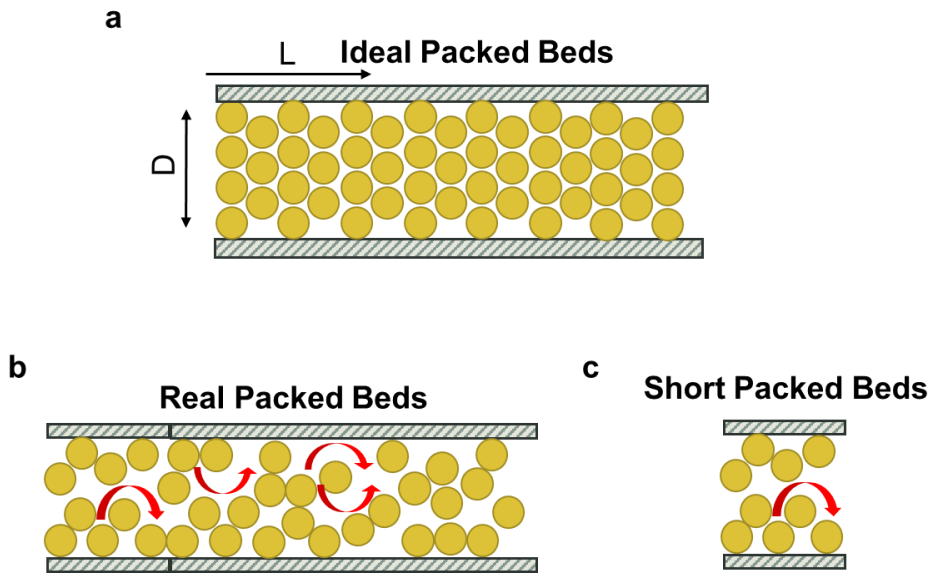

Figure 2.8 Bypass issue in packed bed adsorption contactors. (a) Ideal packed beds with an ordered packing pattern. (b) Real packed beds with random packing, showing local bypass effects of packing defects. (c) Short packed beds with severe bypass.

2.4 Fluid Rheology

2.4.1 Viscosity

Viscosity quantifies the resistance of a fluid to deformation, usually in shear flow. Figure 2.9 illustrates the mathematical definition of viscosity.[22] Depending on the relationship between viscosity and shear rate, fluids can be classified as: (1) Newtonian fluids with constant viscosity independent of shear rate, (2) shear-thickening fluids with

viscosity that increases with shear rate, (3) shear-thinning fluids with viscosity that decreases with the shear rate, (4) Bingham plastics, which behave like solids at low shear rates and like viscous fluids at high shear rates. Typically, polymer-based 3D printing inks exhibit shear-thinning behavior, while suspension-based 3D printing inks exhibit both shear-thinning (at intermediate shear rates) and shear-thickening (at high shear rates).

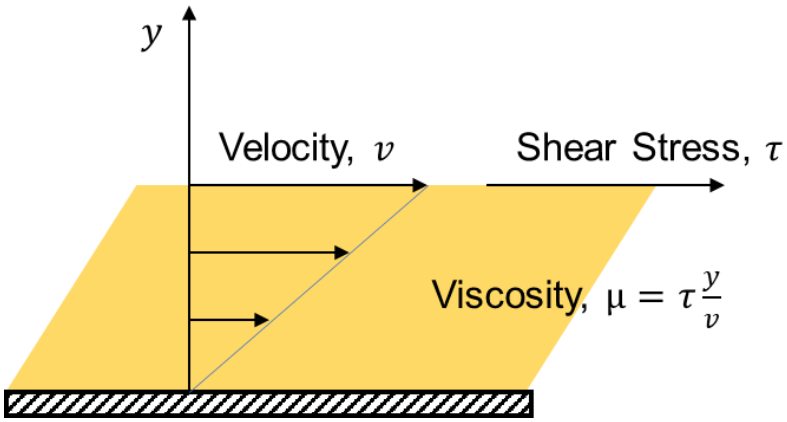

Figure 2.9 Definition of viscosity in simple one-directional shear flow.

Viscosity is usually used by 3D printing researchers to evaluate whether a 3D printing ink can be utilized for a certain 3D printing task. On one hand, viscosity must be low enough to enable sufficiently high flow rates through the nozzle; on the other hand, viscosity (and elasticity) must be high enough to enable steady filament formation without breakage. Assuming the 3D printing ink is an incompressible Newtonian fluid, the pressure drop required to deposit the 3D printing ink through the nozzle can be estimated using the Hagen–Poiseuille equation (Equation 2.2):

$$\Delta p = \frac{8\mu LQ}{\pi R^4} \tag{2.2}$$

where Δp is the pressure drop across the 3D printer nozzle, μ is the viscosity of the 3D printing ink at the operating conditions (e.g., temperature, shear rate, etc.), L is the length of the nozzle, Q is the volumetric flowrate, and R is the nozzle diameter.

2.4.2 Complex Modulus

Successful 3D printing techniques rely on rapid fluid-solid transitions of the 3D printing ink. The transition from fluid to solid can be quantified by measuring the complex modulus via oscillatory rheometry; when applied to solid-like materials, this type of measurement is also referred to as the dynamic mechanical analysis.[23]

The simplest oscillatory shear flow experiment is described in Figure 2.10a. The sample is mounted between two parallel plates. The upper plate is driven by a rotating wheel to exert displacement to the sample. The lower plate is fixed and records the stress exerted by the sample onto the lower plate. The displacement is defined as shear strain, γ, and the stress recorded is defined as shear stress, τ. Driven by the wheel, the shear strain can be described as $\gamma = \gamma_A * \sin(\theta(t))$, where γ_A is the amplitude of the shear strain, and $\theta(t)$ is the rotating angle of the driving wheel as a function of time, t. The shear stress can be described as $\tau = \tau_A * \sin(\theta(t) + \delta)$, where τ_A is the amplitude of the shear stress, and δ is the phase difference between the shear strain and the shear stress. As shown in Figure 2.10b, the strain-stress response for a typical viscoelastic material during the oscillatory test exhibits a phase shift. For an ideal elastic material, δ is zero, while δ is 90º for an ideal viscous material. The phase shift, δ, of a viscoelastic material ranges between 0º and 90º, depending on the balance between elastic and viscous forces, and can vary with frequency of deformation.

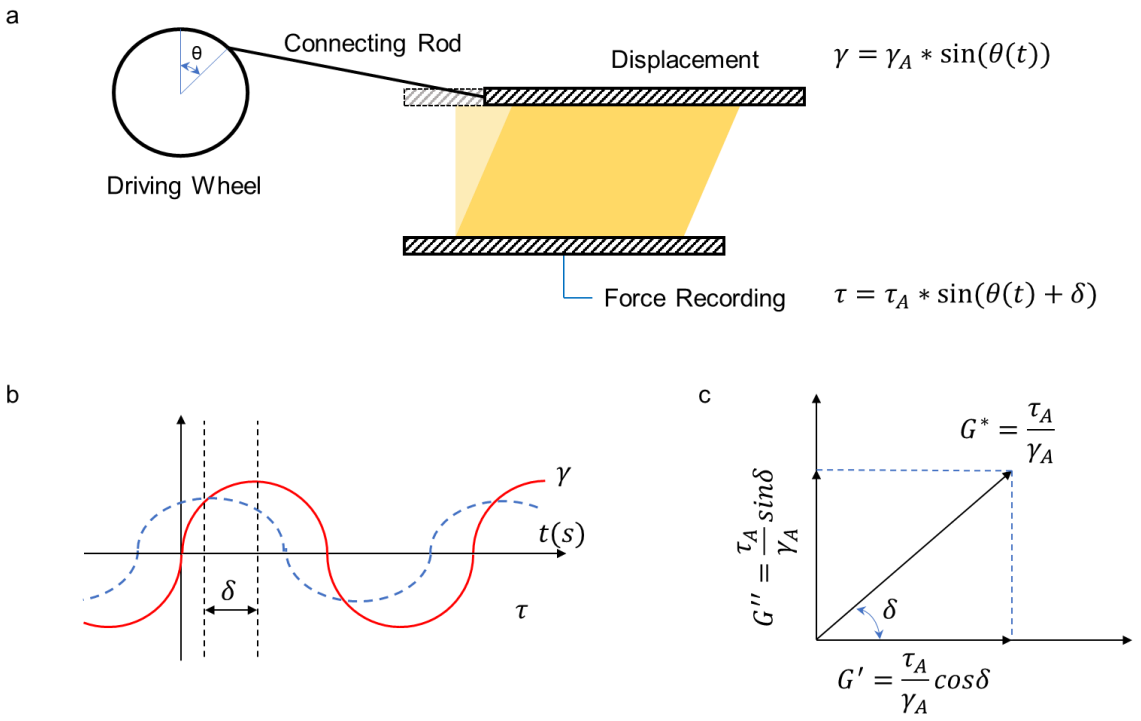

Figure 2.10 Oscillatory test of viscoelastic materials. (a) Scheme of the oscillatory test. (b) The relationship between shear strain, γ, and sheer stress, τ, for a viscoelastic material. (c) Graphical definition of complex modulus.

The viscoelastic behavior during the oscillatory test can be summarized by the complex modulus, G^*, which is defined as the amplitude ratio between shear strain, γ, and shear stress, τ, (Figure 2.10c). The storage modulus, which represents the elastic properties, is defined as $G' = \frac{\tau_A}{\gamma_A} cos\delta$, and loss modulus, which represents the viscous properties, is defined as $G'' = \frac{\tau_A}{\gamma_A} sin\delta$. An ideal 3D printing ink is expected to be predominantly fluid-like ($G'' > G'$, $45° < \delta < 90°$) before deposition, while transitioning into solid-like characteristics ($G' > G''$, $0° < \delta < 45°$) shortly after deposition, before gravity can deform the material significantly.

2.5 References

1. D. M. Ruthven. *Principles of adsorption and adsorption processes*: John Wiley & Sons; **1984**.

2. M. Thommes, K. Kaneko, A. V. Neimark, J. P. Olivier, F. Rodriguez-Reinoso, J. Rouquerol, K. S. Sing. Physisorption of gases, with special reference to the evaluation of surface area and pore size distribution (IUPAC Technical Report). *Pure and Applied Chemistry* **2015**;87(9-10):1051-1069.

3. S. H. Pang, M. L. Jue, J. Leisen, C. W. Jones, R. P. Lively. PIM-1 as a Solution-Processable "Molecular Basket" for CO_2 Capture from Dilute Sources. *ACS Macro Letters* **2015**;4(12):1415-1419.

4. K. S. Walton, R. Q. Snurr. Applicability of the BET method for determining surface areas of microporous metal− organic frameworks. *Journal of the American Chemical Society* **2007**;129(27):8552-8556.

5. M. Minelli, B. R. Pimentel, M. L. Jue, R. P. Lively, G. C. Sarti. Analysis and utilization of cryogenic sorption isotherms for high free volume glassy polymers. *Polymer* **2019**;170:157-167.

6. J. Olivier, W. Conklin, M. Szombathely. Determination of pore size distribution from density functional theory: a comparison of nitrogen and argon results. *Studies in Surface Science and Catalysis.* Vol 87: Elsevier; **1994**:81-89.

7. Y. Ma, M. L. Jue, F. Zhang, R. Mathias, H. Y. Jang, R. Lively. Creation of well‐defined "mid‐sized" micropores in carbon molecular sieve membranes. *Angewandte Chemie* **2019**;131(38):13393-13399.

8. Y. Ma, F. Zhang, S. Yang, R. P. Lively. Evidence for entropic diffusion selection of xylene isomers in carbon molecular sieve membranes. *Journal of Membrane Science* **2018**;564:404-414.

9. D. Cangialosi, H. Schut, A. Van Veen, S. Picken. Positron annihilation lifetime spectroscopy for measuring free volume during physical aging of polycarbonate. *Macromolecules* **2003**;36(1):142-147.

10. W. Chaikittisilp, H.-J. Kim, C. W. Jones. Mesoporous alumina-supported amines as potential steam-stable adsorbents for capturing CO_2 from simulated flue gas and ambient air. *Energy & Fuels* **2011**;25(11):5528-5537.

11. D. A. Bhandari, N. Bessho, W. J. Koros. Hollow fiber sorbents for desulfurization of natural gas. *Industrial & Engineering Chemistry Research* **2010**;49(23):12038-12050.

12. G. Chen, W. J. Koros, C. W. Jones. Hybrid Polymer/UiO-66 (Zr) and Polymer/NaY Fiber Sorbents for Mercaptan Removal from Natural Gas. *ACS Applied Materials & Interfaces* **2016**;8(15):9700-9709.

13. S. J. DeWitt, A. Sinha, J. Kalyanaraman, F. Zhang, M. J. Realff, R. P. Lively. Critical Comparison of Structured Contactors for Adsorption-Based Gas Separations. *Annual review of chemical and biomolecular engineering* **2018**;9:129-152.

14. R. Lively, R. R. Chance, W. J. Koros, H. W. Deckman, B. T. Kelley, Inventors. Sorbent fiber compositions and methods of temperature swing adsorption. US patent 8,133,308 2012.

15. R. P. Lively, R. R. Chance, B. Kelley, H. W. Deckman, J. H. Drese, C. W. Jones, W. J. Koros. Hollow fiber adsorbents for CO_2 removal from flue gas. *Industrial & Engineering Chemistry Research* **2009**;48(15):7314-7324.

16. B. R. Pimentel, A. W. Fultz, K. V. Presnell, R. P. Lively. Synthesis of water-sensitive metal–organic frameworks within fiber sorbent modules. *Industrial & Engineering Chemistry Research* **2017**;56(17):5070-5077.

17. K. S. Sing. Reporting physisorption data for gas/solid systems with special reference to the determination of surface area and porosity (Recommendations 1984). *Pure and Applied Chemistry* **1985**;57(4):603-619.

18. R. P. Lively, D. P. Leta, B. A. DeRites, R. R. Chance, W. J. Koros. Hollow fiber adsorbents for CO2 capture: Kinetic sorption performance. *Chemical Engineering Journal* **2011**;171(3):801-810.

19. F. Zhang, Y. Ma, J. Liao, V. Breedveld, R. P. Lively. Solution‐Based 3D Printing of Polymers of Intrinsic Microporosity. *Macromolecular Rapid Communications* **2018**:1800274.

20. J. Kalyanaraman, Y. Fan, R. P. Lively, W. J. Koros, C. W. Jones, M. J. Realff, Y. Kawajiri. Modeling and experimental validation of carbon dioxide sorption on hollow fibers loaded with silica-supported poly (ethylenimine). *Chemical Engineering Journal* **2015**;259:737-751.

21. U. Army. *Engineering and design: Adsorption design guide, Design Guide No*: DG 1110-1-2;2001.

22. R. B. Bird, W. E. Stewart, E. N. Lightfoot. *Transport phenomena*: John Wiley & Sons; **2007**.

23. T. G. Mezger. *Applied rheology: with Joe flow on rheology road*: Anton Paar; **2015**.

CHAPTER 3. SOLUTION-BASED ADDITIVE MANUFACTURING OF POLYMERIC STRUCTURES*

3D printing of polymer solution is a rising research topic as it can utilize polymers without photoreactivity or melting points. Solution-based Additive Manufacturing (SBAM) was recently reported to fabricate polymeric objects by depositing ternary polymeric inks (e.g., solutions comprising polymer, volatile solvent and nonvolatile nonsolvent), which undergo rapid phase inversion upon evaporation of a relatively small fraction of the volatile component, resulting in hierarchically porous filaments (e.g., pores of diameters ranging from 2 nm to 10 μm). SBAM is conceptually compatible with any solution-processable polymer, which significantly extends the 3D-printable polymeric material spectrum. In addition to the architecture of the printed object, its internal porosity can be manipulated for different applications. Compared with typical direct ink writing of binary polymeric inks, which typically only contain the polymer and a volatile solvent, SBAM is capable of (i) eliminating evaporation-induced shrinkage, and (ii) creating nanopores without the need for templating additives or nanoscale nozzles. The development of SBAM processes involves optimization of polymer solution thermodynamics, rheological engineering, and mass transfer control, which makes it challenging to develop an SBAM protocol for a new polymer. This section provides a practical guide towards the development of ternary polymeric inks, the design of 3D printer hardware for SBAM, and the post-treatment of printed objects for desired porosity. It also discusses solutions to common challenges encountered during this new polymer processing

* This chapter has been published in the *Journal of Advanced Manufacturing and Processing* as "A Guide to Solution-based Additive Manufacturing of Polymeric Structures: Ink Design, Porosity Manipulation, and Printing Strategy".[1]

technology. A case study of developing the optimal SBAM protocol for a commercial polyimide is provided to illustrate the process design.

3.1 Introduction

Additive manufacturing techniques enable the rapid production of complex structures and are powerful tools to aid precise architectural engineering of structured materials for applications that require controlled transport phenomena (heat and mass) or mechanical properties.[2] Compared with traditional manufacturing methods, the cost of additive manufacturing scale much less strongly with the object complexity.[3-5] Current state-of-the-art additive manufacturing techniques for polymeric materials are capable of processing photoreactive resin, photopolymer inks, thermoplastics, and elastomers via stereolithography (SL),[3,5] PolyJet,[6,7] fused deposition method (FDM),[8,9] and direct ink writing (DIW),[10,11] respectively. These additive manufacturing techniques have been utilized to fabricate polymeric objects with complex architectures for various applications such as microfluidics devices,[12] biomedical implants,[9] and light-weight structures;[11,13] however, a wide range of functional polymers of great practical interest due to their unique physical and chemical properties (e.g., polyimides, polymer of intrinsic microporosity, cellulose acetate, polysulfones, etc.) cannot be processed without chemical modification or additional matrix polymers via existing additive manufacturing techniques.[2,14]

Several of these functional polymers are currently processed in the form of polymer solutions.[15-19] By dissolving polymers in their corresponding solvents (such a solution is referred to as a ‘binary solution’ or a ‘binary ink’ in the remainder of this section), these polymers can be fabricated on an industrial scale into pellets, fibers, and films through solvent evaporation. However, binary polymer solutions are not as ideal as 3D printing inks. First, it is difficult to find a balance between fluidity and resistance to deformation.

Concentrated binary polymer solutions exhibit high viscosity, which requires high pressure for ink delivery. Dilute binary polymer solutions are subject to gravity-induced deformation, which negatively impacts shape control and printing resolution. Second, the evaporation of solvent during layer-by-layer 3D printing of binary inks induces anisotropic shrinkage. A few attempts have been made to 3D print highly concentrated binary inks of polylactide (PLA), cellulose acetate and acetoxypropyl cellulose via direct ink writing (DIW).[17,20-24] After ink deposition, the volatile solvent rapidly evaporates, creating solidified dry polymer objects. These preliminary studies established the feasibility of 3D printing of viscoelastic polymeric solutions; however, evaporation-induced anisotropic shrinkage is inevitable in these binary ink formulations. Even for a highly concentrated binary ink with 70 wt% polymer concentration, there is a 30 wt% loss of solvent after evaporation. This leads to filament shrinkage, which can result in significant deformation of the filaments and the overall printed object, especially when it occurs in the lateral dimension.[2] Differential shrinkage between subsequent layers can cause stresses that are difficult to control and predict. Therefore, this greatly impairs the precision of the shape and size of the printed objects.

Alternatively, solution-based additive manufacturing (SBAM) deposits the polymer in the form of a ternary solution (i.e., polymer, solvent, and nonsolvent), which is also referred to as a 'ternary ink'.[2] As illustrated in Figure 3.1, SBAM fabricates objects via layer-by-layer deposition of ternary ink filaments, similar to other processes. This approach is inspired by other solution-processing approaches, most notably, hollow fiber membrane spinning in the dry-jet, wet-quench configuration, in which polymer solution is extruded into a nonsolvent quench bath where it undergoes *nonsolvent-induced phase*

inversion. In the SBAM case, after filament deposition onto the substrate or existing structures, the nascent filament undergoes rapid solidification via *evaporation-induced* and/or *nonsolvent-induced phase inversion* that is triggered by small amounts of evaporation or external vapor sorption, respectively. Phase inversion rapidly transforms the liquid ternary ink into a foam-like phase-separated solid with nanoscale hierarchical pores, which cannot be achieved by other additive manufacturing techniques for polymers. The creation of pores compensates for the anisotropic shrinkage due to solvent evaporation. In our previous research, various objects made of PIM-1 (polymer of intrinsic microporosity 1) were 3D printed via SBAM.[2] The printed PIM-1 objects possess hierarchical micro-/meso-/macropores (by IUPAC definition, this nomenclature refers to pores with a diameter below 2 nm, between 2 nm and 50 nm, and above 50 nm, respectively) and exhibit potential for mass transfer applications.[2] Besides PIM-1, other solution-processable polymers such as cellulose acetate have also been 3D printed via SBAM.[2] While phase inversion of ternary polymer ink results in a hierarchical porous structure, the polymeric objects can be annealed afterward to produce a dense structure on based on use demands (Figure 3.1c). In contrast to the usual anisotropic shrinkage during 3D printing from binary inks, this isotropic shrinkage during post-fabrication annealing does not result in deformation of the overall architecture. In this article, Solution-based Additive Manufacturing (SBAM) is used exclusively for 3D additive manufacturing of multicomponent inks containing polymer, solvent, and nonsolvent.

A successful SBAM protocol requires balancing polymer solution thermodynamics, solution rheology, and mass transfer during evaporation. Multiple 3D printing properties are established concurrently, and various coupled parameters (e.g.,

ternary ink composition, equipment setup, post-treatment, etc.) should be carefully controlled. Without a thorough understanding of the underlying physical phenomena, it is impractical to efficiently develop an optimal SBAM protocol for a new polymer.

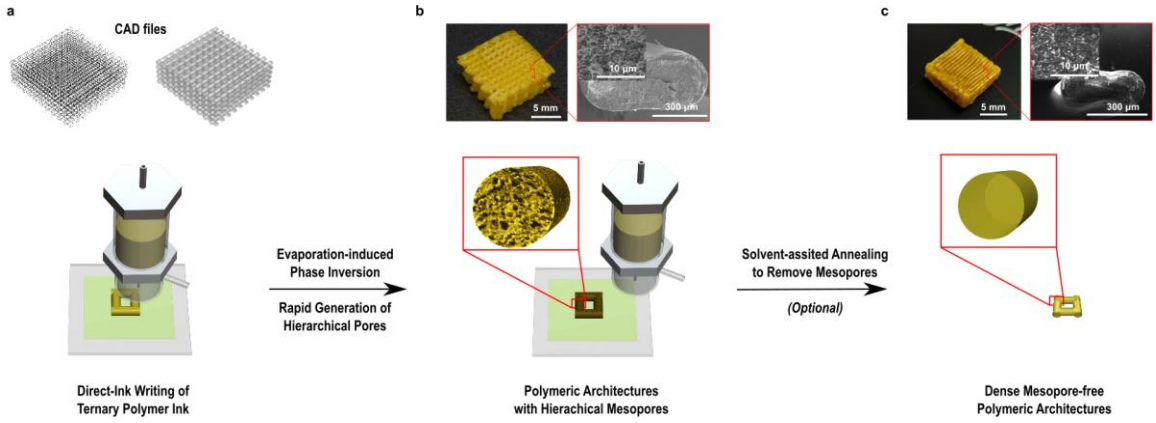

Figure 3.1 Schematic illustration of solution-based additive manufacturing (SBAM). (a) 3D printing of CAD files via direct-ink writing of a special ternary polymer ink. (b) Deposited ternary polymer ink undergoes rapid evaporation-induced phase inversion and generates hierarchical pores. A hierarchically porous Matrimid® 5218 scaffold is demonstrated with filament cross sections revealed by SEM. (c) Optional solvent-assisted annealing removes the hierarchical pores and isotropically shrinks the overall structure. An annealed Matrimid® 5218 scaffold is demonstrated with filament cross sections revealed by SEM.

This section provides a systematic guide for solution-based additive manufacturing of the general class of solution-processable polymer. Conceptually, SBAM is applicable to any polymer that can be dissolved by solvents and for which non-solvents are available. Design principles of the ternary ink and porosity manipulation strategies are discussed. A case study is also presented of the development of the SBAM protocol for the production of monolithic structures of different porosity from a commercially available polyimide.

3.2 Solution-based Additive Manufacturing Methodology

Solution-based additive manufacturing (SBAM) is conducted with a customized 3D printer that is adapted from a generic direct ink writing (DIW) setup.[2] As illustrated in Figure 3.1, the substrate is attached to a moving stage that can move in two orthogonal directions (*x* and *y*). Stepper motors, transmission components, and controllers satisfying the SBAM resolution are selected to control the motion. For instance, the SBAM setup in this work consists of stepper motors with a 1.8° step angle, timing belts with 2 mm pitch, a timing pulley with 14 teeth, and motor driver with 1/16 microstepping; this design results in 9 μm linear resolution for the stage. A stainless-steel ink container is attached to a motion glide that can move in the vertical direction (*z*). The motion glide consists of a stepper motor with a 1.8° step angle, a leadscrew with 1.25 mm pitch, and a motor driver with 1/16 microstepping, which results in 0.5 μm linear resolution. A homogenous ternary ink with optimized rheological properties is pressurized and deposited through the bore of a customized coaxial dual-channel stainless-steel micronozzle (Figure 3.2). The diameter of the micronozzle bore is selected based on the desired resolution. For instance, the SBAM setup in this current study utilizes a 24-gauge needle with an inner diameter of 311 μm. The ternary ink liquid filament travels through a short air gap (the distance between the nozzle exit and the substrate), where volatile solvents evaporate and/or nonsolvents are sorbed into the filament to trigger solidification induced by phase inversion. A carrier gas with a tunable solvent vapor concentration can be delivered through the shell of the micronozzle to control the atmosphere surrounding the filament and thus the solvent evaporation rate (Figure 3.2b).

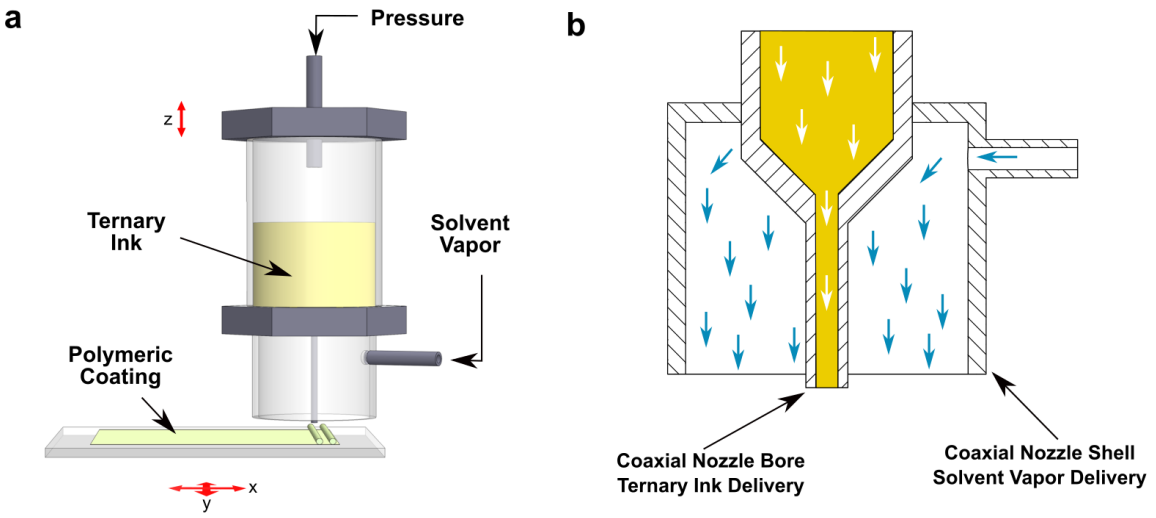

Figure 3.2 General 3D printer setup for SBAM. (a) Direct-ink writing 3D printer equipped with the atmosphere control accessory and a substrate coated with polymer. (b) The scheme of the customized atmosphere control accessory.

High-fidelity DIW 3D printing of a binary ink is inherently difficult. Solvent evaporation from the filament intrinsically leads to the contraction of the individual filaments and deformation of the overall structure.[2] Figure 3.3a illustrates a scenario where the DIW 3D printer attempts to fabricate a cuboid by depositing polymeric filaments from a binary ink in layer by layer fashion. The deposited filaments start shrinking once they are deposited. When a new filament is deposited on top of the previously deposited structure, which has already partially contracted due to evaporation, the larger shrinkage of the fresh filament will cause stresses that bend the old filament and deform the entire object.

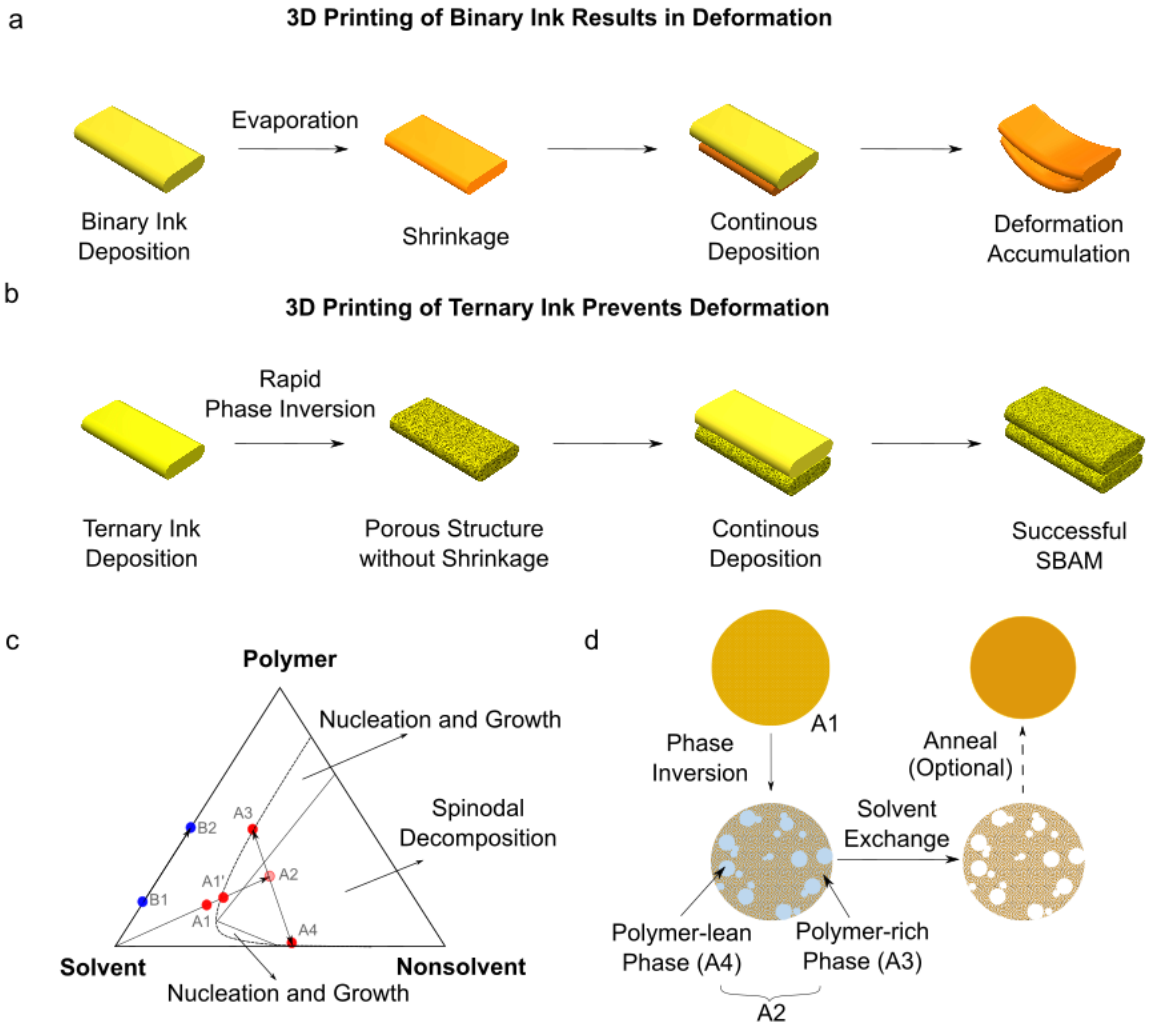

Figure 3.3 Comparison between the solidification mechanisms of binary and ternary inks. (a) Solidification of a binary ink induced by solvent evaporation, resulting in poorly controlled object shrinkage; (b) Solidification of a ternary ink induced by phase inversion without object shrinkage; (c) A typical phase diagram for ternary system (polymer, solvent, and nonsolvent) to guide ink design; (d) Phase inversion route that compensates the evaporation-induced shrinkage via the creation of hierarchical pores. A1: an ideal ternary ink for solution-based additive manufacturing; A1': the liquid-to-solid transition of the ternary ink; A2: the mixture composition of the ternary ink after partial evaporation; A3: the polymer-rich phase after spinodal decomposition; A4: the polymer-lean phase after spinodal decomposition. A1-A1' represent the composition shift required for ternary ink solidification. B1: the binary ink with the viscosity comparable to the ternary ink A1; B2: the liquid-to-solid transition of the binary ink. B1-B2 represent the composition shift required for the binary ink solidification.

Unlike binary inks, in which solidification is achieved by evaporation, solidification of a ternary ink is achieved by phase inversion, which is a common phenomenon used in fiber spinning industries.[25] Phase inversion results in hierarchically porous polymeric structures that avoid the evaporation-induced shrinkage (Figure 3.3b). Phase inversion is typically visualized by the ternary phase diagrams such as the one shown in Figure 3.3c. A general ternary phase diagram can be divided into two regions: the homogeneous, stable one-phase region and the nonhomogeneous, unstable two-phase region. These two regions are separated by the binodal boundary. A ternary ink with a composition in the homogeneous region is transparent and fluidic, while the ternary ink with a composition in the *nonhomogeneous* region is unstable and undergoes phase inversion into a polymer-rich phase and a polymer-lean phase.

Phase inversion can occur via "nucleation and growth" and "spinodal decomposition" processes when the solution composition is shifted from the homogenous into the nonhomogeneous region through solvent evaporation and/or nonsolvent sorption. As shown in Figure 3.3c, the nonhomogeneous region can be further divided by the spinodal boundary into regions of nucleation-and-growth (between the spinodal boundary and the binodal boundary) and spinodal decomposition (within the spinodal envelope). For a mixture in the lower nucleation-and-growth region (the one with lower polymer concentration in Figure 3.3c), polymer nodules are formed resulting in dispersive polymer-rich phases in a continuous polymer-lean phase. After complete drying, the phase inverted mixture produces an agglomeration of powders with low mechanical integrity, which cannot be used for 3D printing of robust polymeric objects. For a mixture in the upper nucleation-and-growth region (the one with higher polymer concentration in Figure 3.3c),

nucleation of dispersive polymer-lean phases generally leads to relatively closed-cell structures in the polymers after complete removal of all solvents and non-solvents. Although such closed-cell structures possess high integrity and compensate the evaporation-induced shrinkages, polymer-lean phases in the closed cells cannot be removed rapidly after phase inversion, which can lead to the collapse of the porosity (this may be desired in certain applications). On the other hand, mixtures that enter the spinodal decomposition region invert into interpenetrated polymer-rich phases and polymer-lean phases. The resulting interconnected hierarchical pores allow rapid removal of residual polymer-lean phases, which effectively prevents the collapsing of pores. Spinodal decomposition is therefore usually desirable for SBAM.

Figure 3.3c and Figure 3.3d illustrate the ideal evolution of ink composition during the spinodal decomposition. A ternary ink filament (composition A1 in the homogeneous region) is extruded from the nozzle. The evaporation of the solvent shifts the ink composition across the binodal boundary to point A2, which possesses higher polymer concentration, lower solvent concentration, and higher non-solvent concentration. This mixture then undergoes spinodal decomposition and inverts into interconnected polymer-rich phases (A3) and polymer-lean phases (A4), which together form a solid-like structure that can withstand gravity. The solidified porous polymer object (A3) can then be dried immediately to get rid of liquids (A4), which leads to isotropic shrinkage. Such isotropic shrinkage will not deform the printed object; however, it leads to a change of object dimension and partial collapse of pores. Alternatively, a post-printing solvent exchange is an optional procedure to avoid shrinkage during drying. During the solvent exchange, the solvent and nonsolvent in the polymer-lean phase are exchanged with solvents with low

surface tension, which then evaporates and leaves mesopores and macropores. The polymer-rich phase dries and results in the formation of robust polymeric skeletons (Figure 3.3d). This pore formation process compensates the volume loss due to solvent evaporation that is dominant in binary inks, thus preventing shrinkage during 3D printing (Figure 3.3b).

Besides volume-loss compensation, ternary inks can also achieve faster solidification (A1-A1' in Figure 3.3c) than binary inks (B1-B2 in Figure 3.3c) when both inks start off initially with comparable, printable viscosities. As suggested by a previous rheological study, the solidification of binary PIM-1 ink (25 wt.% in tetrahydrofuran) requires evaporation of at least 5 wt.% solvents while the solidification of the ternary PIM-1 ink (20 wt.% in tetrahydrofuran and dimethylacetamide) requires less than 1 wt.% removal of nonsolvent.[2] The faster solidification further helps to resist gravity-induced deformation.[2]

The generation of hierarchical pores without templating material is a unique feature of SBAM. Pores at different length scales instill different levels of functionality to the 3D printed architectures. The 3D printer can directly fabricate large macropores, the size of which is usually larger than 100 μm depending on the resolution of the specific 3D printer; these pores can be used to design paths for convective bulk fluid flow. Smaller macropores can be generated via phase inversion of multicomponent polymer solutions. These smaller macropores can serve as fluid distribution channels through diffusion (e.g., mass transfer contactor, microfluidic devices, etc.) or simply reduce the weight of the architecture. Mesopores are also generated by phase inversion and provide fast mass transfer for guest molecules in applications like adsorption, catalysis, membrane separation, etc. Finally, microporosity occurs on the molecular scale and is usually an intrinsic property of

polymers; these smallest pores can provide molecular sieving for separations, and large surface area and active sites for adsorption, catalysis, etc. The combination of hierarchical pores (e.g., macro-/meso-/micro-pores) provides versatile combinations of functionalities for a range of applications.

3.3 General Process-design Guidelines for Solution-based Additive Manufacturing

This section provides a general guide for producing an arbitrary object via solution-based additive manufacturing from a newly selected solution-processable polymer. The semi-empirical process described here includes three keys steps: determination of ternary ink formulation, substrate design, and porosity manipulation.

3.3.1 Determination of Ternary Ink Composition

The ternary phase diagram of the polymer solution guides the phase inversion pathway, which is critical for the SBAM fabrication process. The homogenous region, nonhomogeneous region, and binodal curve can be determined by the cloud-point technique, as described in detail in Section 3.4.1. To facilitate rapid liquid-to-solid transition, the ink composition must be chosen near the binodal curve for fast phase inversion. Figure 3.4a illustrates the determination of ternary ink compositions that allow rapid phase inversion. For an ideal ternary ink consisting of volatile solvent, nonvolatile nonsolvent, and polymer, all the lines (dashed lines denoted as 1) starting from the solvent pole represent potential evaporation trajectories of ternary inks. During SBAM, solvent evaporation shifts a ternary ink (A1) along the trajectory (A1-A2) into the nonhomogeneous region. The phase inversion distance (A1-A2) that the ternary ink should travel before entering the nonhomogeneous region is related to the time required for

solidification. For common SBAM scenarios, gravity-induced deformation can be eliminated by shortening the phase inversion distance A1-A2 to below 1 wt% of solvent removal. The shaded area (3) defines all ink compositions with phase inversion distance (2) shorter than 1 wt%, which represents the "ideal" composition range.

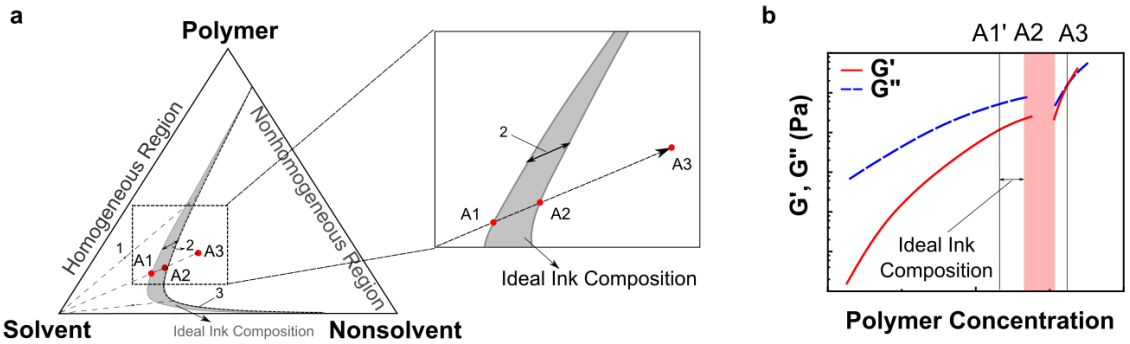

Figure 3.4 Method for determining appropriate ternary ink composition. (a) Typical ternary phase diagram (polymer, solvent, and nonsolvent). 1: dashed trajectories of solvent evaporation; 2: lengths indicate the amount of solvent evaporation assuming instantaneous mass transfer and no phase inversion between the termini of lines; 3: the shaded area denotes compositions that undergo rapid phase inversion; A1: the ideal ternary ink; A2: the transition region indicating phase inversion; A3: the fully phase-inverted ideal ternary ink. insert: Zoomed phase diagram illustrating the ink composition evolution. (b) The typical evolution of complex modulus (G′: storage modulus; G″: loss modulus) during evaporation-induced phase inversion of a ternary ink.

In addition to the requirement for rapid phase inversion, the rheological evolution of the ternary ink must also be considered. The rheological properties of the ternary ink can best be analyzed via investigation of the complex moduli.[2] Figure 3.4b highlights the desired rheological evolution of an optimized ternary ink during the evaporation-induced phase inversion, where the x-axis corresponds to the phase inversion trajectory (A1-A2-A3) in Figure 3.4a. The original ternary ink possesses lower storage modulus than loss modulus, which ensures good fluidity and flow behavior during ink delivery through the nozzle. As the volatile solvent evaporates, the polymer concentration increases and both

the loss modulus and storage modulus increase. The onset of phase inversion (A2) can be detected as a transition region in this type of rheological characterization. As evaporation continues, the ternary ink composition shifts to A3, upon which the phase inversion is completed. The ratio of loss modulus to storage modulus (also known as tan δ) at the complete phase inversion composition (A3) should be smaller than one to avoid structural collapse after initial filament deposition. The shaded region (A2-A3) in Figure 3b indicates the transition during phase inversion. The gap between A1′ and A2 indicates the potential ternary ink composition that meets the rheological requirements; as a rule of thumb we have found that at concentration A1′ the loss modulus should exceed 200 Pa.[2] In Section 3.4.3 and Section 3.4.4, a detailed ternary ink optimization process is described.

It is worth noting that the filament diameter can affect the phase inversion "trajectory" due to heat and mass transfer. For a high-resolution SBAM protocol, the ternary ink composition should be shifted toward the pole representing pure solvent in the ternary phase diagram. The lower polymer concentration then reduces the pressure drop required for extrusion through narrow nozzles, lowers the storage modulus and improves the drawability of the polymeric filaments. Improved drawability promotes higher printing resolution (e.g., thinner filaments), as is discussed in more detail in Section 3.3.2. Finally, a smaller filament diameter results in higher surface area to volume ratio, which facilitates evaporation. By shifting the ink composition away from the binodal curve, solidification of the filament can be delayed until the completion of deposition. Increased volatile solvent concentration retards filament solidification.

3.3.2 Atmosphere Control in Solution-based Additive Manufacturing

Although fast evaporation of the volatile solvent facilitates rapid solidification and avoids gravity-induced deformation of the filaments, an ultra-high evaporation rate also has negative side effects.

First, rapid solvent evaporation could shift the local mixture composition of the skin layer (e.g., the outer radius of the filament) deep into the nonhomogeneous region. This potentially allows the mixture composition to enter the so-called vitrification region, creating a dense polymer skin that retards mass transfer out of the filament.[26-29] Although skin vitrification is widely utilized in hollow fiber membrane spinning industry,[26] it is generally not desired in SBAM, because reduced mass transfer of solvent out of the filament leads to slow phase inversion of the entire filament, thus allowing greater structural deformation due to gravity (this is discussed in more detail in Section 3.5). Moreover, skin layers on the 3D printed structures are not desired in structures for which rapid mass transfer is required in the final application, unless membrane devices are the desired structure being printed.[2]

Second, the rapid removal of solvents can result in poor interlayer adhesion. Interlayer adhesion of SBAM is assisted by partial, localized redissolution of already deposited, phase inverted filaments by newly deposited filaments. The swollen, plasticized nature of the polymer in the filament-filament contact region promotes polymer-polymer interaction, which improves the filament-filament adhesion.

Solvent evaporation rates can be efficiently manipulated by changing the degree of solvent saturation around the filament and printed objects. Evaporation is driven by the

chemical potential difference between the solvent in the ternary ink and the solvent vapor in the adjacent atmosphere, of which the former is mainly determined by the ternary ink composition and the latter is mainly determined by the partial pressure of solvent vapor. Through the use of a secondary nozzle in the SBAM setup (Figure 3.1c), gases with controlled partial pressures of solvent and nonsolvent can be delivered into the atmosphere surrounding the printing stage. For instance, nitrogen saturated with tetrahydrofuran was continuously supplied during the SBAM of PIM-1; this modification significantly slowed evaporation, eliminated the formation of skin layers, and improved the adhesion between adjacent filaments.[2]

3.3.3 Resolution Control of Solution-based Additive Manufacturing

The ability to manufacture small-scale structures through SBAM fundamentally enables the design of novel high-performance polymer devices, but creating such small-scale structures requires high-resolution 3D printing.[30] For instance, an interdigitated microbattery architecture fabricated through direct ink writing has been reported to exhibit high areal energy density (9.7 J cm^{-2}) and power density (2.7 mW cm^{-2}) due to the high aspect ratio of the device.[31] Here, the resolution of the SBAM 3D printer is defined as the linear dimension of the finest feature that can be reproduced, which is either the smallest width of a single polymer filament, or the smallest reproducible gap between two adjacent filaments.

Traditional direct ink writing (DIW) technology deposits the ink onto the substrate with an air gap (the distance between the nozzle and the substrate) equal to the nozzle diameter. While smaller filaments can be produced via nozzles with smaller openings, it is

impractical to use micronozzles (e.g., diameter smaller than 100 μm) to process viscoelastic polymer solutions. First, the pressure drop required for ternary ink delivery is roughly inversely proportional to the second power of the nozzle diameter.[32] Second, die swell of concentrated, viscoelastic polymeric fluids at the nozzle outlet often results in expanded filament diameters, which offsets the gains from the smaller nozzle (Figure 3.5a).[33]

It is important to note that dry-wet fiber spinning techniques are capable of fabricating fibers with diameters smaller than the nozzle (or spinneret) diameter via drawing-induced narrowing. Generally, the viscoelastic polymer solution is extruded through a spinneret and collected on a rotating drum.[29] As the linear speed of the edge of the rotating drum (draw speed) is faster than the linear extrusion speed at the outlet of the spinneret, the final fibers collected on the rotating drum possess smaller diameters than the bore diameter of the spinneret. For instance, hollow fiber membranes with a 200-μm outer diameter and a 100-μm inner diameter can be fabricated via a coaxial spinneret with a 900-μm outer diameter and a 200-μm inner diameter.[29] Such deformation of the viscoelastic filament has also been utilized in recent reports on the direct ink writing of silicone gel to improve 3D printing resolution.[34,35] In these approaches, the deformation of a viscoelastic fluid is harnessed by engineering the air gap height, feed rate, the printing speed. The 3D printing resolution can thus be improved beyond the nozzle size.

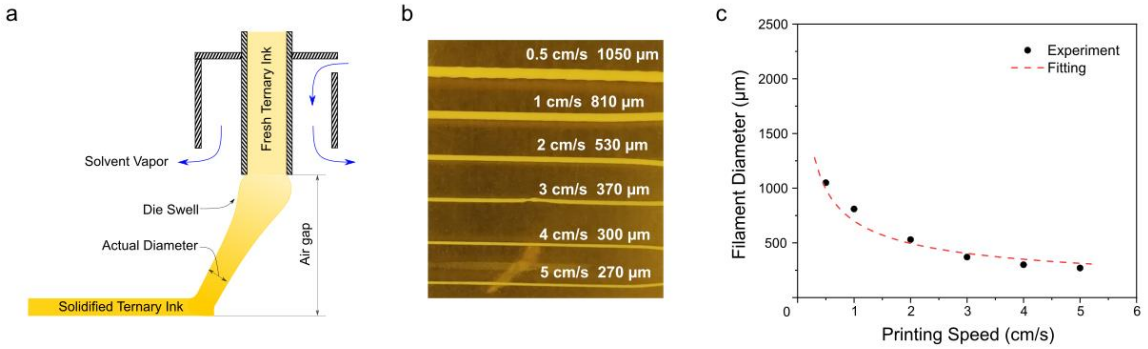

Figure 3.5 (a) Schematic of the resolution control method for solution-based additive manufacturing, which relies on drawing-induced narrowing of a ternary polymeric filament in the air gap; (b) Matrimid® 5218 ternary ink printed with varying linear moving speed, G22 nozzle (inner diameter 413 μm), 1-mm air gap, 10 bar driving pressure; (c) The relationship between filament diameter and printer speed can be easily described by the continuity equation with a lumped factor (Equation 3.2).

Inspired by dry-wet fiber spinning and direct ink writing,[28,29,34] SBAM can also manipulate the 3D printing resolution via controllable drawing-induced filament narrowing, as illustrated in Figure 3.5. During extrusion, the polymer chains are assumed to be aligned due to the high shear rate within the nozzle. Once the fluid flows out of the nozzle, the polymers tend to regain spherical conformations driven by entropy, which increases the filament diameter through a process known as die swell.[33] The deposited filament travels through an air gap (the distance between the nozzle and the substrate) and adheres onto previously deposited filaments. The air gap, which is set to exceed the dimensions of the die swell, is the region where the elongation and thinning of filaments occur. By controlling the printing speed and feed rate, the size of the deposited filament can be tuned in a reproducible manner without changing the nozzle diameter. While the viscoelastic polymer solution may undergo complex shape evolution during the drawing process, the relationship between printing speed and the target resolution can be

straightforwardly determined via continuity equation of incompressible fluids (Equation 3.1).

$$F_{feed}\left(P_{feed}, D_{nozzle}\right) \sim \frac{D_{filament}^2 \cdot v_{print}}{4} \tag{3.1}$$

where F_{feed} is the volumetric feed flowrate for the ternary ink, which is determined by the driving pressure (P_{feed}) and nozzle diameter (D_{nozzle}), $D_{filament}$ is the resulting filament diameter, v_{print} is the linear printing speed.

As shown in Figure 3.5b, Matrimid® 5218 ternary ink was continuously delivered through a micronozzle (inner diameter is 413 μm) driven by 10 bar pneumatic pressure with a 1-mm air gap. By varying the linear printing speed from 0.5 cm/s to 5 cm/s, the width of the deposited filament is varied from 1050 μm to 270 μm. Assuming the ternary ink possess the cylindrical shape after the drawing process, the expected filament width can be calculated via Equation 3.2, which is derived from Equation 3.1 (Figure 3.5c).

$$D_{filament} \sim 2\sqrt{F_{feed}} \frac{1}{v_{print}} \sim A \frac{1}{v_{print}} \tag{3.2}$$

where the lumped factor A, which accounts for minor volume changes during phase inversion, can be generated via data fitting.

There are three determining factors for enabling successful resolution control via viscoelastic manipulation of the filaments. First, the ternary ink should behave as a viscoelastic fluid while in the air gap. Second, the solvent evaporation rate should be controlled within the air gap; rapid evaporation of the volatile solvent could trigger

premature phase inversion or skin layer formation of the filament before it is deposited onto the substrate, which could lead to filament breakage under the unequal drawing speed and feeding speed. Third, good adhesion between filaments and substrates are required. If the deposited filament does not adhere well to the substrate, it will be dragged by the nozzle instead of forming the intended printed architecture.

The experiments with Matrimid ternary ink demonstrate the feasibility of resolution manipulation via drawing-induced narrowing. The target resolution can be easily calculated based on the continuity of fluid. Since the volume shrinkage due to evaporation is compensated by the generation of hierarchical pores, SBAM can achieve different levels of resolution with one nozzle in a straightforward manner. To achieve high-quality 3D additive manufacturing, control software and 3D printing route generation software that considers motor acceleration and deceleration at corners must be developed in the future.

3.3.4 Substrate Design

A 3D printing substrate should ideally hold the printed objects firmly in place during the printing process while also allowing the printed objects to be easily released from the substrate after the printing is completed.

While glass plates have been widely used as universal substrates for 3D printing owing to their flatness and smoothness, these surfaces may not bond tightly with the phase-inverted ternary filaments due to the presence of excess nonsolvent.[2] Applying adhesives to the glass plates is a common approach to secure 3D printed objects in place;[36,37] however, polymeric adhesives often do not provide sufficient interaction with the ternary ink due to the swelling or even complete dissolution induced by the ink solvent or nonsolvent. For

instance, during the solution-based additive manufacturing of PIM-1, the phase inverted ternary ink contained a significant amount of the nonsolvent, DMAc, which served as a lubricant between the glass plate and the printed objects. As a result, the printed PIM-1 objects shifted around on glass plates, which caused significant misalignment between consecutive layers. Instead, polymeric plates or glass plates with a polymeric coating can be good alternative substrates to glass plates. The polymer used as substrate should be miscible with the polymer used for SBAM and can be dissolved by the corresponding solvent and nonsolvent in the ink. Once the bottom layer is deposited onto the polymeric substrates, solvent and nonsolvent in the ternary ink partially dissolve the polymeric surface, allowing polymer chains of the substrate and the deposited polymers to entangle, which secures the deposited object in place. After SBAM, the detachment of printed objects from the substrate can be achieved by removing the bottom sacrificial layer.

For SBAM of polymers that are immiscible with commonly available polymer plates, the most practical substrate is a glass plate coated with a thin (~40 μm) layer of the polymer that is being 3D printed (Figure 3.2a). Such substrates can be prepared by blade casting of a binary polymer solution onto clean glass plates.[38] After SBAM, the printed objects can be detached from the substrate by sliding a razor blade between the polymer film and the glass plate. In the case where a hydrophobic polymer coating is utilized, the detachment can be finished by immersing the substrate and printed objects into a water bath. As the glass plate is hydrophilic while the polymer film is hydrophobic, water peels the film and the bonded objects off the glass plate. The thin polymer film can be destroyed physically (e.g., by sanding) afterwards. The residual polymer film on the 3D printed object

may result in a lower porosity in the bottom layer. A sacrificial bottom layer can be printed and then destroyed when consistent porosity is required.

3.3.5 Porosity Manipulation: Creation and Removal

Phase inversion of polymer solutions results in well-distributed macropores (diameter larger than 50 nm) and mesopores (diameter ranging from 2 nm to 50 nm). Various applications (e.g., membrane separation, heterogeneous catalysis, adsorption, etc.) involving mass transfer utilize the hierarchically porous nature of phase inverted polymer structures. The creation of this pore structure occurs during phase inversion and is mainly determined by the ternary ink composition and the phase inversion route.

Figure 3.6a illustrates a typical evaporation-induced phase inversion route (A1-A2) of a ternary polymer solution (A1) consisting of polymer, volatile solvent and nonvolatile nonsolvent. As shown in the ternary phase diagram, evaporation shifts the solution composition away from the pole representing the volatile solvent, until the phase inversion (A2-A3, A2-A4) is complete. Depending on the position of the local mixture composition (A2) on the tie line connecting the polymer-rich phase (A3) and the polymer-lean phase (A4), the ratio between these two phases varies according to the lever rule. Changing the ink composition can effectively manipulate the resulting porosity. Figure 5b illustrates the methodology of enhancing porosity by decreasing the polymer concentration of the ternary ink. A ternary ink with decreased polymer concentration (B1) undergoes evaporation-induced phase inversion along the trajectory indicated by B1-B2. For the ease of comparison assume that the new demixing mixture composition lies on the same tie line (A3-A4), in which case the new ternary ink with lower polymer concentration results in a

greater fraction of polymer-lean phase after phase inversion (according to the lever rule, B2 is closer to A4 compared with A2), thus increasing the porosity of the final object. Similarly, increasing the polymer concentration can effectively reduce the porosity.

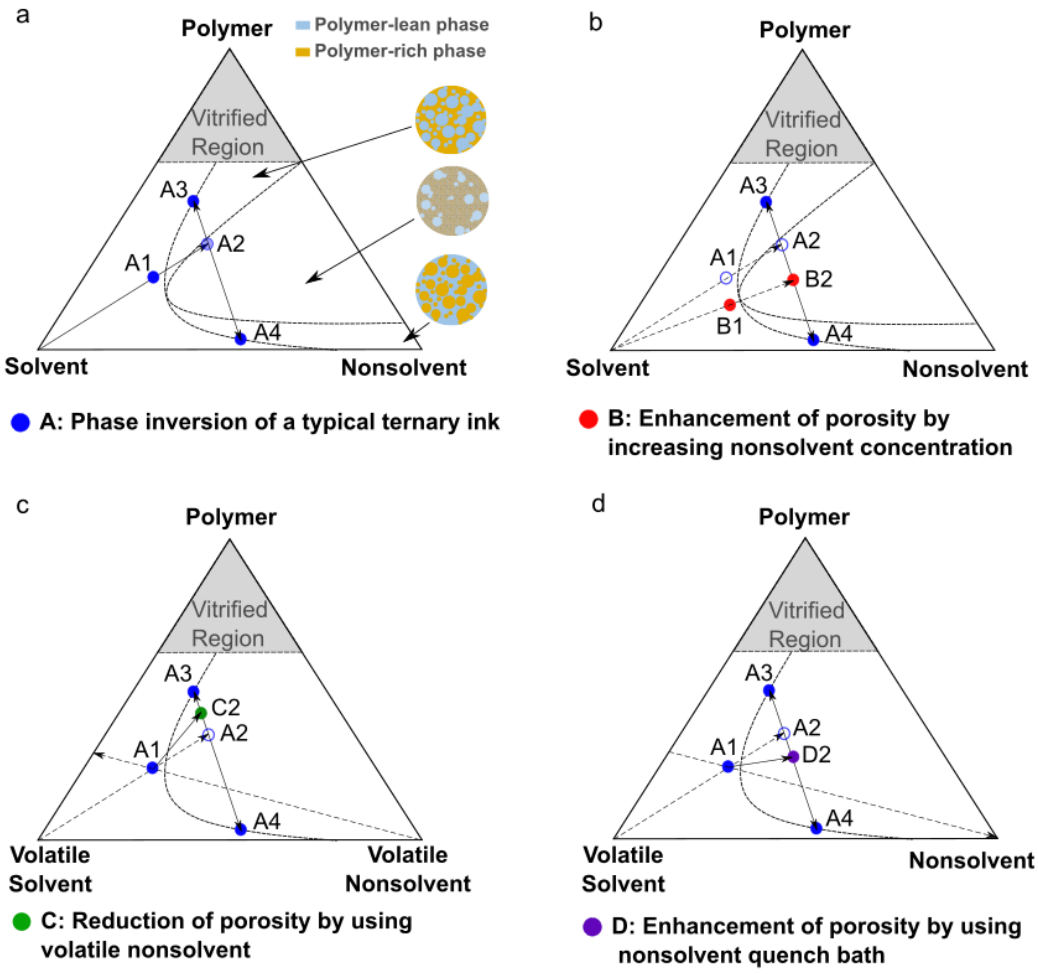

Figure 3.6 Practical filament porosity manipulation via ternary ink composition engineering and phase inversion route engineering. (a) Phase inversion of a ternary polymer solution via volatile solvent evaporation; (b) decreasing polymer concentration in the initial ink (B1, shown in red) increases the porosity of resulting structures; (c) volatile nonsolvent decreases the amount of polymer-lean phase, resulting in less porosity, by adjusting the phase inversion pathway (hypothetical point C2, shown in green); (d) 3D printing into a nonsolvent quench bath or vapor increases the resulting porosity by adjusting the phase inversion pathway (hypothetical point D2, shown in purple).

Manipulating the direction in which the ink composition shifts can also effectively change the resulting porosity. Figure 3.6c illustrates the scenario of replacing the nonvolatile nonsolvent with a volatile nonsolvent and assuming that the ternary phase diagram remains identical. Evaporation of both solvent and nonsolvent shifts the ink composition (A1) away from both the solvent pole and the nonsolvent pole. The final composition shift direction is determined by the ratio of the evaporation rates of solvent and nonsolvent. In this case, a lower porosity in the resulting structure is expected. Figure 3.6d illustrates SBAM under a nonsolvent quench bath, which is similar to dry-wet fiber spinning. [29] After ink deposition in the nonsolvent quench, the solvent is extracted from the ternary ink into the quench bath, and additional nonsolvent is absorbed into the ternary ink. As a result, the ink composition (A2) shifts away from the solvent pole and towards the nonsolvent pole, resulting in a higher porosity. Phase inversion routes can also be manipulated via other parameters (e.g., temperature change, additives, etc.); however, the methods provided in this section are the most practical ones and require no additional modification to the SBAM setup.

To preserve hierarchical pores, the 3D printed objects should not be dried directly, because pores may collapse under the influence of surface-tension-driven interfacial forces from the shrinking (and evaporating) polymer-lean phases.[25] A common strategy to prevent pore collapse is gradually replacing polymer-lean phases with low surface tension nonsolvents, prior to vacuum drying.[28] A variety of nonsolvents can be selected based on miscibility with the ink solvents and nonsolvents.

For applications where porosity within thin filaments is unwanted, solvent-assisted post-fabrication annealing can be used. By immersing the printed objects into plasticizing

nonsolvents, the glass transition temperature of the polymers can be lowered to a practical range. The wet objects can then be annealed in an inert atmosphere. The resulting objects possess denser microstructures and reduced volume. However, in contrast to the shrinkage during 3D printing of binary inks, during the post-fabrication annealing, the entire object undergoes isotropic volume reduction which minimizes deformation.

3.4 Case Study: Solution-based Additive Manufacturing of Matrimid® 5218

3.4.1 Materials and Methods

Matrimid® 5218, the example polymer for solution-based 3D printing, was purchased from Ribelin. As shown in Figure 3.7, the glass transition temperature of Matrimid® 5218 is 320 °C as determined by Differential Scanning Calorimeter (Q200, TA Instruments), which is not applicable for fused deposition modeling. Prior to usage, the Matrimid® 5218 powders were dried overnight under vacuum at 120 °C. All solvents were anhydrous and used as received from either Sigma Aldrich or Alfa Aesar.

A ternary phase diagram of the polymer solution serves to guide the design of the polymer phase inversion process. The homogenous region, the nonhomogeneous region, and the binodal boundary were determined via use of the cloud-point technique.[29] In this technique, a binary polymer solution is first prepared as a standard for the homogenous region. A series of ternary polymer solutions are then prepared with the same polymer concentration but with varied non-solvent and solvent concentrations. The ternary polymer solutions sealed in glass vials are put into a rotating roller (~ 10 rpm) in an oven at 60 °C for at least 3 days. For safety reasons, a secondary container is also utilized. After proper mixing, each sample was cooled down to room temperature and visually examined to

determine the homogeneity. As the nonsolvent concentration increases, the ternary mixtures shift from a transparent fluid to either a solid-liquid mixture or a liquid-liquid mixture. The composition at which the ternary solution turns cloudy, indicating phase separation, is determined to represent the binodal point. Binodal points at different polymer concentrations then form the binodal curve, the boundary between the homogenous phase and the nonhomogeneous phase. The accuracy of the ternary phase diagram is determined by the increments in nonsolvent concentration during this screening process. Considering the trade-off between the efficiency and the accuracy, 10 wt% is usually used for the initial fast scan of the binodal curve, with smaller subsequent increments of 5 wt% and 1 wt% to improve accuracy.

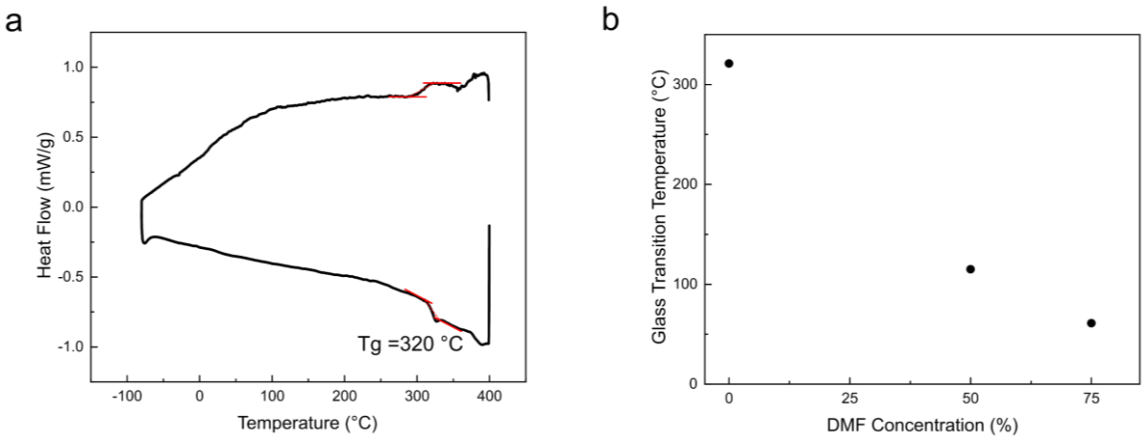

Figure 3.7 Glass transition temperature of Matrimid® 5218 under the influence of dimethylformamide (DMF) / water solution. (a) Differential scanning calorimetry of dry Matrimid® 5218 films; (b) Glass transition temperature of Matrimid® 5218 films after immersion in certain DMF/water solutions for 24 hours.

Mercury porosimetry of the printed objects was conducted by an AutoPore IV (Micromeritics) porosimeter. All the samples for mercury porosimetry were dried at 110 °C for 24 hours. SEM images were collected using a Hitachi SU8230 microscope. Polymer filaments were first soaked in n-hexane and then cracked in liquid nitrogen to expose their

cross-section. All samples for SEM were sputter coated with gold to eliminate charging effects.

3.4.2 Equipment Setup

A customized Cartesian 3D printer was built to process ternary inks. As shown in Figure 3.2a, the 3D printer consists of (i) a stainless-steel ink cartridge, (ii) a coaxial dual-channel micronozzle and (iii) a Cartesian moving substrate.[2] The ternary ink was prepared in the cartridge, by mixing solvent, nonsolvent, and polymer. The cartridge was then sealed via Swagelok® fittings and placed onto a rotating roller (~ 10 rpm) in an oven at 60 °C for at least 3 days to ensure homogeneity. Appropriate G-code (RS-274) commands were written to control the movement of the 3D printer. The ink was extruded through a stainless-steel needle (G22, inner diameter 413 μm) by applying the appropriate pressure (10 bar) from a compressed nitrogen gas cylinder. Linear printing speed was 10 mm s^{-1}. A glass plate coated with a thin Matrimid® 5218 films was used as the printing substrate.

3.4.3 3D printing of Matrimid® 5218/THF/Water Ternary Ink

Tetrahydrofuran (THF) was chosen as the volatile solvent in the ternary ink owing to its high volatility (boiling point 66 °C) and the ability to dissolve Matrimid® 5218. Water was selected as an inexpensive and environmentally friendly non-solvent. The ternary phase diagram for this system at 22 °C is shown in Figure 3.8a. Due to the strong hydrophobicity of Matrimid® 5218, the homogenous region only occupies a small area in the ternary phase diagram.

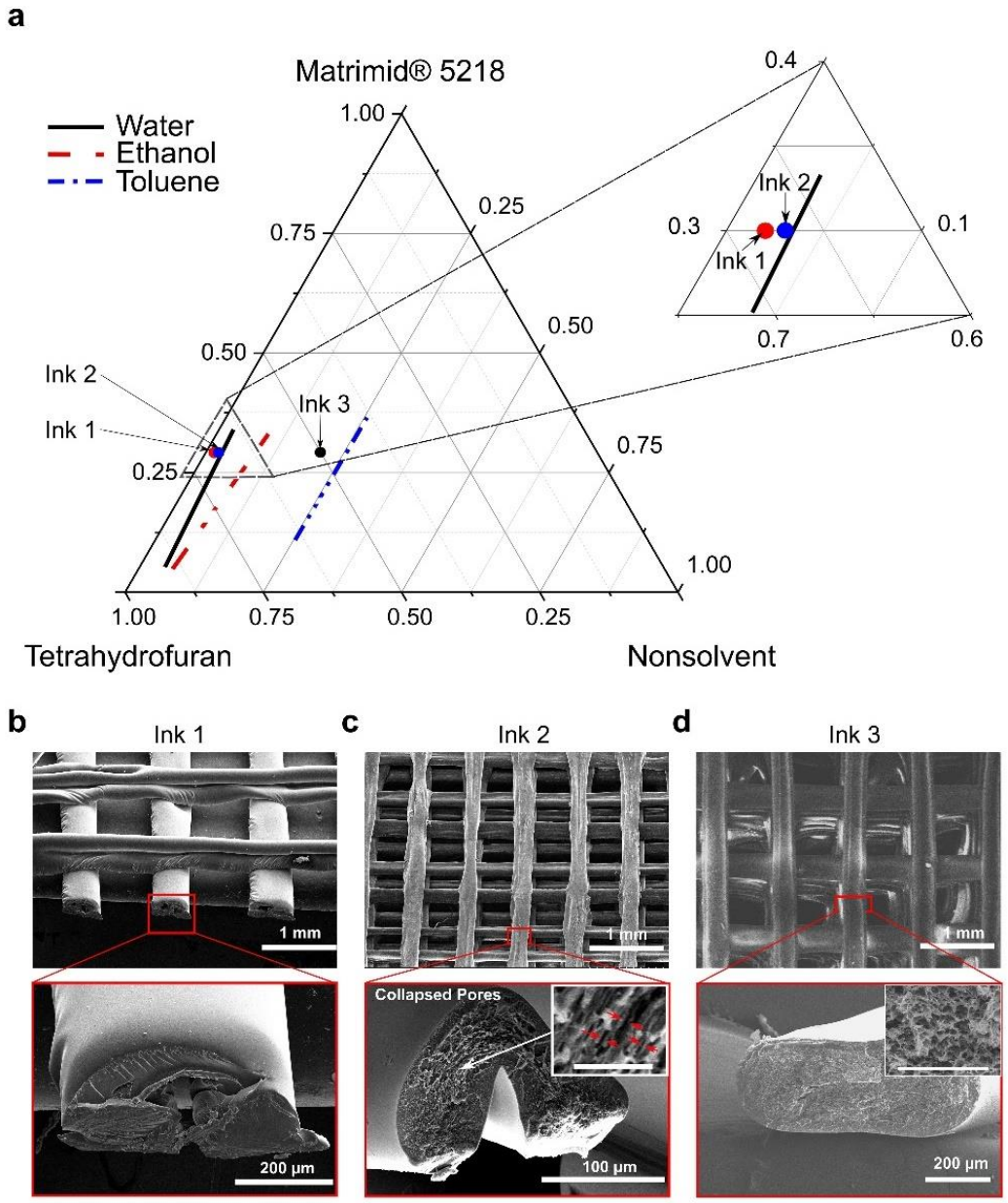

Figure 3.8 Solution Based Additive Manufacturing of Matrimid® 5218. (a) Ternary phase diagrams of Matrimid® 5218 with THF and different nonsolvents at 25 °C; the inset shows the subtle differences in ink composition 1 and 2. (b) Scaffolds printed using the ternary ink consisting of 30 wt.% Matrimid® 5218, 68 wt.% THF and 2 wt.% water. (c) scaffolds printed using the ternary ink consisting of 30 wt% Matrimid® 5218, 67 wt% THF and 3 wt% water; the inset shows magnified collapsed pores (indicated by red arrows) with a scale bar of 10 µm. (d) scaffolds printed using the ternary ink consisting of 30 wt% Matrimid® 5218, 50 wt% THF and 20 wt% toluene; the inset shows magnified intact pores with a scale bar of 10 µm.

We created several ternary inks to highlight the influence of ink composition on filament structure and object creation. The first ternary ink we created contained 30 wt% Matrimid® 5218, 68 wt% THF and 2 wt% water. SBAM with this ink was conducted in a THF saturated atmosphere supplied by the secondary nozzle. As shown in Figure 6b, this preliminary SBAM protocol created Matrimid® 5218 scaffolds without collapse or sagging; however, irregular filaments were created, and slight deformation of the whole scaffold could be observed. The formation of such irregular filaments is due to (1) the formation of discrete skin layers and (2) unbalanced evaporation (Figure 3.9); these issues will be addressed in subsequent sections of the article. The upper parts of the filaments exhibited perfect dome shapes while the bottom parts sunk into the meshes formed by underlying filaments. We hypothesize that such irregular filaments are induced by differences in the evaporation rate at different locations on the filament surface (See Section 3.5.1. for details).

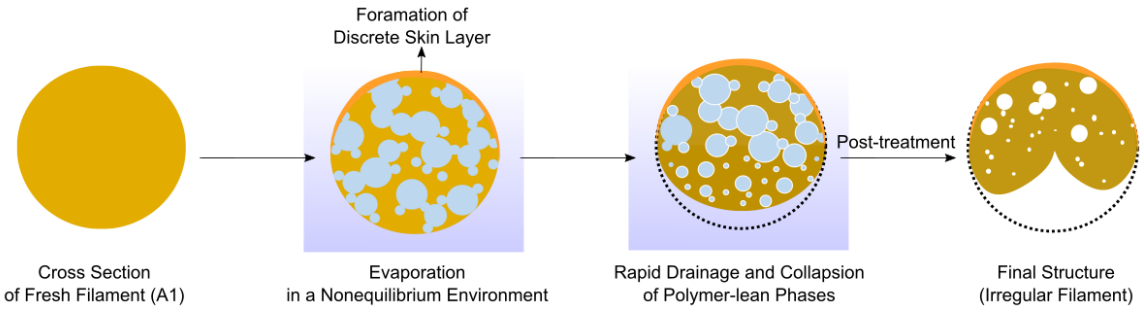

Figure 3.9 Formation of irregular filaments during SBAM of ternary inks consisting of Matrimid® 5218, THF, and water.

We found that decreasing the THF concentration stabilized the filament structure during deposition (the reasons for this stabilization are discussed in more detail in Section 3.5.1). The second ternary ink formulation we created consisted of 30 wt% Matrimid®

5218, 67 wt% THF and 3 wt% water. As shown in Figure 3.8c, this revised SBAM protocol significantly inhibits the creation of irregular filaments. Most filaments possessed flattened, oval shapes. However, a small population of irregular filaments could be observed. Decreasing the THF concentration results in premature phase inversion (Figure 3.8a) of the filament; this suggests that the strong nonsolvent (water) must be changed to a milder one to provide a larger homogenous region in the phase diagram and offer greater flexibility in the ink composition.

3.4.4 3D printing of Matrimid® 5218/THF/Toluene Ternary Ink

Aliphatic alcohols are commonly used as mild alternatives to water in fiber spinning of hydrophobic polymers.[26] With increasing carbon numbers, their nonsolvent strength decreases. However, neither methanol nor ethanol significantly enlarges the homogenous regions (Figure 3.8a). An aromatic organic solvent, toluene was found to be a mild nonsolvent that provided a large homogenous region for manipulation of the ink composition. The third ternary ink formulation consisted of 30 wt% Matrimid® 5218, 50 wt% THF and 20 wt% toluene. Due to the decreased volatile solvent concentration, irregular filaments were successfully eliminated, while macropores were preserved throughout the fiber cross-section (Figure 3.1b and Figure 3.8d). Furthermore, this SBAM ink formulation did not require atmosphere control (Movie S1), which results in a more simple and safe printer operation. To verify the capability of fabricating complex architectures via SBAM, Matrimid® 5218 scaffolds featuring bridging structures are fabricated. The optimized ternary ink can successfully be translated into scaffolds without collapsing (Figure 3.10).

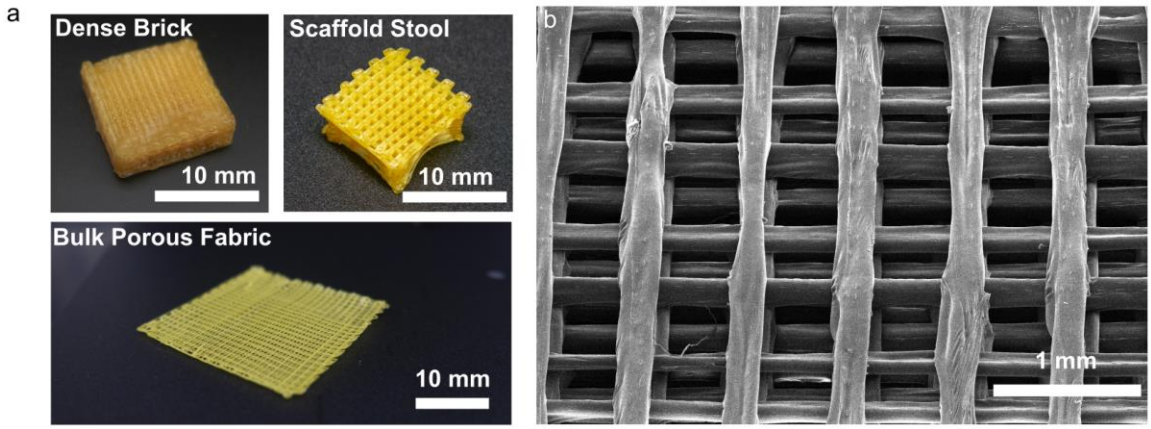

Figure 3.10 Various architectures fabricated via SBAM. (a) Dense brick is printed from a CAD model with the spacing between filaments of scaffolds equal to zero. Solvent-assisted annealing was applied to smooth the surfaces. Scaffold stool features curved bridge-like stands. Bulk porous fabric is a 2cm-by-2cm 4-layer scaffold, the size of which is limited by the travel distance of the current 3D printer setup. (b) The SEM image of the bulk porous fabric shows intact bridging filaments without any sagging. These results suggest that the fundamental mechanism of SBAM is not size-limited.

3.4.5 Post-SBAM Porosity Manipulation

The polymer-lean phases in the 3D printed Matrimid® 5218 objects were exchanged first with methanol and then with n-hexane prior to vacuum drying. These post-treatment steps help preserve the hierarchical pores.[27,28] As indicated by mercury porosimetry, the objects printed from Matrimid® 5218/THF/toluene ternary inks possess hierarchical pores ranging from 5 nm to 1000 nm; such hierarchical porous structures are excellent substrate materials for mass transfer applications.[39-41]

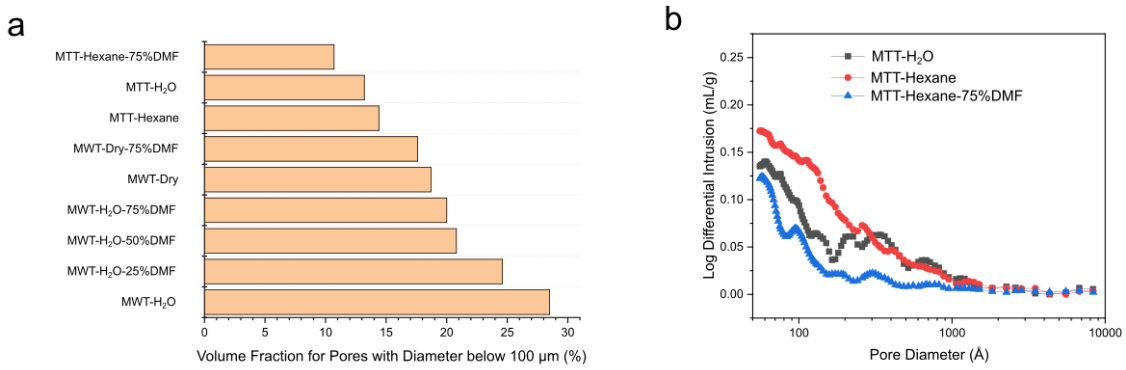

Figure 3.11 Influence of post-treatment on the porosity of Matrimid® 5218 objects revealed by mercury porosimetry. (a) The porosity of 3D printed Matrimid® 5218 with different processing histories, which are recorded by their code name (Table 3.1). For example, MTT-Hexane-75%DMF represents the object printed from the Matrimid/Toluene/THF ternary ink, solvent exchanged with n-hexane, and annealed with the assistance of an 75% aqueous DMF solution at 120 °C for 12 hours. MWT-Dry-75%DMF represents the object printed from the Matrimd/Water/THF ternary ink, without solvent exchange, and annealed with the assistance of the 75% aqueous DMF solution at 120 °C for 12 hours. Only pores with diameter below 100 μm were counted so that contributions from the macroscopic architecture design are excluded. (b) Detailed pore size distribution for objects printed from Matrimid/Toluene/THF ternary ink after different post treatments.

As introduced in section 3.3.5, the hierarchical pores can also be purposely annealed while keeping the macroscopic structures intact (Figure 3.1c). One Matrimid® 5218 scaffold was immersed into 75 wt.% dimethylformamide (DMF) / water solution for 24 hours at 25 °C. Matrimid® 5218 is plasticized by DMF and as a result exhibits a much lower glass transition temperature (61 °C) as shown in Figure 3.7b. After this exposure, the excess solvent was removed from the wet scaffold with an absorbent wipe and the scaffold was then dried in a vacuum oven (85 kPa vacuum, 120 °C) for 24 hours. After the solvent-assisted annealing, the hierarchical pores were significantly decreased (Figure 3.11). Decrease of porosity leads to shrinkage of the overall dimension as shown in Figure 3.1c. However, such isotropic shrinkage during post-treatment will not deform the overall architecture.

Table 3.1 The post treatment histories of 3D printed samples

Ink Composition	Sample Name	Solvent Exchange	Annealing
30 wt% Matrimid® 5218, 50 wt% THF and 20 wt% toluene	MTT-Hexane-75%DMF	Hexane	75% aqueous DMF solution at 120 °C for 12 hours
	MTT-H_2O	H_2O	None
	MTT-Hexane	Hexane	None
30 wt% Matrimid® 5218, 67 wt% THF and 3 wt% water	MWT-Dry-75%DMF	None	75% aqueous DMF solution at 120 °C for 12 hours
	MWT-Dry	None	None
	MWT-H_2O	H_2O	None
	MWT-H_2O-75%DMF	H_2O	75% aqueous DMF solution at 120 °C for 12 hours
	MWT-H_2O-50%DMF	H_2O	50% aqueous DMF solution at 120 °C for 12 hours
	MWT-H_2O-25%DMF	H_2O	25% aqueous DMF solution at 120 °C for 12 hours

3.5 Challenges in Solution-based Additive Manufacturing

Due to the complexity of solution-based additive manufacturing with ternary inks, it is difficult to determine optimal polymeric ink formulations and process parameters without at least some experimental trials and errors. As shown in the case study of developing the SBAM protocol for Matrimid® 5218, initial attempts to 3D print new polymers via solution-based additive manufacturing may encounter challenges. Below, we summarize some of the key challenges, including irregular filament shapes and sizes, delamination of adjacent layers, and object collapse. For each of these challenges, multiple potential solutions exist. As solution-based additive manufacturing involves simultaneous mass transfer, phase inversion, and evolution of rheological properties, trade-offs between different factors must often be considered when developing SBAM protocols.

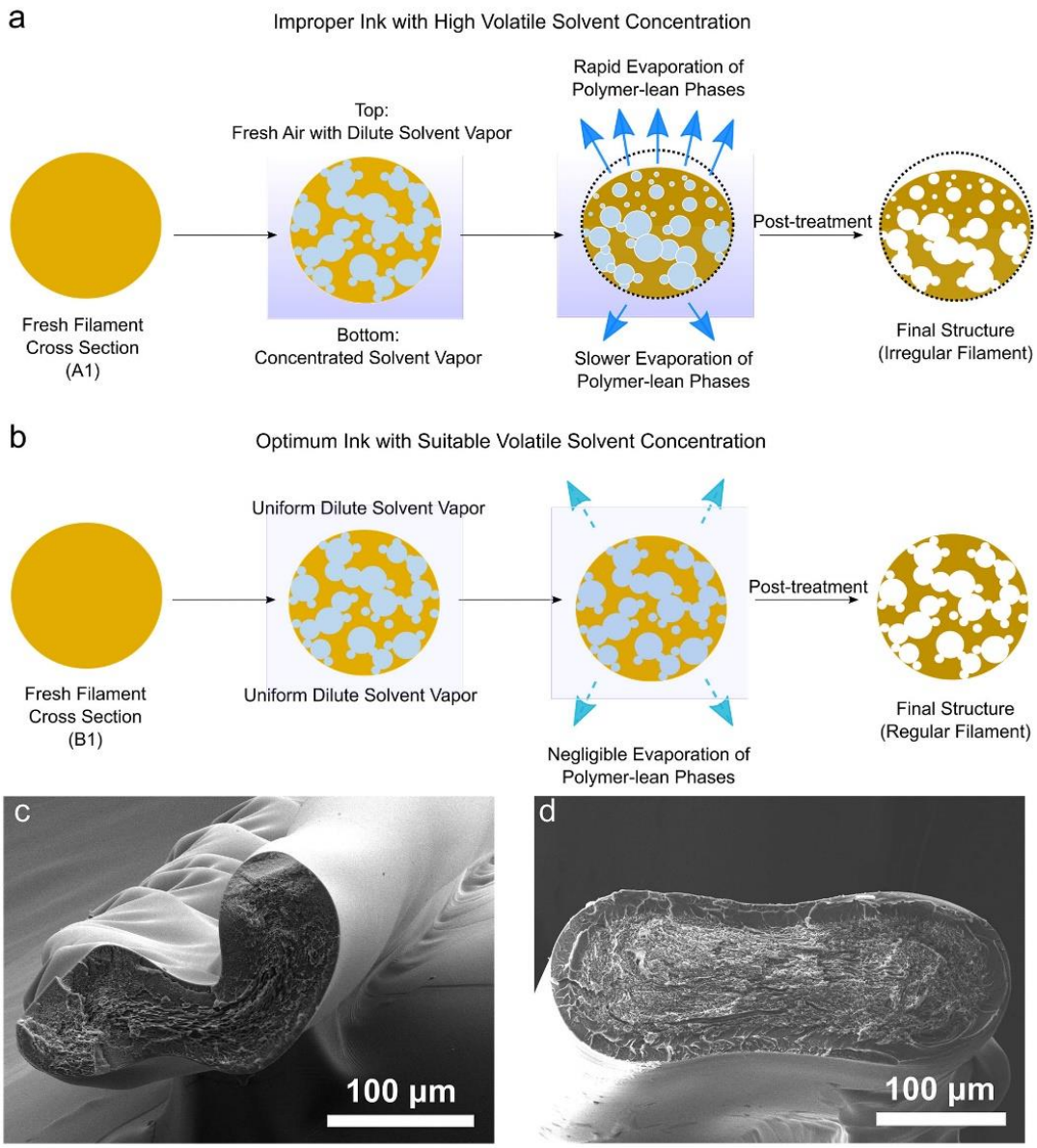

Figure 3.12 Proposed formation mechanism for irregular filaments. (a) Formation of the irregular filaments in a spatially nonuniform environment. Here, mismatched evaporation rates of solvent/nonsolvent around the filament lead to asymmetric phase inversion, ultimately creating an irregular filament (b) the formation of an ideal symmetric filament; (c) an irregular Matrimid® 5218 filament produced from a ternary ink with high concentration of volatile solvent; (d) a regular Matrimid® 5218 filament produced from an optimum ternary ink.

3.5.1 Irregular Filament

Solution-based additive manufacturing produces user-designed objects by depositing oval-shaped or circular filaments at specific positions on a plate or an already-deposited structure. Irregular filaments are unwanted for a variety of reasons, and are defined as filaments with essentially uncontrolled variations in size and shape of cross sections. These can be easily spotted in unsuccessful solution-based additive manufacturing of polymers (Figure 3.12), and are a major contributor to object deformation.

The formation of irregular filaments is a complex problem related to the solution thermodynamics, mass transfer kinetics, and fluid rheology. While various inappropriate SBAM conditions may produce filaments with irregular cross sections, in our experience inappropriate ternary ink formulation is one of the most significant causes of irregular filaments (see details in Section 3.5.3 and 3.4.4). When a strong nonsolvent (a nonsolvent that has a strongly differing Hildebrandt solubility parameter from the polymer) is used, a high concentration of solvent is required to generate homogenous the ternary inks (Figure 3.13). Such ternary inks undergo phase inversion and generate polymer-lean phases and polymer-rich phases with high concentrations of volatile solvents. The high concentration of volatile solvent further amplifies the mismatched evaporation kinetics and inappropriate fluid rheology, which eventually contributes to the collapse of porous structures.

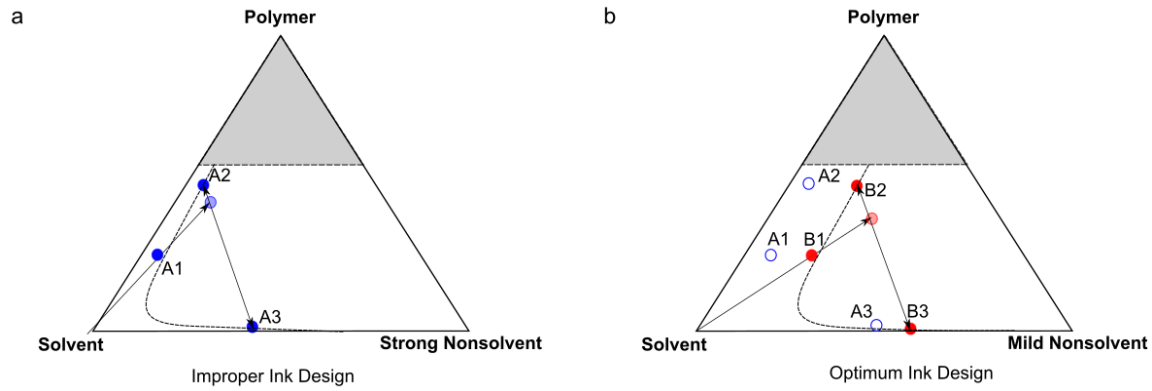

Figure 3.13 Influence of nonsolvent compatibility with the polymer. (a) improper ink design with excessive nonsolvent strength; (b) optimum ink design with mild nonsolvent. When a strong nonsolvent is selected (i.e., a nonsolvent with Hildebrandt solubility parameter that differs greatly from the polymer), the homogenous region occupies only a small area in the ternary phase diagram. After phase inversion, both the continuous polymer-rich phase (A2) and the discrete polymer-lean phase (A3) contain high concentration of volatile solvent. As a result, the evaporation and shrinkage of polymer-lean phase cannot be neglected. The optimum ternary ink consists of mild nonsolvent and the homogenous region occupies a larger area. The corresponding continuous polymer-rich phase (B2) and the discrete polymer-lean phase (B3) contain much less volatile compounds. In that case, the evaporation and shrinkage of the polymer-lean phases can be negligible.

High concentration of volatile components in the ternary ink enhances the driving force for solvent evaporation, which results in a concentrated solvent vapor atmosphere surrounding the previously deposited filaments (Figure 3.12a). As a result, the newly deposited filaments are exposed to a non-uniform atmosphere, where the top parts of the filaments are exposed to fresh air with dilute solvent vapors and the bottom parts of the filaments are exposed to concentrated solvent vapors generated by the previously deposited filaments. While the generation of polymer-lean phases is expected to compensate the volume loss due to evaporation (Figure 3.3b), the evaporation and shrinkage of polymer-lean phases cannot be neglected in cases where ternary inks contains too much volatile solvents (see Section 3.4.3). The atmospheric vapor concentration difference leads to mismatched evaporation kinetics of different parts of the deposited filaments, which may

result in mismatched volume loss of the polymer-lean phases, especially for ternary inks with high volatile compound concentration. As illustrated in Figure 3.12a, the polymer-lean phases in the top parts of the filaments undergo faster evaporation than those in the bottom parts, which leads to unbalanced shrinkage.

High concentration of solvent in the polymer-rich phase also contributes to the collapse of porous structure due to unwanted rheological properties. Due to the favorable interaction between polymer and solvent, solvent-induced plasticization facilitates the relaxation of polymer chains and results in lower storage modulus. The plasticized polymer-rich phases are susceptible to deformation driven by the surface tension of the shrinking polymer-lean phases, which further contributes to the irregular filaments (Figure 3.12c).

In conclusion, the synergistic effects of solution thermodynamics, mass transfer kinetics, and fluid rheology contributes to the formation of irregular filaments. As described above, there are three key factors contributing to the irregular filaments: (1) asynchronous solvent/nonsolvent evaporation around the filament; (2) high concentrations of volatile solvents resulting in a polymer-lean phase that undergoes fast shrinkage after deposition; (3) low storage modulus of the resulting polymer-rich phase. Correspondingly, there are three routes to eliminate irregular filaments. First, conducting 3D printing in a controlled atmosphere saturated with the volatile solvent vapor can minimize evaporation rate differences at different locations of a single filament. A coaxial secondary nozzle can be installed around the nozzle that delivers the ternary ink (Figure 3.3a). During solution-based additive manufacturing, inert gas (e.g., nitrogen) saturated with volatile solvent vapor is delivered through the secondary nozzle to the objects at a controlled gas flow rate.

The gas phase surrounding the deposited filaments is being refreshed so that evaporation rates along the filament surface are equalized. Second, replacing strong nonsolvents with mild nonsolvent can effectively lower the volatile compound concentration in the resulting polymer-lean phase. The milder nonsolvent results in a larger homogenous region, as shown in Figure 3.13b. For ease of comparison, the tie lines connecting the polymer-rich phase (B2) and the polymer-lean phase (B3) are assumed to possess the same slope in these phase diagrams. Following the ternary ink composition design principle (Section 3.3.1), a ternary ink (B1) containing a mild nonsolvent could result in a polymer-lean phase (B3) with less solvent, which undergoes slower evaporation and less shrinkage. Third, increasing polymer concentration of the ternary ink can prevent the polymer-rich phase from undergoing pore collapse, since the storage modulus of a polymer solution is dominated by the polymer concentration.[2] Figure 3.12b illustrates the solidification of the optimum ternary ink with regular filament appearance, which explains the regular cross section of the modified Matrimid® 5218 recipe (Figure 3.12d).

3.5.2 Delamination of Adjacent Layers

A common failure for layer-by-layer 3D printing is the delamination of subsequent layers.[42] Ideally, adhesion between adjacent layers is achieved by wetting and mixing at the junctions of two filaments. However, if the existing filament has lost too much solvent, facile mixing at the filament interface (or junction) may be inhibited. As shown in Figure 3.14a, the first ternary polymeric filament (A1) is deposited onto the substrate and undergoes evaporation-induced separation (A1-A2). After complete phase inversion, the overall composition of the filament surface can be denoted as A2 in the ternary phase diagram. When a fresh filament (A1) is deposited onto this existing filament (A2), the

composition of the filament junction is shifted backward (A5). However, as the previously deposited filament has lost too much solvent, the filament junctions remain in the nonhomogeneous region, and the entanglement of polymer chains is thus inhibited.

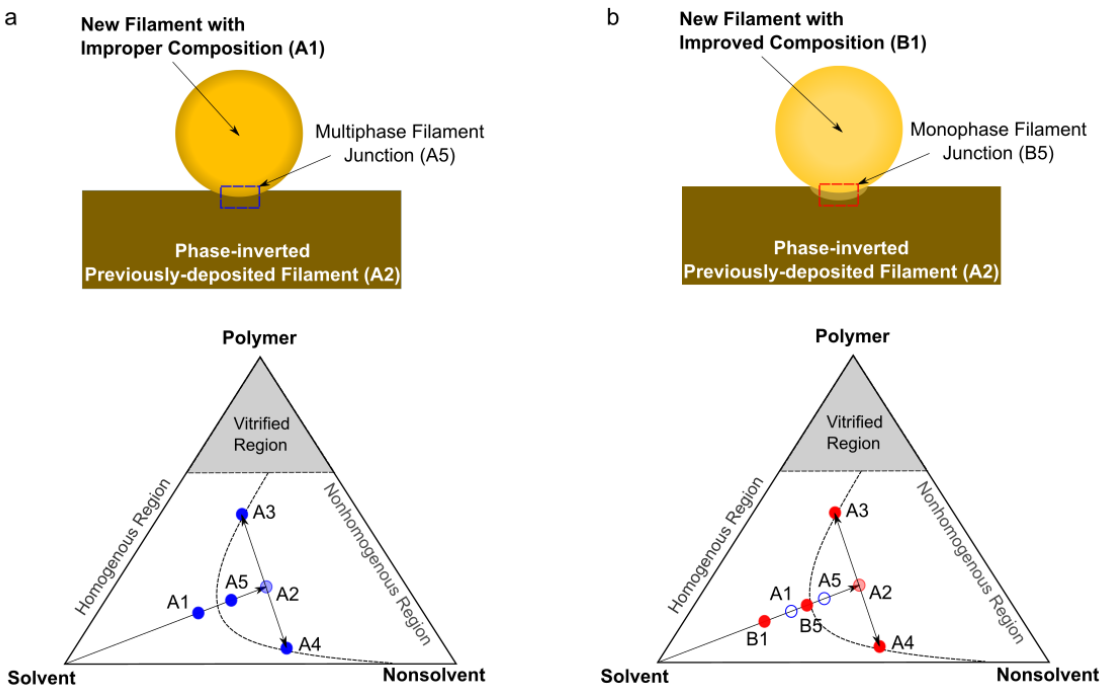

Figure 3.14 Thermodynamic interpretation for filament-layer delamination processes. Case a: Improper ink design results in delamination of adjacent layers due to phase inversion prior to polymer-polymer mixing at the interfaces; Case b: Elimination of the delamination via the increase of solvent concentration in the ink. This retards phase inversion and enables polymer-polymer mixing at the filament-filament interface.

The most straightforward solution to this problem is an increase in the solvent concentration of the ternary ink. As illustrated in Figure 3.14b, with the new ink composition (B1), the composition of the filament junction (B5) is further shifted into the homogenous region. As a result, the second filament partially dissolves the surface of the first filament, which enables polymer-polymer mixing and the formation of a well-adhered junction.

In cases where increasing solvent concentration is not feasible (e.g., storage modulus is too low to resist gravity), a plasticizing nonsolvent can be used. Even though the new filament cannot dissolve the surface of the previous filament, polymer chains can still slowly entangle across the interface in the presence of a plasticizing nonsolvent.

3.5.3 Object Collapse

Improper SBAM protocol can also result in the collapse of bridging structures, and, in the worst cases, a pool of polymer. Figure 3.15a shows examples of collapsed Matrimid® 5218 scaffolds.

The most common reason for object collapse is that the polymer solution is too dilute and possesses insufficient storage modulus to withstand deformation by gravity. In these cases, the ternary ink composition can be slightly changed in two directions to eliminate the object deformation (Figure 3.15b). First, the polymer concentration should be increased, which significantly increases the storage modulus. Second, the ternary ink composition should be shifted closer to the binodal curve, so that the liquid filament can be more easily solidified before deformation occurs.

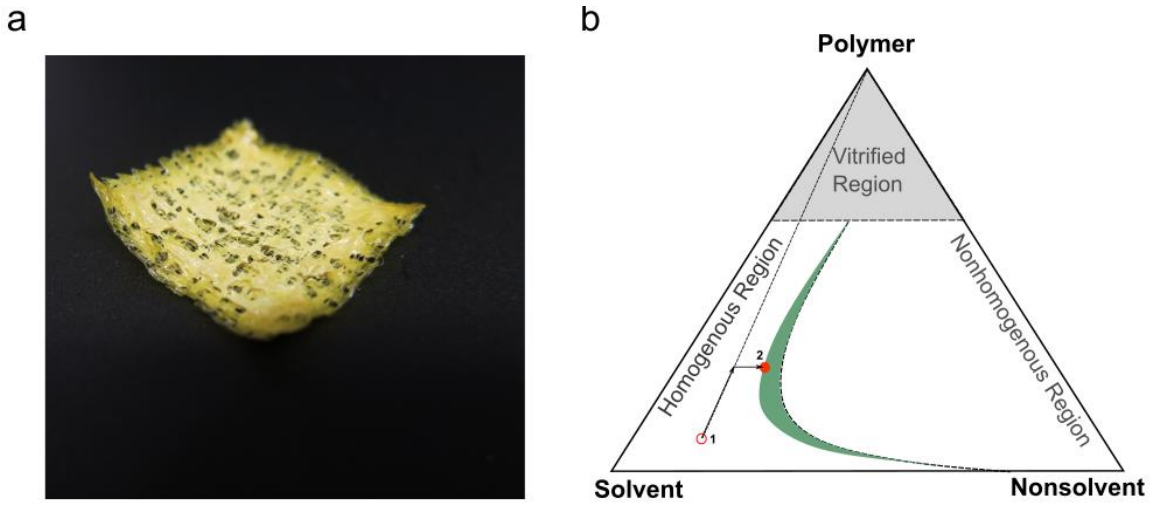

Figure 3.15 Object collapse and potential solutions for this problem. (a) Collapsed Matrimid® 5218 scaffold fabricated using the ternary ink consisting of 20 wt% Matrimid® 5218, 78 wt% THF and 2 wt% water. (b) Improving the ternary ink composition to prevent the object collapse. Point 1 denotes the original ink composition, point 2 denotes the optimized ink composition; dashed arrow represents the route of increasing polymer concentration, and the green area represents the region with acceptable solidification delay.

Beyond an insufficient storage modulus, the formation of a vitrified skin layer can also lead to the collapse of the printed object. A vitrified polymeric skin layer on the outside of the filaments isolate the ternary solution within the filament from the external atmosphere. When this happens, the volatile solvent must diffuse through the skin layer and then escape desorb from the polymeric skin layer into the gaseous phase surrounding the 3D deposited filaments. As a result, the skin layer significantly impedes solvent evaporation and dramatically delays vapor-induced phase inversion, which contributes to gravity-driven object collapse. The formation of skin layers can be prevented by slowing down the solvent evaporation rate or increasing the external nonsolvent vapor sorption rate. To enable the former, the volatile solvent content within the printing ink can be lowered and replaced by a milder nonsolvent (Section 3.5.1). To enable the latter, a nonsolvent vapor can be supplied via the coaxial secondary nozzle to increase the driving force for

nonsolvent vapor sorption (note, a solvent vapor can also be added to lower the solvent evaporation driving force as shown in Section 3.3.2).

3.6 Conclusion

Compared with conventional manufacturing techniques (e.g., injection molding), 3D printing has advantages in the areas of complex structure fabrication, small scale production and prototyping, and personal customization. Existing polymer 3D printing techniques can process polymer melts and photo-curable resins; however, a wide range of polymers of industrial interest cannot be 3D printed directly. We previously reported a novel polymer 3D printing technique, Solution-Based Additive Manufacturing (SBAM), which processes ternary polymer solutions and greatly expands the spectrum of 3D printable polymer materials. In this report, a systematic protocol for SBAM was provided. Optimal SBAM protocols translate virtual designs into real objects that possess tunable hierarchical macro-/mesopores without shrinkage. As SBAM involves solution thermodynamics optimization, rheological engineering, and mass transfer control, developing a suitable protocol for a new polymer is challenging. This section provides a thorough analysis of the ternary ink evolution during SBAM and provides solutions to some common challenges. Matrimid® 5218 was selected to demonstrate the process of developing SBAM protocol.

The solution-based additive manufacturing technique is fundamentally capable of translating solution-processable polymers, a ubiquitous class of polymers, into complex architectures. It is a convenient tool for industries to prototype new architecture design, customize products, and produce small-scale products using traditional solution-

processable polymers. The capability of installing hierarchical pores into polymeric architectures without template material also provides new application areas (e.g., adsorption, catalysis, membrane separation, etc.) for additive manufacturing techniques. Future research on SBAM should be focused on the development of software to translate CAD architecture into print head guidance while considering motor acceleration and deceleration at corners and new applications of the resulting hierarchical porous architectures.

3.7 References

1. F. Zhang, Y. Ma, Y. Kondo, V. Breedveld, R. P. Lively. A Guide to Solution‐based Additive Manufacturing of Polymeric Structures: Ink Design, Porosity Manipulation, and Printing Strategy. *Journal of Advanced Manufacturing and Processing* **2019**:e10026.

2. F. Zhang, Y. Ma, J. Liao, V. Breedveld, R. P. Lively. Solution‐Based 3D Printing of Polymers of Intrinsic Microporosity. *Macromolecular Rapid Communications* **2018**:1800274.

3. J. R. Tumbleston, D. Shirvanyants, N. Ermoshkin, R. Janusziewicz, A. R. Johnson, D. Kelly, K. Chen, R. Pinschmidt, J. P. Rolland, A. Ermoshkin. Continuous liquid interface production of 3D objects. *Science* **2015**;347(6228):1349-1352.

4. D. Bak. Rapid prototyping or rapid production? 3D printing processes move industry towards the latter. *assembly automation* **2003**;23(4):340-345.

5. M. Malinauskas, A. Žukauskas, S. Hasegawa, Y. Hayasaki, V. Mizeikis, R. Buividas, S. Juodkazis. Ultrafast laser processing of materials: from science to industry. *Light: Science & Applications* **2016**;5(8):e16133.

6. M. Vaezi, S. Chianrabutra, B. Mellor, S. Yang. Multiple material additive manufacturing–Part 1: a review: this review paper covers a decade of research on multiple material additive manufacturing technologies which can produce complex geometry parts with different materials. *Virtual and Physical Prototyping* **2013**;8(1):19-50.

7. C. K. Chua, K. F. Leong. *3D Printing and Additive Manufacturing: Principles and Applications (with Companion Media Pack) of Rapid Prototyping Fourth Edition*: World Scientific Publishing Company; **2014**.

8. O. A. Mohamed, S. H. Masood, J. L. Bhowmik. Optimization of fused deposition modeling process parameters: a review of current research and future prospects. *Advances in Manufacturing* **2015**;3(1):42-53.

9. H. N. Chia, B. M. Wu. Recent advances in 3D printing of biomaterials. *Journal of biological engineering* **2015**;9(1):4.

10. V. C.-F. Li, C. K. Dunn, Z. Zhang, Y. Deng, H. J. Qi. Direct Ink Write (DIW) 3D Printed Cellulose Nanocrystal Aerogel Structures. *Scientific Reports* **2017**;7(1):8018.

11. J. A. Lewis. Direct ink writing of 3D functional materials. *Advanced Functional Materials* **2006**;16(17):2193-2204.

12. A. K. Au, W. Huynh, L. F. Horowitz, A. Folch. 3D-printed microfluidics. *Angewandte Chemie International Edition* **2016**;55(12):3862-3881.

13. X. Zheng, H. Lee, T. H. Weisgraber, M. Shusteff, J. DeOtte, E. B. Duoss, J. D. Kuntz, M. M. Biener, Q. Ge, J. A. Jackson. Ultralight, ultrastiff mechanical metamaterials. *Science* **2014**;344(6190):1373-1377.

14. S. C. Ligon, R. Liska, J. r. Stampfl, M. Gurr, R. Mülhaupt. Polymers for 3D printing and customized additive manufacturing. *Chemical Reviews* **2017**;117(15):10212-10290.

15. S. Jiang, L. Chen, M. Briggs, T. Hasell, A. Cooper. Functional porous composites by blending with solution-processable molecular pores. *Chemical Communications* **2016**;52(42):6895-6898.

16. Q. Song, S. Jiang, T. Hasell, M. Liu, S. Sun, A. K. Cheetham, E. Sivaniah, A. I. Cooper. Porous Organic Cage Thin Films and Molecular‐Sieving Membranes. *Advanced Materials* **2016**;28(13):2629-2637.

17. S. W. Pattinson, A. J. Hart. Additive manufacturing of cellulosic materials with robust mechanics and antimicrobial functionality. *Advanced Materials Technologies* **2017**;2(4):1600084.

18. F. C. Krebs. Fabrication and processing of polymer solar cells: a review of printing and coating techniques. *Solar Energy Materials and Solar Cells* **2009**;93(4):394-412.

19. F. E. Ahmed, B. S. Lalia, R. Hashaikeh. A review on electrospinning for membrane fabrication: challenges and applications. *Desalination* **2015**;356:15-30.

20. S. Z. Guo, F. Gosselin, N. Guerin, A. M. Lanouette, M. C. Heuzey, D. Therriault. Solvent‐cast three‐dimensional printing of multifunctional microsystems. *Small* **2013**;9(24):4118-4122.

21. F. Zhang, C. Tuck, R. Hague, Y. He, E. Saleh, Y. Li, C. Sturgess, R. Wildman. Inkjet printing of polyimide insulators for the 3D printing of dielectric materials for microelectronic applications. *Journal of Applied Polymer Science* **2016**;133(18):43361.

22. T.-M. Tenhunen, O. Moslemian, K. Kammiovirta, A. Harlin, P. Kääriäinen, M. Österberg, T. Tammelin, H. Orelma. Surface tailoring and design-driven prototyping of fabrics with 3D-printing: An all-cellulose approach. *Materials & Design* **2018**;140:409-419.

23. S.-Z. Guo, M.-C. Heuzey, D. Therriault. Properties of polylactide inks for solvent-cast printing of three-dimensional freeform microstructures. *Langmuir* **2014**;30(4):1142-1150.

24. R. Passieux, L. Guthrie, S. H. Rad, M. Lévesque, D. Therriault, F. P. Gosselin. Instability‐Assisted Direct Writing of Microstructured Fibers Featuring Sacrificial Bonds. *Advanced Materials* **2015**;27(24):3676-3680.

25. G. R. Guillen, Y. Pan, M. Li, E. M. Hoek. Preparation and characterization of membranes formed by nonsolvent induced phase separation: a review. *Industrial & Engineering Chemistry Research* **2011**;50(7):3798-3817.

26. M. L. Jue, V. Breedveld, R. P. Lively. Defect-free PIM-1 hollow fiber membranes. *Journal of Membrane Science* **2017**;530:33-41.

27. G. Dong, H. Li, V. Chen. Factors affect defect-free Matrimid® hollow fiber gas separation performance in natural gas purification. *Journal of Membrane Science* **2010**;353(1-2):17-27.

28. D. T. Clausi, W. J. Koros. Formation of defect-free polyimide hollow fiber membranes for gas separations. *Journal of Membrane Science* **2000**;167(1):79-89.

29. S. A. McKelvey, D. T. Clausi, W. J. Koros. A guide to establishing hollow fiber macroscopic properties for membrane applications. *Journal of Membrane Science* **1997**;124(2):223-232.

30. T. D. Ngo, A. Kashani, G. Imbalzano, K. T. Nguyen, D. Hui. Additive manufacturing (3D printing): A review of materials, methods, applications and challenges. *Composites Part B: Engineering* **2018**.

31. K. Sun, T. S. Wei, B. Y. Ahn, J. Y. Seo, S. J. Dillon, J. A. Lewis. 3D printing of interdigitated Li‐Ion microbattery architectures. *Advanced Materials* **2013**;25(33):4539-4543.

32. T. Osswald, J. P. Hernández-Ortiz. Polymer processing. *Modeling and Simulation. Munich: Hanser* **2006**:1-651.

33. N. Widjojo, T.-S. Chung, D. Y. Arifin, M. Weber, V. Warzelhan. Elimination of die swell and instability in hollow fiber spinning process of hyperbranched polyethersulfone (HPES) via novel spinneret designs and precise spinning conditions. *Chemical Engineering Journal* **2010**;163(1-2):143-153.

34. H. Yuk, X. Zhao. A New 3D Printing Strategy by Harnessing Deformation, Instability, and Fracture of Viscoelastic Inks. *Advanced Materials* **2017**;30(6):1704028

35. S. Nesaei, M. Rock, Y. Wang, M. R. Kessler, A. Gozen. Additive Manufacturing With Conductive, Viscoelastic Polymer Composites: Direct-Ink-Writing of Electrolytic and Anodic Poly (Ethylene Oxide) Composites. *Journal of Manufacturing Science and Engineering* **2017**;139(11):111004.

36. S. C. Cox, J. A. Thornby, G. J. Gibbons, M. A. Williams, K. K. Mallick. 3D printing of porous hydroxyapatite scaffolds intended for use in bone tissue engineering applications. *Materials Science and Engineering: C* **2015**;47:237-247.

37. R. A. Giordano, B. M. Wu, S. W. Borland, L. G. Cima, E. M. Sachs, M. J. Cima. Mechanical properties of dense polylactic acid structures fabricated by three dimensional printing. *Journal of Biomaterials Science, Polymer Edition* **1997**;8(1):63-75.

38. Y. Ma, F. Zhang, S. Yang, R. P. Lively. Evidence for entropic diffusion selection of xylene isomers in carbon molecular sieve membranes. *Journal of Membrane Science* **2018**;564:404-414.

39. S. J. DeWitt, A. Sinha, J. Kalyanaraman, F. Zhang, M. J. Realff, R. P. Lively. Critical Comparison of Structured Contactors for Adsorption-Based Gas Separations. *Annual review of chemical and biomolecular engineering* **2018**;9:129-152.

40. F. Rezaei, P. Webley. Optimum structured adsorbents for gas separation processes. *Chemical Engineering Science* **2009**;64(24):5182-5191.

41. F. Rezaei, P. Webley. Structured adsorbents in gas separation processes. *Separation and Purification Technology* **2010**;70(3):243-256.

42. Z. Weng, J. Wang, T. Senthil, L. Wu. Mechanical and thermal properties of ABS/montmorillonite nanocomposites for fused deposition modeling 3D printing. *Materials & Design* **2016**;102:276-283.

CHAPTER 4. SOLUTION-BASED ADDITIVE MANUFACTURING OF ULTRA-SHORT POLYMERS OF INTRINSIC MICROPOROSITY[†]

Current additive manufacturing methods have strong limitations in the classes of compatible polymers. Many polymers of significant technological interest cannot currently be 3D printed. Here, the SBAM method for 3D printing of viscous polymer solutions was applied to both "intrinsically porous" (a polymer of intrinsic microporosity, PIM-1) and "intrinsically non-porous" (cellulose acetate) polymers. Successful ternary ink formulations require the balancing of solution thermodynamics (phase separation), mass transfer (solvent evaporation), and rheology. As a demonstration, a microporous polymer (PIM-1) incompatible with current additive manufacturing technologies is 3D printed into a high-efficiency mass transfer contactor exhibiting hierarchical porosity ranging from sub-nanometer to millimeter pores. Short contactors (1.27 cm) can fully purify (< 1 ppm) toluene vapor (10000 ppm) in N_2 gas for 1.7 hours, which is 6 times longer than PIM-1 in traditional structures, and more than 4,000 times the residence time of the gas in the contactor. This solution-based additive manufacturing approach greatly extends the range of 3D-printable materials.

[†] This chapter has been published in *Macromolecular Rapid Communications* as "Solution-Based 3D Printing of Polymers of Intrinsic Microporosity".[1]

4.1 Introduction

Additive manufacturing techniques like 3D printing have revolutionized manufacturing because they can produce complex structures that are difficult or impossible to create using traditional methods. As a result, they have been widely applied in the development of microfluidics devices,[2] structured biomaterials[3-5], and structures with high mechanical strength.[6] In spite of the remarkable progress that has been made, a critical limitation of existing and emerging additive manufacturing techniques is still the relatively narrow range of polymers that can be processed.[7] For instance, fused deposition modeling (FDM) processes thermoplastic polymers with moderate melting points, while stereolithography (SLA) requires polymers that can be photopolymerized or photocrosslinked.[5,8-10] Many advanced functional polymers (e.g., cellulose derivatives, polyimides, microporous ladder polymers) are incompatible with FDM and SLA,[11] yet would immensely benefit from the structural complexity and versatility offered by state-of-the-art additive manufacturing. The development solution-based additive manufacturing (SBAM) greatly extends the design space and capabilities of polymer-based devices and structures.[12,13]

Engineering efficient mass transfer contactors for fluid processing is an emerging area where additive manufacturing could play a critical role. Indeed, development of complex structures (i.e., beyond hollow fiber bundles) for mass transfer applications is of great practical interest. Here, we 3D printed polymer with intrinsic microporosity, PIM-1, via SBAM as a proof-of-concept. PIM-1 is widely used in mass transfer processes but is incompatible with existing 3D printing techniques. Due to inefficient packing of the rigid, contorted backbones, PIM-1 possesses microporosity and exhibits promising performance

in adsorptive and membrane gas separations and heterogeneous catalysis applications.[14] However, existing research on PIM-1 is limited to simple structures, such as powders, films, and fibers.[15-17] To demonstrate the versatility of SBAM technique, cellulose acetate, an inexpensive polymeric support for functional materials, is also 3D printed via SBAM[18]

Inspired by the fundamental principles of hollow fiber membrane spinning, we developed a solution-based 3D printing technique capable of manufacturing more complex structures with hierarchical porosity.[15] We utilized the IUPAC definition of pore sizes, which defines micropores as pores smaller than 2 nm in diameter, mesopores as pores with diameters between 2 nm and 50 nm, and macropores as pores with diameters larger than 50 nm. Hierarchical porosity refers to the coexistence of 2 or 3 types of pores. The printing technique involves three steps: deposition, solidification and mild non-thermal post-treatment. First, a pneumatic micronozzle deposits a filament of viscoelastic polymer solution onto a moving stage coated by a thin film made of the printing polymer (e.g., cellulose acetate or PIM-1), which is utilized to enhance binding between the printed structure and the substrate (Figure 4.1a)**.** Second, the evaporation of volatile solvents in the polymer solution occurs as the polymer filament exits the nozzle and contacts the existing structure. Critically, a binary polymer solution (i.e., polymer and its solvent) yields a dense microstructure within the filament, which is non-ideal for most mass transfer applications, but is potentially useful in applications requiring mechanical strength.[19] A ternary polymer solution (i.e., polymer, solvent, and nonsolvent), in contrast, was found to produce a micro-/meso-/macro-porous structure as a result of spinodal decomposition of the ink and the intrinsic microporosity of the polymer in the case of PIM-1.[15] Finally, the printed structure undergoes room-temperature drying and nonsolvent washing to remove residual printing

solvent. The interlayer adhesion, microstructure, and filament skin layer can be tuned by controlling the ink composition, printing atmosphere (i.e., temperature and solvent saturation level) and the post-treatment conditions.

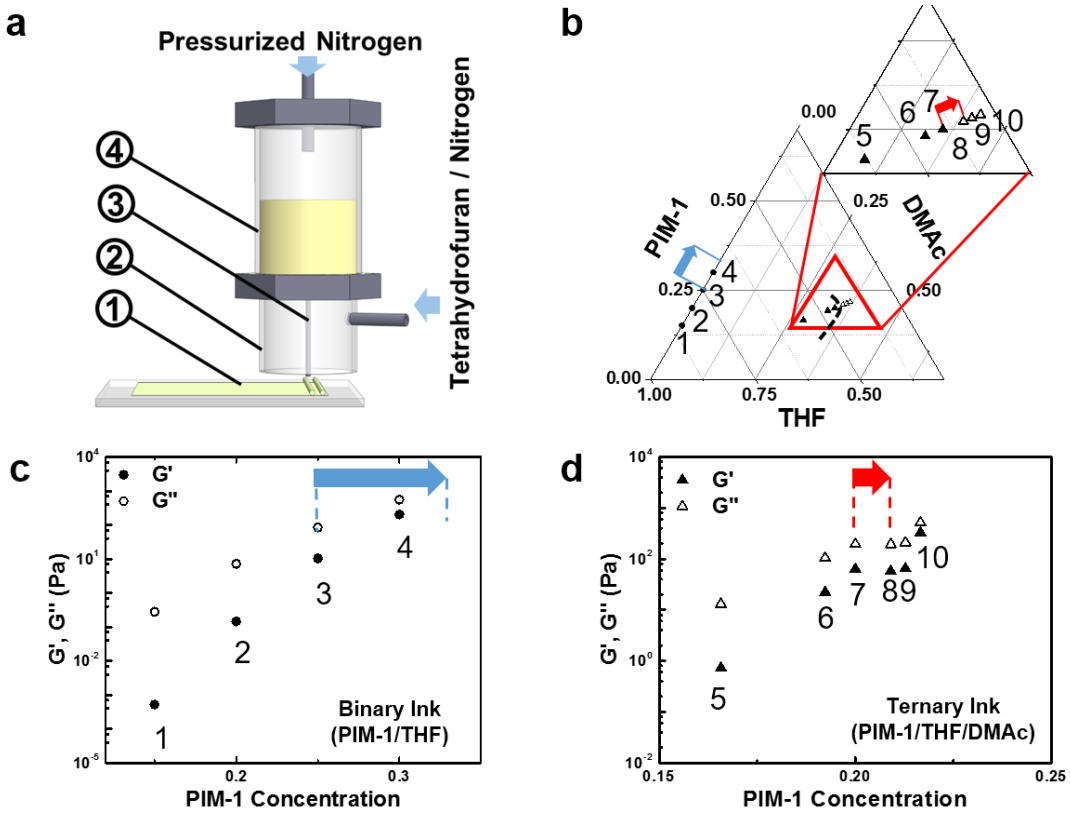

Figure 4.1 Design of solution-based direct-write 3D printer and PIM-1 printing ink. (a) 3D printer setup. 1: substrate covered with a thin PIM-1 film; 2: secondary nozzle generating solvent-saturated atmosphere; 3: primary nozzle delivering inks; 4: pneumatic ink cartridge. (b) Ternary phase diagram of PIM-1 / THF (solvent) / DMAc (nonsolvent). The blue arrow indicates the compositional trajectory of a binary ink (PIM-1/THF) as a result of solvent evaporation. The red arrow across the phase boundary (black dashed line) highlights the compositional trajectory of the ternary ink (PIM-1/THF/DMAc) during solvent evaporation. Detailed ink composition data can be found in Table 4.1. (c) Evolution of complex mechanical moduli of the binary ink as a result of solvent evaporation. The blue arrow corresponds to the same compositional change as shown in Figure 4.1b. (d) Complex moduli evolution of the ternary ink. The composition of the ink utilized to print the final structures in this work is PIM-1:THF:DMAc = 10:23:17, and the red arrow corresponds to the same compositional change as shown in Figure 4.1b.

4.2 Experimental Section

4.2.1 Materials

Tetrafluoroterephthalonitrile (TFTPN, Alfa Aesar) was purified via vacuum sublimation at 140 °C. 5,5′,6,6′-Tetrahydroxy- 3,3,3′,3′-tetramethyl-1,1′-spirobisindane (TTSBI, Alfa Aesar) was purified by recrystallization from methanol. Prior to synthesis, anhydrous potassium carbonate was crushed into a fine powder and stored in a desiccator. All solvents were used as received from various commercial suppliers.

PIM-1 was synthesized as described by Jue et. al.[20] After synthesis, PIM-1 was washed by DMF and methanol sequentially to remove unreacted monomers and oligomers. According to GPC analysis, Mn of the purified PIM-1 is 50,166 with Mw/Mn around 1.65.

Polymer solutions were prepared as described below to prevent the deleterious influence of water vapor, to which PIM-1 solutions are extremely sensitive. PIM-1 powder was vacuum dried overnight at 80 °C to remove any residual solvents. Solvent, nonsolvent, and polymer were mixed together within a sealed stainless-steel cartridge made of Swagelok® fittings. To ensure homogeneity, the stainless-steel cartridges loaded with undissolved polymer solutions were then loaded onto a rotating rack enclosed in the oven. After slow rotation under 50 ºC for 12 hours, the PIM-1 was fully dissolved and the solution (or "ink") was ready for printing. The cartridge containing these homogenous PIM-1 solutions was mounted into a customized 3D printer (Figure 4.1a).

4.2.2 Ternary Phase Diagram

The ternary phase diagram for PIM-1/THF/DMAc was determined by the cloud-point technique. PIM-1 solutions with different compositions were prepared by mixing DMAc, THF, and PIM-1 sequentially in a glass vial. After rapid dispersion aided by a vortex mixer, these PIM-1 solutions were then transferred onto a roller and heated by heating lamps to around 50 ºC. After slow rotation mixing for 3 days, the solutions were then transferred into a 25 ºC incubator to cool them down for another 1 day. After that, the clarity and fluid flow properties were examined by the eye. A clear flowing liquid indicates a homogenous phase, while any other appearance indicates a 2-phase system. The binodal curve (the boundary between the homogenous region and 2-phase region) was located by comparing adjacent dopes that exhibited a homogenous composition and an inhomogeneous composition.

4.2.3 Rheology Characterization

The rheological properties of 3D printing inks were measured by an Anton Paar MCR 302 Rheometer (Anton Paar GmbH, Austria-Europe) with Couette geometry. The measuring bob has a diameter of 16.66 mm, and the measuring cup has a diameter of 18.07 mm. A vapor lock around the Couette geometry was pre-filled with THF to prevent sample evaporation; THF in the vapor lock was replenished every 10 minutes. Prior to rheological characterization, all inks were heated up to 50 ºC to ensure homogeneity and then cooled down to room temperature. Viscosity measurements were carried out over a range of shear rates from 0.01 s^{-1} to 100 s^{-1}. Oscillatory shear measurements were carried out in frequency sweep mode (strain amplitude fixed at 0.1 with angular frequency ranging from 0.01 rad s^{-}

^{1} to 628 rad s^{-1}) and amplitude sweep mode (angular frequency fixed at 1 rad s^{-1} with strain amplitude ranging from 0.01 to 10).

4.2.4 Solution-based 3D Printing

All 3D printed PIM-1 adsorption devices were produced using a custom-built Cartesian 3D printer that is designed to handle polymer solution inks. An example optimized ternary ink composition was PIM-1:THF:DMAc = 10:23:17. Appropriate G-code commands were written to control the movement of the 3D printer. The ink is extruded through a stainless-steel needle (G24, inner diameter 311 μm) by applying the appropriate pressure (350 - 1300 kPa) from a nitrogen gas cylinder, which is controlled by a regulator. Structures printed in this section were fabricated at linear speeds ranging from 1 mm·s^{-1} to 10 mm·s^{-1}.

4.2.5 Adsorption Performance Test

The kinetic adsorption of toluene experiment was conducted to simulate hazardous gas removal from the closed system without forced airflow. A 4-layered PIM-1 scaffold was placed in the chamber of a Dynamic Vapor Sorption System (DVS Vacuum, Surface Measurement Systems) where a vapor toluene environment with a specific pressure was generated. The mass change of the sample during exposure to toluene vapor was monitored. To compare the differences between different geometries of PIM-1 sorbents, dense PIM-1 pellets, and porous PIM-1 fibers were also tested.

PIM-1 adsorption modules were assembled by fixing a 3D printed PIM-1 monolith into a customized stainless steel enclosure. Toluene/nitrogen mixtures were sent through

the adsorption column at a flow rate of 30 cm^3 s^{-1}. The outlet gas was analyzed in real-time using a quadrupole mass spectrometer (Omnistar GSD 301 C, Pfeiffer Vacuum). Before each run, the PIM-1 adsorption column was heated to 100 ºC under vacuum for 12 hours to remove residual solvent or toluene. As a comparison, PIM-1 powder and fibers[15] were also tested following the same protocol.

4.2.6 Nitrogen Physisorption

BET surface area and pore size distribution of PIM-1 samples were obtained from nitrogen physisorption experiments at 77 K using a BELSORP-max (MicrotracBEL). Before measurement, the samples were refreshed by methanol to eliminate any confounding aging effects.[20]

4.2.7 Mercury Porosimetry

Mercury porosimetry was used to measure the hierarchical pore structure of 3D printed PIM-1 and cellulose acetate scaffolds. The scaffolds were refreshed with methanol and then measured in an AutoPore IV (Micromeritics) porosimeter.

4.3 Results and Discussion

4.3.1 3D Printing of Ternary Polymer Solution

Typical inks for direct-write 3D printing of microporous materials often contain high loadings of solid particles that prevent deformation of printed filaments at low apparent ink viscosities by creating yield stress.[21-23] Pure polymer solutions such as those utilized here, on the other hand, require a rapid shift from a liquid to a solid-state. A method

to enable this phase transition is to process a highly viscous polymer solution containing a volatile solvent. After deposition of a filament onto the existing substrate, evaporation of the solvent (tetrahydrofuran, THF, in this study) increases the polymer concentration within the filament and induces solidification (when storage modulus becomes higher than loss modulus) either through vitrification or phase inversion. To avoid extremely high pressure through the printer nozzle at room temperature, the PIM-1 concentration cannot exceed 25 wt% (Figure 4.2). Figure 4.2a and b show that the polymer solutions can be approximated as incompressible Newtonian fluids and that laminar flow is expected in the nozzle. The pressure drop (ΔP) is calculated by the Hagen-Poiseuille equation, $\Delta P = {8\mu LQ}/{\pi R^4}$, where L, the length of the micronozzle, is 5 mm, Q, the volumetric flowrate of the polymer solution, ranges from 0.005 $cm^3\ s^{-1}$ to 0.5 $cm^3\ s^{-1}$ and R, the inner radius of the micronozzle, is 156 μm. Although binary ink 4 could achieve the fastest solidification among all binary inks, its high viscosity prevents flow even under high extrusion pressures (~2000 kPa). As a result, ink 3 was chosen with a sacrifice of rapid liquid-to-solid transition. However, ternary ink 7 exhibits a good balance between "flowability" and rapid solidification: it lies next to the binodal boundary (Figure 4.1b) and requires achievable driving pressures.

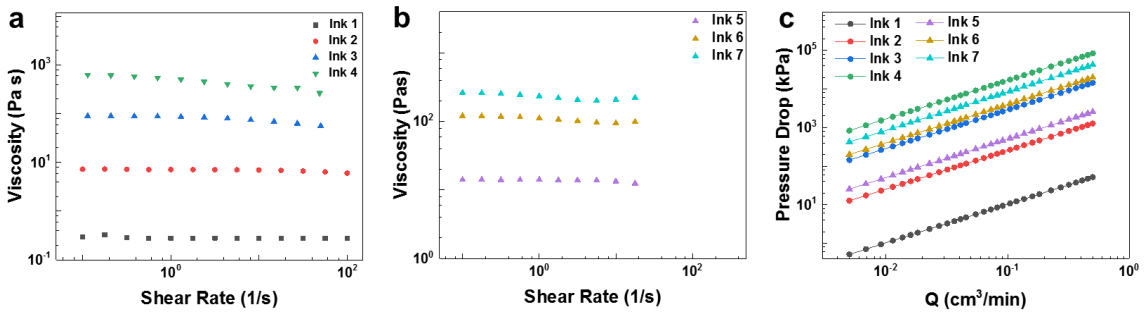

Figure 4.2 Dynamic viscosity (μ) of (a) binary inks and (b) ternary inks measured at 25 oC. (c) Estimated pressure drop across the micronozzle for binary inks and ternary inks.

Figure 4.3 shows an example of a scaffold printed from a 25 wt% PIM-1/THF solution; the changes in solution rheology during the printing stage are shown in Figure 4.1b (blue arrow) and Figure 4.1c (ink compositions are listed in Table 4.1). Importantly, 3D printing of binary polymer solutions has three drawbacks: first, it takes a relatively long time for a printable polymer solution to be fully solidified, because 5 wt% of the ink must evaporate, which leads to gravity-driven deformation after deposition (Figure 4.3). Second, solvent evaporation causes an enrichment of the polymer concentration at the filament surface and results in a dense (i.e., no meso-/macro-porosity) skin layer via polymer vitrification (Figure 4.4a); this layer would dramatically slow down mass transfer between the polymer filament and surroundings and render the printed structure unsuitable for mass transfer applications such as adsorption and catalysis. Third, due to the density difference between polymer solution and dry polymer, the formation of dense filaments inevitably leads to shrinkage (Figure 4.4c and Figure 4.3). At elevated temperatures (Figure 4.3c and d), the evaporation rate of THF increases while the viscosity of polymer solution decreases. As a result, printed filament becomes both denser and exhibits greater deformation.

Table 4.1 3D printing ink composition by weight ratio.

Sample	PIM-1	THF	DMAc
Ink 1	0.150	0.850	0.000
Ink 2	0.200	0.800	0.000
Ink 3	0.250	0.750	0.000
Ink 4	0.300	0.700	0.000
Ink 5	0.166	0.552	0.282
Ink 6	0.192	0.481	0.327
Ink 7	0.200	0.460	0.340
Ink 8	0.209	0.436	0.355
Ink 9	0.213	0.426	0.362
Ink 10	0.217	0.415	0.368

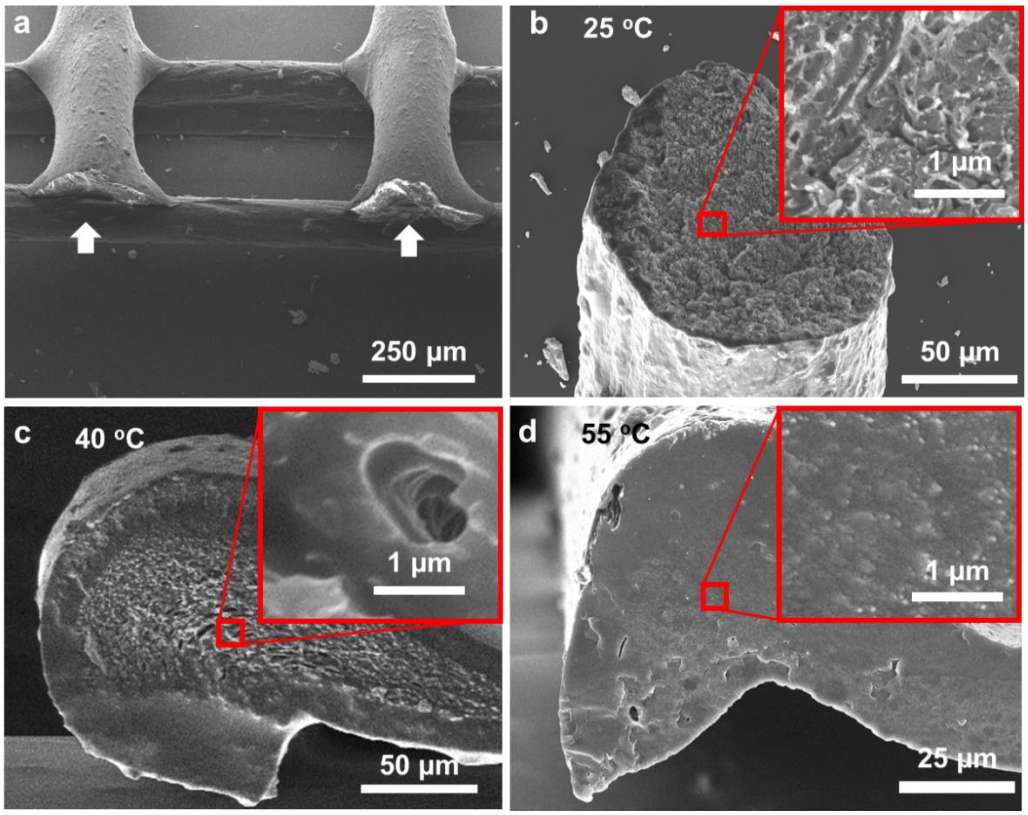

Figure 4.3 SEM micrographs of PIM-1 scaffold printed from 25 wt% PIM-1/THF solution. (a) Gravity-driven deformation of filaments printed at 25 ºC. Magnification and cross section of filaments printed at (b) 25 ºC, (c) 40 ºC and (d) 55 ºC reveal thick skin layers and dense microstructures. insert: dense morphologies of the core of the filaments.

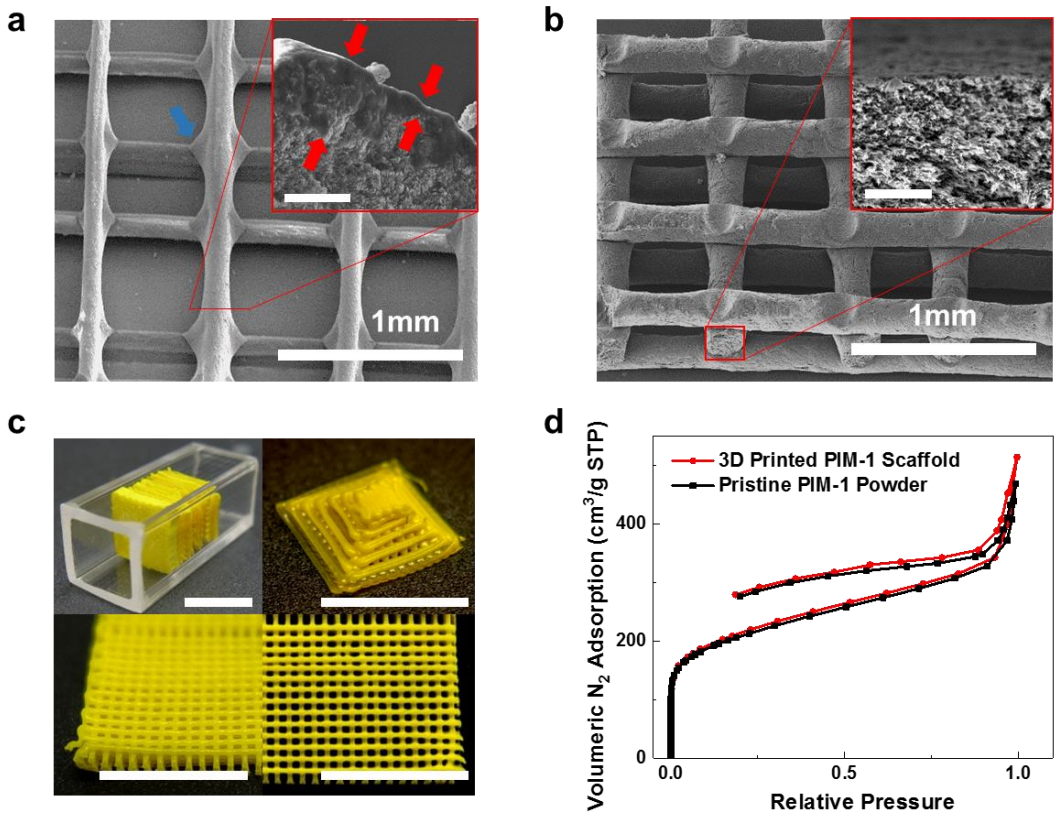

Figure 4.4 3D printed PIM-1 structures. (a) SEM image of 3D printed scaffold created using a binary ink (PIM-1/THF). Blue arrow highlights the deformation of PIM-1 filaments due to delayed solidification. inset: SEM image of the filament cross-section. The red arrows highlight a dense skin layer, which is deleterious for mass transfer applications. The inset scale bar is 20 µm. (b) SEM image of 3D printed scaffold created using a ternary ink (PIM-1/THF/DMAc). Here, the top layers were removed to reveal the intersection of two adjacent filaments. *inset*: SEM image of filament cross-section. Scale bar is 20 µm. (c) Optical photographs of various PIM-1 scaffolds created via 3D printing of ternary polymer solutions. Top left: monolith adsorber; top right: pyramid; bottom left: multi-layered scaffold; bottom right: top view of the scaffold. The inset scale bars are 1 mm. (d) Nitrogen physisorption isotherms at 77 K of PIM-1 powder and 3D printed PIM-1. BET surface area of 3D printed PIM-1 (748 ± 5 $m^2 g^{-1}$) is comparable with that of pristine PIM-1 powder (726 ± 3 $m^2 g^{-1}$).

To prevent filament deformation, eliminate shrinkage, and introduce hierarchical porosity throughout the 3D printed structure, we developed a ternary 3D printing ink consisting of PIM-1, solvent (THF) and nonsolvent (dimethylacetamide, DMAc, in this study). The addition of nonvolatile nonsolvent dramatically changes the solution

thermodynamics and the rheology of the system (Figure 4.1b and Figure 4.1d). In this case, evaporation of a relatively small fraction (0.9 wt% loss of the ink) of the volatile solvent shifts the composition of the nascent ink across the binodal boundary (black dashed line in Figure 4.1b) to induce spinodal decomposition of the solution, which results in solidification and the formation of interconnected meso-/macro-pores. As shown by the rheological data along the trajectory (red arrow in Figure 4.1b and d) of THF evaporation from the ternary solution, both the storage modulus (G′) and loss modulus (G″) increase as solvent is removed. Once the filament composition moves into the 2-phase region, there is a delayed change of these complex moduli because of phase inversion solidification. Strain amplitude sweep measurements (Figure 4.5) reveal that the rapidly solidified macroporous filament is more brittle than slowly solidified dense filaments, which implies formation of kinetically-trapped porous structures when using the ternary ink. Compared with the binary inks, ternary inks exhibit a good balance between "flowability" and rapid solidification (Figure 4.3 and Figure 4.4b). Evaporation-induced phase separation also produced mesopores and macropores that accelerate mass transfer processes (Figure 4.4b, Figure 4.6 and Figure 4.7). The formation of meso-/macro-pores within the printed filaments also greatly reduces structural shrinkage effects from solvent evaporation. This work suggests that 3D printing of polymers from solution can be achieved without needing to compensate for evaporation-induced shrinkage (Figure 4.4c).

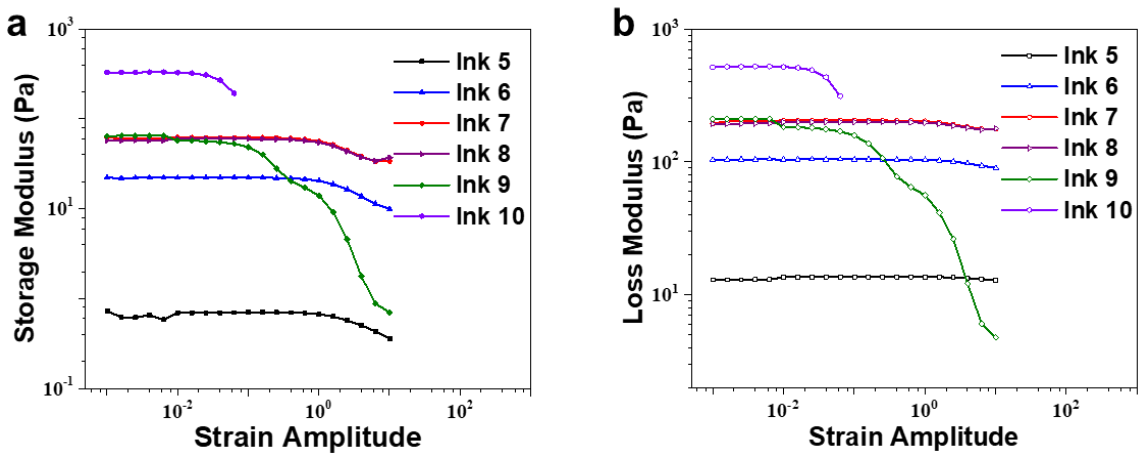

Figure 4.5 (a) Storage modulus (G′) of ternary polymer solutions measured via amplitude sweep in the dynamic mechanical analysis. (b) Loss modulus (G″) of ternary polymer solutions measured by amplitude sweep. Ink compositions are tabled in Table 4.1.

Although the addition of nonsolvent enables rapid solidification and formation of interconnected meso-/macro-pores within a single filament, it inhibits adhesion between the depositing filament and filaments already incorporated into the structure. We hypothesized that excessively rapid evaporation of the volatile solvent resulted in filaments that had effectively solidified before contacting the structure to which they were being added. To reduce the solvent evaporation rate in the air gap between the micronozzle and the printed structure, we installed a secondary nozzle that ejected an atmosphere saturated with the volatile solvent. The increase in solvent partial pressure around the nascent filament reduces the driving force for solvent evaporation, thus suppressing the evaporation rate. By controlling the degree of saturation in this atmosphere, the time for solvent evaporation could be tuned so that the appropriate balance between storage and loss moduli could be reached that enables strong filament-filament adhesion without significant filament deformation or structural collapse (Figure 4.8). Low evaporation rate of volatile

solvent also inhibits evaporation-induced surface vitrification thus eliminating skin layer formation (Figure 4.4b and Figure 4.8).

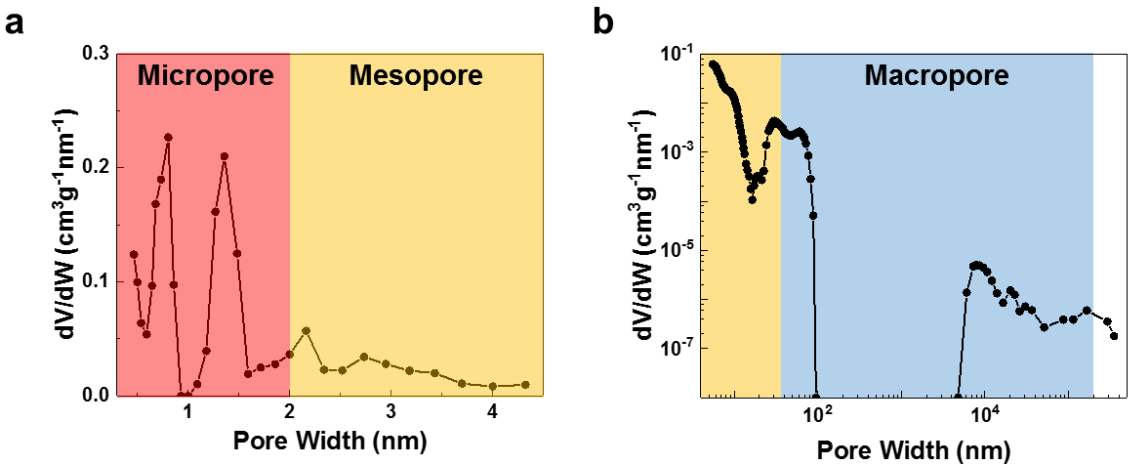

Figure 4.6 Pore size distribution of 3D printed PIM-1 from ternary ink. The red area represents the microporous region (< 2 nm), the yellow area represents the mesoporous region (2 nm – 50 nm), and the blue area represents the macroporous region (> 50 nm). (a) Pore size distribution was obtained by fitting nitrogen physisorption isotherms at 77 K with the 2D-NLDFT model for slit pore geometry. (b) Pore size distribution measured by mercury porosimetry.

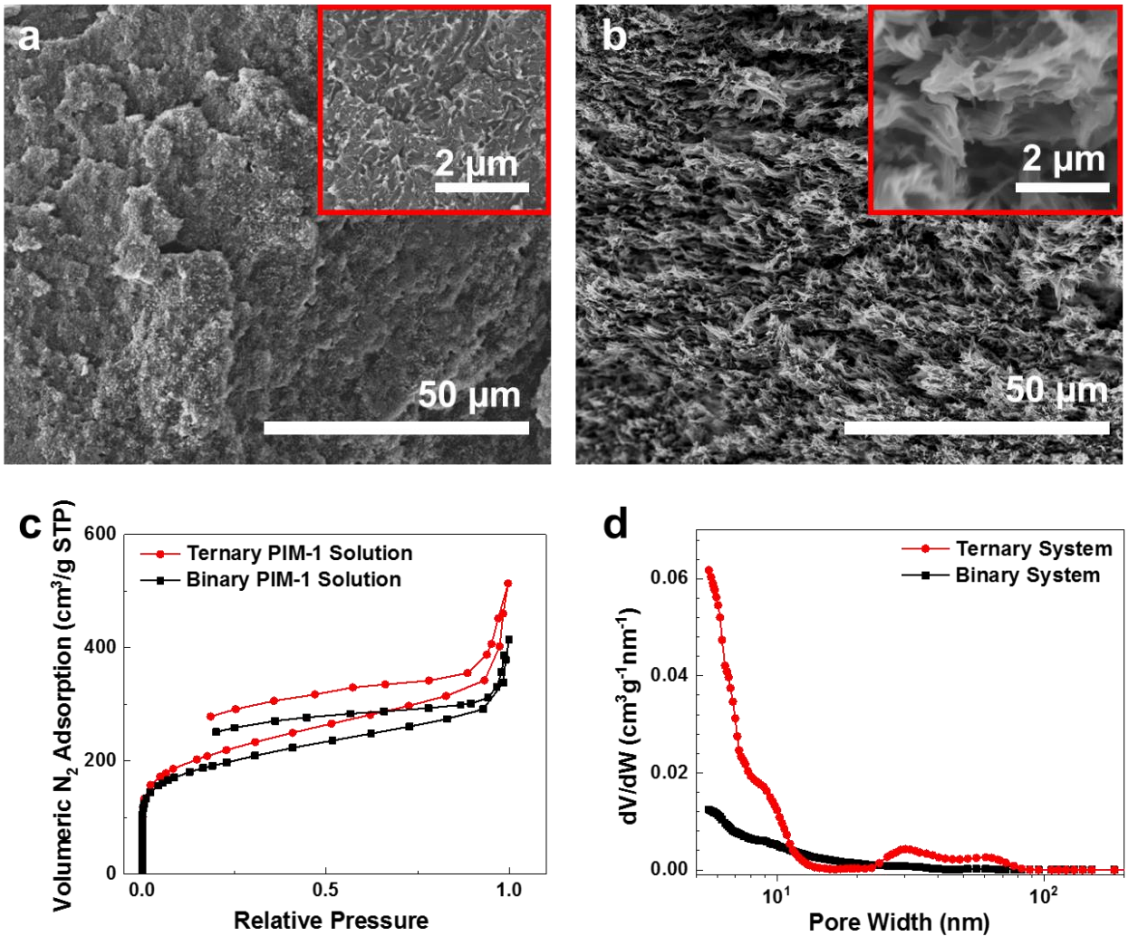

Figure 4.7 Comparison of cross-sections of PIM-1 filaments printed from (a) binary solution and (b) ternary solution. insets: high-magnification images. (c) Nitrogen physisorption isotherms at 77 K of 3D printed PIM-1 based on ternary solution and binary solutions; BET surface areas of PIM-1 printed from ternary solution (748 ± 5 m^2 g^{-1}) and binary solution (679 ± 3 m^2 g^{-1}) are comparable, as solution-based 3D printing does not the alter intrinsic properties of the polymer. (d) Pore size distributions measured by mercury porosimetry reveal that a ternary solution generates more mesopores (2 nm - 50 nm) and macropores (> 50 nm).

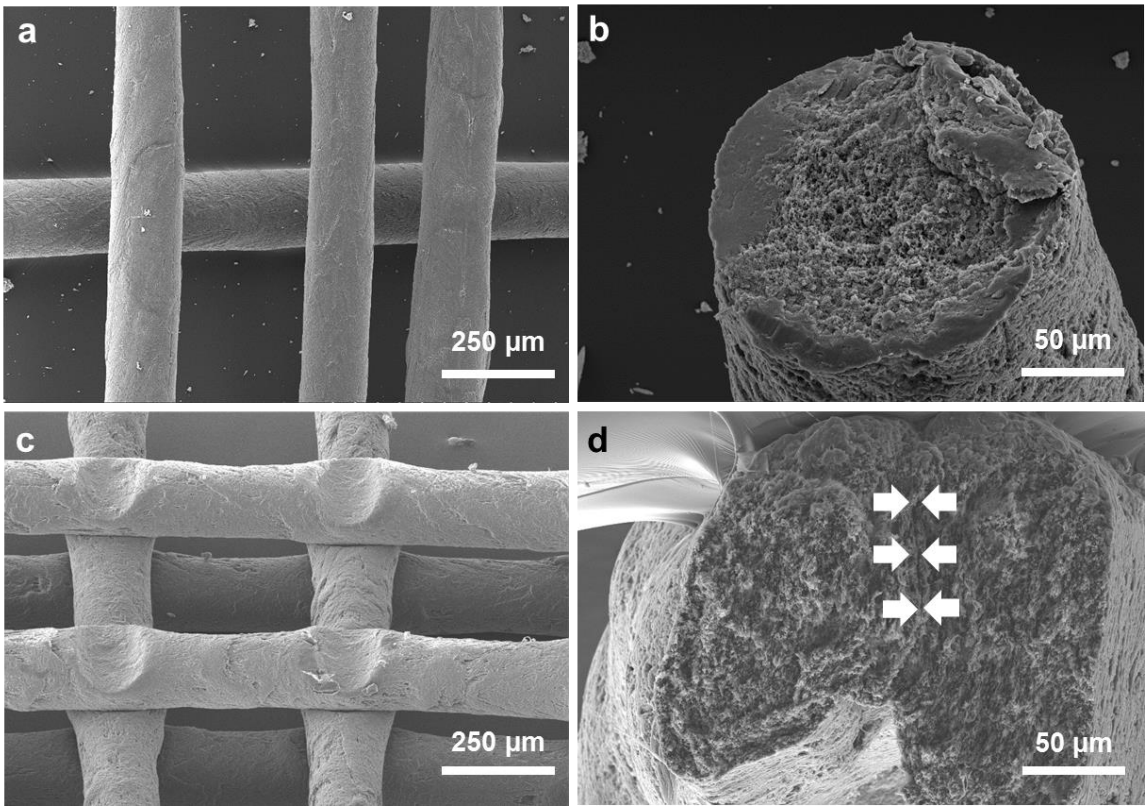

Figure 4.8 SEM micrographs of PIM-1 scaffold printed from optimized ternary ink (PIM-1:THF:DMAc = 10:23:17) at 25ºC with different degree of THF-saturation in the printing atmosphere. (a, b) 0% THF saturation and (c, d) 100% THF saturation. When printed in dry atmosphere, there is nearly no interlayer adhesion as most volatile solvent rapidly evaporated, which results in packing of individual filaments. At 100% THF saturation, interlayer adhesion is so strong that no delamination was observed (highlighted by white arrows in d). As printing atmosphere is more and more THF saturated, THF evaporation is slowed down and solvation bind adjacent filament together. At lower THF evaporation rate, skin layer formation is also inhibited (compare b and d).

After printing, the PIM-1 structures were washed with methanol and hexane sequentially, followed by a low-temperature drying step (85 kPa vacuum, 80 ºC) to get rid of residual organic solvent. The solvent exchange process uses a sequence of nonsolvents with decreasing surface tensions to prevent the collapse of meso-/macro-pores during the post-fabrication drying process.[20] This mild activation process maintains the micro-/meso-/macro-porosity of the printed PIM-1 structures. As shown in Figure 4.4d and Figure 4.9a,

the 3D printed PIM-1 scaffold exhibits similar BET surface areas and toluene vapor uptakes as neat PIM-1 powders.

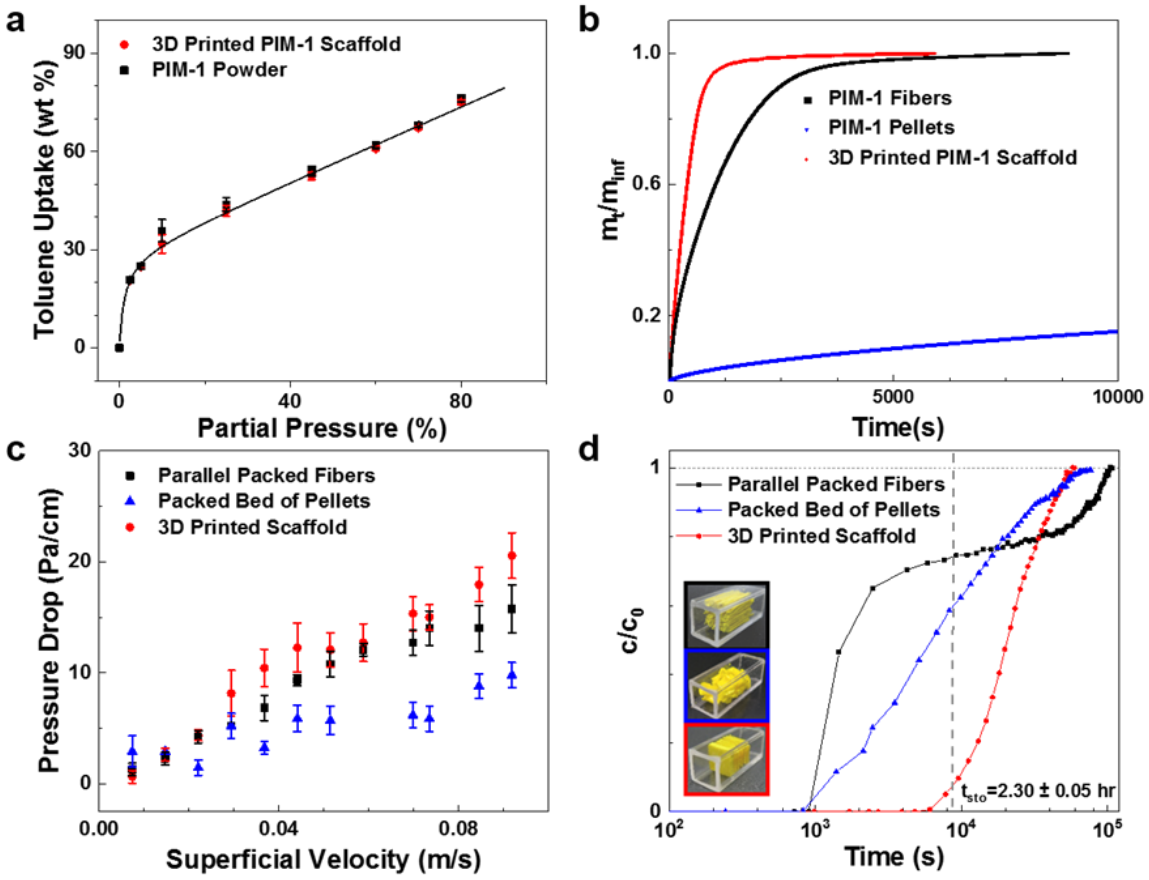

Figure 4.9 Adsorption performance of 3D printed PIM-1 structured materials. (a) Toluene adsorption isotherms of 3D-printed PIM-1 and PIM-1 powders. The isotherm is fitted with a dual mode equation.[24] (b) Kinetic uptake of toluene into PIM-1 fibers, pellets and 3D printed scaffold. (c) Air pressure drop across the three adsorption beds as a function of superficial air velocity. (d) Toluene vapor breakthrough experiment carried out at 30 ºC. A feed of toluene vapor (10000 ppm) in nitrogen flows through PIM-1 adsorbers at 30 cm^3 s^{-1}. insert: Images of columns for illustration. Black framed image shows parallel packed fibers, blue framed image a packed bed of pellets and the red framed image is the 3D printed scaffold.

Importantly, the creation of hierarchical porosity during the printing process via phase inversion is not limited to PIM-1. A cellulose acetate scaffold printed using a ternary ink that was formulated according to the same general approach as described for PIM-1

(with solvents/nonsolvents specific to cellulose acetate) also exhibits hierarchical macro-/meso-porosity (Figure 4.10). A large variety of hierarchically porous polymers has already been fabricated via phase inversion in dry-wet fiber spinning, and we hypothesize that these polymers can also be 3D printed using the techniques described here.[13,25] State-of-art laser-based stereolithography can manufacture features with 100-nm resolution while macropores with diameters from 0.5 μm to 100 μm can be produced via emulsion-based techniques.[10,26] However, all of the aforementioned pore structures are macroporous. By contrast, 3D printing of ternary polymer solution creates both mesopores and macropores. Moreover, through the use of PIM-1 we also create micropores to truly have multi-scale hierarchical porosity; this latter population of pores is unique to this choice of polymer, which cannot be processed with the other printing methods. In our current solution-based 3D printing approach, phase inversion is induced by evaporation and therefore requires the careful selection of volatile solvents and less-volatile nonsolvents for each specific target polymer (volatile nonsolvents could in principle be used as well by introducing a nonsolvent-enriched gas environment, as is widely used in wet-dry fiber spinning[13,15]). Although the minimum feature size of our current setup is around 200 μm, it is potentially possible to utilize smaller diameter micronozzles and harness ink deformation to increase resolution and create periodic features, as shown by Zhao and coworkers. [27]

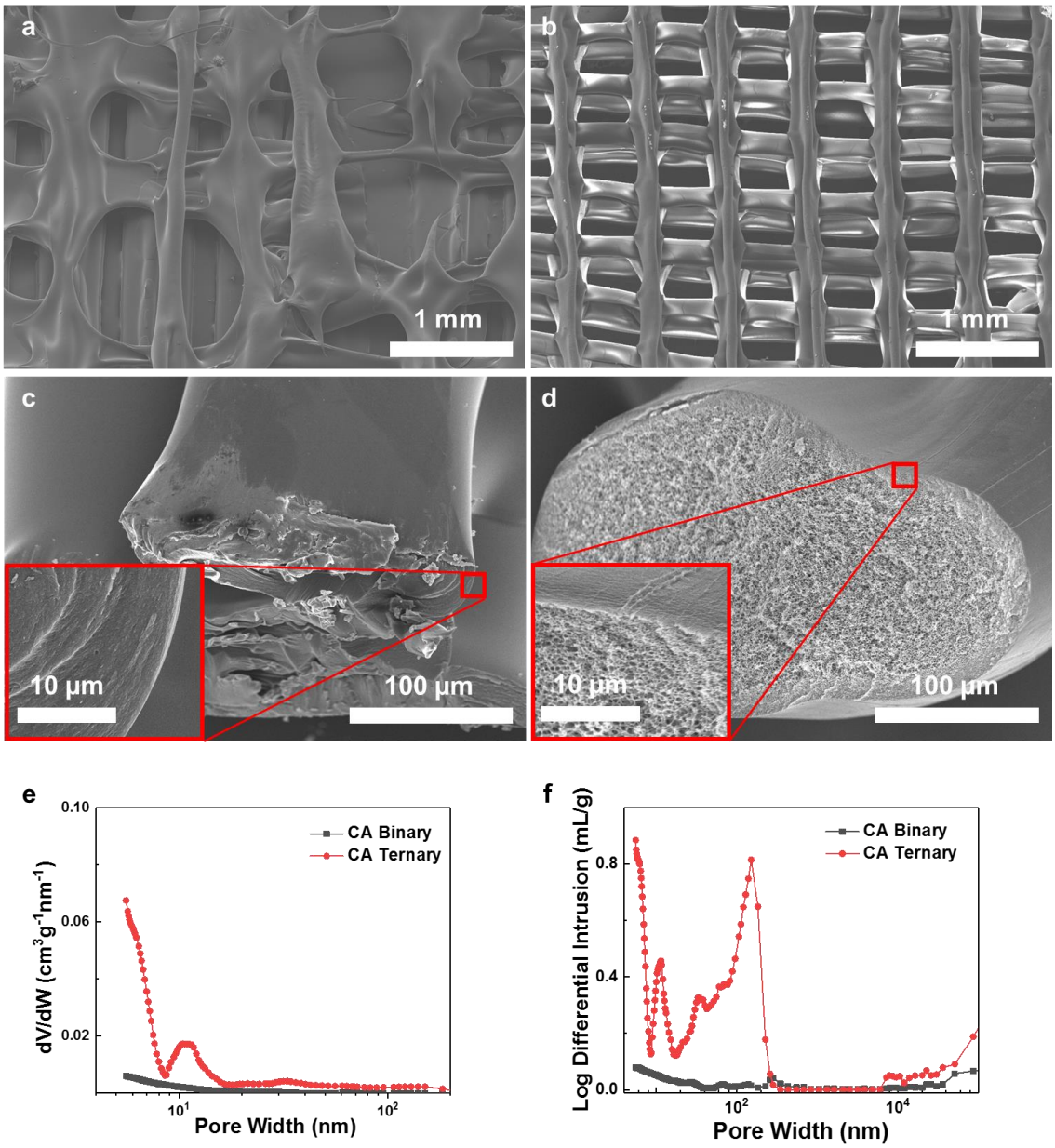

Figure 4.10 Comparison of cellulose acetate (CA) scaffolds printed from (a, c) binary ink (CA:Acetone = 25:75) and (b, d) optimized ternary ink (CA:Acetone:Water = 23:52:25). The ternary ink largely avoids deformation at relatively low polymer concentrations compared with the binary inks of similar polymer concentrations owing to rapid phase inversion of the former. Moreover, the binary ink forms a flat dense filament while the ternary inks tend to form round, porous filaments. (e, f) Pore size distributions measured by mercury porosimetry reveal that ternary solution generates more mesopores (2 nm to 50 nm) and macropores (> 50 nm), which agrees with the observation in PIM-1 system.

4.3.2 3D Printing Energy-Efficient Adsorption Contactor

Structured materials with precisely designed mass flow channels and solid-fluid interfaces provide unprecedented opportunities for engineering microscale transfer phenomena, which are beneficial for sensors,[28,29] pressure-drop-efficient adsorbers,[21,22,30] catalytic devices,[31] membrane modules,[32] etc. As a proof-of-concept, we printed PIM-1 monolith structures for removal of a model volatile organic compound (VOC, toluene in this study) from a gaseous feed. We assessed the kinetic uptake of dilute toluene atmospheres (0.71 torr of toluene, which is 2.5% of the saturation pressure) into a PIM-1 scaffold (average diameter of filaments is 200 μm) made via 3D printing. This scaffold was benchmarked against more traditional packed beds of fiber-type (half thickness 150 μm) and pellet-type PIM-1 adsorbent (short cylinders with 2 mm diameter). As shown in Figure 4.9b, it takes the 3D printed PIM-1 adsorbent only 320 s and 2800 s to reach 50% and 99% saturation, respectively, whereas the fiber-type and pellet-type samples exhibit significantly slower kinetic uptake rate. The rapid kinetic performance of the 3D printed scaffold is attributable to the smaller characteristic length of the filaments when compared to the fiber or pellet samples. Figure 4.11 normalizes the influence of characteristic length difference so that the fractional mass uptake rate is solely determined by apparent diffusivity, and in this case, the sample kinetics of the various materials are nearly identical, which suggests that the 3D printed structures do not contain deleterious skin layers or other mass transfer resistances not present in the fiber. The hierarchical porous PIM-1 structures (PIM-1 fibers and 3D printed PIM-1 scaffolds) exhibit significantly improved apparent diffusivity compared with dense PIM-1 structures.

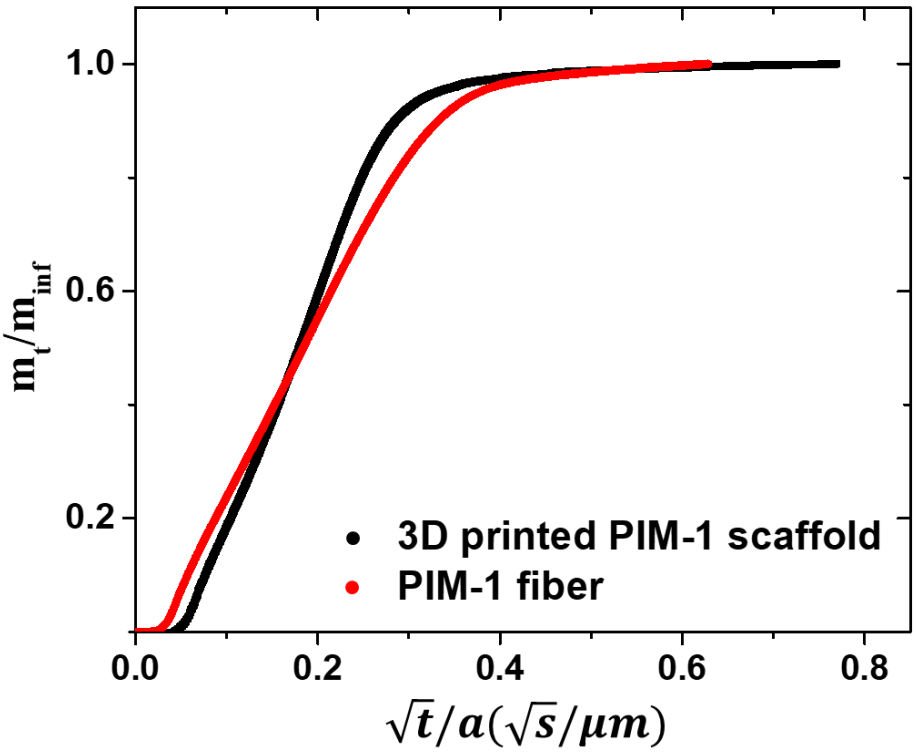

Figure 4.11 Change of fractional mass uptake, $\frac{m_t}{m_{inf}}$, as a function of $\frac{\sqrt{t}}{a}$, where m_t is the weight difference between current sample and initial dry sample, m_{inf} is the weight difference between sample at equilibrium and initial dry sample, t is time and a is characteristic length for mass transfer of each sample (100 μm for 3D printed scaffold and 150 μm for fibers).

With proper design, 3D printed mass transfer contactors can provide highly uniform fluid-solid contact paths and thus achieve more efficient mass transfer. Traditional randomly packed adsorbent beds contain flow channels with wide size distributions; the larger channels in such distributions allow fluid to bypass the adsorbent without effective mass transfer of the adsorbate into the adsorbent. Such a bypass problem is not significant for industry-scale adsorbent beds with length-to-diameter ratios over 50, but can be critical for miniature packed beds that would be suitable for small-scale applications like personal protection equipment. To demonstrate the improved mass transfer efficiency of 3D printed

structures, three PIM-1 adsorbent beds were assembled using different packing structures (Figure 4.12): (i) a 3D printed scaffold with 256 parallel channels of 300 μm × 300 μm uniform dimension, (ii) parallel packed fibers, and (iii) a packed bed of pellets. Adsorbent weight (410 ± 5 mg) and adsorption column dimensions (square column cross section of 0.95 cm by 0.95 cm and column length of 1.27 cm) were kept identical. Toluene breakthrough experiments were then carried out to compare the adsorption and pressure drop performance of these adsorbers. The pressure drop for all three materials was found to be approximately the same (Figure 4.9c), and will be discussed below in conjunction with the breakthrough performance of the beds. A gas feed of 10000 ppm toluene in nitrogen was introduced into the adsorption columns at 30 $cm^3 s^{-1}$ (superficial gas velocity 0.55 cm s^{-1}) and the composition of the product gas was monitored via mass spectrometry. Figure 4.9d shows breakthrough curves of these three types of adsorbers. Although all three adsorbers capture roughly the same amount of toluene eventually, the remarkable result is that the 3D printed scaffold produced clean gas (i.e., toluene concentration below the 1 ppm detection limit) for nearly 1.7 hours, which is close to the stoichiometric breakthrough time (2.3 ± 0.05 hours) and almost 6 times as long as the other two adsorbers. The difference in effective operation time, during which there is no toluene present in the product gas, is attributed to the difference of characteristic lengths and the gas flow channel designs. Given that the length-to-diameter ratio of these adsorbers is only 1.33 and the nominal residence time of gas in the adsorbers is only around 1.5 s, any bypass would result in a sharp increase of the toluene concentration in the outlet stream. Owing to its precisely designed gas flow channels, the 3D printed PIM-1 scaffold exhibited a sharp breakthrough front, which means all adsorbent filaments were saturated at similar time. Said differently,

random packing leads to inefficient utilization of adsorbents; non-uniform straight channels in parallel packed fibers create bypasses and result in a step increase of product toluene concentration, whereas regions with lower packing density in a packed bed of pellets have much higher local flowrate and become saturated earlier than the other parts, which results in a broad breakthrough curve. This hypothesis is consistent with the pressure drop measurements of gas flow across adsorbers measured at different superficial airflow velocities. Specifically, packed beds of pellets are expected to have the highest airflow resistance due to drastic inertial loss of momentum induced by collision between fluids and pellets. However, at such a low length-to-diameter ratio, the packed bed of pellets exhibited the lowest resistance, which means bypass created by inefficient packing resulted in a channeling effect. As parallel-packed fibers and the 3D printed structure had similar airflow channels and identical porosity, they exhibited similar pressure drops. The excellent adsorption performance of this proof-of-principle adsorber is a synergistic effect of an inherently good absorbent material (PIM-1) and an efficient column design enabled by 3D printing. The comparison between different contactor designs highlights the important role that uniform mass transfer channels play in improving adsorptive separations.

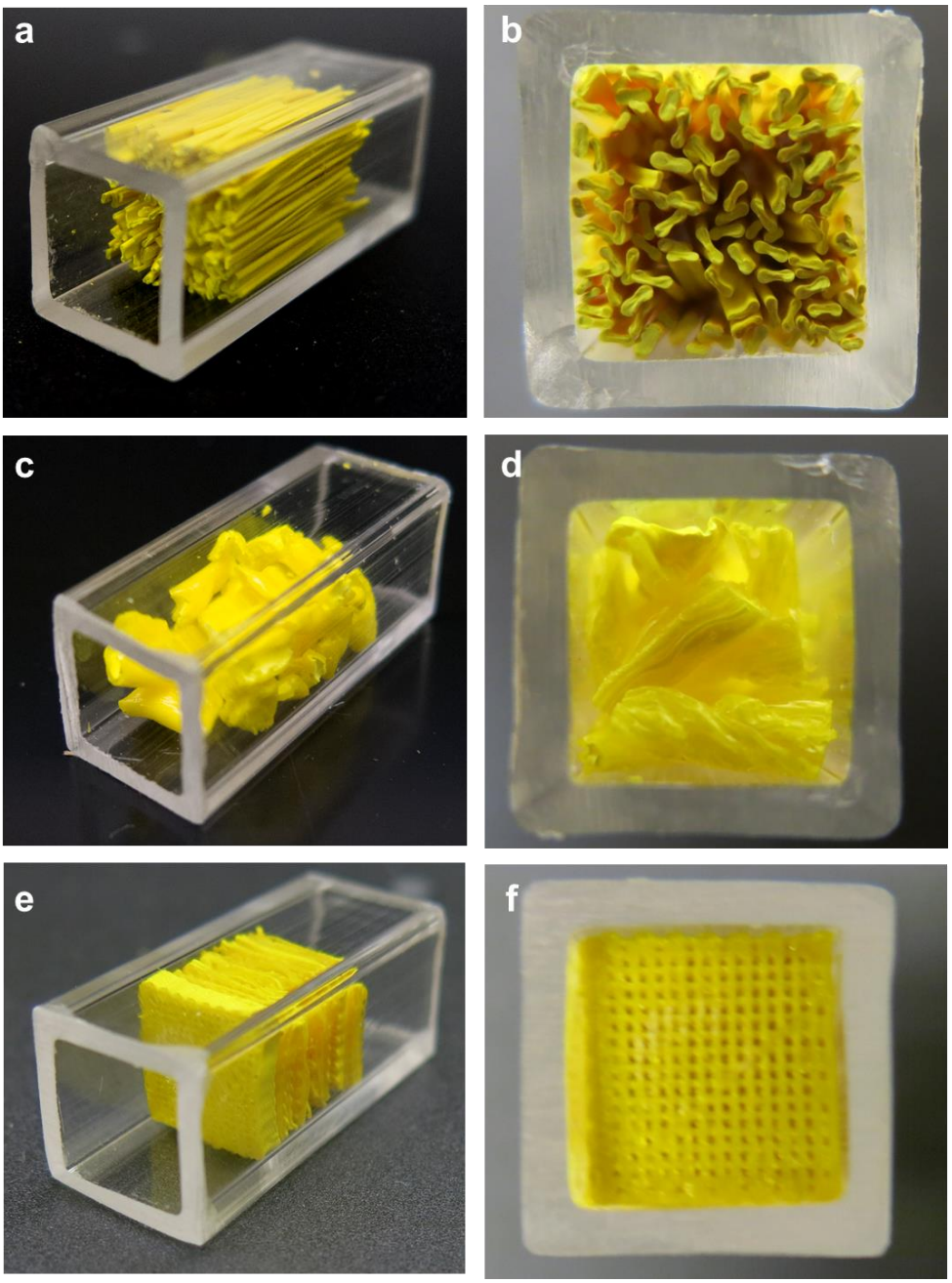

Figure 4.12 Images of PIM-1 adsorbent columns utilized in toluene breakthrough experiments. For the purpose of visualization, the adsorbents were enclosed in acrylic tubes packed the same pattern as those tested in experiments (the housing utilized in the experiments was stainless steel). (a, b) Parallel-packed PIM-1 fibers with non-uniform but straight gas flow channels. (c, d) Packed bed of PIM-1 pellets with non-uniform and tortuous gas flow channels. (e, f) 3D printed PIM-1 scaffold with uniform gas flow channels.

4.4 Conclusions

In summary, we report the solution-based additive manufacturing (SBAM) of polymer of intrinsic microporosity 1, which cannot be utilized in existing additive manufacturing schemes. Optimization of ternary polymer solution composition and printing atmosphere resulted in the fabrication of polymer scaffolds with well-formed three-dimensional structures possessing hierarchical macro-/meso-porosity (and microporosity when polymers with contorted, rigid backbones—such as PIM-1—are utilized). 3D printed PIM-1 adsorption structures exhibited large (i.e., up to 30 wt%) and rapid uptake of toluene (a model volatile organic compound, VOC). Short (around 1 cm) beds of these scaffolds were challenged with a flowing stream of toluene/nitrogen at gas residence times in the bed of approximately 1.5 second, yet these short beds were able to completely remove toluene from the gas stream for nearly two hours. Overall, this work lays the foundation for prototyping mass transfer contactors via SBAM.

4.5 References

1. F. Zhang, Y. Ma, J. Liao, V. Breedveld, R. P. Lively. Solution‐Based 3D Printing of Polymers of Intrinsic Microporosity. *Macromolecular Rapid Communications* **2018**:1800274.

2. A. K. Au, W. Huynh, L. F. Horowitz, A. Folch. 3D-printed microfluidics. *Angewandte Chemie International Edition* **2016**;55(12):3862-3881.

3. R. A. Barry, R. F. Shepherd, J. N. Hanson, R. G. Nuzzo, P. Wiltzius, J. A. Lewis. Direct‐Write Assembly of 3D Hydrogel Scaffolds for Guided Cell Growth. *Advanced Materials* **2009**;21(23):2407-2410.

4. B. G. Compton, J. A. Lewis. 3D‐printing of lightweight cellular composites. *Advanced Materials* **2014**;26(34):5930-5935.

5. S. J. Hollister. Porous scaffold design for tissue engineering. *Nature materials* **2005**;4(7):518.

6. X. Zheng, H. Lee, T. H. Weisgraber, M. Shusteff, J. DeOtte, E. B. Duoss, J. D. Kuntz, M. M. Biener, Q. Ge, J. A. Jackson. Ultralight, ultrastiff mechanical metamaterials. *Science* **2014**;344(6190):1373-1377.

7. Z.-X. Low, Y. T. Chua, B. M. Ray, D. Mattia, I. S. Metcalfe, D. A. Patterson. Perspective on 3D printing of separation membranes and comparison to related unconventional fabrication techniques. *Journal of Membrane Science* **2017**;523:596-613.

8. M. Zarek, M. Layani, I. Cooperstein, E. Sachyani, D. Cohn, S. Magdassi. 3D printing of shape memory polymers for flexible electronic devices. *Advanced Materials* **2016**;28(22):4449-4454.

9. B. C. Gross, J. L. Erkal, S. Y. Lockwood, C. Chen, D. M. Spence. Evaluation of 3D printing and its potential impact on biotechnology and the chemical sciences. *Analytical Chemistry* **2014**;86:3240–3253.

10. M. Malinauskas, A. Žukauskas, S. Hasegawa, Y. Hayasaki, V. Mizeikis, R. Buividas, S. Juodkazis. Ultrafast laser processing of materials: from science to industry. *Light: Science & Applications* **2016**;5(8):e16133.

11. F. Zhang, C. Tuck, R. Hague, Y. He, E. Saleh, Y. Li, C. Sturgess, R. Wildman. Inkjet printing of polyimide insulators for the 3D printing of dielectric materials for microelectronic applications. *Journal of Applied Polymer Science* **2016**;133(18):43361.

12. D.-Y. Koh, B. A. McCool, H. W. Deckman, R. P. Lively. Reverse osmosis molecular differentiation of organic liquids using carbon molecular sieve membranes. *Science* **2016**;353(6301):804-807.

13. D. T. Clausi, W. J. Koros. Formation of defect-free polyimide hollow fiber membranes for gas separations. *Journal of Membrane Science* **2000**;167(1):79-89.

14. N. B. McKeown, P. M. Budd. Polymers of intrinsic microporosity (PIMs): organic materials for membrane separations, heterogeneous catalysis and hydrogen storage. *Chemical Society Reviews* **2006**;35(8):675-683.

15. M. L. Jue, V. Breedveld, R. P. Lively. Defect-free PIM-1 hollow fiber membranes. *Journal of Membrane Science* **2017**;530:33-41.

16. P. M. Budd, E. S. Elabas, B. S. Ghanem, S. Makhseed, N. B. McKeown, K. J. Msayib, C. E. Tattershall, D. Wang. Solution‐processed, organophilic membrane derived from a polymer of intrinsic microporosity. *Advanced Materials* **2004**;16(5):456-459.

17. S. H. Pang, M. L. Jue, J. Leisen, C. W. Jones, R. P. Lively. PIM-1 as a Solution-Processable "Molecular Basket" for CO_2 Capture from Dilute Sources. *ACS Macro Letters* **2015**;4(12):1415-1419.

18. R. P. Lively, R. R. Chance, B. Kelley, H. W. Deckman, J. H. Drese, C. W. Jones, W. J. Koros. Hollow fiber adsorbents for CO_2 removal from flue gas. *Industrial & Engineering Chemistry Research* **2009**;48(15):7314-7324.

19. S.-Z. Guo, M.-C. Heuzey, D. Therriault. Properties of polylactide inks for solvent-cast printing of three-dimensional freeform microstructures. *Langmuir* **2014**;30(4):1142-1150.

20. M. L. Jue, C. S. McKay, B. A. McCool, M. Finn, R. P. Lively. Effect of Nonsolvent Treatments on the Microstructure of PIM-1. *Macromolecules* **2015**;48(16):5780-5790.

21. H. Thakkar, S. Eastman, A. Al-Mamoori, A. Hajari, A. A. Rownaghi, F. Rezaei. Formulation of Aminosilica Adsorbents into 3D-Printed Monoliths and Evaluation of Their CO_2 Capture Performance. *ACS Applied Materials & Interfaces* **2017**;9(8):7489-7498.

22. H. Thakkar, S. Eastman, A. Hajari, A. A. Rownaghi, J. C. Knox, F. Rezaei. 3D-Printed Zeolite Monoliths for CO_2 Removal from Enclosed Environments. *ACS Applied Materials & Interfaces* **2016**;8(41):27753-27761.

23. S.-z. Guo, X. Yang, M.-C. Heuzey, D. Therriault. 3D printing of a multifunctional nanocomposite helical liquid sensor. *Nanoscale* **2015**;7(15):6451-6456.

24. E. K. McGuinness, F. Zhang, Y. Ma, R. P. Lively, M. D. Losego. Vapor Phase Infiltration of Metal Oxides into Nanoporous Polymers for Organic Solvent Separation Membranes. *Chemistry of Materials* **2019**;31(15):5509-5518.

25. M. R. Kosuri, W. J. Koros. Defect-free asymmetric hollow fiber membranes from Torlon®, a polyamide–imide polymer, for high-pressure CO 2 separations. *Journal of Membrane Science* **2008**;320(1):65-72.

26. D. W. Johnson, C. Sherborne, M. P. Didsbury, C. Pateman, N. R. Cameron, F. Claeyssens. Macrostructuring of Emulsion‐templated Porous Polymers by 3D Laser Patterning. *Advanced Materials* **2013**;25(23):3178-3181.

27. H. Yuk, X. Zhao. A New 3D Printing Strategy by Harnessing Deformation, Instability, and Fracture of Viscoelastic Inks. *Advanced Materials* **2017**;30(6):1704028

28. V. Dua, S. P. Surwade, S. Ammu, S. R. Agnihotra, S. Jain, K. E. Roberts, S. Park, R. S. Ruoff, S. K. Manohar. All‐organic vapor sensor using inkjet‐printed reduced graphene oxide. *Angewandte Chemie International Edition* **2010**;49(12):2154-2157.

29. R. Liu, H. Ding, J. Lin, F. Shen, Z. Cui, T. Zhang. Fabrication of platinum-decorated single-walled carbon nanotube based hydrogen sensors by aerosol jet printing. *Nanotechnology* **2012**;23(50):505301.

30. Z. C. Kennedy, J. F. Christ, K. A. Evans, B. W. Arey, L. E. Sweet, M. G. Warner, R. L. Erikson, C. A. Barrett. 3D-printed poly (vinylidene fluoride)/carbon nanotube composites as a tunable, low-cost chemical vapour sensing platform. *Nanoscale* **2017**;9(17):5458-5466.

31. C. R. Tubio, J. Azuaje, L. Escalante, A. Coelho, F. Guitián, E. Sotelo, A. Gil. 3D printing of a heterogeneous copper-based catalyst. *Journal of Catalysis* **2016**;334:110-115.

32. J.-Y. Lee, W. S. Tan, J. An, C. K. Chua, C. Y. Tang, A. G. Fane, T. H. Chong. The potential to enhance membrane module design with 3D printing technology. *Journal of Membrane Science* **2016**;499:480-490.

CHAPTER 5. MODULAR PEI/PIM-1 ADSORPTION CONTACTORS FABRICATED BY SOLUTION-BASED ADDITIVE MANUFACTURING FOR ENERGY-EFFICIENT CO_2 CAPTURE

Traditional packed-bed adsorption contactors are widely applied in the modern industry owing to the ease of fabrication. However, the tortuous fluid distribution system in these contactors results in a significant trade-off between mass transfer kinetics and pressure drop. Alternatively, structured contactors feature precisely designed fluid distribution channels with better-balanced mass transfer kinetics and pressure drop, but the complexity of fabrication has hindered systematic studies in this area. As shown in Chapter 3 and Chapter 4, 3D printing can fabricate complex structures at much lower costs and can be used for the rapid prototyping of next-generation mass transfer contactors. Here, with the help of solution-based additive manufacturing, we proposed a modular adsorption contactor design that achieves a balance between design freedom and scalability. By manipulating the adsorbent packing densities on the adsorber cross-section and along the fluid flow direction, the mass transfer efficiency and heat transfer efficiency can be manipulated. As a demonstration, hierarchically porous PIM-1 adsorption contactor modules were impregnated with PEI for CO_2 capture from flue gas simulant, and various configurations of these modules were tested. The optimized adsorption contactor assembly exhibits 33% higher breakthrough capacity and 75% lower pressure drop than traditional packed-bed adsorption contactors made of the same material.

5.1 Introduction

The energy infrastructure of modern society has a strong dependence on fossil fuels. Currently, 70% to 80% of global energy consumption is contributed by fossil fuel combustion.[1] The intensive fossil fuel consumption is associated with extensive CO_2 emissions and, consequently, an elevated global atmospheric CO_2 concentration elevation and global warming.[2] The rising CO_2 concentration has inspired researchers to develop techniques to capture CO_2 from various sources (e.g., power plant flue gas, the atmosphere, etc.). While the amine scrubbing technique has been well developed, it suffers from a high energy penalty and requires complex heat integration, which restricts amine scrubbing to specific applications and prohibits its usage to capture CO_2 from a more diverse range of sources.

Adsorption is a promising alternative separation technique, which is achieved by driving a mixture fluid through an adsorptive contactor. During the contact between the fluid mixture and the solid adsorptive material, molecules can be differentiated based on their different affinity with the adsorbent material, thus enabling separation. In a regeneration step, the adsorbed molecules can be released, and adsorbent material can be reused. Compared with the mainstream absorption-based CO_2 capturing technology, adsorption achieves higher energy efficiency by avoiding partial phase change of the mixture during regeneration.

The last few decades have witnessed tremendous progress in the development of advanced adsorbent materials, such as zeolites, MOFs, and microporous polymers.[3] However, the technical difficulties associated with the translation of advanced materials

into practical contactors inhibits their widespread application in modern industries. Owing to the ease of large-scale fabrication, packed bed adsorption contactors are widely applied in industrial adsorption processes. In the packed bed adsorption contactor, adsorbent pellets are randomly packed, and fluids are delivered through the voids between pellets. Such a disordered fluid distribution system suffers from the trade-off between pressure drop and mass transfer efficiency, which increases the operational cost. For example, a 600 MW coal-fired power plant generates 500 m^3/s flue gases.[4] To process fluids with such a high flow rate, a common packed-bed adsorption contactor (e.g., 1 m long contactor packed of pellets with 2 mm diameters). requires a high pressure drop. Such a high pressure (3 kPa) and flow rate (500 m^3/s) would contribute to blower electricity costs of approximately \$30/tonne CO_2. According to the Department of Energy, the maximum allowable operational cost of the next-generation adsorption technique is \$30/tonne CO_2, which cannot be achieved through the use of packed bed adsorption contactors.

The low energy efficiency of traditional packed beds has inspired engineers to developed structured adsorption contactors such as monoliths and fiber sorbents. Structured adsorption contactors provide organized fluid distribution, which results in more uniform and controlled flow patterns and thus enables better heat management, faster adsorption kinetics, and lower pressure drop penalty. Structured adsorption contactors provide engineers higher design freedom. The design parameters of packed bed adsorption contactors are limited to pellet sizes, pellet porosity, and packing density. By contrast, engineers can in principle manipulate more parameters (e.g., material packing density, fluid velocity profile, etc.) at every position of the structured adsorption contactors to improve performance. However, due to limitations imposed by the manufacturing processes of the

adsorbent materials, state-of-the-art adsorption contactors are exclusively limited to monolithic structures, fibers, sheets, etc.[5-7] To date, little research has been conducted on the relationship between adsorption contactor design and adsorption behavior.

3D printing techniques fabricate objects by directly adding materials to the designed structure. Different from traditional manufacturing techniques, the cost of 3D printing does not scale significantly with increasing structural complexity. Such a unique feature makes 3D printing a cost-effective tool to prototype advanced adsorption contactor design. Solution-based additive manufacturing (SBAM) is one of the most suitable 3D printing techniques to fabricate mass transfer contactors. As noted in Chapter 3, SBAM processes multicomponent polymer inks consisting of polymer, solvents, and nonsolvents. After deposition, the viscoelastic 3D printing inks rapidly transform into a polymer "sponge" with hierarchical porosity (e.g., micro-/meso-/macropores). The creation of hierarchical pores requires no sacrificial templates, which make SBAM distinct from other expensive template-based pore-generation methods. The hierarchical pores in the objects fabricated via SBAM provide rapid mass transfer routes, which is essential for mass transfer related applications (e.g., adsorption, catalysis, membrane separation, etc.). The other advantage of solution-based 3D printing over state-of-the-art polymer 3D printing technique is the expanded material spectrum. Polymers that are widely applied in adsorbent fabrication (e.g., polyamides, cellulose acetates, PIM-1, etc.) can only be directly processed in the form of polymer solutions without further modification.

Here, we propose a modular design of ultra-short contactors as illustrated in Figure 5.1. Each module features a monolithic type structure that is tailored to be compatible with parallel 3D printing techniques while also providing fundamental insight into the

relationship between structure and performance. The contactor structure can be easily described in a Cartesian coordinate system, where the *z*-axis is aligned with the fluid flowing direction. The contactors are fabricated in a layer-by-layer manner. In each layer, which defines the *x*-*y* plane, the 3D printer lays down parallel adsorbent filaments in either *x*-direction or *y*-direction. By adjusting the filament size and the gaps between adjacent filaments, the local velocity profile in each layer can be controlled. By controlling the filament diameter and interlayer spacing along the *z*-axis, the material packing density can be adjusted. Compared with monoliths, the structure proposed by this work provides higher design freedom and better tolerance for dead channels due to the interconnectivity of all fluid distribution channels.

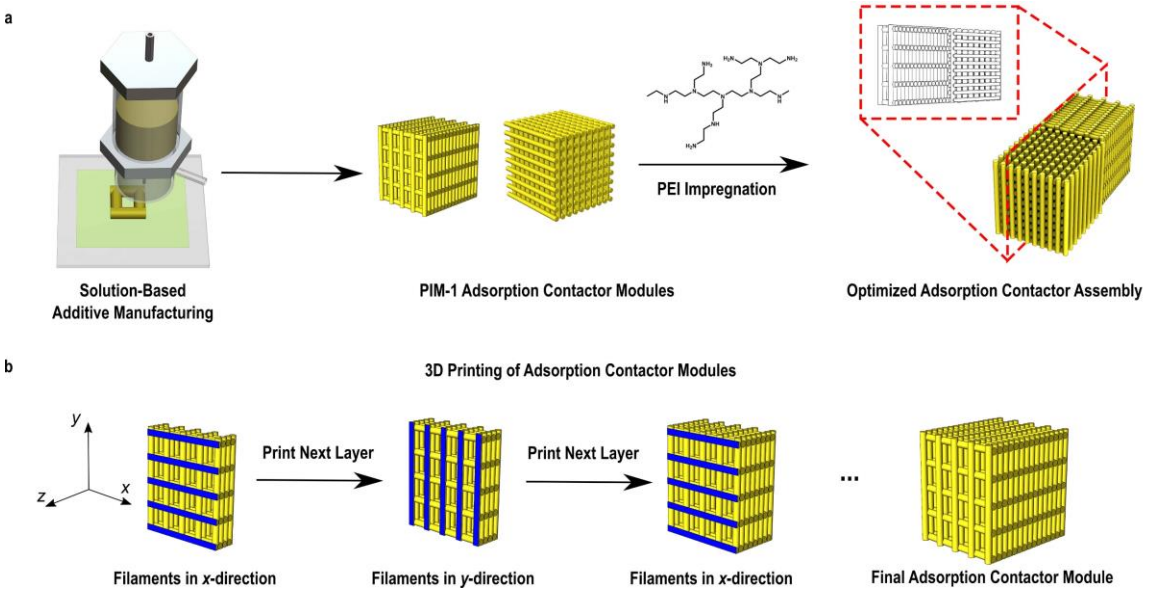

Figure 5.1 (a) Scheme of ultra-short adsorption contactor modules prototyped via solution-based additive manufacturing. (b) Fabrication of the adsorption contactor modules.

Here, we discuss a systematic series of experiments to investigate the potential of modular scaffold-type adsorption contactor designs. Specifically, the influence of

contactor structure and module assembly on breakthrough behavior is investigated, because this is a critical performance indicator for adsorption contactors.

5.2 Experimental Section

5.2.1 PIM-1 Synthesis

The PIM-1 synthesis procedure is described in prior publications.[8,9] Briefly, purified tetrafluoroterephthalonitrile (TFTPN, Alfa Aesar) and 5,5′,6,6′-tetrahydroxy-3,3,3′,3′-tetramethyl-1,1′-spirobisindane (TTSBI, Alfa Aesar) undergo polymerization in the presence of potassium carbonate fine powder and anhydrous dimethylformamide (DMF) at 65 C for 72 hours. H_2O was added into the synthesis mother solution to dissolve the remaining potassium carbonate and quench out PIM-1. The PIM-1 was then dried and dissolved by chloroform and quenched out by methanol. After that, PIM-1 was washed by DMF and methanol sequentially to remove unreacted monomers and oligomers. The weight average molecular weight of the PIM-1 used in this study is 50,200 Da with a polydispersity index around 1.65 according to GPC.

5.2.2 Solution-Based Additive Manufacturing of PIM-1 contactor

After synthesis and purification, PIM-1 was fabricated into adsorption contactors via solution-based additive manufacturing using the processes developed in Chapters 3 and 4. The ternary PIM-1 ink was prepared by mixing PIM-1, dimethylacetamide (DMAc), n-methyl-2-pyrrolidone (NMP), and tetrahydrofuran (THF) with a mass ratio of 20:24:10:46. A customized 3D printer resembling the cartesian direct-ink-writing 3D printer with a coaxial vapor nozzle was utilized. The pressurized ternary ink was deposited onto a moving

glass plate that is coated with a 100-μm thick PIM-1 membrane. During solution-based additive manufacturing, THF-saturated nitrogen was delivered through the vapor nozzle to the printed structure, which prevented the formation of a skin layer and irregular filaments. After solution-based additive manufacturing, the solidified PIM-1 adsorber was removed by immersing the substrate into the deionized water bath. To prevent the collapse of the hierarchical pores, the printed PIM-1 adsorber was then solvent exchanged with water, methanol, and n-hexane. Solvent exchange with each solvent was finished by 3-hour immersion in the corresponding fresh solvent 3 times. After the solvent exchange, the n-hexane-saturated adsorber was dried under vacuum at 80 °C for 12 hours.

The PIM-1 adsorbers were packed into customized stainless-steel housings.[10] Specifically, 16-μm thick aluminum foil is packed in the gap between the housing and the adsorber to avoid bypass pathways. Glass wool was packed in the tubing that connects the adsorber modules to ensure a uniform gas concentration profile in the radial direction between modules; this design helps to elucidate the role of contactor structure in each module when several modules are combined.

5.2.3 Wet-Impregnation of PEI

PEI (Mw = 800 Da) was loaded into 3D printed PIM-1 adsorber via wet impregnation as described in a previous study.[3] Briefly, a solution of PEI in methanol was used to fill the adsorber module with the glass wool temporarily removed. The mass of PEI was determined based on the target PEI loading with the assumption that all PEI will be captured by PIM-1, which is a reasonable assumption for PEI solutions with a

concentration lower than 5 wt.%. The amount of methanol was designed to fully immerse the PIM-1 adsorber.

The modules filled with PEI solution were sealed with tube caps and stored for 12 hours at room temperature to ensure diffusion and adsorption of PEI molecules throughout the PIM-1 module. Afterward, the tube caps of the modules were removed and the modules were dried at 100 °C under vacuum to remove methanol. After this wet impregnation process, the PEI/PIM-1 adsorber modules were stored in a nitrogen atmosphere before the breakthrough experiments to prevent PEI degradation.

5.2.4 CO_2 Adsorption

CO_2 adsorption isotherms of the PEI/PIM-1 composites were collected using a Dynamic Vapor Sorption instrument (Surface Measurement Systems Ltd.). Small fractions of PEI-impregnated PIM-1 were loaded onto the microbalance, which was located in an airtight sample chamber. Prior to the experiment, a high vacuum (10^{-5} Pa) and heat (80 °C) treatment were applied to the whole system to desorb CO_2 and solvent from the sample. During the measurement, pure CO_2 was continuously delivered into the sample chamber at a constant flow rate and evacuated by a vacuum pump. The valve between the sample chamber and the vacuum pump was controlled by the computer to maintain a desired sample chamber pressure. The equilibrium sample weights at a series of CO_2 pressures were recorded to establish the adsorption isotherm.

5.2.5 Porosity Characterization

The macropores and mesopores of the 3D printed structures were characterized via mercury porosimetry. The polymer structures were dried under vacuum at 80 °C for 12 hours to remove residual solvent. The dry samples were then characterized in an AutoPore IV (Micromeritics) porosimeter. Within the equipment, mercury was pressurized from 0.5 psi to 32500 psi, which corresponds to pores ranging from 358 μm to 5.6 nm.

Micropores of the 3D printed structures were characterized via 77K nitrogen physisorption. Prior to nitrogen physisorption, samples were dried at 80 °C under vacuum for 12 hours.

5.2.6 CO_2 Breakthrough

The carbon capture performance of adsorption modules was evaluated via a CO_2 breakthrough experiment setup as shown in Figure 5.2, which was designed to simulate carbon capture from flue gas generated from the coal-fired power plants. A premixed gas stream (CO_2/helium/nitrogen = 12.5/12.5/75) was delivered by a mass flow controller into the adsorption modules being tested. The adsorption module was enclosed by an incubator at 25 °C. A mass spectrometer was attached to the breakthrough system and the gas composition at the outlet of the adsorption module was analyzed in real-time. The calculation of breakthrough capacity was described in Section 2.3.

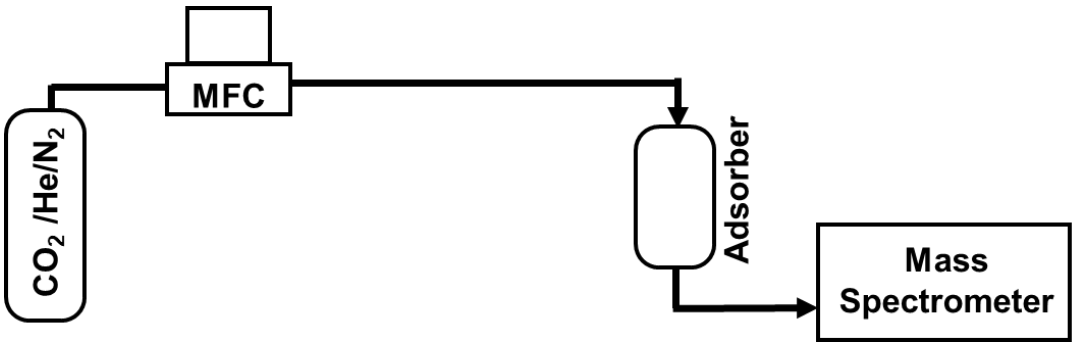

Figure 5.2 Setup for the CO_2 breakthrough experiment.

The adsorption contactors were wrapped with heating tape. A PID controller was used to maintain the temperature at the target value. After each breakthrough experiment, the adsorption contactors were regenerated by 120 ºC heating with nitrogen purging. During the regeneration process, the outlet gas was analyzed by the mass spectrometer. The heating process usually lasts for 2 hours until the CO_2 emission is below 20 ppm. To avoid the error introduced by PEI degradation, all the breakthrough experiments were conducted in a random sequence.

5.3 Results and Discussion

5.3.1 Short Adsorption Modules

To investigate the influence of the gas distribution system design on the breakthrough behavior of CO_2, ultra-short PEI/PIM-1 adsorption modules are fabricated via solution-based additive manufacturing and subsequent wet impregnation of PEI. The 3D models of the three adsorption modules utilized in this section are illustrated in Figure 5.3. These adsorption contactors are fabricated in a layer-by-layer manner. Layers of filaments are packed in the z-direction and each layer in one contactor consists of the same number of filaments. Filaments in adjacent layers are deposited in orthogonal directions.

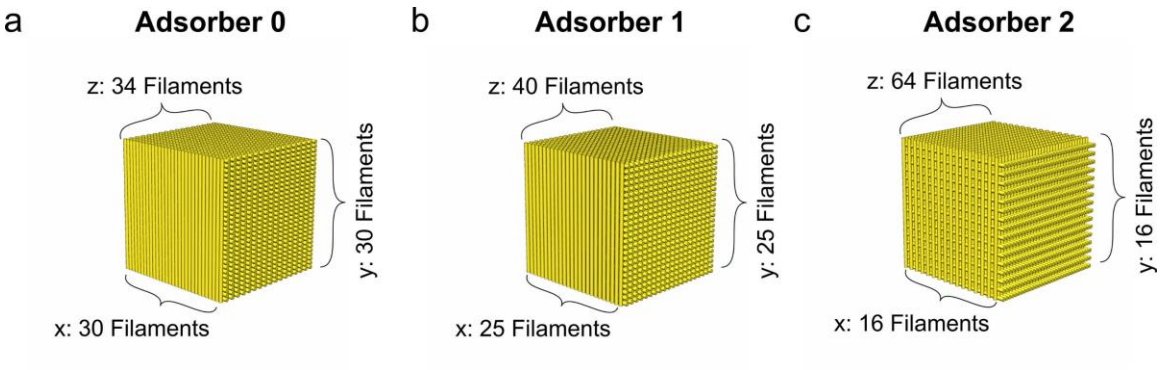

Figure 5.3 The 3D models of the ultra-short PEI/PIM-1 adsorption modules used in this research. (a) Adsorber 0 with 30 filaments in the *x*-*y* plane and 34 layers in the *z*-direction. (b) Adsorber 1 with 25 filaments in the *x*-*y* plane and 40 layers in the *z*-direction. (c) Adsorber 2 with 16 filaments in the *x*-*y* plane and 64 layers in the *z*-direction.

To enable a fair comparison of adsorption performance, the three adsorption modules possess the same overall dimension (0.9 cm × 0.9 cm × 0.9 cm) and the same material loading (0.27 g PIM-1 with 0.09 g PEI). Since the adsorbers are fabricated via the same SBAM protocol, each filament of the adsorption modules possesses the same porosity (40 %) associated with the hierarchical pores throughout the 3D printed adsorbent filaments (Figure 5.4). The apparent density of the fresh PIM-1 filaments is 0.6 g/mL probed by mercury porosimetry. The void fraction of each adsorption module is 0.383.

These three adsorption contactors differ from each other with respect to their filament packing patterns. The 34-layer Adsorber 0 possesses 30 filaments in each layer of the contactor with a 52-μm edge-to-edge gap. The 40-layer Adsorber 1 possesses 25 filaments in each layer of the contactor with a 115-μm edge-to-edge gap. The 64-layer Adsorber 2 possesses 16 filaments in each layer of the contactor with a 333-μm edge-to-edge gap.

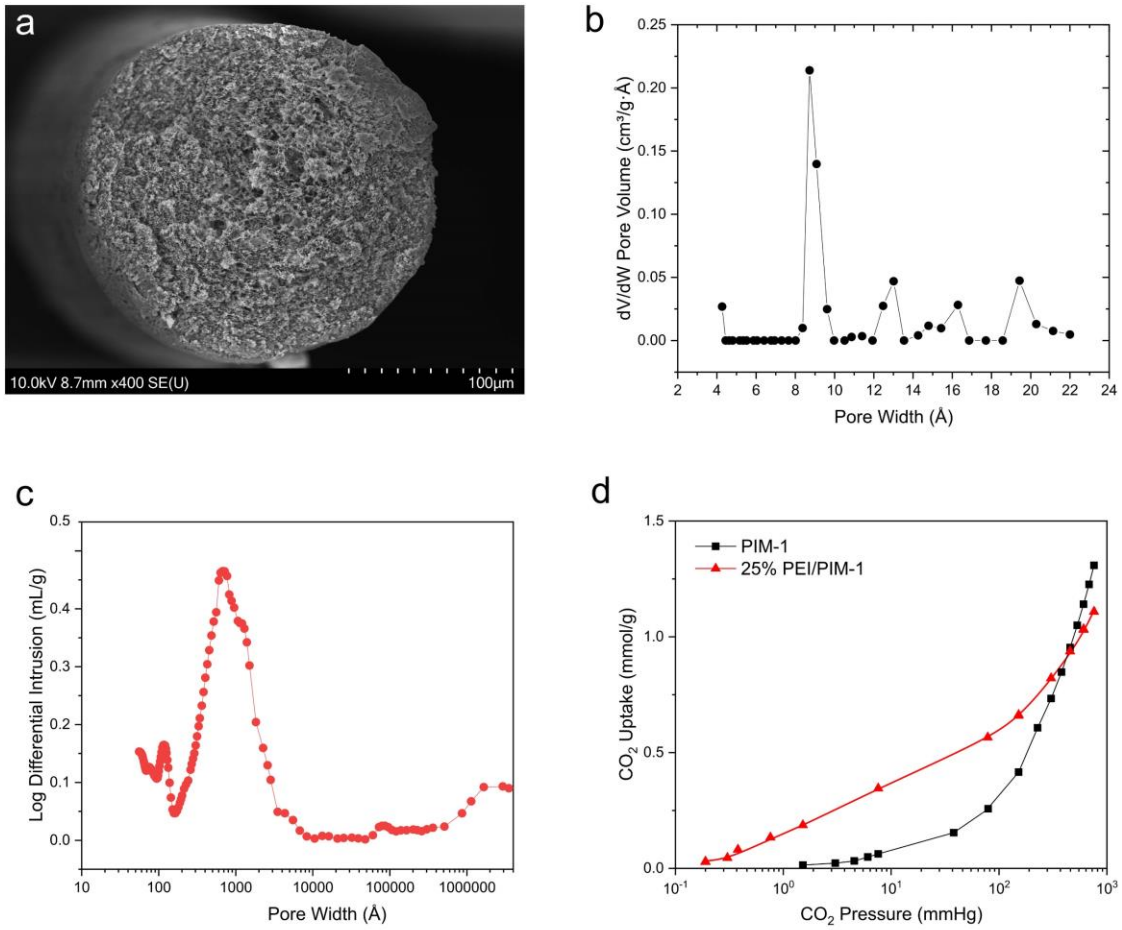

Figure 5.4 Hierarchical porosity of filaments produced via solution-based additive manufacturing of PIM-1. (a) SEM image of the filament cross-section. (b) The pore size distribution of PIM-1 filaments probed by nitrogen at 77 K. HS-2D-NLDFT model is used to calculate the pore size distribution. (c) Pore size distribution probed by mercury porosimetry. (d) CO_2 adsorption isotherms for PIM-1 and 25wt% PEI/PIM-1 composite at 25 °C.

In order to prototype an energy-efficient adsorption contactor, the relationship between the adsorption contactor design and the adsorption performance must be investigated. There are three characteristics of the adsorption contactor design that are hypothesized to strongly influence the adsorption performance: (1) fluid channel diameter, (2) packing density of adsorbent material along the *z*-axis, and (3) the assembly sequence of adsorption contactor modules. The adsorption performance are determined from two

perspectives: (1) mass transfer kinetics, and (2) heat transfer kinetics. In the following sections, a series of experiments are conducted to investigate the influence of the adsorption contactor design on the breakthrough behaviour.

5.3.2 The Influence of Structure and Mass Transfer Kinetics

To begin with, pristine PIM-1 adsorbers were utilized to investigate the influence of the adsorption contactor design on the breakthrough behavior of CO_2. Since CO_2 physisorption in PIM-1 exhibits relatively low heat of adsorption (28.4 kJ/mol) compared with amine-based adsorbents (50 kJ/mol ~ 100 kJ/mol),[11-13] the different CO_2 breakthrough behavior is mainly contributed by the mass transfer efficiency of the adsorber design.

As all of the adsorption contactor modules have the same material loading and void fraction, they are expected to exhibit the same kinetic adsorption performance. Each adsorption module is challenged with a flue gas simulant (CO_2/He/N_2 = 12.5/12.5/75) at flow rates ranging from 5 cm^3/min and 40 cm^3/min. As these adsorption modules possess the same void volume, these flue gas simulant flow rates are translated into the same residence times (3.3 s to 0.4 s) regardless of the adsorber designs.

The CO_2 breakthrough results for plain PIM-1 adsorption contactors are shown in Figure 5.5. Since Adsorber 1 and Adsorber 2 have the same amount of PIM-1 (0.27 g), they exhibit the same total CO_2 capacity as expected, 0.05 ± 0.01 mmol, under all flue gas simulant flow rates. The adsorption modules tested also exhibit similar 0% CO_2 breakthrough time, which is defined as the moment when the CO_2 concentration first deviates from the baseline. For example, when the adsorption contactors are challenged with flue gas simulant under 20 cm^3/min, the 0% CO_2 breakthrough times for Adsorber 1

and Adsorber 2 are 10.2 s and 7.7 s respectively (Figure 5.5c). The similar breakthrough time indicates a similar residence time in each adsorption contactor. No by-pass was observed in all experiments, which indicates high-quality fluid distribution systems.[10]

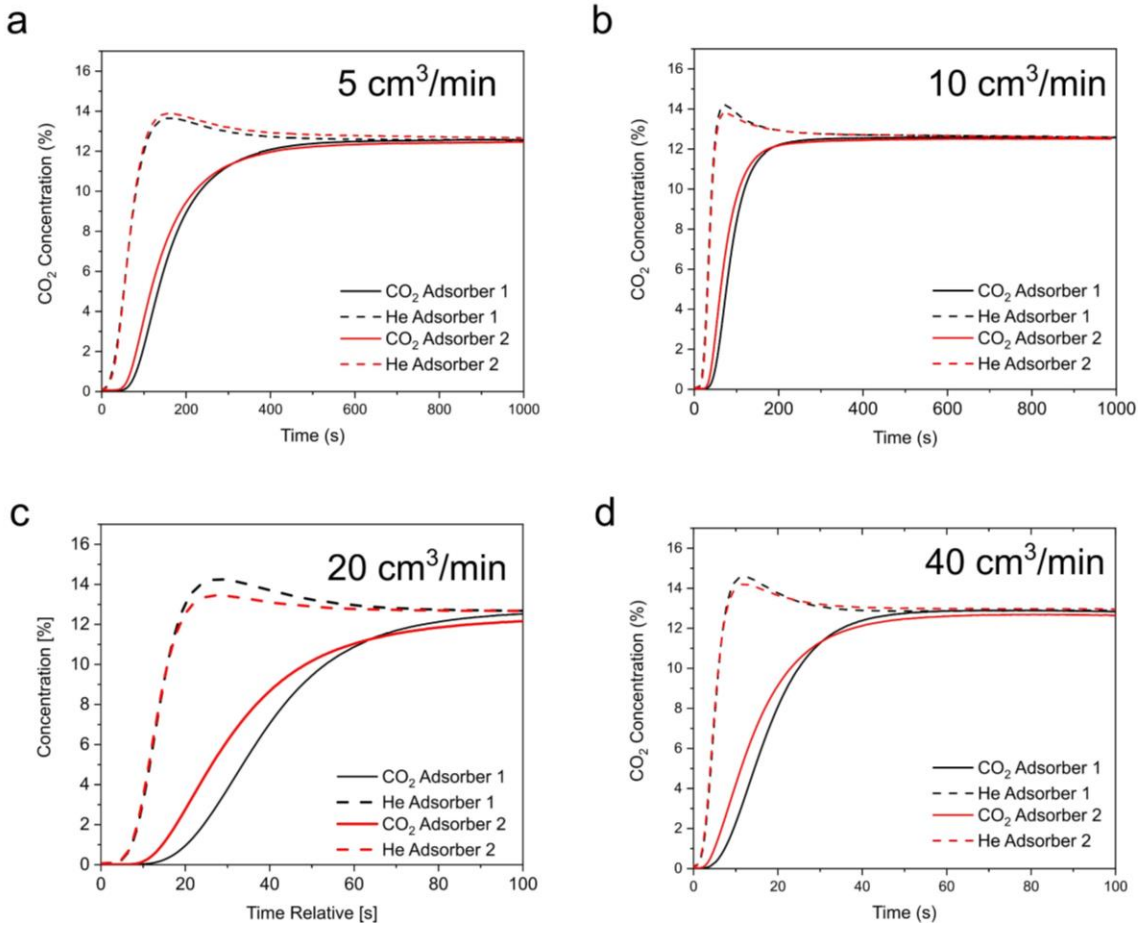

Figure 5.5 Example CO_2 breakthrough curves for single adsorption modules (PEI-free) at flow rates of (a) 5 cm^3/min, (b) 10 cm^3/min, (c) 20 cm^3/min, and (d) 40 cm^3/min.

While Adsorber 1 and Adsorber 2 exhibit similar 0% breakthrough times, the CO_2 breakthrough curves have different shapes. CO_2 breakthrough curves of Adsorder 1 increase rapidly before reaching 6% concentration but increase slowly afterwards. Consequently, the CO_2 breakthrough curves of these two adsorbers exhibit crossover at CO_2 concentrations between 10% to 12%; the following discussion refers to these as

crossover points. The different shapes of the CO_2 breakthrough curves result in significantly different CO_2 breakthrough capacities. This result suggests the possibility of maximizing CO_2 breakthrough capacity via contactor structural optimization. Figure 5.6a compares the CO_2 breakthrough capacities of Adsorber 1 and Adsorber 2 when the flue gas flow rate is 5 cm^3/min. When the CO_2 emission threshold is 5% feed concentration, Adsorber 1 possesses a higher breakthrough capacity (0.0079 mmol) than Adsorber 2 (0.0043 mmol). With a smaller fluid channel width, Adsorber 1 exhibits higher mass transfer efficiency and result in nearly doubled breakthrough capacity when challenged with a 5 cm^3/min flue gas simulant. When the CO_2 emission threshold is higher than the crossover point, the difference in breakthrough capacities between Adsorber 1 and Adsorber 2 decreases. For instance, with a 95% CO_2 emission threshold, the breakthrough capacity for Adsorber 1 is 0.051 mmol and the higher the breakthrough capacity for Adsorber 1 is 0.047 mmol, the difference between which is below 10%. Similar results were observed in all the experiments as shown in Figure 5.6.

As explained at the beginning of this section, pure PIM-1 adsorber releases less heat during adsorption than PEI/PIM-1 adsorbers. Therefore, it is reasonable to conclude that the difference in CO_2 breakthrough capacities is contributed by the different mass transfer kinetics of the adsorbers. Given the same material loading, the same overall adsorber dimension, and the same void fraction, adsorbers with the smaller fluid channel width exhibit more efficient mass transfer kinetics.

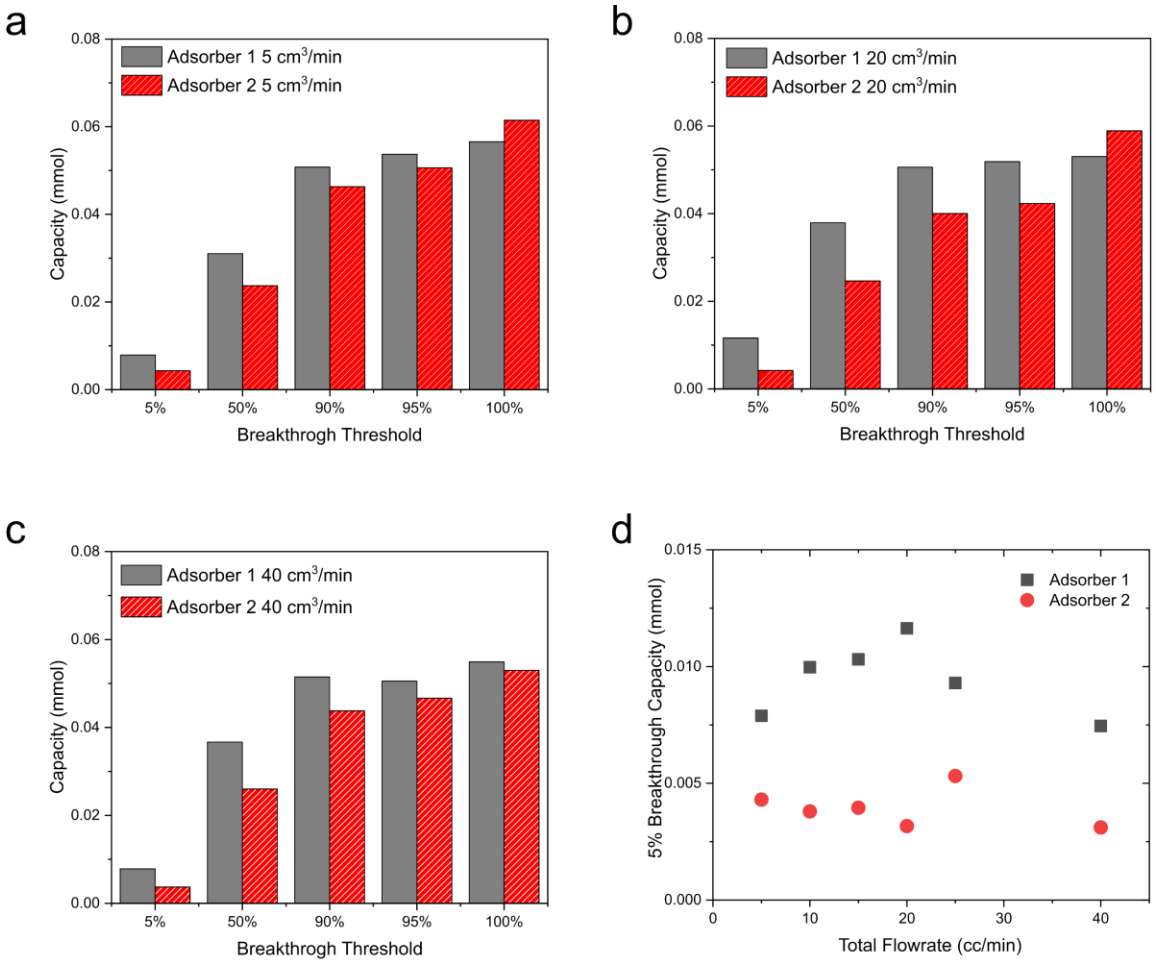

Figure 5.6 Analysis of CO_2 breakthrough curves for single adsorption modules. Breakthrough capacity with different breakthrough threshold under flowrates of (a) 5 cm^3/min, (b) 20 cm^3/min, and (c) 40 cm^3/min. (d) 5% breakthrough capacities at different flowrates.

5.3.3 The Influence of Structure and Heat Transfer Kinetics

Owing to the higher CO_2 capacity, PEI/PIM-1 is a more promising adsorbent material compared with pristine PIM-1.[3] In this section, PEI/PIM-1 adsorbers are utilized to investigate the influence of contactor structure on breakthrough behavior. Since CO_2 chemisorption of PEI/PIM-1 exhibits higher heat of adsorption than CO_2 physisorption of pristine PIM-1, the heat effect during adsorption must be considered.

Since all the contactors have the same amount of PEI (0.09 g) and PIM-1 (0.27 g), they all exhibit the same total CO_2 capacity, 0.22 ± 0.02 mmol, under all flue gas simulant flowrates. The CO_2 breakthrough results for PEI/PIM-1 adsorption contactors shown in Figure 5.7 are different from the plain PIM-1 adsorption contactors. While the CO_2 breakthrough curves for plain PIM-1 adsorption contactors exhibit single crossovers, the CO_2 breakthrough curves for PEI/ PIM-1 adsorption contactors exhibit double "crossovers".

The significant change of the breakthrough curve shapes is hypothetically contributed by the influence of the adsorption contactor design on the mass transfer and heat transfer as shown in Figure 5.8. During the initial CO_2 concentration increase, the shapes of the breakthrough curves are determined by the overall mass transfer coefficient. Adsorber 1 has a higher packing density in the *x*- and *y*- direction and possesses smaller fluid channels. As a result of the lower porosity in the *x*-*y*-plane, the local fluid velocity is higher, which enhances mass transfer (CO_2 adsorption). Owing to the efficient adsorption, Adsorber 1 exhibits a delayed CO_2 breakthrough and a sharper breakthrough curve compared with Adsorber 2. Since the two adsorbers have the same total adsorption capacity, two crossover points are observed in each pair of their breakthrough curves. For instance, in Figure 5.8a, the first crossover point is observed at 93 s and 2.0 % CO_2 concentration. The second crossover point is observed at 657 s and 11.8 % CO_2 concentration.

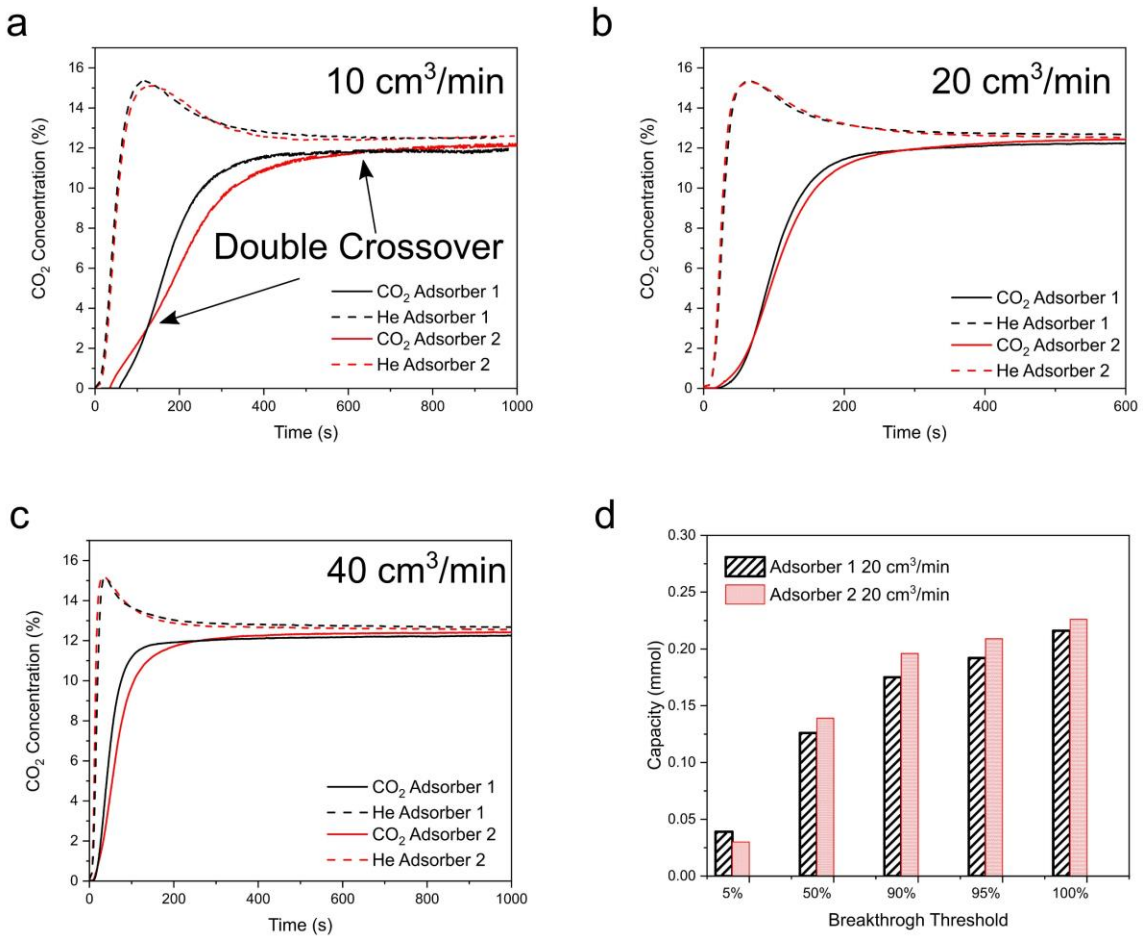

Figure 5.7 Example CO_2 breakthrough curves for single adsorption modules (25wt% PEI) at flow rates of (a) 10 cm^3/min, (b) 20 cm^3/min, and (c) 40 cm^3/min. (d) The breakthrough capacities with different breakthrough thresholds at 20 cm^3/min.

Chemisorption of CO_2 by PEI/PIM-1 composite is associated with large heats of adsorption. When a significant amount of CO_2 is captured, the heat accumulates and elevates the temperature of the adsorbent, which temporarily lowers the local CO_2 capacity. The hot adsorbent experiences reductions in uptake until it slowly cools down and then adsorbs more CO_2. These heat effects affect the shapes of the final portion of the breakthrough curves: when the CO_2 concentration reaches around 90% of the feed concentration, a long tail appears (Figure 5.8). The faster the cooling process, the shorter and steeper the tail is. The cooling rate of the adsorber is influenced by the packing density

in the *z*-direction. As shown in Figure 5.8, the adsorber with lower packing density in the *z*-direction and higher packing density in the *x*-*y*-plane has larger stagnant voids between adjacent layers in the *z*-direction. The stagnant fluid cannot effectively transfer heat generated by the adsorbent filament, which is consistent with the research about catalytic contactor design.[14-16] As a result, the adsorber with delayed CO_2 breakthrough exhibits a longer CO_2 concentration tail, which leads to the second crossover of the CO_2 breakthrough curves. The second crossover point is not observed in pure PIM-1 adsorbers because of the much weaker heat effects.

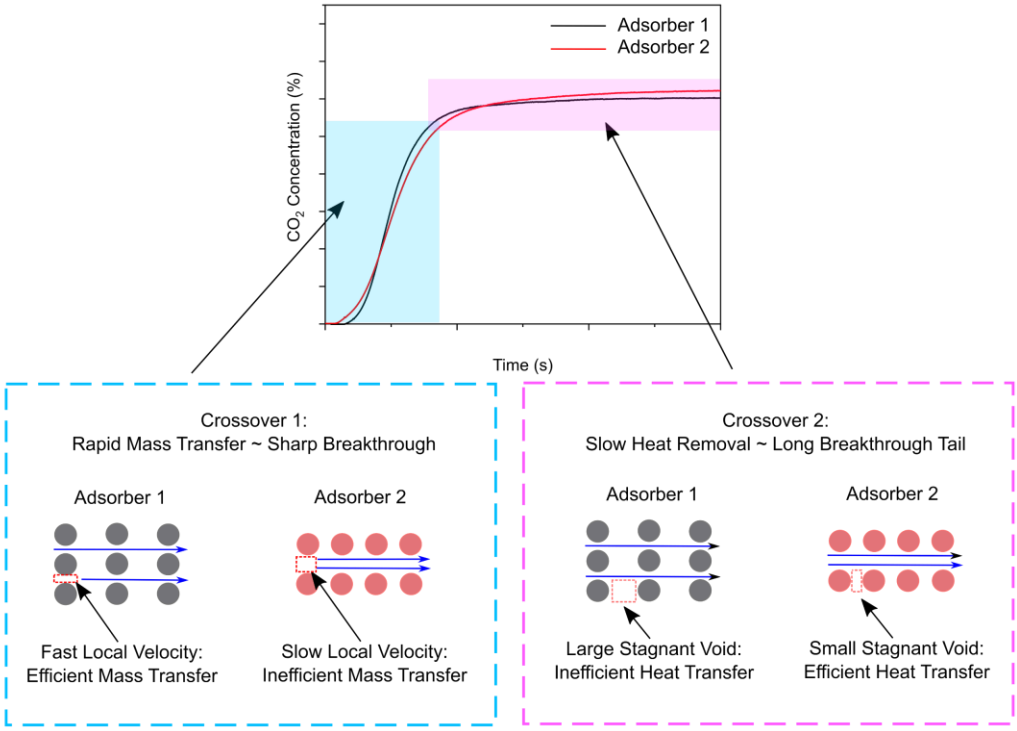

Figure 5.8 Schematic explanation of the double crossover of the CO_2 breakthrough curves.

The double crossover of the breakthrough curves influences the breakthrough capacities of the adsorption contactors. As shown in Figure 5.7d, when the CO_2 emission

threshold is 5%, Adsorber 1 possesses higher breakthrough capacity (0.39 mmol) than Adsorber 2 (0.30 mmol). However, when the CO_2 emission threshold is higher than the first crossover, the Adsorber 2 starts to outperform Adsorber 1. For instance, with a 90% CO_2 emission threshold, the breakthrough capacity for Adsorber 2 is 0.196 mmol, which is higher than the 0.175 mmol breakthrough capacity for Adsorber 1.

This experiment reveals that different design strategies of adsorption contactors should be employed for different applications. For applications requiring a high recovery rate (e.g., flue gas carbon capture) or applications with minimal adsorption heat (e.g., physisorption), the packing density orthogonal to the fluid flow direction should be increased for rapid adsorbate capture. For applications that require complete CO_2 capacity utilization (e.g., direct air capture), the packing density in the fluid flow direction should be increased for more efficient heat removal.

5.3.4 The Influence of Module Assembly on Breakthrough Behavior

Section 5.3.3 has shown that the structure of a single PEI/PIM-1 adsorption contactor influences the CO_2 breakthrough behavior: the mass transfer efficiency and heat transfer efficiency can be enhanced selectively, by manipulating the adsorbent packing density in different directions. We hypothesize that by connecting adsorption modules with different structures in a specific sequence, the overall CO_2 breakthrough behavior can be manipulated to maximize the breakthrough capacity. In this section, different module assembly strategies are tested to investigate the effect of varying the structure along the flow direction on the overall CO_2 breakthrough behavior.

Adsorption modules are packaged individually in customized stainless-steel cubic tubes. 16-μm aluminum foil is used to seal the gaps between stainless steel house and the structured adsorbent to avoid leaking pathways. Glass wool is packed between adsorption modules to avoid gas composition variation in the radial direction. For the ease of discussion, the Adsorber 1-2 assembly strategy shown in Figure 5.9a is referred to as the "expanding channel", since the fluid channels in Adsorber 1 are smaller (width 115 μm) than in Adsorber 2 (width 333 μm). By contrast, the Adsorber 2-1 assembly strategy shown in Figure 5.9b is referred to as the "shrinking channel".

These two adsorption module assemblies were challenged with a flue gas simulant (CO_2/He/N_2 = 12.5/12.5/75) at flow rates ranging from 10 cm^3/min, 20 cm^3/min, 30 cm^3/min, and 40 cm^3/min. As shown in Figure 5.9c to Figure 5.9f, a double crossover effect was observed when comparing the breakthrough curves for expanding and shrinking channel assemblies in the same graph. The difference between the two modular assemblies is more pronounced than those observed in the single module experiments (Figure 5.7). For example, the times required for CO_2 concentration to reach 50% feed concentration (referred to as 50% breakthrough time in the following discussion) are 179.3 s for the shrinking channel assembly and 240.6 s for the expanding channel assembly at 20 cm^3/min flow rate (Figure 5.9d). The difference in 50% breakthrough time for these two assemblies is 61.3 s. As a comparison, the difference in 5% breakthrough time for Adsorber 1 (99.9 s) and Adsorber 2 (105.8 s) at the same flow rate is only 5.9 s.

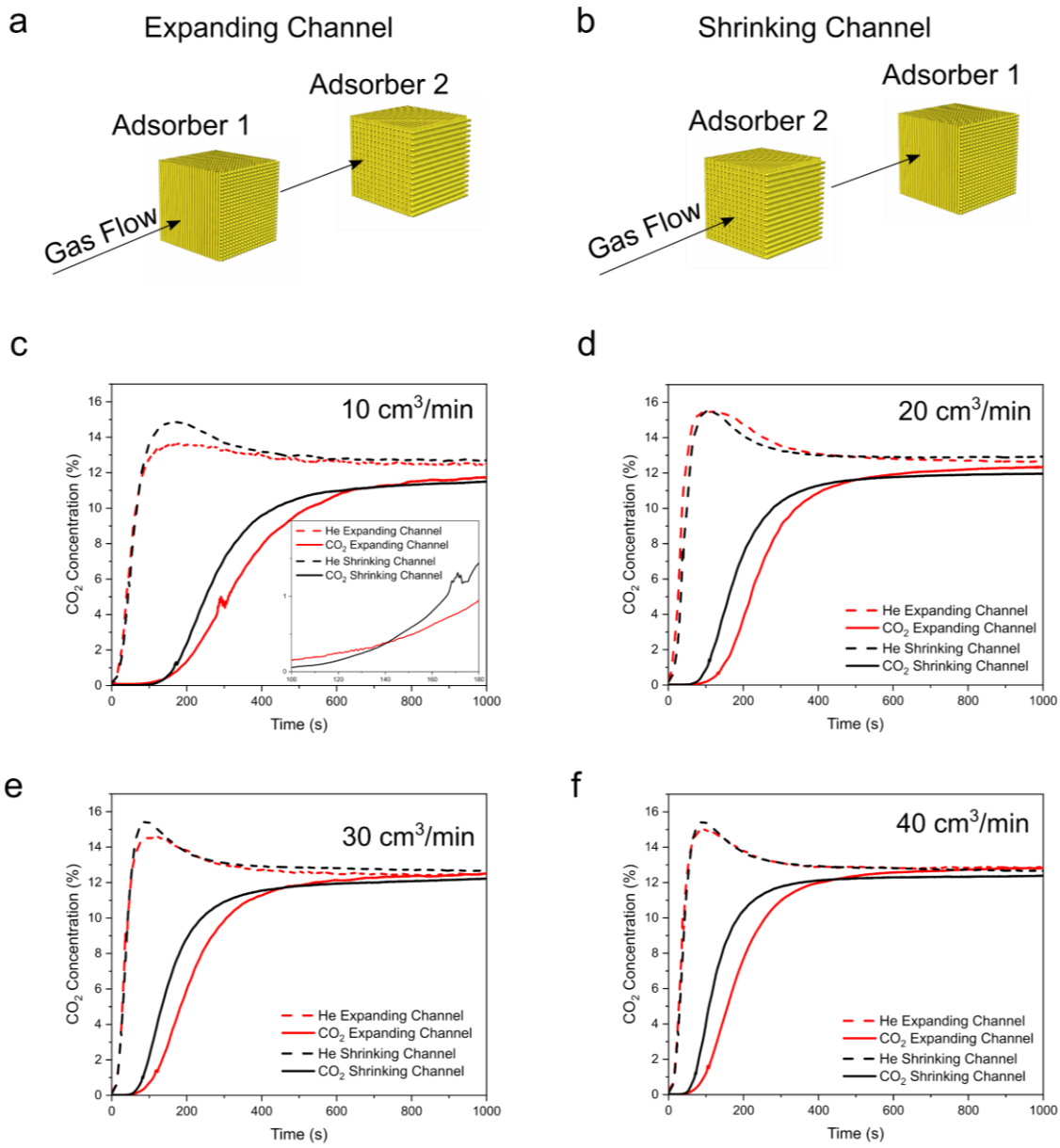

Figure 5.9 The influence of PEI/PIM-1 adsorption module assembly on CO_2 breakthrough behavior. (a) Expanding channel adsorption module assembly. (b) Shrinking channel adsorption module assembly. CO_2 breakthrough curves at different flue gas simulant flowrates. (c) 10 cm^3/min, (d) 20 cm^3/min, (e) 30 cm^3/min, and (f) 40 cm^3/min.

Figure 5.10 shows the influence of the order of PEI/PIM-1 adsorption modules on the CO_2 breakthrough capacities. For all the experiments, the average total capacity (100% breakthrough threshold) is about 0.5 ± 0.1 mmol, which agrees with the CO_2 isotherms

shown in Figure 5.4d. At 10 cm^3/min (Figure 5.4a), the expanding channel assembly provides higher breakthrough capacities than the shrinking channel assembly when 5%, 50%, and 90% breakthrough thresholds are applied. However, when the 95% breakthrough threshold is applied, the shrinking channel assembly outperforms the expanding channel assembly. The experiment results at 10 cm^3/min are similar to the experimental results of single-module adsorption experiments. However, when the gas flow rate is increased to 20 cm^3/min (Figure 5.10b), 30 cm^3/min (Figure 5.10c), and 40 cm^3/min (Figure 5.10d), the expanding channel assembly outperforms the shrinking channel assembly at all the four breakthrough threshold (5%, 50%, 90%, and 95%). This result shows that the shrinking channel assembly achieves a better balance between mass transfer efficiency and heat dissipation. Figure 5.10e summarizes the 5% breakthrough capacities of the two assemblies at different gas flow rates. The expanding channel assembly provides nearly double the 5% breakthrough capacity of the shrinking channel assembly at intermediate and high flow rates.

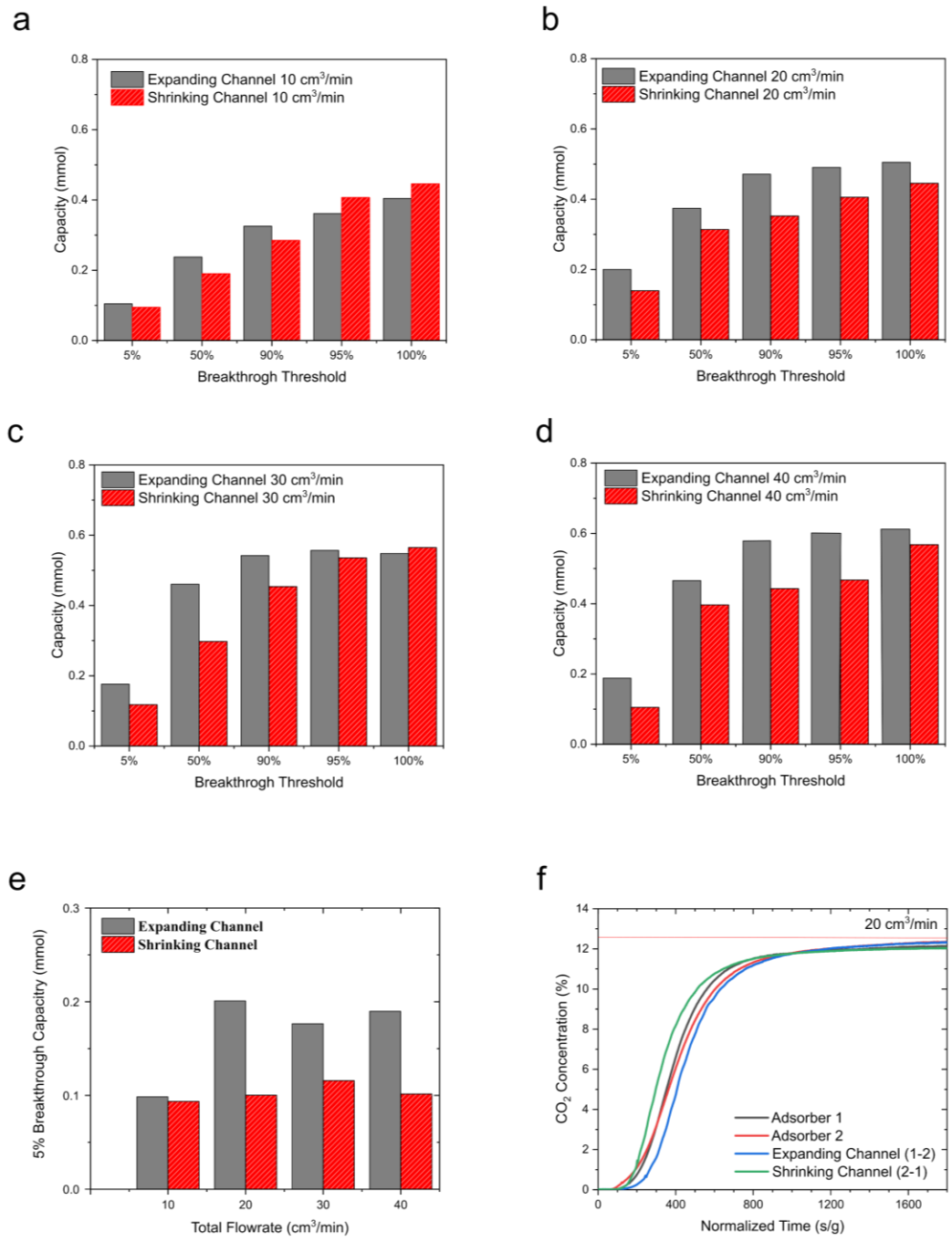

Figure 5.10 The influence of the PEI/PIM-1 adsorption module assembly on the CO_2 breakthrough capacity at the flow rate of (a) 10 cm^3/min, (b) 20 cm^3/min, (c) 30 cm^3/min, and (d) 40 cm^3/min. (e) The comparison of 5% breakthrough capacity at different flowrates. (f) Normalized CO_2 breakthrough curves for single Adsorber 1, single Adsorber 2, the expanding channel assembly, and the shrinking channel assembly at 20 cm^3/min gas flowrate.

As discussed in Section 5.3.3, Adsorber 1 and Adsorber 2 have different advantages with regards to mass and heat transfer. Adsorber 1 has faster mass transfer, while Adsorber 2 has faster heat transfer. By combing these different adsorption modules in proper sequences, they could provide better performance than utilizing single adsorption modules. Figure 5.10f compares the CO_2 breakthrough behaviors of single Adsorber 1, single Adsorber 2, the expanding channel assembly Adsorber 1-2, and the shrinking channel assembly Adsorber 2-1 at 20 cm^3/min gas flowrate. The CO_2 breakthrough curves are normalized against the weight of PIM-1. The figure clearly shows that the individual modules exhibit similar CO_2 breakthrough curves, which fall inside the envelope formed by the breakthrough curves of the two modular assemblies. Compared with either module that is utilized alone, the expanding channel assembly further delays the CO_2 concentration, while the shrinking channel assembly results in a faster CO_2 concentration increase.

We hypothesize that the effect of modular assembly on the CO_2 breakthrough dynamics can be explained by the heat propagation. Different from the individual module experiments, the heat generated in one assembled module will influence the following modules. Therefore, the arrangement of adsorption modules has a significant influence on the performance of a modular assembly. As shown in Figure 5.11a, during the adsorption in the mass transfer zone, heat is generated and results in hot inert gas. The hot inert gas flows to the following adsorbent sections and elevates the local temperature. Owing to the elevated temperature, the CO_2 capacity of this fresh adsorbent section decreases. When the flue gas enters this heated adsorbent section, the amount of CO_2 that can be adsorbed is much lower than the theoretical capacity. The heated adsorbent cools down over time and captures more CO_2.

Heat propagation negatively impacts the adsorption kinetics of the adsorber, especially the sections at the back of the adsorber. To offset the impact of heat propagation, the adsorber with high heat transfer efficiency should be deployed at the end of the adsorber. As discussed in Section 5.3.3, Adsorber 1 has rapid mass transfer, and Adsorber 2 has rapid heat dissipation. When these two adsorption modules are connected in the expanding channel mode (Figure 5.11b), the module in the front rapidly remove CO_2 from the flue gas and generate hot inert gas for the following modules. The following heat-transfer-efficient module dissipates the heat to the exit. The rapid heat dissipation results in faster cooling and a shorter CO_2 "tail" in the breakthrough curves (Figure 5.10f). By contrast, the shrinking channel assembly intensifies the impact of heat propagation due to the improper module sequence. As shown in Figure 5.11c, the shrinking channel assembly possesses the heat-transfer-efficient module in the front and the heat-transfer-inefficient module at the back. During the adsorption process, the module in the front captures CO_2 and passes the adsorption heat to the following module. The following module is inefficient in heat dissipation and requires longer cooling time.

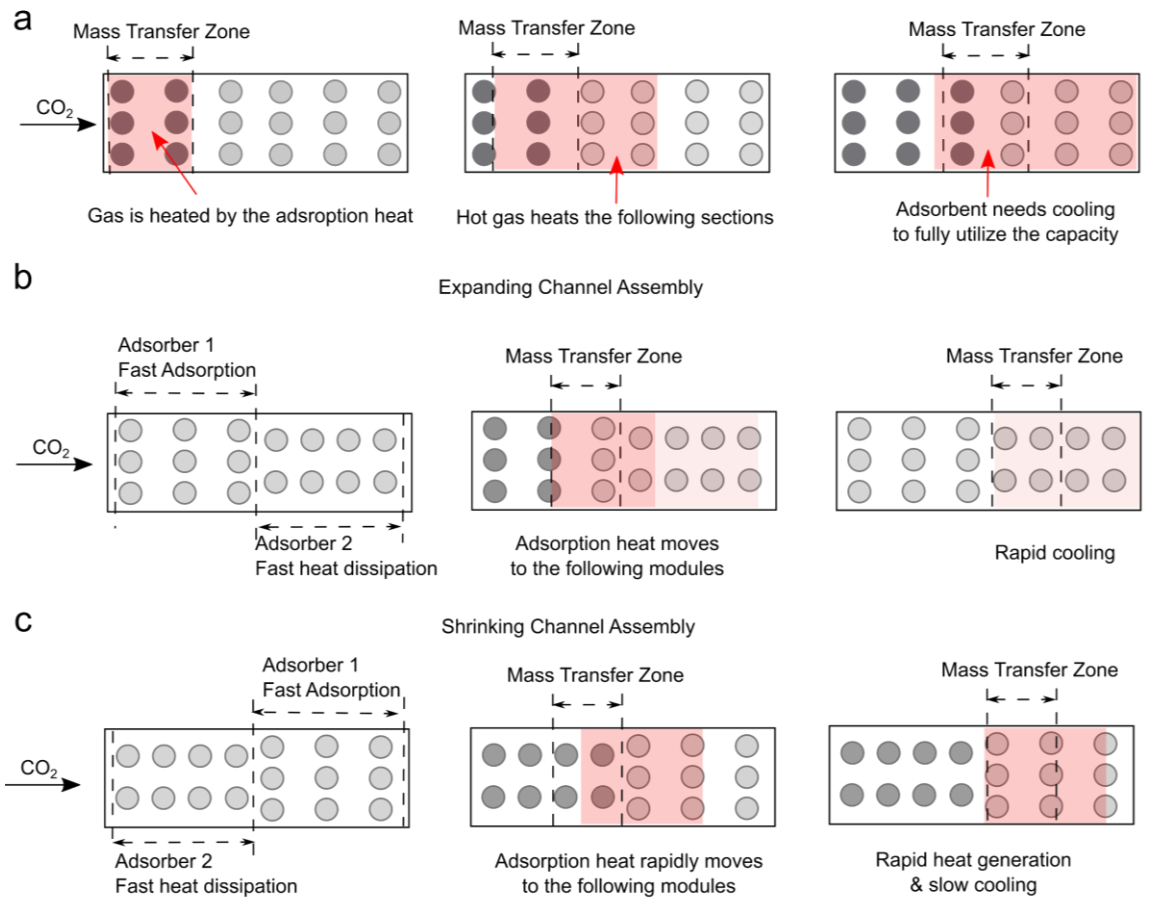

Figure 5.11 Adsorption heat propagation along (a) single adsorption module, (b) the expanding channel adsorption contactor assembly, and (c) the shrinking channel adsorption contactor assembly.

5.3.5 Comparison with Packed-Bed Adsorber

The adsorption contactor assembly with expanding channel design was compared with a traditional packed-bed adsorber. To exclude the influence of internal mass transfer resistance, the multicomponent PIM-1 solution is printed into random coils via the SBAM and then cut into 1-cm long fibers.[10] Owing to the identical processing history, the PIM-1 fibers and the PIM-1 adsorption contactor modules possess identical porosities and thus identical internal mass transfer coefficients. The PIM-1 fibers are then impregnated with

25 wt% PEI and packed into the same stainless steel housing. The PEI/PIM-1 (0.18 g / 0.54 g) packed bed (0.9 cm × 0.9 cm × 1.8 cm) was challenged with the same flue gas simulant at 20 cm^3/min. As shown in Figure 5.12a, the packed bed adsorber and the expanding channel assembly exhibit significantly different CO_2 breakthrough curves, while they have the same void fraction, the same adsorbent amount, and the same overall dimensions. As shown in Figure 5.12a, the packed bed adsorber exhibits a slightly earlier CO_2 breakthrough (59 s) and a rapid CO_2 concentration increase from 0 to 9.8% in 100 s. As a comparison, The expanding channel assembly exhibits a delayed CO_2 breakthrough (77 s) and slower CO_2 concentration increase from 0 to 9.8% in 250 s. The early CO_2 breakthrough of the packed bed adsorber results from the bypasses in the loosely packed region in the packed bed. The tortuous fluid distribution channels also result in more efficient mass transfer, which leads to a rapid CO_2 concentration increase. Such phenomenon is also observed in previous study.[10] The packed bed adsorber exhibits a longer and flater CO_2 breakthrough tail than the expanding channel assembly, which indicates less efficient heat removal in the packed bed adsorber. The packed bed adsorber exhibits a 5% breakthrough capacity of 0.15 mmol and a full capacity of 0.38 mmol. As a comparison, the expanding channel assembly exhibits a 33% increase in the 5% breakthrough capacity.

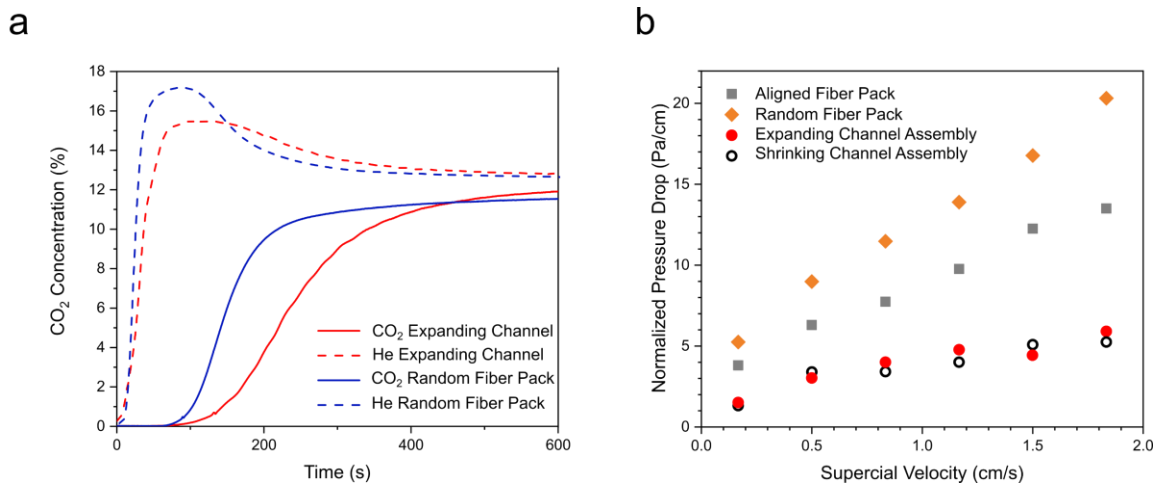

Figure 5.12 Comparison between the expanding channel assembly and the random packed-bed of fibers. (a) CO_2 breakthrough curves at 20 cm^3/min flow rate. (b) The normalized pressure drop across each adsorber.

Another advantage of the modular adsorption contactors is the low pressure drop. In Figure 5.12b shows the normalized pressure drop across the modular adsorption contactor assembly and the packed beds of fibers when exposed to nitrogen with superficial velocities ranging from 0.16 cm/s to 1.83 cm/s. When packed into ultra-short adsorbers (1.8 cm length), packed beds consisting of aligned fibers exhibits bypass effects, which was also observed in Section 4.3.2. The adsorber with random fiber packing eliminates the by-passes but results in high resistance to fluid: it requires 20 Pa pressure drop to flow nitrogen across a 1-cm adsorber at 1.83 cm/s. By contrast, the nitrogen flowing at 1.83 cm/s only induced 5 Pa pressure drop across every 1 cm of the modular adsorption contactor assembly, which is a 75% pressure drop decrease. No pressure drop difference was observed between the expanding channel assembly and the shrinking channel assembly, which is in agreement with expectations. Since the individual adsorption modules are much longer than the diameter of the flow channels, fully developed flow is expected in most of the assembly; as a result, entrance effects due to expansion and contraction should not play

a significant role and the order of the modules should therefore not matter with regards to flow resistance.

5.4 Conclusion

In this Chapter, the scalable modular design of adsorption contactors was prototyped via solution-based additive manufacturing (SBAM). Owing to the precisely designed fluid distribution system, the monolithic adsorption module design achieves a balance between design freedom and scalability. By manipulating the adsorbent packing densities on the adsorber cross-section and along the fluid flow direction, the mass transfer efficiency and heat transfer efficiency can be manipulated. For adsorption processes with massive heat generation, the expanding channel assembly strategy with mass-transfer-efficient modules in the front and heat-transfer-efficient module at the back can be deployed. As a demonstration, the hierarchically porous PIM-1 adsorption contactor module was impregnated with PEI for CO_2 capture from flue gas simulant. The optimized adsorption contactor assembly exhibits 33% higher breakthrough capacity and 75% lower pressure drop than traditional packed-bed adsorption contactors made of the same material.

5.5 References

1. G. Tverberg. World energy consumption since 1820 in charts. *Our Finite World* **2012**.

2. B. Bereiter, S. Eggleston, J. Schmitt, C. Nehrbass‐Ahles, T. F. Stocker, H. Fischer, S. Kipfstuhl, J. Chappellaz. Revision of the EPICA Dome C CO_2 record from 800 to 600 kyr before present. *Geophysical Research Letters* **2015**;42(2):542-549.

3. S. H. Pang, M. L. Jue, J. Leisen, C. W. Jones, R. P. Lively. PIM-1 as a Solution-Processable "Molecular Basket" for CO_2 Capture from Dilute Sources. *ACS Macro Letters* **2015**;4(12):1415-1419.

4. T. C. Merkel, H. Lin, X. Wei, R. Baker. Power plant post-combustion carbon dioxide capture: An opportunity for membranes. *Journal of Membrane Science* **2010**;359(1-2):126-139.

5. H. Thakkar, S. Eastman, A. Al-Mamoori, A. Hajari, A. A. Rownaghi, F. Rezaei. Formulation of Aminosilica Adsorbents into 3D-Printed Monoliths and Evaluation of Their CO_2 Capture Performance. *ACS Applied Materials & Interfaces* **2017**;9(8):7489-7498.

6. H. Thakkar, S. Eastman, Q. Al-Naddaf, A. A. Rownaghi, F. Rezaei. 3D-printed metal–organic framework monoliths for gas adsorption processes. *ACS Applied Materials & Interfaces* **2017**;9(41):35908-35916.

7. S. J. DeWitt, A. Sinha, J. Kalyanaraman, F. Zhang, M. J. Realff, R. P. Lively. Critical Comparison of Structured Contactors for Adsorption-Based Gas Separations. *Annual review of chemical and biomolecular engineering* **2018**;9:129-152.

8. M. L. Jue, C. S. McKay, B. A. McCool, M. Finn, R. P. Lively. Effect of Nonsolvent Treatments on the Microstructure of PIM-1. *Macromolecules* **2015**;48(16):5780-5790.

9. E. K. McGuinness, F. Zhang, Y. Ma, R. P. Lively, M. D. Losego. Vapor Phase Infiltration of Metal Oxides into Nanoporous Polymers for Organic Solvent Separation Membranes. *Chemistry of Materials* **2019**;31(15):5509-5518.

10. F. Zhang, Y. Ma, J. Liao, V. Breedveld, R. P. Lively. Solution‐Based 3D Printing of Polymers of Intrinsic Microporosity. *Macromolecular Rapid Communications* **2018**:1800274.

11. H. A. Patel, C. T. Yavuz. Noninvasive functionalization of polymers of intrinsic microporosity for enhanced CO_2 capture. *Chemical Communications* **2012**;48(80):9989-9991.

12. J. Al-Marri, K. Al-Saad, M. Saad, D. Cortes, M. Khader. Thermodynamics of CO_2 adsorption on polyethyleneimine mesoporous silica and activated carbon. **2017**.

13. S. Choi, J. H. Drese, P. M. Eisenberger, C. W. Jones. Application of amine-tethered solid sorbents for direct CO_2 capture from the ambient air. *Environmental science & technology* **2011**;45(6):2420-2427.

14. C. Busse, H. Freund, W. Schwieger. Intensification of heat transfer in catalytic reactors by additively manufactured periodic open cellular structures (POCS). *Chemical Engineering and Processing-Process Intensification* **2018**;124:199-214.

15. A. Davó-Quiñonero, D. Sorolla-Rosario, E. Bailón-García, D. Lozano-Castelló, A. Bueno-López. Improved asymmetrical honeycomb monolith catalyst prepared using a 3D printed template. *Journal of Hazardous materials* **2019**;368:638-643.

16. G. Do, T. Stiegler, M. Fiegl, L. Adler, C. Körner, A. Bösmann, H. r. Freund, W. Schwieger, P. Wasserscheid. Electrophoretic Deposition of Boehmite on Additively Manufactured, Interpenetrating Periodic Open Cellular Structures for Catalytic Applications. *Industrial & Engineering Chemistry Research* **2017**;56(45):13402-13410.

CHAPTER 6. INTERTWINED NANOPOROUS ALO_X/PIM-1 COMPOSITE AS SOLUTION-PROCESSABLE "AMINE BASKETS" FOR CO_2 ADSORPTION

Energy-efficient CO_2 adsorptive capture requires both adsorbent materials with high CO_2 capacity and structured adsorption contactors with high mass transfer kinetics and low pressure drop. State-of-the-art research mainly focuses on "hard" adsorbents such as mesoporous zeolites and MOFs, which exhibit high CO_2 capacity but are challenging to be translated into structured contactors. PIM-1, a solution-processable microporous polymer, is a 'softer' alternative that can be easily fabricated into structured adsorption contactors. In our prior research, PIM-1 has been utilized as "molecular baskets" for poly(ethylene imine) (PEI), and the resulting PEI/PIM-1 composites exhibit nanoscale dispersion, excellent processability, and moderate CO_2 adsorption capacity. In this chapter, PIM-1 reinforced with amorphous aluminum oxide (AlO_x) nanostrands is utilized as a molecular basket for PEI. Compared with pristine PIM-1, AlO_x/PIM-1 composite provides a more rigid hierarchically porous "molecular basket" for PEI. The infiltrated AlO_x nanostrands improve the amine efficiency (CO_2 capacity normalized by the number of amine groups) and result in a comparable CO_2 capacity to PEI-loaded mesoporous oxides.

6.1 Introduction

As discussed in Chapter 5, an energy-effective and cost-effective CO_2 adsorption process require adsorbent materials with high CO_2 capacity and advanced structural design. An optimized adsorption contactor design could significantly unleash the performance of

the adsorbent material. While traditional inorganic porous supports (e.g., activated carbons, zeolites, etc.) exhibit high CO_2 capacity and fast mass transfer kinetics, these inorganic adsorbents are challenging for structured adsorbent fabrication.

Polymer of intrinsic microporosity 1, PIM-1, is a linear polymer that can be solution-processed into various structured adsorption contactors. PIM-1 has conjugated polymer chains connected via spirocarbons. The unique PIM-1 polymer backbone cannot pack efficiently, which results in interconnected permeant micropores.[1] PIM-1 has demonstrated its potential as adsorptive material with compatibility with solution-based manufacturing techniques. Simon and co-workers demonstrated the potential of PEI/PIM-1 composites as CO_2 capturing materials.[2] In their report, PIM-1 can be solution-processed into various structures and then impregnated with PEI oligomers as CO_2 adsorbents. As a flexible microporous support, PIM-1 disperses PEI molecules throughout the polymer network, creating diffusion pathways for CO_2 to access exposed amines. Compared with traditional support materials such as mesoporous zeolites, PIM-1 results in better exposure and dispersion of PEI oligomers, which is beneficial for high amine efficiency (e.g., CO2 capacity normalized by the number of amine groups) and fast adsorption kinetics.

However, the linear polymer structure of PIM-1 is subject to the plasticization of PEI. Overloading of PEI into PIM-1 will result in collapsing of adsorber architecture and reduction of amine efficiency. To effectively disperse amine and expose amine groups, PIM-1 must be rigidified to provide stable support for PEI. One strategy to stabilize microporous polymers without damaging the polymer property is post-fabrication vapor phase infiltration.[3] Vapor phase infiltration intertwines the PIM-1 polymer chains with aluminum oxide nanostrands, which prevents the PIM-1 polymer chains from relaxing,

swelling, and plasticizing. As proven by the organic solvent separation study in Appendix A, the AlO_x/PIM-1 maintains the microstructure in the presence of guest molecules.

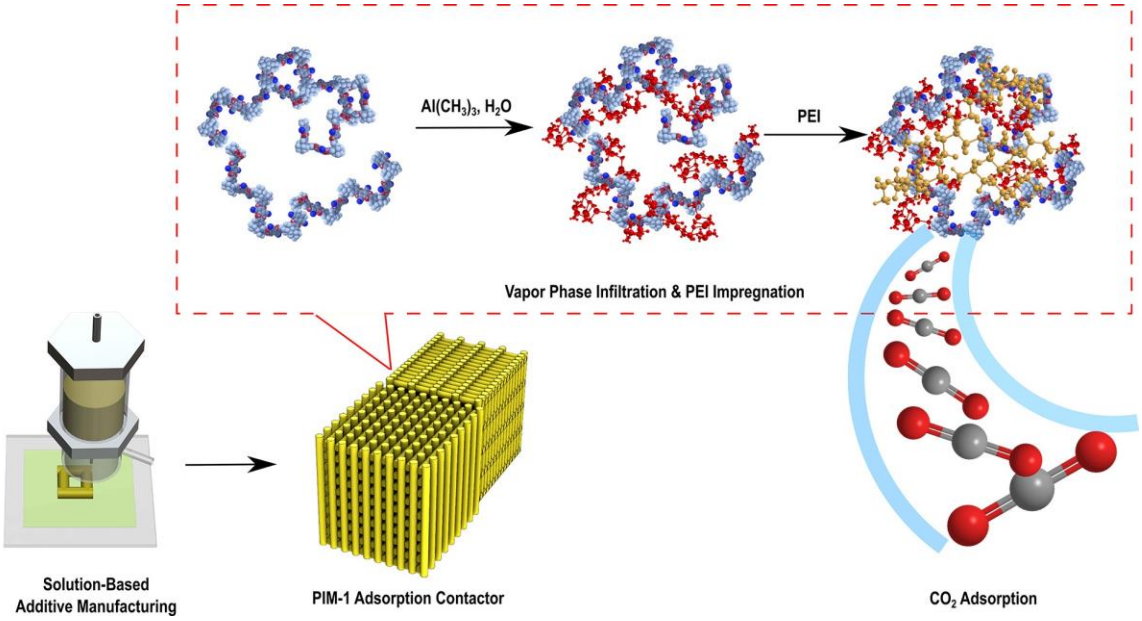

Figure 6.1 Fabrication process of PEI/AlO_x/PIM-1 adsorption contactors for CO_2 capture.

Here, vapor phase infiltration is deployed to stabilize PIM-1 with aluminum oxide, which is illustrated in Figure 6.1. PIM-1 mass transfer contactor is fabricated via solution-based additive manufacturing (SBAM). The mass transfer contactor is then assembled into adsorption modules, within which vapor phase infiltration of AlO_x is conducted. PEI is then impregnated into the AlO_x/PIM-1 composite via methanol immersion. After post-processing, the PEI/AlO_x/PIM-1 mass transfer contactor can be used for CO_2 capture.

6.2 Experimental Section

6.2.1 PIM-1 Synthesis

The PIM-1 synthesis procedure is described in prior publications.[3,4] Purified Tetrafluoroterephthalonitrile (TFTPN, Alfa Aesar) and 5,5′,6,6′-Tetrahydroxy- 3,3,3′,3′-tetramethyl-1,1′-spirobisindane (TTSBI, Alfa Aesar) undergo polymerization in the presence of potassium carbonate fine powder and anhydrous DMF at 65 °C for 72 hours. H_2O is added into the synthesis mother solution to dissolve remaining potassium carbonate and quench out PIM-1. The PIM-1 is then dried and dissolved by chloroform and quenched out by methanol. After that, PIM-1 was washed by DMF and methanol sequentially to remove unreacted monomers and oligomers. Mn of the PIM-1 used in this study is 50,200 Da with Mw/Mn around 1.65 as analyzed by GPC.

6.2.2 Vapor Phase Infiltration

Vapor phase infiltration was carried out following the procedure detailed in our previous publication.[3] Prior to infiltration, PIM-1 samples were soaked in methanol for 2 hours to reset the processing history and then dried in a fume hood for 30 minutes. The PIM-1 samples were exposed to trimethylaluminum, water, trimethylaluminum, and water sequentially at 90 ºC. Each exposure lasted for 5 hours for thorough infiltration.

6.2.3 Wet-Impregnation of PEI

PEI (Mw = 800 Da) was loaded into 3D printed PIM-1 adsorber via wet impregnation following the previous study.[2] Methanol solution of PEI was filled into the adsorber module with glass wool taken out temporarily. The mass of PEI was calculated based on the target PEI loading with the assumption that all the PEI was captured by PIM-1, which is a reasonable assumption for PEI solutions with a concentration lower than 5 wt.%.[2]

6.2.4 CO_2 Adsorption

CO_2 adsorption isotherms of the PEI/PIM-1 composites were collected using Dynamic Vapor Sorption equipment (Surface Measurement Systems Ltd.). Small fractions of PEI-impregnated PIM-1 adsorber was loaded onto the microbalance, which was located in an airtight sample chamber. Prior to the experiment, a high vacuum (10^{-5} Pa) and heat (80 °C) are applied to the whole system to desorb CO_2 and solvent from the sample. During the measurement, pure CO_2 was continuously delivered into the sample chamber at a constant flow rate and evacuated by a vacuum pump. The valve between the sample chamber and the vacuum pump was controlled by the computer to maintain a desired sample chamber pressure. The equilibrium sample weights at a series of CO_2 pressure were recorded to establish the adsorption isotherm.

One example 35 °C CO_2 kinetic adsorption curve of a 35wt% PEI/AlO_x/PIM-1 composite is shown in Figure 6.2. While the hierarchically porous fiber samples capture roughly 60% of the capacity within several minutes' exposure to CO_2, it takes hours to be fully saturated. Such a phenomenon is common for all supported PEI adsorbents. Adsorbed CO_2 molecules "crosslink" the exposed two amine groups and form a relatively dense layer inhibiting the CO_2 diffusion towards the unexposed amines.[2] To achieve a good balance between characterization feasibility and data accuracy, the adsorption is considered in an equilibrium state when the weight change is below 0.005% for 1 min. It is worth noting that the adsorption isotherms measured in this section are lower than the theoretical value. Considering the slow adsorption kinetics to fully utilize the CO_2 capacity, it is reasonable to underestimate the PEI-based sample in this way.

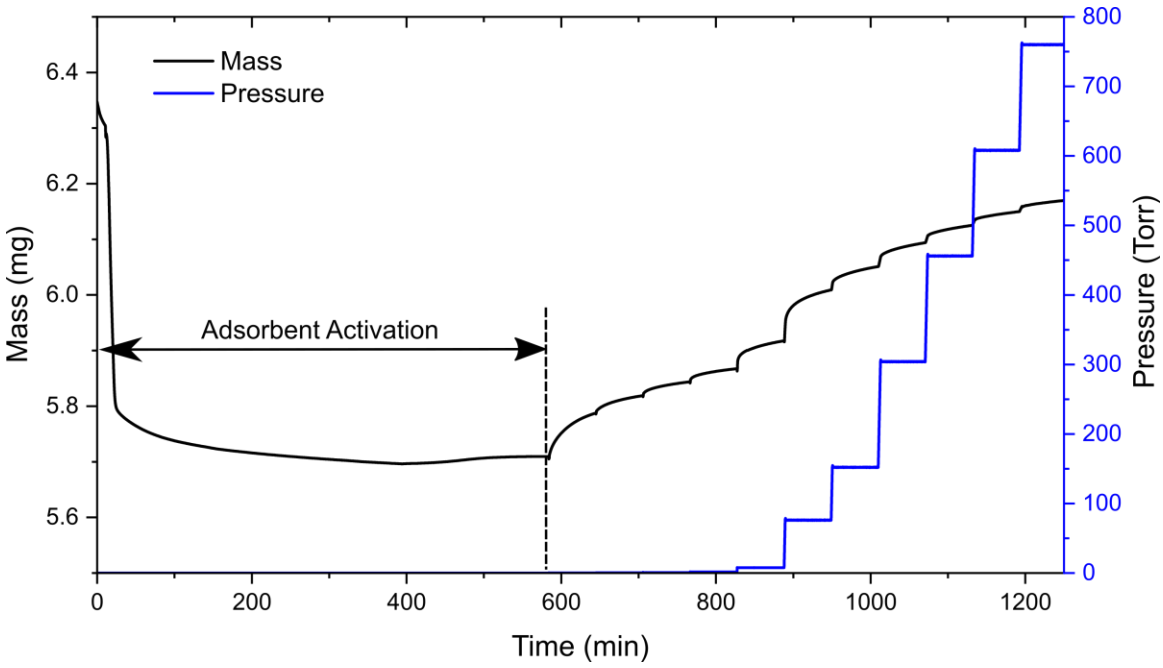

Figure 6.2 Example CO_2 kinetic adsorption of a PEI/AlO_x/PIM-1 composite fiber (35 wt% PEI loading) at 35 °C.

6.2.5 Porosity Characterization

Macropores and mesopores of the 3D printed structures are characterized via mercury porosimetry. The polymer structures were dried under vacuum at 80 °C for 12 hours to get rid of solvent residues. The dry samples are then characterized in an AutoPore IV (Micromeritics) porosimeter. Micropores of the composite are characterized via 77 K nitrogen physisorption. Prior to nitrogen physisorption, samples are dried at 80 °C under vacuum for 12 hours.

6.3 Results and Discussion

6.3.1 The Microstructure of PEI/AlO_x/PIM-1 Composite

The PIM-1 fibers used for vapor phase infiltration and PEI impregnation were produced via SBAM. Owing to the spinodal decomposition process, the PIM-1 fibers possess hierarchical porosity. Figure 6.3a shows the SEM images of the cross-section of a hierarchically porous PIM-1 fiber. Interconnected macropores distribute throughout the fiber. The fuzzy PIM-1 skeleton minimized the diffusion characteristic length down to the sub-micronmeter, which accelerates the adsorption process. No intact skin layer surrounding the fiber was observed. The porous outer surface allows rapid gas exchange with the external atmosphere, which benefits the adsorption kinetics.

The microporosity of PIM-1 and PIM-1-based composites were characterized via nitrogen physisorption at 77 K. As shown in Figure 6.3b, pristine PIM-1 exhibits a classical dual-mode nitrogen adsorption isotherm.[5,6] The steep nitrogen adsorption curve at low-pressure range (relative pressure < 0.05) indicates the interconnected micropores formed by the inefficient packing of the polymer backbone. While the following slow nitrogen adsorption is induced by the swelling effect induced by guest nitrogen molecules. The polymeric structure of PIM-1 is prone to swelling, and it is known that plasticizing guest molecules could interrupt the microstructure of PIM-1.[7] In order to provide a rigid gas transport network for PEI, the PIM-1 fibers are reinforced with AlO_x nanostrands. Infusing PIM-1 with AlO_x is achieved via vapor phase infiltration (VPI).[3] With the optimized VPI protocol, the AlO_x/PIM-1 fibers used in this section contain 13 wt% AlO_x and 87 wt% PIM-1.

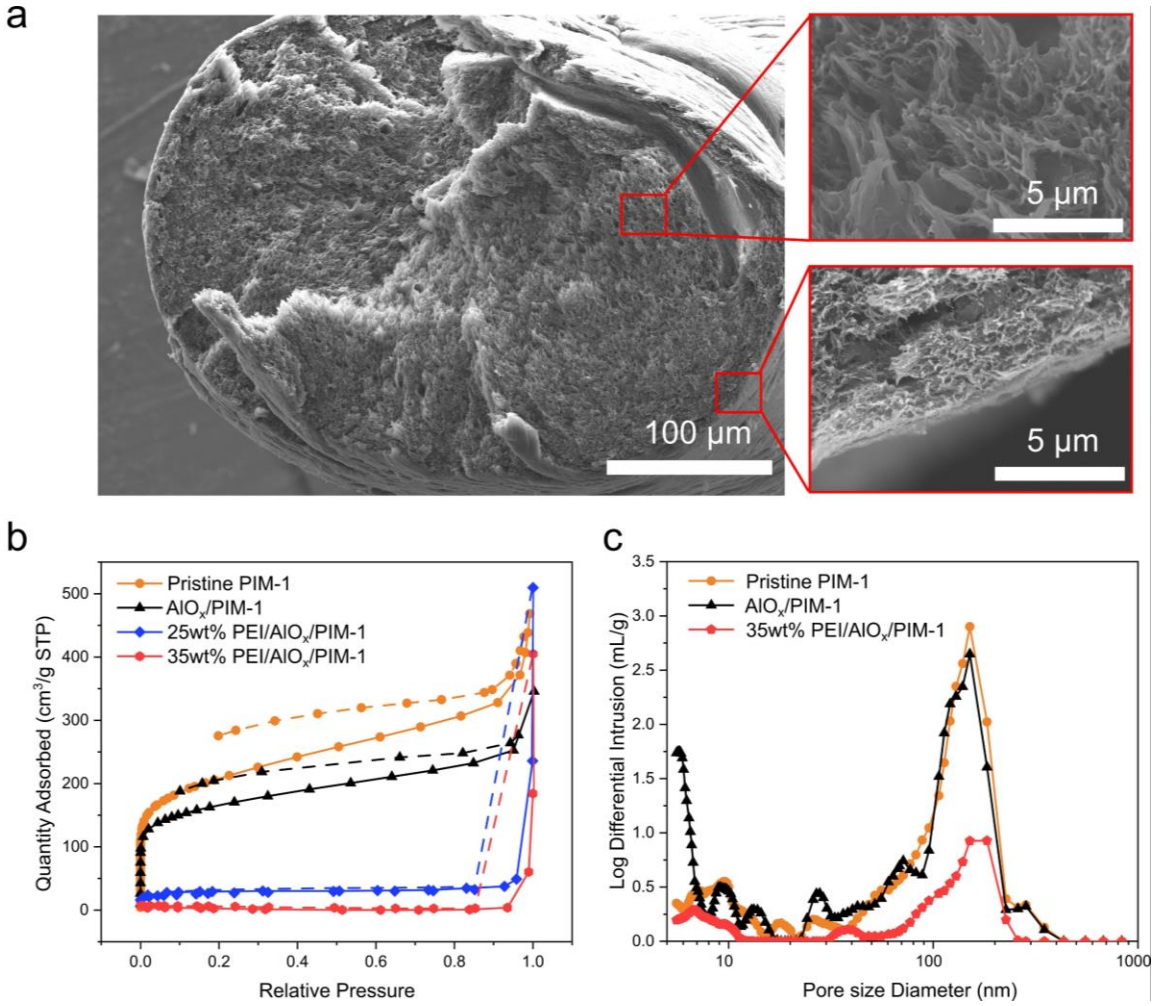

Figure 6.3 Microstructure of the PIM-1, AlO_x/PIM-1, and PEI/AlO_x/PIM-1. (a) SEM images of the PIM-1 fibers fabricated via SBAM. (b) 77K nitrogen physisorption isotherms. (c) Mercury porosimetry of PIM-1 fibers, AlO_x/PIM-1 fibers, and PEI/AlO_x/PIM-1 (35 wt% PEI loading) fibers.

AlO_x/PIM-1 is a more rigid hybrid nanoporous network. As shown in Figure 6.3b, the nitrogen physisorption isotherm of AlO_x/PIM-1 retains its micropore-contributed steep nitrogen adsorption at the low-pressure region (relative pressure < 0.05) but significantly inhibits the swelling-contributed slow nitrogen adsorption at high-pressure region. As expected, the infiltrated AlO_x nanostrands occupy spaces in the PIM-1 micropores, reducing the total pore volume from 0.50 cm^3/g to 0.41 cm^3/g. However, when the pore

volume is normalized by the mass of PIM-1 instead of the whole composite, the pore volume shrinkage is not as significant as it appears. As shown in Table 6.1, 1 gram of PIM-1 provides 0.50 cm^3 pore volume in the pristine state, and it provides 0.47 cm^3 pore volume when intertwined with AlO_x nanostrands. Considering the error associated with the characterization technique and potential polymer swelling, the difference in normalized pore volumes is negligible. This result suggests that the flexible PIM-1 micropores swell in VPI precursor vapors to accommodate the AlO_x nanostrands.

Table 6.1 BET surface areas and total pore volumes calculated based on 77 K nitrogen physisorption isotherms.

Sample	BET Surface Area (m^2/g)	Pore Volume (cm^3/g)	Normalized Pore Volume (cm^3/g_{PIM-1})
PIM-1	723	0.50	0.50
AlO_x/PIM-1	597	0.41	0.47
25wt% PEI/AlO_x/PIM-1	95	0.049	0.075
35wt% PEI/AlO_x/PIM-1	32	0.005	0.009

During the wet impregnation process, PEI is expected to diffuse through the swollen microporous support and fill the mesopores and micropores. Based on the pore volume (0.47 cm^3/g) of AlO_x/PIM-1 fibers, the maximum theoretical loading of PEI is roughly 33 wt %. As expected, the impregnation of PEI inevitably leads to reduced BET surface areas, lower nitrogen physisorption, and smaller pore volume (Figure 6.3b, Figure 6.3c, Table 6.1).

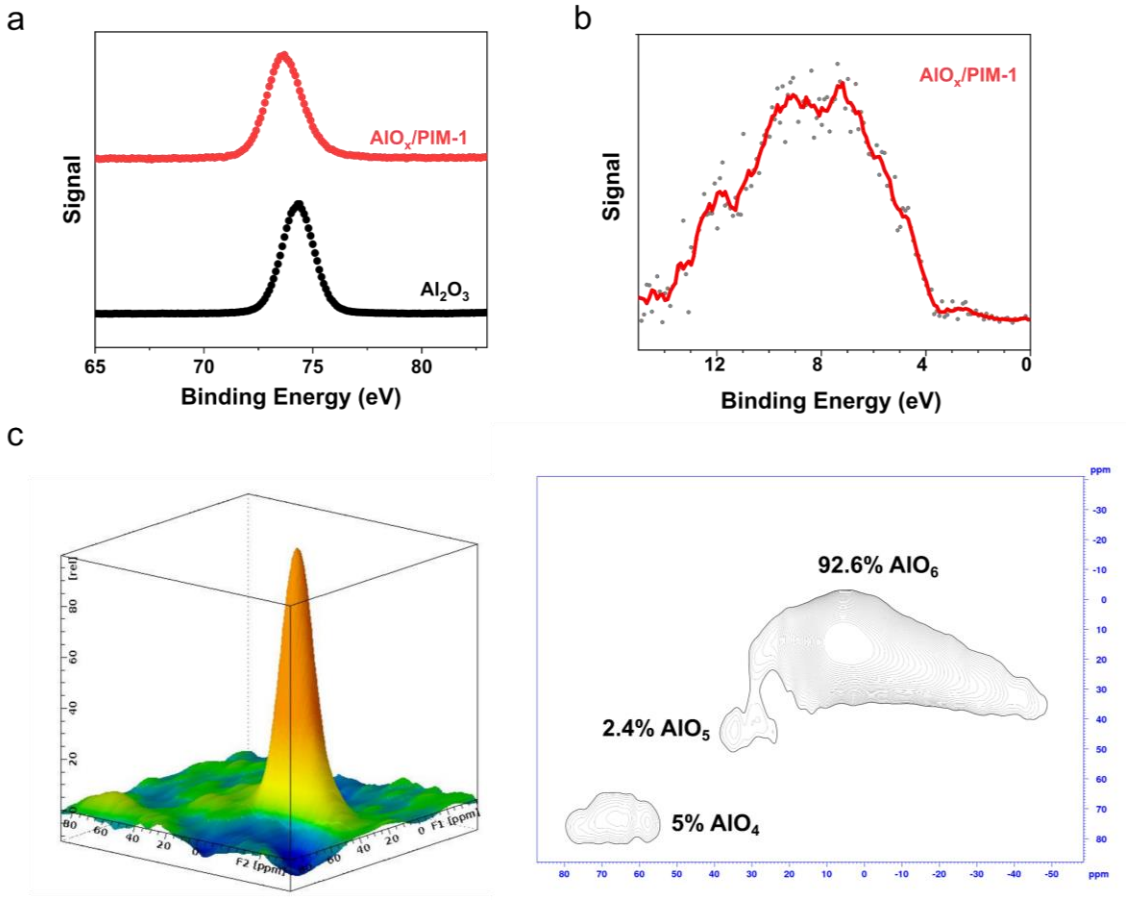

Figure 6.4 Chemical properties of the AlO_x nanostrands in the PIM-1 fibers. (a) Al 2p XPS spectrum, (b) valence XPS spectrum, and (c) Solid-state ^{27}Al NMR for AlO_x/PIM-1 composite.

The amorphous AlO_x nanostrands that intertwines with the PIM-1 network provides abundant hydroxyl groups. While vapor phase infiltration is based on the same chemistry mechanism as atomic layer deposition, the confinement of micropores inhibits the metal oxide crystal growth and result in amorphous aluminum hydroxide nanostrands. The AlO_x constituent has a distinct chemistry nature from alumina. Figure 6.4a.shows the Al 2p spectra for AlO_x/PIM-1 and α-alumina. 2p electrons of the aluminum atoms in the AlO_x/PIM-1 exhibit slightly lower binding energy than those in the reference metal oxide produced by atomic layer deposition. The decrease of binding energy for Al 2p electrons

suggests the existence of aluminum hydroxides instead of aluminum oxide in AlO_x/PIM-1. The Al 2p electron binding energies for aluminum hydroxides have been reported to be 0.8 ~ 0.3 eV lower than that for alumina.[8] The single-peak XPS valence spectrum at 8 eV of AlO_x/PIM-1 composite (Figure 6.4b) resembles gibbsite, which further proves the formation of aluminum hydroxide.[8]

The formation of aluminum hydroxide is hypothetically contributed by the confinement of PIM-1 micropores. As indicated by the solid-state ^{27}Al NMR (Figure 6.4c), most aluminum atoms take the octahedral coordination, which could result in more tortuous nanostrands to dwell in the tortuous micropores.

6.3.2 CO_2 Adsorption Performance

Figure 6.5a and Figure 6.5b show the 35 ºC CO_2 adsorption isotherms for PEI/PIM-1 composites and PEI/AlO_x/PIM-1 composites with different PEI loading. Similar to nitrogen physisorption isotherms, the CO_2 isotherms for PEI/PIM-1 and PEI/AlOx/PIM-1 also exhibit classical dual-mode behavior: a steep Langmuir-type contribution in the low-pressure range (relative pressure < 0.05) and a slow Henry's-law contribution in the following pressure range. For pure PIM-1, the Langmuir-type contribution is not significant. The adsorption isotherm for PIM-1 is mainly contributed by Henry's law sorption, which is associated with the interaction between CO_2 and the nitrile group.[9] The infiltrated AlO_x nanostrands exhibit a limited influence on the CO_2 adsorption performance. As shown in Figure 6.5, the CO_2 adsorption isotherms for PIM-1 and AlO_x/PIM-1 are almost identical.

Compared with bare PIM-1 fibers, the PEI/PIM-1 composites exhibit significantly enhanced CO_2 uptakes at the CO_2 pressures ranging from 10 mmHg to 400 mmHg. However, there is limited CO_2 capacity increase at high CO_2 pressure. This could be attributed to the loss of surface area and the thicken PEI surface that inhibits the full utilization of amine groups.

While AlO_x nanostrands do not directly enhance CO_2 adsorption, AlO_x significantly improved the CO_2 capacity of PEI/AlO_x/PIM-1 composite. As shown in Figure 6.5b, given the same PEI loading, PEI/AlO_x/PIM-1 composites exhibit a 30 % to 100 % capacity increase compared with PEI/PIM-1 composites. Figure 6.5e compares the 35 ºC CO_2 capacities for different samples at 76 mmHg, which simulates flue gas generated by coal-fired plants. As PEI loading increases from 15 wt% to 35 wt%, the CO_2 capacity for PEI/PIM-1 composites increases from 0.41 mmol/g to 0.80 mmol/g while the CO_2 capacity for PEI/AlO_x/PIM-1 composites increases from 0.96 mmol/g to 1.19 mmol/g. Further increasing PEI loading to 41 wt% decreased the CO_2 capacity of PEI/AlO_x/PIM-1, suggesting that excess PEI molecules accumulate at the external surface of the AlO_x/PIM-1 fibers and inhibit the exposure of amine groups to CO_2. As a comparison, SBA-15 and mesoporous alumina with similar PEI loading (40 wt%) capture 1.61 mmol/g and 1.73 CO_2 at 25 ºC.[10] The 35 wt% PEI/AlO_x/PIM-1 achieves 70% CO_2 capacity of 40 wt% PEI loaded in mesoporous hard supports. Considering the difference in PEI loading and adsorption temperature, PEI/AlO_x/PIM-1 matches the CO_2 capacity of the state-of-the-art PEI-based inorganic adsorbents.

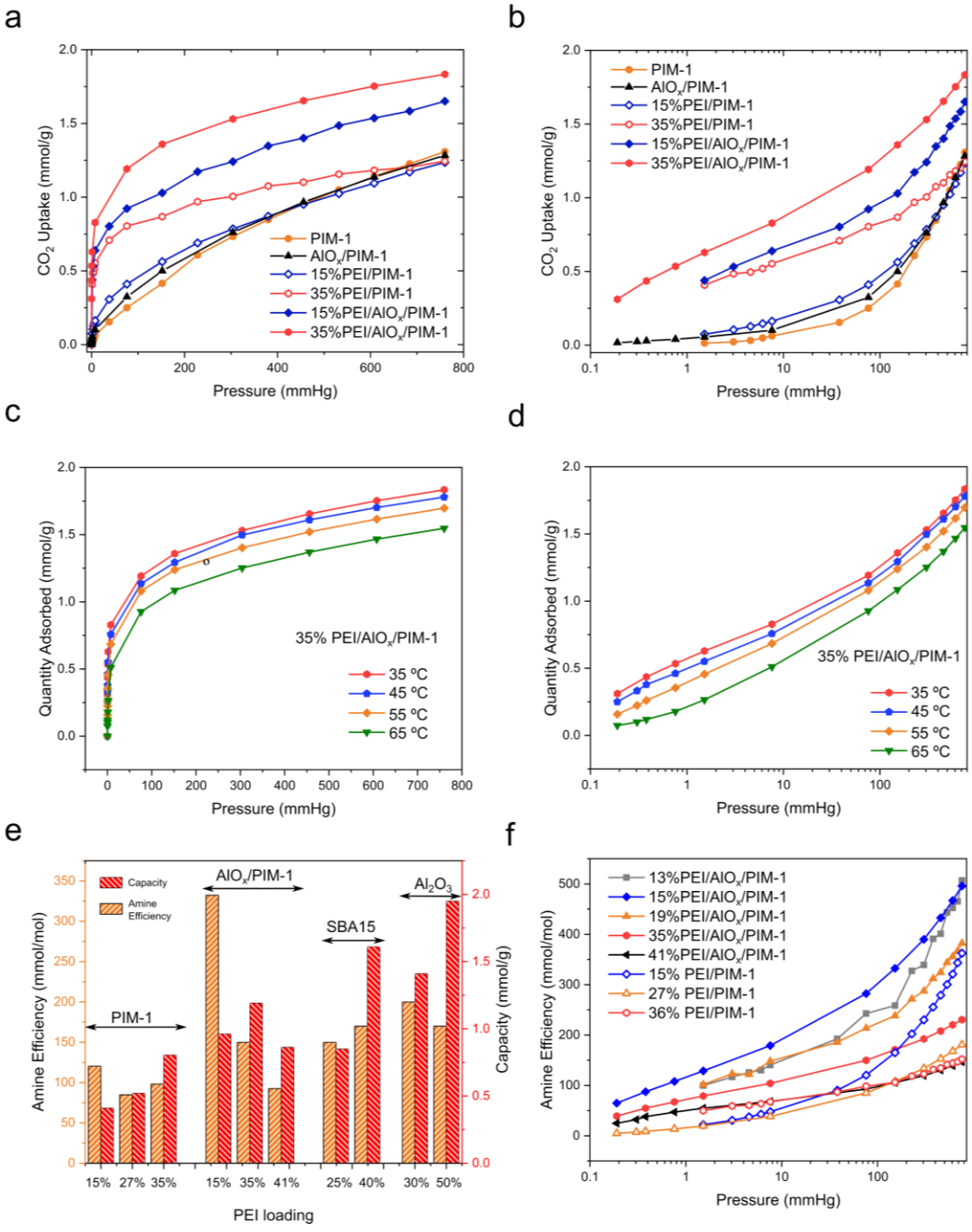

Figure 6.5 CO_2 adsorption performance of PEI/AlO_x/PIM-1. (a, b) 35 ºC CO_2 adsorption isotherms for PIM-1 and AlO_x/PIM-1 loaded with PEI. (c, d) CO_2 adsorption isotherms for 35wt% PEI/AlOx/PIM-1 at 35 ºC, 45 ºC, 55 ºC, and 65 ºC. (e) Amine efficiency and capacity at 35 ºC and 76 mmHg CO_2. PEI loaded in SBA-15 and mesoporous alumina are plotted as a reference. (f) Amine efficiencies of PEI/PIM-1 and PEI/AlOx/PIM-1 derived from 35 ºC CO_2 adsorption isotherms.[10]

The infiltrated AlO_x also increased the amine efficiency (CO_2 adsorption quantity normalized by nitrogen atom quantity) of PEI distributed in PIM-1. Figure 6.5f compares the amine efficiencies of PEI/PIM-1 composites and PEI/AlO_x/PIM-1 composites. Amine efficiencies are calculated by normalizing the CO_2 adsorption isotherm with the nitrogen atom quantity of PEI. Compared with PEI/PIM-1 composites, PEI/AlO_x/PIM-1 composites exhibit significantly increased amine efficiency at the same PEI loading. The high amine efficiency in PEI/AlO_x/PIM-1 composites suggests that infiltrated AlO_x nanostrands frustrate PEI packing and the CO_2 capture mechanism is probably different from the PEI/PIM-1 composite.[11-14] The ratio between primary amine, secondary amine, and tertiary amine for the PEI oligomer used in this study is reported to be 44:33:23.[15] Since tertiary amine (nitrogen) does not contribute to CO_2 adsorption and ammonium carbamate formation in dry condition consumes two adjacent amine groups, the highest amine efficiency is 380 mmol/mol.[2] However, PEI/AlO_x/PIM-1 composites with 13 wt% and 15 wt% PEI loading reach this theoretical upper limit at 300 mmHg CO_2 pressure and exceed as pressure increases. At 300 mmHg, Henry's law sorption in PIM-1 skeleton is negligible, and the CO_2 adsorption can be solely contributed to amines, which guarantees the reliability of amine efficiency calculation. Compared with PEI/PIM-1, 15 wt% PEI/AlO_x/PIM-1 exhibit nearly 100% amine efficiency increase in the low CO_2 pressure region (< 100 mmHg). Two hypotheses can explain this phenomenon. First, the infiltrated AlO_x nanostrands inhibit the densification of PEI molecules, and expose more amine groups to CO_2 molecules. Second, the hydroxyl groups on AlO_x nanostrands may influence the carbamate formation and change the adsorption mechanism. Further investigation is required to explain the amine efficiency improvement.[16,17]

6.4 Conclusion

In this chapter, a new solution-processable amine support is developed for CO_2 capture. After fabrication into adsorption contactors, PIM-1 is reinforced with AlO_x nanostrands via vapor phase infiltration (VPI). The infiltrated AlO_x nanostrands intertwine with the PIM-1 network, resulting in a robust hierarchically porous support for functional materials. PEI oligomers are wet impregnated into the AlO_x/PIM-1 composite and provide adsorption sites for CO_2. The infiltrated AlO_x constituents significantly improved the microstructure stability: AlO_x/PIM-1 can accommodate the PEI with 41 wt% loading without noticeable morphology change, while PEI/PIM-1 composite turns into a gel at 40 wt% loading due to the plasticizing effect of PEI. Compared with PEI/PIM-1 composites, PEI/AlO_x/PIM-1 composites exhibit significantly improved CO_2 capacity and amine efficiency at the same PEI loading: 1 g PEI/AlO_x/PIM-1 with 35 wt% PEI loading captures 1.19 mmol CO_2 at 76 mmHg with an amine efficiency of 150 mmol/mol. By contrast, 1 g PEI/AlOx/PIM-1 with 35 wt% PEI loading captures 0.8 mmol with an amine efficiency of 98 mmol/mol under the same condition. PEI/AlO_x/PIM-1 delivers comparable CO_2 adsorption performance with classical PEI-loaded mesoporous hard adsorbents. Further investigation about adsorption mechanism and structured adsorption contactor fabrication is required.

6.5 References

1. P. M. Budd, E. S. Elabas, B. S. Ghanem, S. Makhseed, N. B. McKeown, K. J. Msayib, C. E. Tattershall, D. Wang. Solution‐processed, organophilic membrane derived from a polymer of intrinsic microporosity. *Advanced Materials* **2004**;16(5):456-459.

2. S. H. Pang, M. L. Jue, J. Leisen, C. W. Jones, R. P. Lively. PIM-1 as a Solution-Processable "Molecular Basket" for CO_2 Capture from Dilute Sources. *ACS Macro Letters* **2015**;4(12):1415-1419.

3. E. K. McGuinness, F. Zhang, Y. Ma, R. P. Lively, M. D. Losego. Vapor Phase Infiltration of Metal Oxides into Nanoporous Polymers for Organic Solvent Separation Membranes. *Chemistry of Materials* **2019**;31(15):5509-5518.

4. M. L. Jue, C. S. McKay, B. A. McCool, M. Finn, R. P. Lively. Effect of Nonsolvent Treatments on the Microstructure of PIM-1. *Macromolecules* **2015**;48(16):5780-5790.

5. M. Minelli, D. R. Paul, G. C. Sarti. On the interpretation of cryogenic sorption isotherms in glassy polymers. *Journal of Membrane Science* **2017**;540:229-242.

6. M. Minelli, B. R. Pimentel, M. L. Jue, R. P. Lively, G. C. Sarti. Analysis and utilization of cryogenic sorption isotherms for high free volume glassy polymers. *Polymer* **2019**;170:157-167.

7. D. Fritsch, P. Merten, K. Heinrich, M. Lazar, M. Priske. High performance organic solvent nanofiltration membranes: Development and thorough testing of thin film composite membranes made of polymers of intrinsic microporosity (PIMs). *Journal of Membrane Science* **2012**;401:222-231.

8. S. Thomas, P. M. Sherwood. Valence band spectra of aluminum oxides, hydroxides, and oxyhydroxides interpreted by X. alpha. calculations. *Analytical Chemistry* **1992**;64(21):2488-2495.

9. P. M. Budd, K. J. Msayib, C. E. Tattershall, B. S. Ghanem, K. J. Reynolds, N. B. McKeown, D. Fritsch. Gas separation membranes from polymers of intrinsic microporosity. *Journal of Membrane Science* **2005**;251(1-2):263-269.

10. W. Chaikittisilp, H.-J. Kim, C. W. Jones. Mesoporous alumina-supported amines as potential steam-stable adsorbents for capturing CO_2 from simulated flue gas and ambient air. *Energy & Fuels* **2011**;25(11):5528-5537.

11. J. Al-Marri, K. Al-Saad, M. Saad, D. Cortes, M. Khader. Thermodynamics of CO_2 adsorption on polyethyleneimine mesoporous silica and activated carbon. **2017**.

12. S. Choi, J. H. Drese, P. M. Eisenberger, C. W. Jones. Application of amine-tethered solid sorbents for direct CO_2 capture from the ambient air. *Environmental science & technology* **2011**;45(6):2420-2427.

13. N. R. Stuckert, R. T. Yang. CO_2 capture from the atmosphere and simultaneous concentration using zeolites and amine-grafted SBA-15. *Environmental science & technology* **2011**;45(23):10257-10264.

14. C.-J. Yoo, L.-C. Lee, C. W. Jones. Probing intramolecular versus intermolecular CO2 adsorption on amine-grafted SBA-15. *Langmuir* **2015**;31(49):13350-13360.

15. J. C. Hicks, J. H. Drese, D. J. Fauth, M. L. Gray, G. Qi, C. W. Jones. Designing adsorbents for CO2 capture from flue gas-hyperbranched aminosilicas capable of capturing CO2 reversibly. *Journal of the American Chemical Society* **2008**;130(10):2902-2903.

16. S. A. Didas, M. A. Sakwa-Novak, G. S. Foo, C. Sievers, C. W. Jones. Effect of amine surface coverage on the co-adsorption of CO2 and water: spectral deconvolution of adsorbed species. *The journal of physical chemistry letters* **2014**;5(23):4194-4200.

17. M. B. Yue, L. B. Sun, Y. Cao, Z. J. Wang, Y. Wang, Q. Yu, J. H. Zhu. Promoting the CO2 adsorption in the amine-containing SBA-15 by hydroxyl group. *Microporous and Mesoporous Materials* **2008**;114(1-3):74-81.

CHAPTER 7. INVESTIGATION OF 3D PRINTING INKS FOR MOF/POLYMER COMPOSITES

7.1 Introduction

Owing to their high surface area, and abundant tunable adsorption sites, Metal-Organic Frameworks (MOFs) have been viewed as promising adsorbent materials with outstanding CO_2 capacity. However, fabricating solid crystalline MOFs into structured adsorption contactors is more challenging than fabricating solution-processable materials.[1] Limited by fabrication techniques, MOFs are usually utilized in the industry in the form of packed pellet beds, which suffer from high pressure drop, inefficient mass transfer, and difficult heat integration.[2] Moreover, the palletization process often damages the relatively "soft" MOF materials. As shown in Chapter 5, structured adsorption contactors provide precisely designed fluid distribution systems that could utilize advanced adsorbent materials in more efficient ways. To fabricate structured MOF-based adsorption contactors, new fabrication methods need to be developed.

Recently, several groups have reported the 3D printing of MOFs. Rezaei and coworkers fabricated MOF monoliths via 3D printing of clay slurries.[3] In their approach, MOF (Ni-MOF-74 and Co-UTSA-16) particles were dispersed in clay, poly(vinyl alcohol), water, and ethanol as a slurry-type 3D printing ink. The research groups led by Magdassi and Lee fabricated MOF scaffolds via stereolithography (SLA).[4] In their approach, HKUST-1 nanoparticles were dispersed in a photocurable resin. SLA was then conducted using this mixed-matrix resin and results in structured MOF/polymer composites.

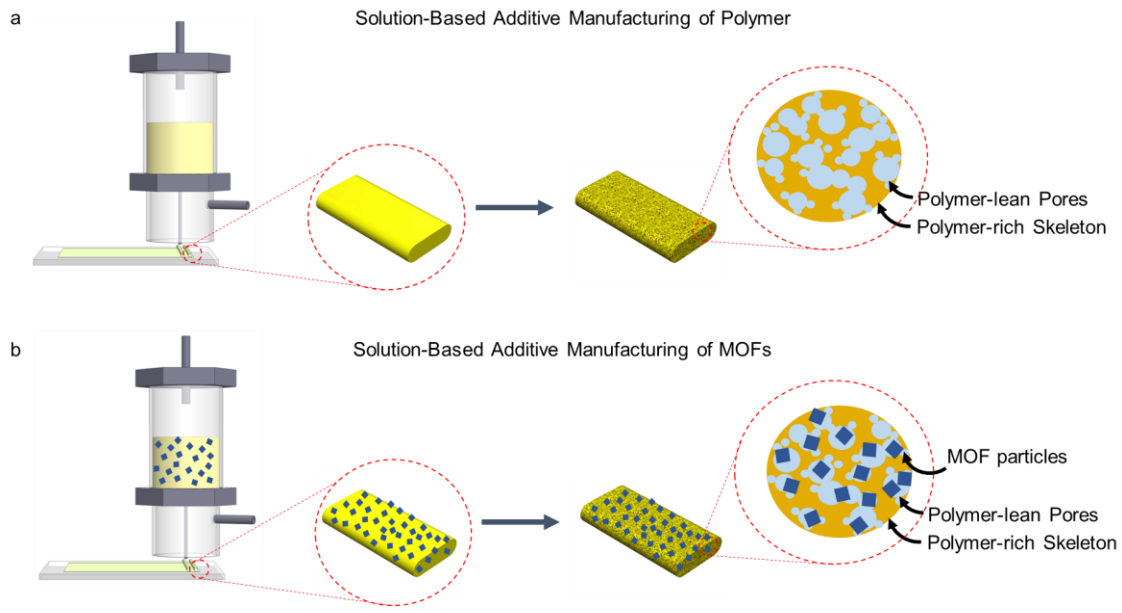

Figure 7.1 Scheme of solution-based additive manufacturing of (a) polymer solution and (b) MOF/polymer composite.

While these approaches towards MOF 3D printing successfully translated the MOFs into different structures, they failed to create hierarchical pores (by IUPAC definition, a combination of micropores, mesopores, and macropores) throughout the resulting structures, which is critical for rapid mass transfer. Solution-based additive manufacturing (SBAM), as described in Chapters 3 and 4, is a promising 3D printing technique that is capable of producing hierarchically porous structures without the use of sacrificial template materials. SBAM translates multicomponent polymer solutions into hierarchically porous polymer structures via evaporation-induced phase inversion (Figure 7.1a). Multicomponent polymer inks are deposited on a substrate via a Direct Ink Write (DIW) 3D printer. The deposited polymer ink undergoes evaporation of the volatile solvent, which triggers phase inversion. During phase inversion, the unstable polymer solution separates into a continuous polymer-rich skeleton and continuous polymer-lean

phase. After washing out the polymer-lean phase, hierarchical pores are created throughout the composite.

The addition of a large concentration of MOFs to polymer solutions significantly changes the ink rheology; as a result, 3D printing of MOFs requires different considerations regarding ink design than pure polymer solutions. Fiber spinning of hierarchical porous MOF/polymer composites, which is also based on phase inversion, has been developed successfully, which suggests that MOF SBAM should be feasible as well.[2,5-7] In this chapter, SBAM protocols are developed for MOF/polymer composite. The ink formulation is modified to protect the water-unstable MOFs and create the desired hierarchical porosity.

7.2 Experimental Section

7.2.1 PIM-1 Synthesis

The PIM-1 synthesis procedure is described in prior publications.[8,9] Purified Tetrafluoroterephthalonitrile (TFTPN, Alfa Aesar) and 5,5′,6,6′-Tetrahydroxy- 3,3,3′,3′-tetramethyl-1,1′-spirobisindane (TTSBI, Alfa Aesar) went through polymerization in the presence of potassium carbonate fine powder and anhydrous DMF at 65 ºC for 72 hours. After synthesis, H_2O was added into the yellow mother solution to dissolve the remaining potassium carbonate and quench out PIM-1. The precipitated PIM-1 was recovered via filtration and dried. To obtain high-purity PIM-1, the crude PIM-1 was dissolved by chloroform and quenched out by methanol to get rid of unreacted monomers. After that, PIM-1 was washed by DMF and methanol sequentially to remove oligomers. Weight averaged molecular weight of the PIM-1 used in this study is 50,200 Da with PDI around 1.65 as analyzed by GPC.

7.2.2 MOF Synthesis

Hydrothermal MIL-101 nanoparticles were synthesized according to literature.[10] $Cr(NO_3)_3 \cdot 9H_2O$ (10.0 g, 50 mmol), terephthalic acid (8.3 g, 50 mmol), and deionized water (100 mL) were mixed in a Teflon-lined autoclave reactor. The reactor was heated in an oven at 218 °C for 18 h. After the synthesis, the MOF particles were separated from the mother solution via centrifugation. The solids were intensively washed with water, methanol, and acetone. The resulting solids were placed in N, N-dimethylformamide (100 mL) and sonicated for 10 min. The suspension was then kept in the oven at 70 °C for 12 hours. The resulting solids were separated by centrifugation, repeatedly washed with methanol and acetone.

HKUST-1 powder samples were synthesized according to published methods.[7] In one glass beaker, 6 g of $Cu(NO_3)_2 \cdot 2.5\ H_2O$ was dissolved in 250 mL of deionized water. In another beaker, 4 g of H_3BTC and 250 mL of an equimolar H_2O/ethanol mixture. These two solutions were added into a Teflon-lined autoclave and heated to 110 °C for 19 h. After synthesis, the autoclave was air-cooled to room temperature, and the HKUST-1 particles were separated from the mother solution via centrifuging. The solids were washed with excessive equimolar H_2O/ethanol solution and then dried under vacuum at 80 °C for 12 hours.

7.2.3 Preparation of MOF/PIM-1 3D Printing Inks

To prepare well-dispersed 3D printing inks, MOFs were firstly dispersed in solvent mixtures and sonicated for 1 hour. Tetrahydrofuran (THF, ACS grade, Alfa Aesar) was selected as the solvent, and dimethylacetamide (DMAc, ACS grade, Alfa Aesar) is selected

as nonsolvent.[11,12] Sonication could effectively inhibit the particle agglomeration. The MOF suspension was then transferred into the 3D printer ink cartridge. Dry PIM-1 fine powders were then added into the MOF suspension. The cartridge containing the crude mixture was sealed and put into a rotating oven at 80 °C for 12 hours to dissolve the polymer and create a homogeneous dispersion. After cooling, the ink was promptly used for solution-based additive manufacturing.

7.2.4 Porosity Characterization

Macropores and mesopores of the 3D printed MOF/PIM-1 composite were characterized via mercury porosimetry. The composites were dried under vacuum at 150 °C for 12 hours to get rid of solvent residues and then characterized by an AutoPore IV (Micromeritics) porosimeter. Micropores of the 3D printed MOF/PIM-1 composite were characterized via N_2 physisorption at 77K. Prior to nitrogen physisorption, samples are dried at 200 °C under vacuum for 12 hours to remove trapped solvents.

7.2.5 CO_2 Adsorption

CO_2 adsorption isotherms of the 3D printed MOF/PIM-1 composites were obtained via the gravimetric method. Dynamic Vapor Sorption (DVS Vacuum) produced by Surface Measurement Systems was used to conduct the measurement. The composite samples were activated at 200 ºC under a high vacuum for 12 hours to remove solvent residue. The activated samples were then exposed to CO_2 under specific pressure. The equilibrium adsorption capacity was determined when the change of sample mass was below 0.002 wt%/min.

7.3 Results and Discussion

7.3.1 Porosity Manipulation

Similar to SBAM of pure polymer solutions (see Chapter 3), the porosity of the 3D printed MOF/polymer composite can be manipulated by changing the solvent/nonsolvent ratio in the 3D printing ink. To evaluate the influence of ink solvent composition on the porosity of the final MOF/PIM-1 composition, water-stable MIL-101 nanoparticles were selected for the demonstration.

Table 7.1 Composition of 3D printing inks and corresponding BET surface areas and pore volumes.

Sample	Ink Composition				BET Surface Area (cm^2/g)	Pore Volume by N_2 (cm^3/g)	Pore Volume by Hg (cm^3/g)
	MOF (g)	PIM-1 (g)	THF (g)	DMAc (g)			
PIM-1	-	1	-	-	723	0.50	
MIL-101	1	-	-	-	2893	1.47	-
MIL-PTD-A1	2	1	7	0	-	-	1.06
MIL-PTD-A2	2	1	6	1	1784	0.82	1.50
MIL-PTD-A3	2	1	5	2	1862	0.92	1.72
MIL-PTD-A4	2	1	4	3	1863	0.94	2.34
HKUST-1	1	-	-	-	1650	0.71	-
HKUST-PTD-A1	4	1	4.7	3.5	1208	0.53	2.01

As shown in Table 7.1, MIL-PTD series 3D printing inks consist of MIL-101 nanoparticles, PIM-1, THF, and DMAc. MIL-PTD-A1 is a control sample without the addition of nonsolvent. The nonsolvent concentration for MIL-PTD-A2, MIL-PTD-A3, MIL-PTD-A4 gradually increase. The highest nonsolvent concentration is 30 wt% (MIL-PTD-A4). DMAc concentrations higher than 30 wt% result in a highly viscous paste that cannot be 3D printed.

These suspension-type inks were 3D printed via SBAM into single filaments. After 3D printing, the wet composites were vacuum dried at 100 °C for 12 hours. The porosities

of the resulting dry samples were characterized via 77 K nitrogen physisorption (Figure 7.2a and b) and mercury porosimetry (Figure 7.3). MIL-101 is a mesoporous adsorbent material with a high BET surface area of 2893 m^2/g. The 3D printed MIL-101/PIM-1 composites contain 66 wt% MIL-101 and mathematically is expected to possess BET surface area higher than 2140 m^2/g (1909 m^2/g contributed by MIL-101 and 231 m^2/g contributed by PIM-1). However, the BET surface areas of MIL-PTD-A2, MIL-PTD-A3, and MIL-PTD-A4 range from 1784 m^2/g to 1863 m^2/g (Table 7.1). We hypothesize that PIM-1 polymer chains can penetrate into the mesopores of MIL-101 nanoparticles. These clogged pores are then inaccessible to nitrogen molecules and result in PIM-1 densification at the interface between MIL-101 and PIM-1. Such a hypothesis agrees with the pore volume probed by nitrogen physisorption (Table 7.1). Pristine MIL-101 possesses 1.47 cm^3/g pore volume and is expected to contribute 0.96 cm^3/g pore volume in the composite with 66 wt% MIL-101 loading. Considering the additional pore volume contributed by PIM-1, the ideal MIL-101/PIM-1 composites should possess 1.13 cm^3/g. However, the experimental pore volumes of these composites range from 0.82 cm^3/g to 0.94 cm^3/g. The loss of pore volume suggests pore occupation and material densification.

It is worth noting that a full nitrogen physisorption isotherm for MIL-PTD-A1 was not obtained. While the MIL-PTD-A1 filaments have the same overall dimension as the other MIL-101/PIM-1 composite samples, the nitrogen physisorption for MIL-PTD-A1 could not be finished within 2 days, which is the maximum continuous operation time for the equipment. The slow adsorption kinetics suggest that MIL-PTD-A1 possesses a dense PIM-1 matrix, which results in a much larger characteristic length of diffusion than the other composites.

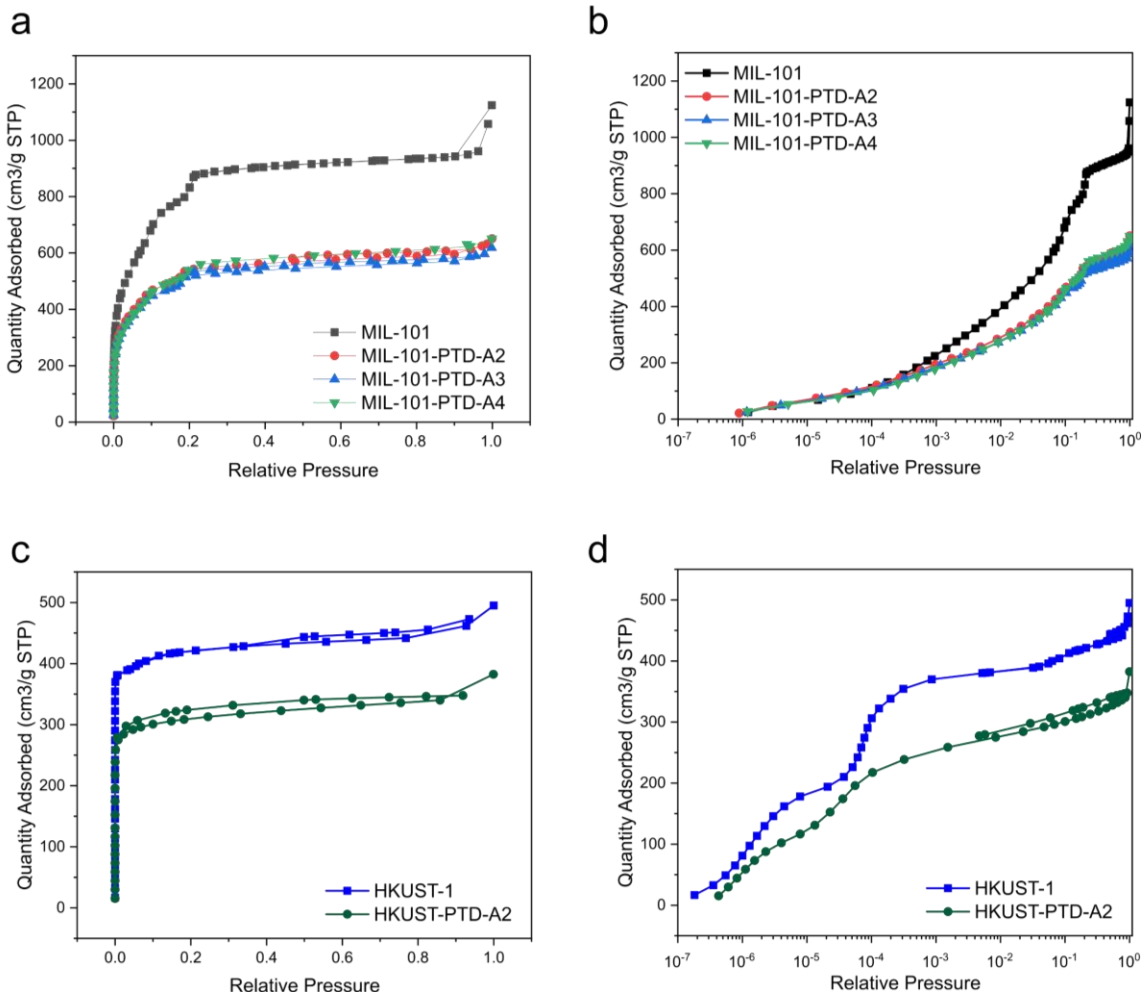

Figure 7.2 77 K nitrogen physisorption isotherms for 3D printed (a, b) MIL-101/PIM-1 composites, (c, d) HKUST-1/PIM-1 composites.

Different from SBAM of PIM-1 solution, SBAM of MIL-101/PIM-1 inks eliminates the need for post-fabrication solvent exchange. Skipping solvent exchange prevents the disastrous impact that could be induced by additional solvent treatment, such as nanoparticle leaching, loss of functional material, or material degradation. Since the hierarchical porous structure is generated during the phase inversion process, skipping the solvent exchange process will not change the porosity significantly. As shown in Table 7.1, the more nonsolvent is added into the ink, the higher the observed pore volume is (probed by mercury porosimetry). However, sample drying with non-volatile plasticizing solvent

residue could anneal the polymer matrix and results in unwanted pore shrinkage. As shown in Figure 7.3, MIL-PTD-A1 composite possesses mesopores around 9 nm and macropores around 100 nm. MIL-PTD-A2 and MIL-PTD-A3 composites possess mesopores around 7 nm and macropores around 100 nm. The addition of nonsolvent in MIL-PTD-A2 and MIL-PTD-A3 is expected to create (or enlarge) more mesopores and macropores in the PIM-1 matrix. However, residual DMAc also acts as plasticizer during the drying process and partially anneals mesopores. This annealing effect of nonsolvent addition is compensated by excessive nonsolvent addition: MIL-PTD-A4 composites possess mesopores around 9 nm and macropores around 200 nm.

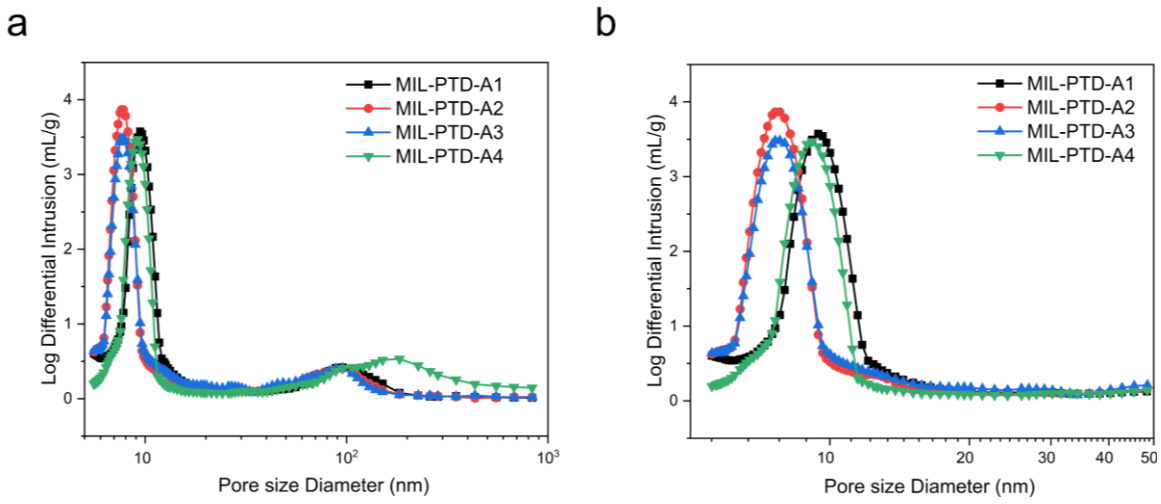

Figure 7.3 Pore size distribution of MIL101/PIM-1 composites probed by mercury porosimetry. (a) Mesopores and macropores. (b) Mesopores.

The SBAM process does not exert a negative impact on MIL-101. Figure 7.4 demonstrates the 35 °C CO_2 adsorption isotherms for MIL-101 particles and the 3D printed MIL-101/PIM-1 composites. Within the tested CO_2 pressure range, the CO_2 uptakes of MIL-101/PIM-1 composites are roughly 66% of the CO_2 uptakes for pristine MIL-101. Different from the nitrogen physisorption experiments, the adsorption capacities of the

composites agree with the mass balance calculation. Such a different adsorption experiment results can be explained by the different molecule sizes and different adsorption temperature. The kinetic diameter of a CO_2 molecule is 0.330 nm, which is much smaller than the kinetic diameter of N_2 (0.364 nm). Also, the experimental temperature for CO_2 adsorption is 308.15 K, which is much higher than the experimental temperature for nitrogen physisorption (77 K). As a result, CO_2 molecules exhibit higher diffusivities and can diffuse through the clogged pores. Therefore, CO_2 can reach the pores that are inaccessible to nitrogen. MIL-PTD-A4 exhibits higher CO_2 capacity than the other composites across the entire pressure range. We hypothesize that the highly porous structure of MIL-PTD-A4 facilitates the CO_2 diffusion through the PIM-1 matrix, which results in higher CO_2 uptake especially in the low-pressure range.

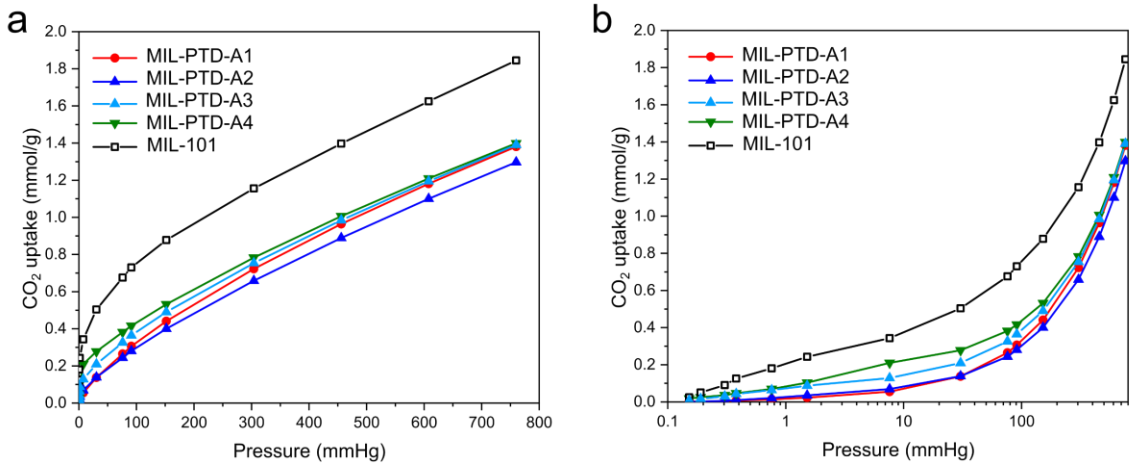

Figure 7.4 CO_2 adsorption isotherms for MIL-101/PIM-1 composites at 35 °C on (a) linear and (b) logarithmic scales.

7.3.2 SBAM of Water -sensitive MOFs

Processing water-sensitive MOF is challenging for traditional adsorption contactor fabrication techniques. For instance, dry-wet fiber spinning usually utilizes water quench

bathes to achieve phase inversion of the polymer matrix. The direct immersion in liquid water is known to destroy MOFs such as HKUST-1. To avoid the MOF degradation during fiber spinning, engineers have to use an organic solvent quench bath, short water immersion time, secondary growth, etc.[1,7]

Different from dry-wet fiber spinning, SBAM relies on evaporation-induced phase inversion, which can be achieved without contact with the water. 3D printing of water-sensitive HKUST-1 is demonstrated here as an example. The 3D printing ink for HKUST-1 is modified from the ink for MIL-101. As shown in Table 7.1, HKUST-PTD-A1 consists of 40 wt% HKUST-1, 10 wt% PIM-1, 47 wt% THF, and 35 wt% DMAc. The SBAM procedure for MIL-PTD inks is used for HKUST-PTD-A1. The solvent exchange procedure was skipped to avoid degradation of HKUST-1. After the drying process, an HKUST-1/PIM-1 composite with 80 wt% HKUST-1 loading is obtained.

Figure 7.2c and Figure 7.2d show the 77 K nitrogen isotherms for pristine HKUST-1 particles and HKUST-PTD-A1 composites. Both samples exhibit typical Type I isotherms. HKUST-1 exhibits a BET surface area of 1650 m^2/g, and HKUST-PTD-A1 exhibits a BET surface area of 1208 m^2/g. According to the composition, the BET surface area of HKUST-PTD-A1 composite is expected to be around 1464 m^2/g (1320 m^2/g contributed by HKUST-1 and 144 m^2/g contributed by PIM-1). The 17 % reduction from the ideal BET surface area can be attributed to the densification of PIM-1 around HKUST-1 particles, which act as diffusion barriers to nitrogen. Further investigation is required to explain the change in BET surface area.

7.4 Conclusion

Solution-based additive manufacturing (SBAM) processes multicomponent polymer solutions into complex architectures via evaporation-induced phase inversion. The template-free generation of hierarchical pores makes SBAM a successful tool for the adsorption contactor prototyping. In this chapter, the material spectrum of SBAM is extended from solution-processable polymers to polymer solution containing functional nanoparticles, such as MOFs. In this chapter, a series of preliminary experiments was conducted on SBAM of MOF/PIM-1 composite. First, the influence of MIL-101/PIM-1 ink formulation on the final hierarchical porosity was investigated. Given the same MOF/polymer ratio and the same SBAM process, a higher nonsolvent/solvent ratio generates higher pore volume and enlarged macropores. The mesopore evolution is controlled by the competition between nonsolvent-induced annealing and nonsolvent-induced pore-formation. Second, SBAM of HKUST-1/PIM-1 composite is conducted. By restricting the exposure to water, SBAM successfully processed HKUST-1/PIM-1 composite without HKUST-1 degradation. These preliminary tests of SBAM of MOF/polymer composite provide a feasible method for MOF adsorption contactor prototyping. The relationship between MOF adsorption contactor design and breakthrough behavior should be further investigated in future work.

7.5 References

1. Y. Ma, F. Zhang, R. P. Lively. Manufacturing Nanoporous Materials for Energy-Efficient Separations: Application and Challenges. *Sustainable Nanoscale Engineering*: Elsevier; **2020**:33-81.

2. S. J. DeWitt, A. Sinha, J. Kalyanaraman, F. Zhang, M. J. Realff, R. P. Lively. Critical Comparison of Structured Contactors for Adsorption-Based Gas

Separations. *Annual review of chemical and biomolecular engineering* **2018**;9:129-152.

3. H. Thakkar, S. Eastman, Q. Al-Naddaf, A. A. Rownaghi, F. Rezaei. 3D-printed metal–organic framework monoliths for gas adsorption processes. *ACS Applied Materials & Interfaces* **2017**;9(41):35908-35916.

4. O. Halevi, J. M. Tan, P. S. Lee, S. Magdassi. Hydrolytically Stable MOF in 3D‐Printed Structures. *Advanced Sustainable Systems* **2018**;2(2):1700150.

5. R. Lively, R. R. Chance, W. J. Koros, H. W. Deckman, B. T. Kelley, Inventors. Sorbent fiber compositions and methods of temperature swing adsorption. US patent 8,133,308 2012.

6. R. P. Lively, R. R. Chance, B. Kelley, H. W. Deckman, J. H. Drese, C. W. Jones, W. J. Koros. Hollow fiber adsorbents for CO_2 removal from flue gas. *Industrial & Engineering Chemistry Research* **2009**;48(15):7314-7324.

7. B. R. Pimentel, A. W. Fultz, K. V. Presnell, R. P. Lively. Synthesis of water-sensitive metal–organic frameworks within fiber sorbent modules. *Industrial & Engineering Chemistry Research* **2017**;56(17):5070-5077.

8. M. L. Jue, C. S. McKay, B. A. McCool, M. Finn, R. P. Lively. Effect of Nonsolvent Treatments on the Microstructure of PIM-1. *Macromolecules* **2015**;48(16):5780-5790.

9. E. K. McGuinness, F. Zhang, Y. Ma, R. P. Lively, M. D. Losego. Vapor Phase Infiltration of Metal Oxides into Nanoporous Polymers for Organic Solvent Separation Membranes. *Chemistry of Materials* **2019**;31(15):5509-5518.

10. L. Bromberg, Y. Diao, H. Wu, S. A. Speakman, T. A. Hatton. Chromium (III) terephthalate metal organic framework (MIL-101): HF-free synthesis, structure, polyoxometalate composites, and catalytic properties. *Chemistry of Materials* **2012**;24(9):1664-1675.

11. F. Zhang, Y. Ma, Y. Kondo, V. Breedveld, R. P. Lively. A Guide to Solution‐based Additive Manufacturing of Polymeric Structures: Ink Design, Porosity Manipulation, and Printing Strategy. *Journal of Advanced Manufacturing and Processing* **2019**:e10026.

12. F. Zhang, Y. Ma, J. Liao, V. Breedveld, R. P. Lively. Solution‐Based 3D Printing of Polymers of Intrinsic Microporosity. *Macromolecular Rapid Communications* **2018**:1800274.

CHAPTER 8. CONCLUSIONS AND FUTURE DIRECTIONS

8.1 Dissertation Overview

This dissertation focuses on the creation of a new 3D printing technique, Solution-Based Additive Manufacturing (SBAM), which can be used to engineer high-efficiency adsorption contactors via 3D printing of microporous polymers. SBAM can process various adsorptive materials and generate hierarchically porous adsorption contactors, which can potentially enable solutions for demanding separation applications such as volatile organic compounds (VOCs) capture and CO_2 capture. A modular adsorption contactor design is proposed to maximize the breakthrough capacity via manipulation of the packing density in individual modules and the arrangement of the module sequence in the assembly. While SBAM is mainly demonstrated with pure polymers, the material spectrum also includes organic-inorganic hybrids (e.g., PEI/AlO_x/PIM-1) and MOFs (e.g., MIL-101 and HKUST-1). This thesis provides fundamental guidance for the creation of adsorption contactor prototyping via the use of 3D printing, which will drive the development of structured adsorbers forward.

8.2 Summary and Conclusions

8.2.1 Chapter Summaries

Sustainable development requires significant improvements in industrial energy efficiency, especially in the separation process sector.[1] Adsorption is an energy-efficient alternative technique to traditional thermally-driven separation techniques.[1-3] Successful adsorption processes can be achieved via the use of customizable modular energy-efficient

adsorption contactors for operation in sites with limited spaces (e.g., submarine), distributed point sources (e.g., vehicle emission treatment), high throughput processes (e.g., flue gas treatment), highly exothermic applications (e.g., chemisorption), among others. The overarching goal of this thesis is to prototype energy-efficient mass transfer contactors via 3D printing of adsorptive materials. This thesis starts with the introduction and fundamental theories provided in the first two chapters. Chapter 1 introduces the importance of sustainable development, energy-efficient separation techniques, state-of-the-art separation contactors, microporous separation materials, and fundamentals of 3D printing. Chapter 2 provides a fundamental background for porous materials, adsorption processes, and fluid rheology.

Traditional adsorption contactors (e.g., packed pellets bed) suffer from high pressure drop, inefficient mass transfer, and difficult heat integration. The limitation of traditional adsorption contactors inspires the development of energy-efficient structured contactors via 3D printing. There exist at least three challenges facing this overarching goal. First, current 3D printing methods have strong limitations in the classes of compatible materials. Many polymers used in adsorption industries cannot currently be 3D printed. Second, little research has been conducted on the relationship between adsorption contactor design and adsorption behavior. Third, the improvement of 3D printed adsorption contactor over traditional contactors has not been reported. In this thesis, these challenges are addressed by a series of demonstrative experiments.

In Chapter 3, a generalizable Solution-Based Additive Manufacturing (SBAM) method for printing viscous polymer solutions was developed for solution-processable polymers. SBAM fabricates polymeric objects by depositing ternary polymeric inks (e.g.,

solutions comprising polymer, volatile solvent and nonvolatile nonsolvent), which undergo rapid phase inversion upon evaporation of a relatively small fraction of the volatile component, resulting in hierarchically porous filaments (e.g., pores of diameters ranging from 2 nm to 10 μm). In addition to the architecture of the printed object, its internal porosity can be manipulated for different applications. SBAM is conceptually compatible with any solution-processable polymer with or without functional particles (e.g., zeolites), which significantly extends the 3D-printable polymeric material spectrum.

In Chapter 4, a microporous polymer (PIM-1) -incompatible with current additive manufacturing technologies- is 3D printed into a high-efficiency mass transfer contactor exhibiting hierarchical porosity ranging from sub-nanometer to millimeter pores. Short contactors were observed to fully purify gases loaded with concentrated toluene vapor for six times longer than PIM-1 in traditional structures, and more than 4000 times the residence time of the gas in the contactor. This demonstration strongly suggests that 3D printing could produce ultra-short adsorbers with precisely designed fluid distribution system without gas bypass.

In Chapter 5, a scalable, modular design of mass transfer contactors was explored via the use of the SBAM process. Such modular contactors possess high freedom in the engineering of characteristic lengths of diffusion, fluid distribution systems, fluid channel sizes, adsorbent loadings, etc. A systematic study in the structural design was conducted to maximize the breakthrough capacity while minimizing the pressure drop across the contactor. As a demonstration, PIM-1 was 3D printed into adsorption modules with hierarchical porosity. These adsorption modules served as “molecular baskets” for branched polyethyleneimine (PEI). The PEI/PIM-1 composite adsorption modules were

then used for CO_2 capture from simulated flue gas. These experiments revealed that by optimizing the adsorption module assembly strategy, the breakthrough capacity can be improved by nearly half without sacrificing pressure drop.

In Chapter 6, the "molecular basket", PIM-1, was reinforced with oxide nanostrands via vapor phase infiltration of the oxide material's precursors. The infiltrated oxide strands intertwine with the PIM-1 network, resulting in a robust hierarchical porous support for functional materials. PEI oligomers were loaded into the organic-inorganic hybrid. The infiltrated oxide constituent significantly improved the microstructural stability. Compared with PEI/PIM-1 composites, oxide/PEI/PIM-1 composites exhibit significantly improved CO_2 capacity and amine efficiency at the same PEI loading. The improvement of the CO_2 capacity and amine efficiency was hypothesized to derive from reinforcement of the PIM-1 support and the abundant hydroxyl groups provided by the oxide strands.

In Chapter 7, the processable material spectrum of SBAM was expanded from solution-processable polymers to metal-organic frameworks (MOFs). These adsorptive nanoparticles were dispersed in multicomponent polymer solutions to form a 3D printable slurry. The addition of a large concentration of MOFs to polymer solutions significantly changes the ink rheology; as a result, 3D printing of MOFs requires different considerations regarding ink design than polymer solution. Similar to SBAM of the polymer solution, the slurry filaments deposited by the 3D printer undergo evaporation-induced phase inversion, which resulted in hierarchical pores throughout the composite. Besides the creation of hierarchical porosity, SBAM of nanoparticles provides protection to water-unstable MOFs, such as HKUST-1. After SBAM, the MOF particles dispersed in the polymer retain their

surface areas. The SBAM process does not negatively impact the MOF structure or block the micropores.

8.2.2 Conclusions and Impact

A versatile 3D printing technique, Solution-based Additive Manufacturing (SBAM), is developed for both polymers and functional nanoparticles. Our research provides a practical guide towards the development of ternary polymeric inks, the design of 3D printer hardware for SBAM, and the post-treatment of printed objects for desired porosity. SBAM significantly broadens the material spectrum for 3D printing techniques. While this thesis focuses on the adsorption process, SBAM can process various functional materials into complex structures for the development of microfluidics devices,[4] structured biomaterials[5-7], and structures with high mechanical strength.[8]

8.3 Future Research Directions

8.3.1 Heat Integration in 3D Printed Adsorption Contactor

During the adsorption process, the heat of sorption is released in the mass transfer region, which can rapidly increase the local temperature. Without efficient heat management, thermal waves can be observed within the adsorption contactor, which ultimately results in nonisothermal operation and reductions in breakthrough capacity.[3,9,10] Heat management has proven successful in hollow fiber adsorption contactors, which resembles tubular heat exchangers. By flowing coolant (e.g., cooling water) in the bore side and gas mixture in the shell side, the heat generated during adsorption can be promptly removed.

3D printing enables high-freedom engineering of individual fluid distribution channels; for instance, coolant can theoretically be precisely delivered to the hot spots. Inspired by heat management integrated hollow fiber adsorption contactor, two adsorption contactor designs with heat integration are proposed in Figure 8.1.

In Figure 8.1a, the parallel flow paths for the feed mixture and coolant are placed in adjacent, closed channels. The coolant flow occurs in the same direction as the feed gas and promptly capture the heat of sorption from the mass transfer zone. Compared with hollow fiber adsorption contactors, the 3D printed contactor can be directly integrated with fluid distribution headers, which reduces the capital cost and further minimize the footprint. One drawback of such co-current flow path design is that the heated coolant flows towards the fresh adsorbent sections and result in temporal temperature increase. The coolant flow rate must be carefully manipulated to cool the fresh adsorbent sections before the mass transfer happens.

Figure 8.1b proposed one alternative design. The adsorption contactor consists of orthogonal flow paths for the feed mixture and the coolant. The coolant is delivered by a special header system that precisely delivers the fresh coolant to the mass transfer zone, which is moving from the inlet to the outlet. Compared with the co-current heat management illustrated in Figure 8.1a, the orthogonal heat management is more precise but requires complex coolant delivery systems and accurate heat transfer modelling.

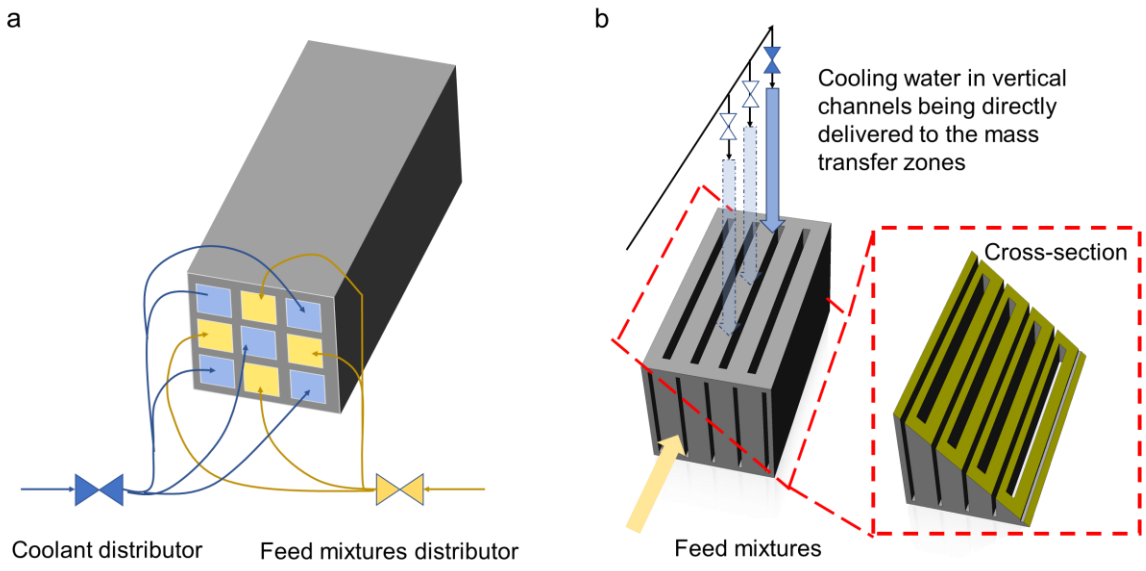

Figure 8.1 Heat integrated adsorption contactors with (a) co-current flow paths and (b) orthogonal flow paths.

While the majority of this thesis focuses on adsorption, desorption process also plays an important role in the adsorption separation process.[11] Desorption process with low energy consumption, rapid regeneration, and high product purity can significantly improve the efficiency of the overall adsorption process.[11] Heat integrated adsorption contactor could enable rapid temperature swing adsorption, which has been proven to increase the process productivity and reduce operational cost.[9,11] In the future, the influence of hot stream (e.g., hot water, hot steam, etc.) flowrate, feeding position, and heat recovery on the overall adsorption process will be investigated.

8.3.2 Optimization of Adsorption Contactors

As described in Section 2.3.2, the dynamic adsorption process in an arbitrary adsorption contactor can be described by the linear driving force (LDF) model.[12-14] As proven by existing research on hollow fiber adsorption contactors, LDF models exhibit a

good balance between simulation accuracy and calculation efficiency.[13] The fundamental mass transfer parameters (e.g., interfacial mass transfer coefficients) can be obtained by fitting the experimental breakthrough curves for simple contactors with LDF models. The LDF models established on reliable mass transfer parameters exhibit outstanding accuracy in the breakthrough curve prediction for new adsorption contactor design.

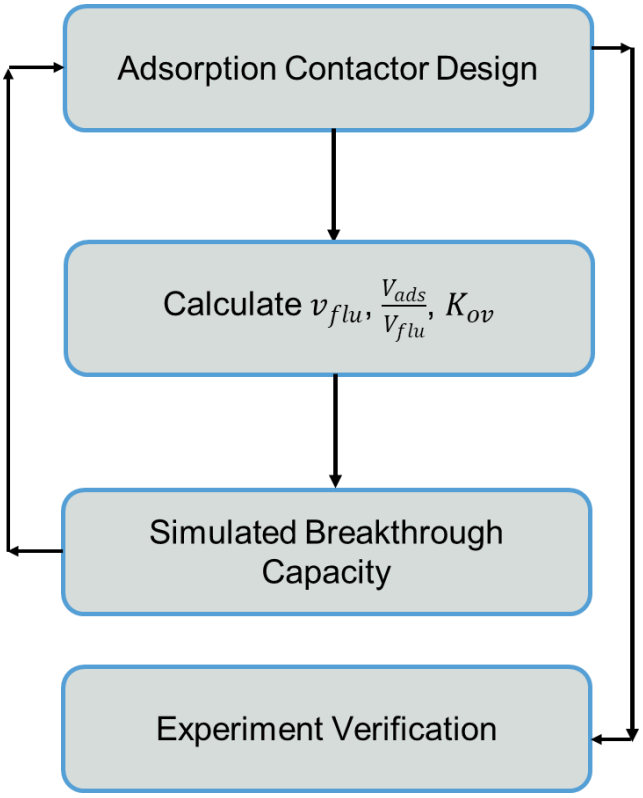

Figure 8.2 The flow diagram for adsorption contactor structure optimization.

Figure 8.2 highlights a proposed flow diagram for adsorption contactor structural optimization. To begin with, new adsorption contactor structures designed with CAD software are analyzed to calculate v_{flu}, $\frac{V_{ads}}{V_{flu}}$, and K_{ov} as functions of the position in the adsorption contactor. After the contactor structure evaluation, the breakthrough curves and corresponding breakthrough capacities can be obtained.

Guided by the general relationship between the adsorption contactor structure and the breakthrough behavior, the researcher can accordingly adjust the adsorption contactor structural design to delay adsorbate breakthrough time and increase the breakthrough capacity. By repeating this iterative optimization, the contactor design with the highest breakthrough capacity with given constraints (e.g., maximum pressure drop) can be predicted. The predicted adsorption contactor should be 3D printed and evaluated experimentally.

8.3.3 3D Printed Catalysis Contactor

In this thesis, the 3D printed mass transfer contactors are prototyped for adsorptive applications. By optimizing the mass transfer and potentially heat transfer at different positions of the contactor, the overall performance (e.g., breakthrough capacity) can be maximized. Similar strategies can also be applied to catalysis by adding reaction terms into the mass transfer governing equation and 3D printing catalytic compounds.

Researchers have conducted a variety of proof-of-concept experiments about prototyping catalytic contactors via 3D printing.[15-17] For instance, prototyped an asymmetric honeycomb catalytic contactor with expanding fluid channels, which exhibits improved catalysis performance than regular tubular reactors.[15] While these preliminary trials provide promising results, there is a lack of theoretical guidance for contactor design. A systematic investigation about the relationship between contactor design and process throughput could guide the contactor optimization for all researchers.

8.4 References

1. D. S. Sholl, R. P. Lively. Seven chemical separations: to change the world: purifying mixtures without using heat would lower global energy use, emissions and pollution--and open up new routes to resources. *Nature* **2016**;532(7600):435-438.

2. W. J. Koros, R. P. Lively. Water and beyond: Expanding the spectrum of large‐scale energy efficient separation processes. *AIChE Journal* **2012**;58(9):2624-2633.

3. R. P. Lively. *Hollow fiber sorbents for post-combustion CO_2 capture*, Georgia Institute of Technology; 2011.

4. A. K. Au, W. Huynh, L. F. Horowitz, A. Folch. 3D-printed microfluidics. *Angewandte Chemie International Edition* **2016**;55(12):3862-3881.

5. R. A. Barry, R. F. Shepherd, J. N. Hanson, R. G. Nuzzo, P. Wiltzius, J. A. Lewis. Direct‐Write Assembly of 3D Hydrogel Scaffolds for Guided Cell Growth. *Advanced Materials* **2009**;21(23):2407-2410.

6. B. G. Compton, J. A. Lewis. 3D‐printing of lightweight cellular composites. *Advanced Materials* **2014**;26(34):5930-5935.

7. S. J. Hollister. Porous scaffold design for tissue engineering. *Nature materials* **2005**;4(7):518.

8. X. Zheng, H. Lee, T. H. Weisgraber, M. Shusteff, J. DeOtte, E. B. Duoss, J. D. Kuntz, M. M. Biener, Q. Ge, J. A. Jackson. Ultralight, ultrastiff mechanical metamaterials. *Science* **2014**;344(6190):1373-1377.

9. R. P. Lively, R. R. Chance, W. J. Koros. Enabling low-cost CO2 capture via heat integration. *Industrial & Engineering Chemistry Research* **2010**;49(16):7550-7562.

10. K. Kim, Y. Son, W. B. Lee, K. S. Lee. Moving bed adsorption process with internal heat integration for carbon dioxide capture. *International Journal of Greenhouse Gas Control* **2013**;17:13-24.

11. S. J. DeWitt, A. Sinha, J. Kalyanaraman, F. Zhang, M. J. Realff, R. P. Lively. Critical Comparison of Structured Contactors for Adsorption-Based Gas Separations. *Annual review of chemical and biomolecular engineering* **2018**;9:129-152.

12. M. Goto, J. Smith, B. J. McCoy. Parabolic profile approximation (linear driving-force model) for chemical reactions. *Chemical Engineering Science* **1990**;45(2):443-448.

13. J. Kalyanaraman, Y. Fan, R. P. Lively, W. J. Koros, C. W. Jones, M. J. Realff, Y. Kawajiri. Modeling and experimental validation of carbon dioxide sorption on hollow fibers loaded with silica-supported poly (ethylenimine). *Chemical Engineering Journal* **2015**;259:737-751.

14. S. Sircar, J. Hufton. Why does the linear driving force model for adsorption kinetics work? *Adsorption* **2000**;6(2):137-147.

15. A. Davó-Quiñonero, D. Sorolla-Rosario, E. Bailón-García, D. Lozano-Castelló, A. Bueno-López. Improved asymmetrical honeycomb monolith catalyst prepared using a 3D printed template. *Journal of Hazardous materials* **2019**;368:638-643.

16. C. R. Tubio, J. Azuaje, L. Escalante, A. Coelho, F. Guitián, E. Sotelo, A. Gil. 3D printing of a heterogeneous copper-based catalyst. *Journal of Catalysis* **2016**;334:110-115.

17. F. Kazenwadel, E. Biegert, J. Wohlgemuth, H. Wagner, M. Franzreb. A 3D‐printed modular reactor setup including temperature and pH control for the compartmentalized implementation of enzyme cascades. *Engineering in Life Sciences* **2016**;16(6):560-567.

APPENDIX A. VAPOR PHASE INFILTRATION OF METAL OXIDES INTO NANOPOROUS POLYMERS FOR ORGANIC SOLVENT SEPARATION MEMBRANES[‡]

Membrane-based organic solvent separations promise a low-energy alternative to traditional thermal separations but require materials that operate reliably in chemically aggressive environments. While inorganic membranes can withstand demanding conditions, they are costly and difficult to scale. Polymeric membranes, such as polymer of intrinsic microporosity 1 (PIM-1), are easily manufactured into forms consistent with large-scale separations (e.g., hollow fibers), but perform poorly in aggressive solvents. Here, a new post-fabrication membrane modification technique, vapor phase infiltration (VPI), is reported that infuses PIM-1 with inorganic constituents to improve stability while maintaining the polymer's macroscale form and nanoporous internal structure. The atomic-scale metal oxide networks within these hybrid membranes protect PIM-1 from swelling or dissolving in solvents. This stability translates to improved separation performance in a variety of solvents, including solvents capable of dissolving PIM-1. The infiltrated inorganic phase also appears to give new control over solute sorption in organic solvent nanofiltration (OSN). These hybrid membranes further show promising performance for organic solvent reverse osmosis (OSRO) separations in challenging solvents, even at small molecular weight differentials (14 Da). Because the VPI process can be integrated with

[‡] This chapter has been published in *Chemistry of Materials* as "Vapor Phase Infiltration of Metal Oxides into Nanoporous Polymers for Organic Solvent Separation Membranes".[1]

state-of-the-art membrane modules, this treatment could be readily adopted into the large-scale manufacturing of advanced membranes.

A.1 Introduction

Modern chemical manufacturing depends on efficient chemical separations. Today, most separations are achieved with energy-intensive thermal approaches based on phase changes (e.g., distillation), which account for 10-15% of global energy usage.[2] In contrast, membrane separations—which differentiate molecules based on variations in molecular size, shape, and physicochemical interaction parameters—require minimal energy input. For instance, membrane-based desalination uses 90% less energy than the most optimized thermally driven processes (i.e., highly engineered multi-stage flash evaporation consumes ap-proximately 45 kWh/m^3 whereas commercial reverse osmosis plants consume approximately 4.5 kWh/m^3).[3]

Most current commercial membrane separation technologies are deployed for gaseous chemicals or aqueous media (e.g., brine). However, membrane usage in organic solvent separation (e.g., xylene separation, organic solvent dehydration, product separation of synthesis solution, etc.) is becoming more prevalent in the modern chemical industry due to its potential energy and carbon savings. For instance, the separation of benzene derivatives requires approximately 430 TWh of energy each year;[2] membrane processes such as organic solvent nanofiltration (OSN) and organic solvent reverse osmosis (OSRO) can potentially drive this energy cost down by an order of magnitude.[4] For successful integration into industrial processing, OSN and OSRO processes require membranes that retain their mechanical integrity and microstructure when operating in aggressive organic

solvents.[5] State-of-the-art organic solvent separation membrane materials include zeolites,[6,7] MOFs,[8] carbon molecular sieves,[4,9] porous organic cages,[10] porous ceramics,[11] crosslinked polymer networks,[12,13] microporous polymers,[14] conjugated microporous polymers,[15] etc. While inorganic membranes, like zeolites, can be stable in organic solvents, they are costly and challenging to scale up in a defect-free manner.[12] Solution-processable polymers can be mass-produced into defect-free membranes but lack the requisite levels of organic solvent stability. The stability of some polymeric membranes can be improved by promoting crosslinking through the careful selection of polymer chemistry and processing.[12,13] However, this method cannot be expanded to all polymer chemistries.

One polymer class of interest for organic solvent separation is polymers of intrinsic microporosity.[11] A prototypical polymer of intrinsic microporosity is polymer of intrinsic microporosity 1 (PIM-1). At ambient conditions, PIM-1 is a solution-processable, rigid, glassy polymer with high levels of microporosity, but like other polymer membranes, it has limited stability and selectivity when exposed to plasticizing solvents or highly sorptive solutes.[14,16-18] Several post-fabrication techniques have been developed to enhance the solvent stability of polymer membranes like PIM-1, including crosslinking to create interconnected polymer networks and thermal pyrolysis to create carbon molecular sieves.[4,19] While these techniques show promise towards creating solvent-stable scalable membranes, both lead to dramatic changes in the membrane's microscopic structure and higher probability of defect formation. These post-fabrication techniques also consume large amounts of chemicals and solvents, require additional equipment, and generate added costs.

Vapor phase infiltration (VPI) is a gas-phase, solvent-free process that has emerged from the atomic layer deposition (ALD) community to load the bulk of polymers with inorganics (e.g., metal oxides).[20-24] While atomic layer deposition modify the external surfaces of materials, vapor phase infiltration involves complex diffusion and heterogenous reaction to modify the voids (e.g., micropores and mesopores) between polymer chains. Previously, VPI has been used to load polysulfone membranes with aluminum oxide,[25] increase the resilience of polymeric nanopillars,[26] strengthen spider silk,[27] and provide UV protection to Kevlar fibers.[28] The VPI kinetics and final hybrid material's physiochemical structure varies with polymer chemistry, polymer microstructure, metal-organic precursor chemistry, and processing temperature.[20-22]

A.2 Experimental Section

A.2.1 Polymer of Intrinsic Microporosity 1 (PIM-1) Synthesis

A room-temperature condensation of tetrafluoroterephthalonitrile (TFTPN, Alfa Aesar) and 5,5',6,6'-Tetrahydroxy- 3,3,3',3'-tetramethyl-1,1'-spirobisindane (TTSBI, Alfa Aesar) was conducted in anhydrous dimethylformamide (DMF, Alfa Aesar) in the presence of K_2CO_3 (Alfa Aesar) fine powders for 72 hours. The reaction was conducted at 65 °C with stirring. Prior to synthesis, TTSBI and TFTPN were purified via vacuum sublimation and recrystallization, respectively. Monomers and oligomers were removed by post-synthesis washing using DMF and methanol. The purified PIM-1 (Mn = 50,200, Mw/Mn = 1.65) was then stored in sealed jars. The molecular weight was determined by gel permeation chromatography (GPC) in tetrahydrofuran compared with polystyrene standards. Unless declared, all organic solvents used in this section were generic, ACS grade purchased from Sigma-Aldrich or Alfa Aesar without further treatment. Styrene

dimers and polystyrene oligomers were purchased from Agilent. Matrimid® 5218 was purchased from Huntsman. p-Xylylenediamine was purchased from Sigma-Aldrich.

A.2.2 Flat PIM-1 Membrane Casting

The dry PIM-1 powder was dissolved in anhydrous chloroform with a mass ratio of 1:200. After complete dissolution, the PIM-1 solution was filtered through a PTFE filter with 0.45 μm pores. The clear yellow PIM-1 solution was then transferred into a nitrogen glove bag that had been saturated with chloroform. The PIM-1 solution was then poured into a PTFE petri dish. After 48 hours of slow evaporation, the flat PIM-1 membrane was transferred into a vacuum oven (990 mbar, 80 °C) to dry thoroughly. The thickness of the flat PIM-1 membranes was controlled by varying the amount of PIM-1 solution poured into PTFE petri dishes. These flat PIM-1 membranes were then used to study VPI infiltration depth profiles, contact angle, and transmission FTIR.

A.2.3 PIM-1 Hollow Fiber Membrane Spinning

PIM-1 hollow fiber membranes were fabricated via dry-wet spinning as described by Jue, et al. As a result of phase inversion, PIM-1 hollow fiber mem-branes exhibit hierarchical porosity, which minimizes the characteristic diffusion length of VPI precursors and results in thorough metal oxide infiltration (vide infra).

A.2.4 PIM-1 Thin Film Composite Membrane Fabrication

Matrimid® 5218 support membranes were fabricated via nonsolvent induced phase inversion. Matrimid® 5218, tetrahydrofuran, ethanol, water, $LiNO_3$, and N-methyl-2-pyrrolidone were mixed with a mass ratio of 16:10:3:1:1:69 in a sealed container. Once the

polymer was fully dissolved, the homogeneous solution was then cast into a liquid film via a blade on a clean glass plate. The liquid film was then transferred to a well-ventilated hood to assist the formation of a partial skin layer. After 30 seconds, the liquid film was immersed into a deionized water bath. Phase inversion was completed within 1 hour resulting in an opaque porous membrane. The membrane was then stored in a new water bath for 12 hours, followed by three washing cycles in methanol and three washing cycles in n-hexane sequentially. During each washing step, the membrane was immersed in the solvent bath for 3 hours. After vacuum drying at 200 °C for 12 hours, these support membranes were stored in the ambient environment before crosslinking. These Matrimid® membranes were crosslinked by p-xylylenediamine. Dry Matrimid® membranes were immersed in 10 weight percent p-xylylenediamine methanol solution for 24 hours at room temperature. After crosslinking, the membranes were washed with methanol and n-hexane three times, respectively. After vacuum drying at 100 °C for 12 hours, these cross-linked Matrimid® support membranes were stored in a sealed vessel that was saturated with hexane vapor before spin coating. PIM-1 thin films were coated onto these crosslinked Matrimid® support membranes via spin coating. A 0.5 wt% PIM-1 in chloroform solution at 4 °C was dropped onto the crosslinked Matrimid® support membranes and spun at 500 rpm for 1 min and then ramped to 1000 rpm for 10 min. During the spin coating process, the membrane processing chamber was saturated with chloroform vapor to slow the drying process. After spin coating, the resulting PIM-1 thin film composite membranes were dried under vacuum at 100 °C for 24 hours.

A.2.5 Vapor Phase Infiltration

Vapor phase infiltration was conducted in a automized hot-wall reactor (Figure A.2a). [29] Prior to VPI, PIM-1 membranes except the thin film composites were soaked in methanol for 2 hours to reset the PIM-1 micropore structure, and dried under vacuum for 30 minutes.[30] The membrane sample is then transferred into the reactor. The reactor was then heated to 90 ˚C and purged with nitrogen to remove solvent residues. After the purging procedure, the chamber was evacuated to vacuum (~60 mTorr). Trimethylaluminum (Strem Chemicals, 98%, DANGER: Pyrophoric) vapor was dosed into the reactor for 1 second. The PIM-1 membrane adsorbs TMA for the gas phase for various times. After the TMA adsorption, the reactor was purged with nitrogen for 5 minutes and evacuated to baseline for 5 minute. Room temperature water vapor was then dosed into the reactor for 5 seconds, which increases the reactor pressure to roughly 1.5 Torr. The PIM-1 membrane then adsorb water for a period equivalent to TMA exposure. After that, the reactor was purged and evacuated again before the remaining VPI cycles.

A.2.6 Fourier-Transform Infrared Spectroscopy

Fourier-transform infrared spectroscopy (FTIR) was used to characterize changes in the vibrational spectrum of PIM-1's functional groups after VPI. 10-μm flat PIM-1 films were thoroughly infiltrated with AlO_x (90 °C, two cycles of VPI, 5-hour exposures) and characterized with a Thermo Scientific iS50 FT-IR Spectrometer (Thermo Fisher Scientific) using transmission mode.

A.2.7 X-ray Photoelectron Spectroscopy

X-ray Photoelectron Spectroscopy (XPS) was used to determine the existence and chemical bonding states of hybrid materials. PIM-1 hollow fiber membranes thoroughly infiltrated with AlO_x (90 °C, two cycles of VPI, 5-hour exposure time) were ground into fine powders and analyzed with a Thermo K-Alpha XPS (Thermo Fisher Scientific). Since metal oxide/PIM-1 hybrids are nonconductive, electrons aggregated on the sample surface resulting in significant peak shifts. Peak position was calibrated via an internal standard method. For each hybrid material, two pools of sample powders were prepared, one of which was mixed with silver nanoparticles. C1s peak position was firstly calibrated according to the Ag3d peaks detected in the sample mixed with silver nanoparticles. The other peaks in the sample without additives were then calibrated according to the C1s peak shifts. Metal oxides were also coated onto silicon wafers via atomic layer deposition and analyzed by XPS. O1s peak positions of these metal oxides were used as a comparison.

A.2.8 Solid-State NMR

Solid-state NMR was used to identify chemical states of carbon, hydrogen, and aluminum atoms in the hybrid materials. PIM-1 hollow fiber membranes thoroughly infiltrated with AlO_x (90˚C, two cycles of VPI, 5-hour exposure time) were ground into fine powders and packed into the zirconium NMR rotor. Solid-state NMR was then carried out via Bruker Avance III 400.

A.2.9 X-ray Powder Diffraction

X-ray powder diffraction was used to analyze the crystallinity of the intertwined networks of metal oxide and PIM-1. PIM-1 hollow fiber membranes thoroughly infil-trated with AlO_x (90˚C, two cycles of VPI, 5-hour exposure time) were ground into fine powders and then analyzed by Panalytical XPert PRO Alpha-1 XRD (Malvern Panalytical).

A.2.10 Transmission Electron Microscopy

Transmission Electron Microscopy (TEM) was used to determine the homogeneity of the hybrid material. TEM grids with carbon lace were dip-coated in a 0.5 weight percent PIM-1 chloroform solution and dried in a glove bag filled with nitrogen. After 24-hour slow evaporation, the PIM-1 coated grids were further dried in vacuum at 100 °C for 24 hours. The PIM-1 coated grids were then thoroughly infiltrated with AlO_x (90 °C, two cycles of VPI, 5-hour exposure time). The microstructure of the hybrid membranes on these grids was then analyzed with a Hitachi HT7700 TEM.

A.2.11 Scanning Electron Microscopy and Energy-dispersive X-ray Spectroscopy

Cross section images of the membranes were obtained with a Hitachi 8230 FE-SEM. Membranes were soaked in n-hexane for 10 minutes and fractured in liquid nitrogen to get clean cross sections. Crystallized hexane prevents the collapse of macropores during fracturing, and the low surface tension of hexane avoids the collapse of macropores and mesopores during evaporation. Fractured membranes were also sputtered with gold to reduce electron charging. Energy-dispersive X-ray (EDX) spectroscopy was used to obtain the element mapping of the membranes.

A.2.12 Thermogravimetric Analysis

Weight loading of metal oxides in PIM-1 membranes was determined by thermogravimetric analysis (TGA Q500, TA Instruments). Hollow fiber membranes were placed in platinum sample pans and heated in flowing air. During each thermogravimetric analysis run, the temperature was first maintained at 110 °C for 1 hour to get rid of solvent residues. After this in situ drying process, the temperature was ramped to 900 °C at 10 °C /min. The remaining mass was assumed to be the inorganic loading fraction and the weight percent was calculated as the mass remaining after burnout over the mass of the fiber following the drying step. PIM-1 hollow fiber membranes treated with methanol and infiltrated with AlO_x (2-cycle VPI at 90 °C with 5-hour exposure time) were transformed into porous alumina hollow fibers as by-products of thermogravimetric analysis.

A.2.13 Nitrogen Physisorption

Nitrogen physisorption was conducted at 77 K using a BELSORP-max (MicrotracBEL). PIM-1 hollow fiber membranes infiltrated with aluminum oxide were ground into fine powders and then dried under vacuum at 110 °C for 12 hours. BET surface areas were calculated from the low-pressure region ($p/p^{sat} < 0.3$) of the cryogenic nitrogen physisorption isotherm. Pore size distribution was calculated via a N_2 DFT model.

A.2.14 Mercury Porosimetry

Mercury porosimetry was conducted by an AutoPore IV (Micromeritics) porosimeter. Prior to the measurement, PIM-1 hollow fiber membranes were cleaned with n-hexane and then dried under vacuum at 110 °C for 12 hours.

A.2.15 Toluene and Water Uptake

Toluene and water isotherms were measured using a Dynamic Vapor Sorption system (DVS Vacuum, Surface Measurement Systems). PIM-1 hollow fiber membranes with and without VPI treatment were placed and in situ dried at 110 ºC in the sample chamber of the DVS. The samples were then exposed to toluene or water vapors of a prescribed pressure at 25 ºC. Equilibrium criteria was set to less than 0.001 weight percent change within 10 minutes. Each isotherm was determined at least 3 times to calculate a standard deviation.

A.2.16 Organic Solvent Nanofiltration (OSN) and Organic Solvent Reverse Osmosis (OSRO)

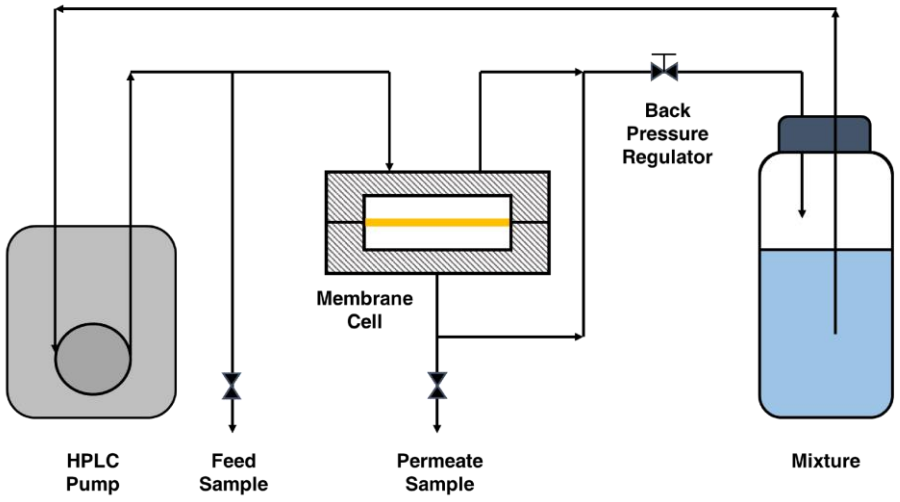

Figure A.1 Organic solvent separation system setup.

OSN and OSRO experiments were con-ducted in a customized cross-flow permeation system (Figure A.1). During the OSN experiments, styrene dimer, polystyrene oligomers, 1,3,5-triisopropylbenzene, and 1,3-diisopropylbenzene were used as marker

solutes to measure the molecular weight cut-off of the membranes in ethanol, n-heptane, tetrahydrofuran, and toluene. During the OSRO experiments, alcohol mixtures (methanol, ethanol, and propanol) and aromatic mixtures (toluene, 1,3-diisopropylbenzene, and 1,3,5-triisopropylbenzene) were used to quantify the molecule differentiation capability of the membranes. Feed solutions were pressurized and delivered by an Azura P 4.1S pump (KNAUER). Feed flowrate was set to at least ten times that of the permeation rate. Trans-membrane pressure was maintained at 10 bar for thin film composite membranes and 10 psi for hollow fiber membranes (pristine PIM-1 hollow fiber membranes cannot with-stand higher pressures than this when exposed to ethanol). Permeates were collected in glass sample vials. The Thermo Evolution 220 UV-vis system (Thermo Fisher Scientific) was used to determine the dye rejection, an Agilent 1260 High Performance Liquid Chromatography (HPLC) was used to determine the change of marker solute concentration after OSN experiments, and an Agilent Gas 7890 Chromatography (GC) was used to determine the change of organic solvent composition after OSRO.

A.3 Results and Discussion

A.3.1 Microstructure of the Metal Oxide / PIM-1 Hybrid Membranes

Vapor phase infiltration of PIM-1 hollow fiber membranes with several different metal-organic precursors results in amorphous metal oxide homogeneously distributed throughout the polymer bulk. Figure A.2a illustrates how the VPI process creates metal oxide / PIM-1 hybrid membranes. Pristine PIM-1 membranes (e.g., thin film composites, hollow fiber membranes, or free-standing membranes) are fabricated and then placed in a customized isothermal reaction chamber maintained at 90 °C (Figure A.2a). After

evacuation to rough vacuum (60 mTorr), the membranes are sequentially exposed to trimethylaluminum (TMA) and water vapor. During metal-organic precursor exposure, precursor molecules sorb and diffuse into the PIM-1 membranes (Figure A.2b). After a purge-pump cycle to remove byproducts, the membrane saturated with metal-organic precursors is exposed to water vapor. The metal-organic and water react within the membrane creating an intertwined metal oxide network (Figure A.2b-f).

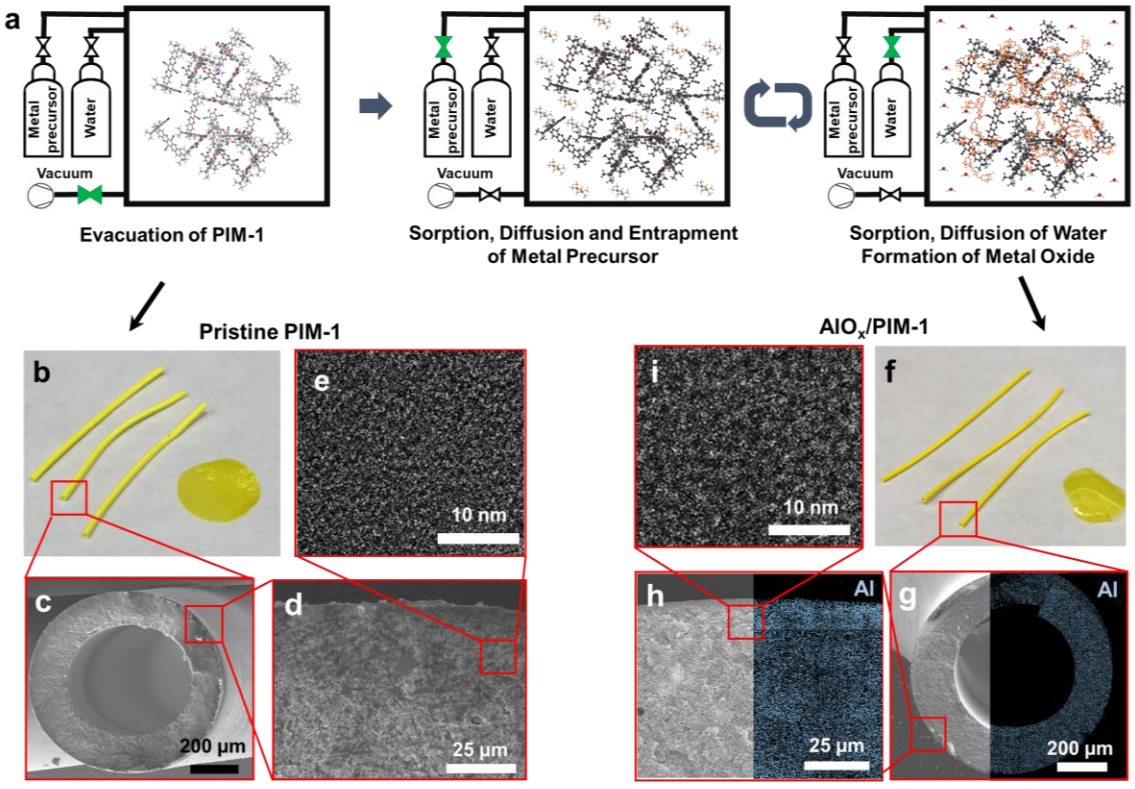

Figure A.2 Schematic of vapor phase infiltration (VPI) and morphology characterization of pristine and hybrid PIM-1 membranes. (a) Schematic depiction of VPI process: precursor sorption, diffusion, and entrapment. (b) Photographs, (c, d) SEM images, and (e) TEM images of pristine PIM-1 membranes. (i) Photographs, (h, g) SEM/EDX images, and (f) TEM images PIM-1 after infiltration with trimethylaluminum and water (2 cycles). Blue pixels in EDX map show aluminum distribution throughout the hybrid membrane.

Different from atomic layer deposition that deposit inorganic layer on the external surface of the material, vapor phase infiltration is designed to decorate the micropores of the material. In order to achieve through infiltration into the membrane, the precursor dosing time, precursor exposure time, and infiltration cycle number must be optimized. Since it is challenging to fully infiltrate dense thick PIM-1 membranes in reasonable timeframes, membranes with a thin PIM-1 selective layer (thin film composite membrane and hollow fiber membranes) are used in the following experiments to ensure thorough infiltration of the metal oxide. As shown in Figure A.3a, longer precursor exposure time and higher VPI cycle numbers increase AlOx loading and decrease BET surface areas.

After thorough infiltration of AlO_x, the microporosity of PIM-1 is preserved and the material is rigidified. Figure A.3b exhibits the 77-K nitrogen physisorption isotherms for PIM-1, AlO_x/PIM-1, and AlO_x/PIM-1 with methanol treatment prior to VPI. Pristine PIM-1 exhibits classical dual-mode isotherm. The Langmuir-type rapid increase of the isotherm in the low pressure region ($p/p^{sat} < 0.1$) is contributed by the micropores. The following linear increase in the high pressure region is contributed by the polymer chain swelling induced by nitrogen. The infiltrated metal oxide networks inhibit the swelling without significant sacrificing the microporosity.

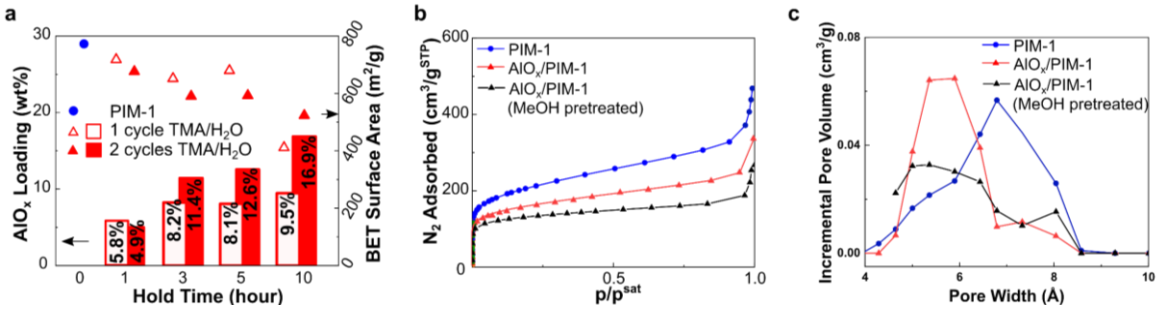

Figure A.3 Influence of VPI chemistry and processing conditions on inorganic loading fraction, microporosity, and chemical stability of hybrid membranes. (a) AlO_x loading (bar graphs) and BET surface area (dot plots, errors are smaller than markers) of AlO_x/PIM-1 hybrid membranes as a function infiltration time and number of infiltration cycles. (b) Nitrogen isotherms at 77 K for pristine and infiltrated PIM-1 membranes (2 cycles of VPI with 5-hour exposure time). (c) Pore size distribution of PIM-1, AlO_x/PIM-1, and AlO_x/PIM-1 with methanol pretreatment.

With the help of DFT model, pore size distribution of the corresponding samples is calculated from the nitrogen physisorption isotherms. As shown in Figure A.3c, the width of the micropores of PIM-1 is distributed around 7 Å. After AlO_x infiltration, the width shrinks to 6 Å. The shrinkage of pore width is contributed by the occupation of micropore by AlO_x.

The infiltrated AlO_x constituent is expected to be interconnected. AlO_x/PIM-1 hollow fibers are annealed in air at 900 °C. An alumina membrane was obtained after the burning of PIM-1 networks. As shown in Figure A.4a, the alumina membrane retains the structural integrity. Nitrogen physisorption reveals that the alumina hollow fibers possess micropores (Figure A.4b). The significant pore shrinkage shown in Figure A.4c can be contributed to the strong interaction between adjacent AlO_x, which collapsed or closed the pores in the absence of PIM-1 skeleton. The intact alumina hollow fiber membrane indicates the thorough infiltration of metal oxide into PIM-1 hollow fiber membranes. The

porosity exhibited by the alumina hollow fiber membrane is consistent with our hypothesis that metal oxide nanostrands reside in the micropores of PIM-1, which is a porous template. The reduced porosity is likely due to sintering of the structure during heating.

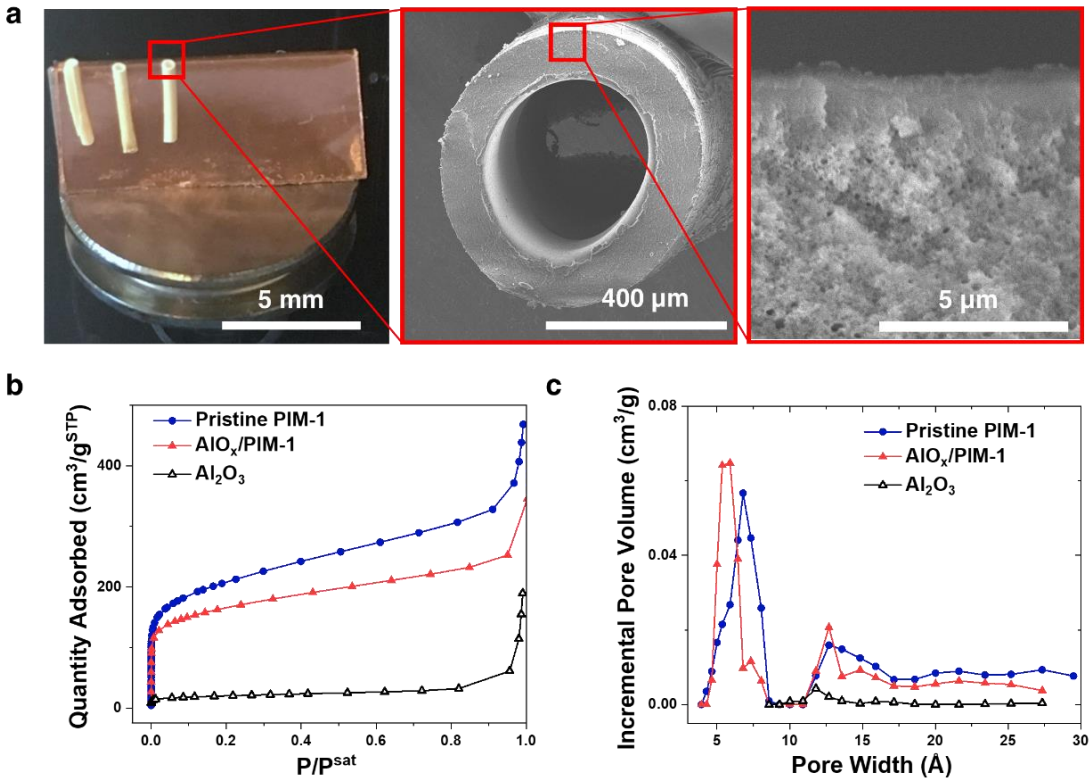

Figure A.4 Alumina hollow fiber membrane obtained by annealing AlO_x/PIM-1 hybrid hollow fiber membranes in air (900 °C). Heat treating in air combusts the polymer and leaves just an AlO_x nanoporous structure. (a) Photographs and SEM images of the alumina hollow fiber membrane after burn out; (b) cryogenic nitrogen physisorption of these alumina hollow fiber membranes compared with that of pristine PIM-1 hollow fiber membranes and AlO_x/PIM-1 hollow fiber membranes; (c) pore size distribution of alumina hollow fiber membranes compared that of pristine PIM-1 hollow fiber membranes and AlO_x/PIM-1 hollow fiber membranes.

Figure A.2b-f presents photographic and electron microscopy analysis of the microstructure and chemical composition of pristine PIM-1 membranes and PIM-1 membranes infiltrated with aluminum oxide networks (AlO_x/PIM-1). The infiltrated, hybrid membranes show negligible change in macrostructure: the characteristic

hierarchically porous support layer and the dense selective layer are preserved. At the nanoscale, the infiltrated metal oxide is homogeneously dispersed throughout the entire membrane (SEM/EDX). Owing to the confinement of the micropores of PIM-1, there is no formation of metal oxide crystals. As shown in Figure A.2e and i, TEM can not spot any metal oxide crystals formed in AlO_x/PIM-1 membranes. XRD can not detect metal oxide crystallinity either (Figure A.5). Characteristic XRD peaks of PIM-1 at 13°, 18°, and 23° indicate the interlayer spacing of 6.8 Å, 4.92 Å, and 3.85 Å. These peaks were also observed at the identical position in AlO_x/PIM-1, which suggests that the infiltrated metal oxides do not interrupt the nanoporous structures of PIM-1. None of the characteristic peaks corresponding to the crystal structures of metal oxides were found. These results reveal that PIM-1 membranes accommodate homogeneous inorganic loading fractions up to 30 wt% without significant changes in microstructure.

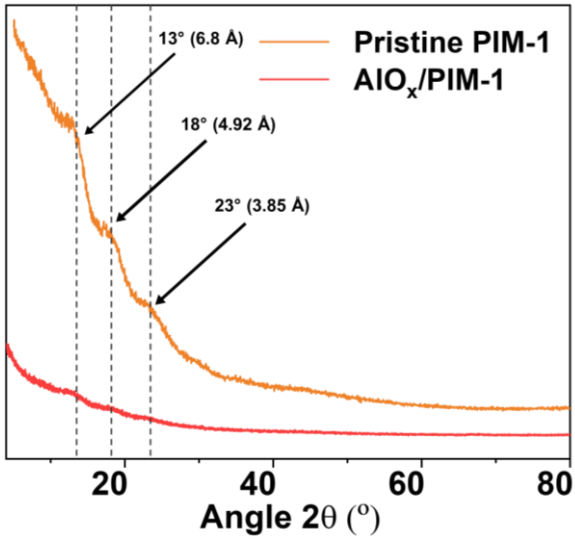

Figure A.5 XRD patterns of pristine PIM-1 and AlO_x/PIM-1.

Chemical characterization has revealed that the infused AlO_x constituent does not change the PIM-1 backbone. The infiltration exerts negligible change to the polymer chemistry, which suggests physically intertwined polymer chains and metal oxide networks. Ex-situ XPS and FTIR (Figure A.6) indicates that the PIM-1 backbone remains unchanged after infiltration with AlO_x. XPS results (Figure A.6a) show negligible change in the binding energy of PIM-1's nitrogen and oxygen. After deconvolution, the O^{1s} spectrum of AlO_x/PIM-1 contains a peak associated with the aluminum oxide (530.9 eV) and a peak of the PIM-1 backbone (533.4 eV). Similarly, FTIR (Figure A.6b) detects no shifts of the peaks for the polymer's functional group.

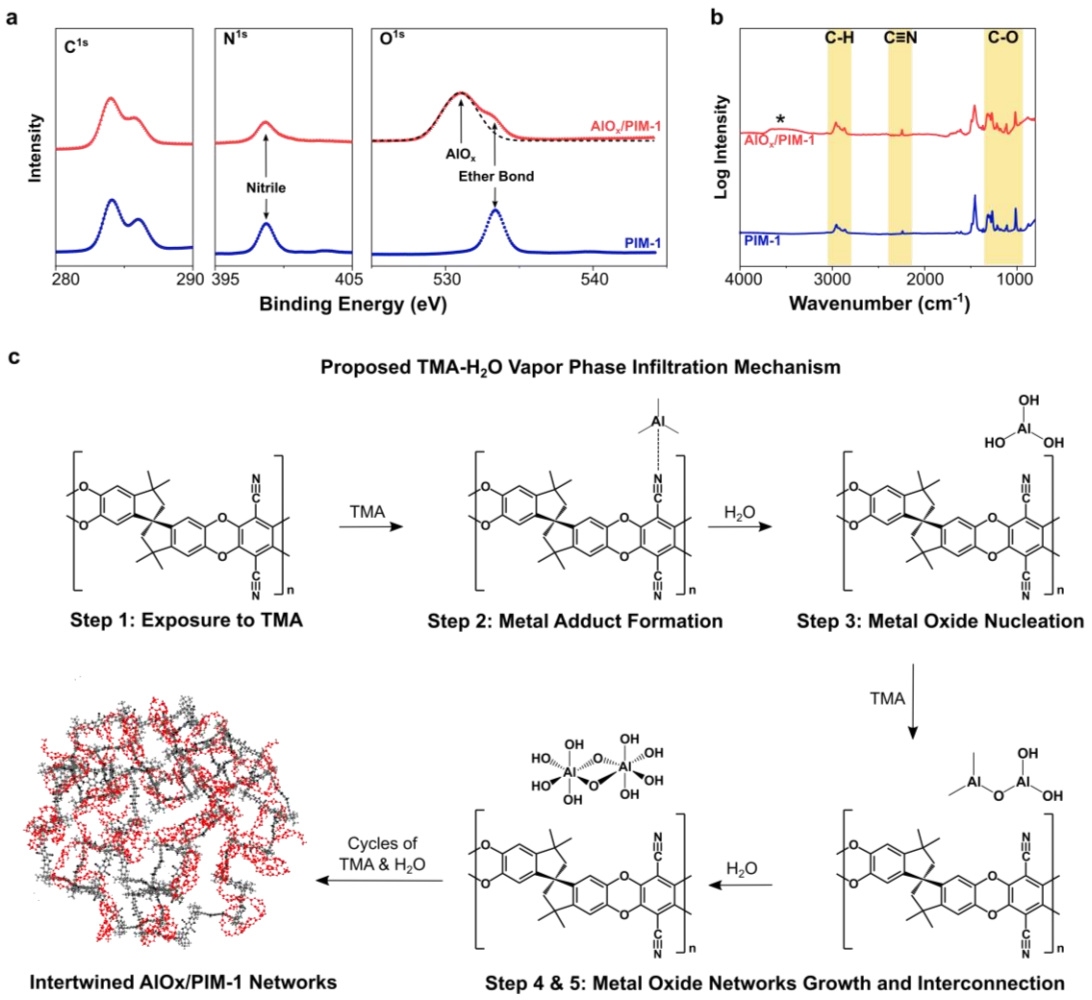

Figure A.6 Chemical Characterization of pristine PIM-1 and metal oxide / PIM-1 hybrids. (a) C^{1s}, N^{1s}, and O^{1s} XPS spectra and (b) logarithmic FTIR spectra for pristine PIM-1 and PIM-1 infiltrated with AlO_x. (c) Proposed mechanism for metal oxide network formation via TMA VPI of PIM-1. The figures of the metal oxide network are provided only for illustration.

Based on the chemical and structural information, we hypothesize that during VPI, metal-organic precursors form semi-permanent adducts with PIM-1's nitrile groups, similar to the interaction previously observed between TMA and amine or nitro functional groups in other VPI related processes.[31] Upon water exposure, these metal-organic precursors are oxidized, the ad-ducts release, and the newly formed metal oxide clusters becomes unbound from the polymer (Figure A.6c). Further condensation reactions and

repeated VPI cycling can interconnect these metal oxide clusters into an inorganic network. Regardless of purge time between the TMA and H_2O dosing, AlO_x/PIM-1 hybrids are found to have nearly equivalent inorganic mass loadings, supporting the formation of these semi-permanent precursor-polymer adducts.

Owing to the infiltrated AlO_x network, the AlO_x/PIM-1 membrane exhibits significantly improved solvent stability. The AlO_x/PIM-1 membranes are challenged with good solvents for PIM-1 (tetrahydrofuran [THF], dichloromethane [DCM], and chloroform [$CHCl_3$]). After 3 months of immersion, the weight loss of the AlO_x/PIM-1 membrane is lower than 10 wt%. By contrast, pristine PIM-1 membranes completely dissolve within minutes. The hybrid membranes exhibit negligible swelling in toluene vapors. As shown in Figure A.7a, the toluene isotherms can be well fitted by dual-mode sorption equations, which is a combination of Langmuir-type adsorption and Henry-type sorption. By comparing the change in the contribution of Henry-type sorption, we found that the toluene-induced swelling in AlO_x/PIM-1 has been reduced by 39%. This trends reveal that the interpenetrating metal oxide networks protect PIM-1 membranes from swelling while preserving their vital membrane characteristics. The hybrid membranes also exhibit more Langmuir-type N_2 isotherms with increasing metal oxide loading (Figure A.3b).

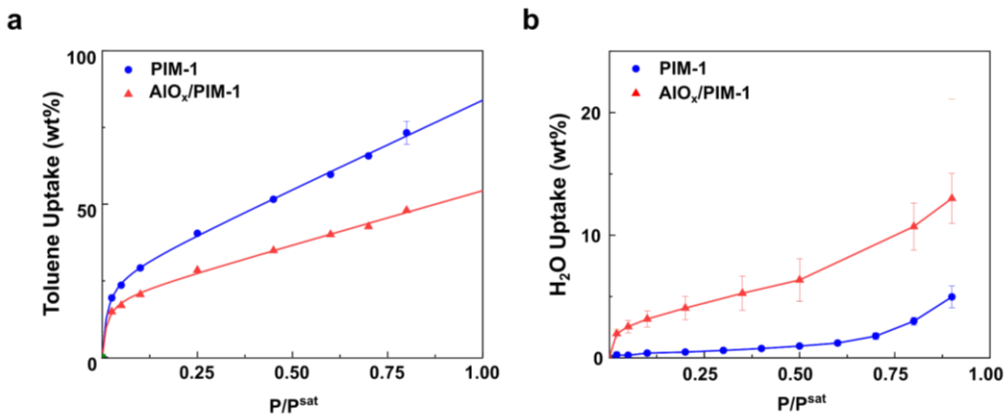

Figure A.7 Influence of interpenetrating metal oxide networks on the interaction between guest molecules (toluene and water) and PIM-1 membranes. (a) Toluene swelling reduction. A reduction in swelling is observed in the toluene adsorption isotherms measured at 25 °C. (b) H_2O sorption isotherms measured at 25 °C.

Figure A.7b compares the water adsorption isotherms for PIM-1 and AlO_x/PIM-1. While pristine PIM-1 is hydrophobic, the metal-oxide-infiltrated PIM-1 hollow fiber membranes show significantly higher water uptake. This increase in water molecule affinity results from additional adsorption sites provided by the interpenetrating metal oxide networks. The hybrid membranes also show a change in hydrophilicity as proven by water sorption experiments that could open new pathways for aqueous separations.

A.3.3 AlO_x/PIM-1 membranes for organic solvent separation

To evaluate the organic solvent nanofiltration (OSN) and organic solvent reverse osmosis (OSRO) performance of these hybrid membranes, AlO_x/PIM-1 thin film composite membranes were tested in a continuous cross-flow filtration system (Figure A.1) with ethanol, n-heptane, toluene, and tetrahydrofuran as solvents. PIM-1 thin film composites were fabricated on crosslinked Matrimid® 5218 supports via spin coating and then underwent two VPI cycles of TMA-H_2O with 10 minute precursor exposure times at 90˚C.

Figure A.8a plots the polystyrene oligomer retention of these membranes as a function of molecular weight in ethanol, n-heptane, toluene, and tetrahydrofuran. This plot illustrates the size-based molecular separation performance of the membranes in different solvent environments. For the thin, pristine PIM-1 membranes, the 90% molecular weight cut-off (MWCO; the smallest molecular weight the membrane "successfully" rejects) is about 600 g/mol in n-heptane and toluene, solvents that do not significantly swell or plasticize PIM-1. However, in ethanol, a solvent that is known to plasticize and significantly swell PIM-1, the pristine polymer membranes fail to reject polystyrene oligomers less than 1200 g/mol. In tetrahydrofuran, the PIM-1 selective layer dissolves completely, and no separation is possible. This loss of size-based separation performance in plasticizing solvents and dissolution in good solvents is consistent with prior separation experiments on pure, polymeric PIM-1 membranes reported in the literature.[14]

In contrast, hybrid AlO_x/PIM-1 membranes show consistent (more than 95%) polystyrene dimer rejection in all four solvents (ethanol, n-heptane, toluene, and tetrahydrofuran). Using 1,3,5-triisopropylbenzene and 1,3-diisopropylbenzene as marker "solutes", the MWCO of the AlO_x/PIM-1 membrane was determined to be 204 g/mol, which is 400 g/mol lower than the MWCO of the control PIM-1 membrane, and 100-200 g/mol lower than the MWCO for PIM-1 chemically crosslinked with poly(ethyleneimine).[12]

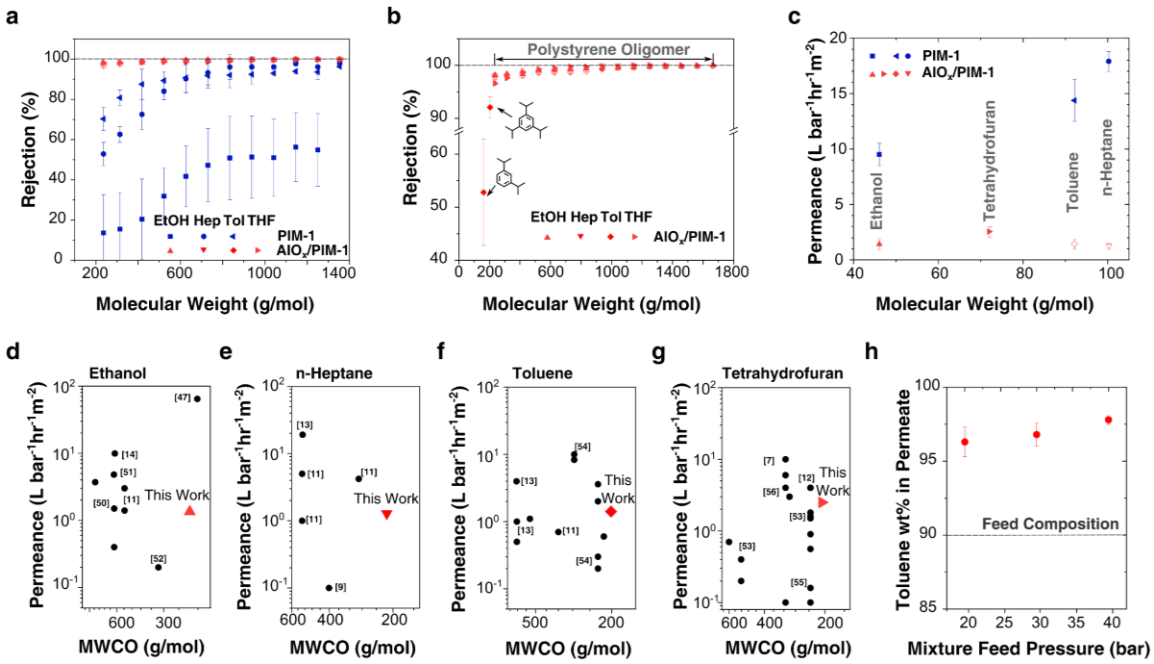

Figure A.8 Organic solvent nanofiltration (OSN) and organic solvent reverse osmosis (OSRO) performance of PIM-1 and AlO_x/PIM-1 hybrid thin film composite membranes (2 cycles of TMA and H_2O infiltration, with 10-minute precursor exposures). (a) Molecular weight cut-off curves of PIM-1 and AlO_x/PIM-1 thin film composites in different solvents using polystyrene oligomers as markers. (b) Detailed molecular weight cut-off curves of AlO_x/PIM-1 thin film composites using polystyrene oligomers, 1,3,5-triisopropylbenzene, and 1,3-diisopropylbenzene as markers. (c) Steady-state organic solvent permeance of PIM-1 and AlO_x/PIM-1 thin composite films under 30-bar transmembrane pressure. OSN performance comparison with literature in (d) ethanol,[12,15,32-35] (e) n-heptane,[13,14,33,36-38] (f) toluene,[13,14,35-38] and (g) tetrahydrofuran.[13,14,36-38] (h) Organic solvent reverse osmosis separation of toluene (90 wt%) from 1,3,5-triisopropylbenzene (5 wt%), and 1,3-diisopropylbenzene (5 wt%).

The different rejection rates of these marker solutes exemplify the size-based molecular sieving capabilities of the AlO_x/PIM-1 hybrid membrane (Figure A.9). Diisopropylbenzene, with a critical diameter (5.5 Å) smaller than that of the AlO_x/PIM-1 hybrid's micropores (~ 6 Å, probed by nitrogen), permeates with less restriction (rejection = 52.8%) than triisopropylbenzene and styrene dimers that have critical diameters (6.7 Å) larger than the hybrid's micropores, which are mostly rejected (rejection > 90%) by these membranes. This reduction in MWCO is expected based on the infiltrated AlO_x slightly

reducing the membrane's micropore size (Figure A.3). This smaller microporosity and narrower pore size distribution serves to improve the selectivity of these hybrid membranes in separations where precise molecular sieving between molecules with small size differentials is needed.

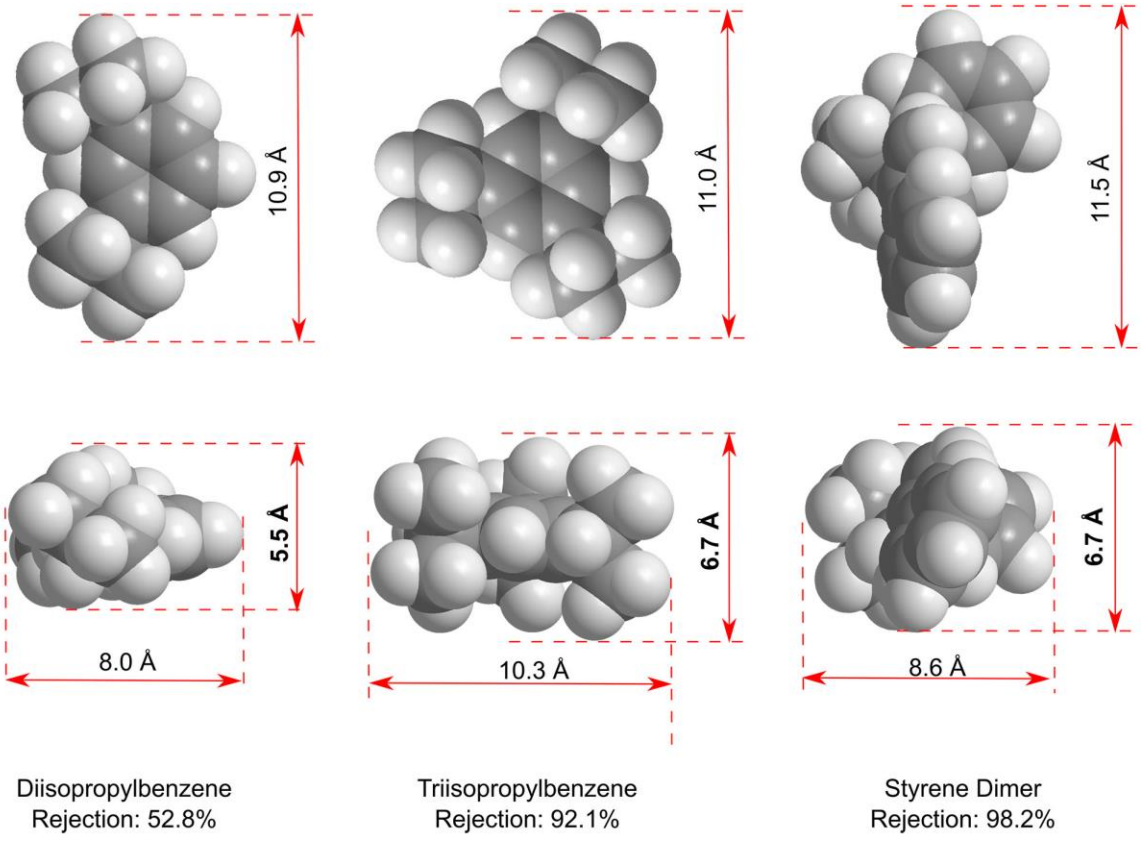

Figure A.9 Size-based molecular sieving effects of the AlOx/PIM-1 hybrid membrane.

While the infiltration of AlO_x decreases the membrane permeance by roughly one order of magnitude (Figure A.8c), the AlO_x/PIM-1 thin composite membranes still deliver comparable permeance to state-of-the-art OSN mem-branes that exhibit MWCOs lower than 500 Da. Emerging membrane separation challenges require membranes with high selectivity, provided an adequate permeance can be met.1, 4, 48 As shown in Figure A.8d-g, compared with other highly permeable membranes that could be fabricated at large scale,

the AlO_x/PIM-1 thin composite membrane pro-vides unprecedented selectivity, which is indicated by the low MWCO (< 204 Da). Moreover, this hybrid membrane is robust. After 1 week of OSN operation in each solvent, AlO_x/PIM-1 membranes did not exhibit any significant loss in inorganic loading (Figure A.10).

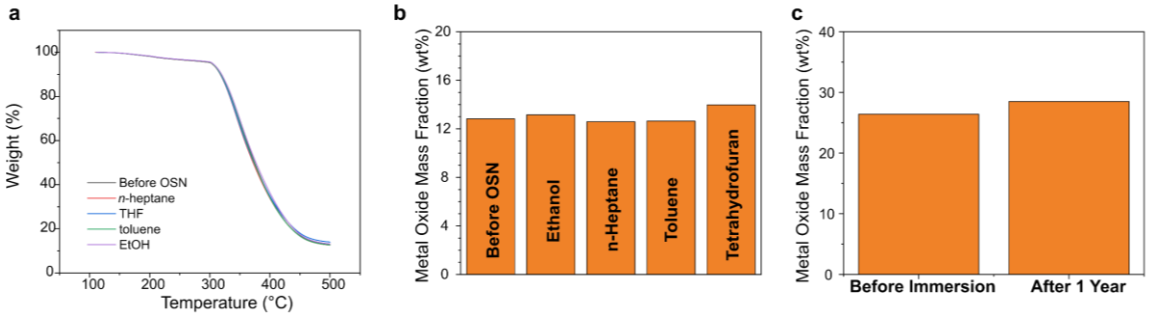

Figure A.10 The infiltrated metal oxide networks retain the majority of their inorganic component during the organic solvent separation processes. (a) Thermogravimetric analysis curves of free-standing AlO_x/PIM-1 hollow fiber membranes with different operation histories (before use in organic solvent nanonfiltration and after 1 week of continuous OSN in n-heptane, tetrahydrofuran, toluene, or ethanol). (b) The weight percent loading of the inorganic component of AlO_x/PIM-1 freestanding hollow fiber membranes after 1-week of continuous organic solvent separation in n-hexane, ethanol, toluene, and tetrahydrofuran. (c) The change in weight percent loading of the inorganic component in AlO_x/PIM-1 freestanding hollow fiber membranes after 1-year of immersion in tetrahydrofuran.

Also contributing to the improved performance of AlO_x/PIM-1 hybrid membranes for organic solvent separation is the modification of the hybrid membrane's mechanical properties (Figure A.11a). The hybrid, free-standing hollow fiber membranes are found to be stiffer than the pristine polymer as indicated by a greater Young's modulus. The hybrid membranes also show a modest decrease in their strength at the break as well as in their elongation at break. These results are expected as the inclusion of a ceramic material should result in more brittle behavior relative to the pristine polymer. However, in dead-end OSN testing, the free-standing AlO_x/PIM-1 hollow fiber membranes withstand 1.6 times the

pressure of pristine PIM-1 hollow fiber membranes in an equimolar mixture of THF and ethanol and twice the pressure in pure ethanol (Figure A.11b, c). Therefore, while some mechanical properties are reduced relative to the pristine polymer, those that are most pertinent to separation performance show a marked improvement.

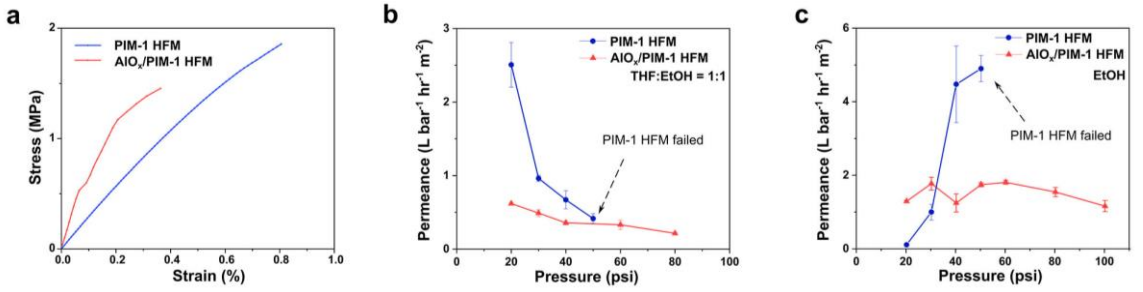

Figure A.11 Mechanical stability of free-standing PIM-1 hollow fiber membranes and AlO_x/PIM-1 (2 cycles of infiltration of TMA and H_2O with 5-hour exposure times) hollow fiber membranes. (a) Stress-strain curves of the dry hollow fiber membranes. The AlO_x/PIM-1 exhibit a higher modulus of elasticity but smaller strength at break and strain at break, which indicates that the AlO_x/PIM-1 are stiffer and more brittle than pristine PIM-1 hollow fiber membranes. (b) Mechanical stability of pristine and hybrid hollow fiber membranes in the equal molar mixture of tetrahydrofuran and ethanol. Pristine PIM-1 hollow fiber membranes exhibit high permeance due to swelling and rupture at 3.45 bar while AlO_x/PIM-1 hollow fiber membranes exhibit stable permeance until delaminated from the swollen epoxy sealing at 5.52 bar (c) Mechanical stability in ethanol. Pristine PIM-1 hollow fiber membranes exhibit high permeance due to swelling and rupture at 3.45 bar while AlO_x/PIM-1 hollow fiber membranes exhibit stable permeance until delaminated from the swollen epoxy sealing at 6.89 bar.

When performing OSN on dye molecules (Rose Bengal) in ethanol, AlO_x/PIM-1 hybrid hollow fiber membranes reject twice as much dye as pristine PIM-1 membranes (86% versus 43%, Figure A.12). This result suggests that the intertwined AlO_x networks within these hybrid membranes interrupt the strong interaction between these dye molecules and the membrane, reducing dye permeation through the membrane. VPI modification provides sufficient stabilization and resistance to swelling to enable the

rejection of strongly sorptive solutes (such as Rose Bengal), which are typically challenging for polymer-based membranes to remove.

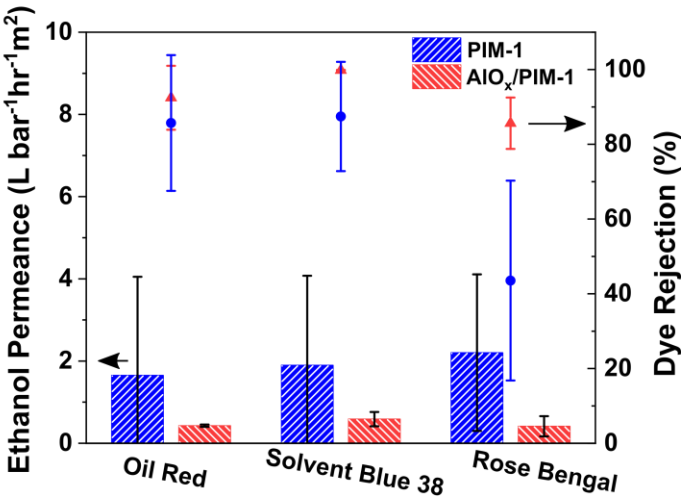

Figure A.12 Organic solvent nanofiltration of dye solutions.

Besides organic solvent nanofiltration, which separates solutes from solvents, AlO_x/PIM-1 membranes are also capable of organic solvent reverse osmosis (OSRO), which separates solvents from other solvents without a phase change. A successful OSRO membrane must have relatively rigid, narrow micropores so that guest molecules exhibit distinctly different diffusivities.[39] Owing to guest-induced plasticization and swelling, common polymeric membranes usually cannot fulfill this requirement and therefore cannot differentiate between organic solvent molecules. Contrary to traditional polymeric membranes, AlO_x/PIM-1 membranes possess micropores with high resistance to plasticization and swelling. As a result, AlO_x/PIM-1 hybrid membranes can be used for OSRO operations. This capability was explored using a cross-flow system loaded with AlOx/PIM-1 thin film composite mem-branes, which were used to separate a mixture of 90 wt% toluene, 5 wt% 1,3,5-triisopropylbenzene, and 5 wt % 1,3-diisopropylbenzene.

During OSRO, the transmembrane pressure must overcome osmotic pressure. The feed mixture consists of 90 wt% toluene, 5 wt% triisopropylbenzene, and 5 wt% diisopropylbenzene. Toluene is treated as the main component (denoted as component 1) and the other components are treated as the dilute components (denoted as component 2, collectively). We assume the activity coefficient of toluene to be one. In the case where the permeate is 97% toluene (the experimental data at 40 bar transmembrane pressure), osmotic pressure can be calculated as following.

$$\boldsymbol{\pi = -\frac{RT}{\widehat{V}_1}\left(\frac{\gamma_{1,permeate}x_{1,permeate}}{\gamma_{1,retentate}x_{1,retentate}}\right) = 16.1\ bar} \qquad \text{(A.1)}$$

By applying a transmembrane pressure of 40 bar (TMP; the hydraulic pressure difference across the membrane) beyond the osmotic pressure to the liquid mixture, toluene concentration is enriched from 90.0 wt% to 97.8 ± 0.3 wt% (Figure A.8d). Moreover, AlO_x/PIM-1 thin film composite membranes can be used to enrich the methanol concentration in methanol/ethanol mixtures from 99.0 wt% to 99.8 ± 0.3 wt% (TMP = 30 bar, permeance = 8.1 ± 0.5 $Lm^{-2}h^{-1}bar^{-1}$), and enrich the methanol concentration in the methanol/2-propanol mixtures from 90 weight percent to 95.4 ± 0.5 weight percent (TMP = 30 bar, permeance = 7.8± 0.3 $Lm^{-2}h^{-1}bar^{-1}$). The successful separation of these alcohol mixtures proves the capability of AlO_x/PIM-1 membranes to differentiate molecules with small molecular weight differences (~ 14 Da). These preliminary results reveal the potential of AlO_x/PIM-1 membranes in organic solvent separation and distillation debottlenecking via OSRO with minimal added energy.

A.4 Conclusion

In summary, vapor phase infiltration can be used to create unbound but intertwined atomic-scale metal oxide networks within nanoporous polymer membranes like PIM-1. Unlike pristine polymer membranes, these organic-inorganic hybrid membranes strongly resist swelling and dissolution in aggressive solvent environments. With this added chemical stability, hybrid PIM-1 membranes not only outperform untreated PIM-1 membranes for chemical separations in standard environments but also provide consistent performance in environments that would otherwise swell or even completely dissolve the pristine polymer. These membranes can even be applied for organic solvent reverse osmosis, which is difficult to realize using pristine PIM-1.

The unique, intertwined metal oxide / polymer structure proposed here, while likely generalizable, will certainly vary with polymer and precursor chemistry and VPI processing conditions. Therefore, further exploration into the physio-chemical structure and the processing conditions required to synthesize it is necessary. Ultimately, though, this work establishes a new, scalable, solvent-free, post-synthesis treatment for transforming nanoporous polymers into novel hybrid membranes with increased stability that have the potential to supplant energy intensive distillation processes for organic solvent separations.

A.5 References

1. E. K. McGuinness, F. Zhang, Y. Ma, R. P. Lively, M. D. Losego. Vapor Phase Infiltration of Metal Oxides into Nanoporous Polymers for Organic Solvent Separation Membranes. *Chemistry of Materials* **2019**;31(15):5509-5518.

2. D. S. Sholl, R. P. Lively. Seven chemical separations: to change the world: purifying mixtures without using heat would lower global energy use, emissions

and pollution--and open up new routes to resources. *Nature* **2016**;532(7600):435-438.

3. W. J. Koros, R. P. Lively. Water and beyond: Expanding the spectrum of large‐scale energy efficient separation processes. *AIChE Journal* **2012**;58(9):2624-2633.

4. D.-Y. Koh, B. A. McCool, H. W. Deckman, R. P. Lively. Reverse osmosis molecular differentiation of organic liquids using carbon molecular sieve membranes. *Science* **2016**;353(6301):804-807.

5. P. Marchetti, M. F. Jimenez Solomon, G. Szekely, A. G. Livingston. Molecular separation with organic solvent nanofiltration: a critical review. *Chemical Reviews* **2014**;114(21):10735-10806.

6. Z. Lai, G. Bonilla, I. Diaz, J. G. Nery, K. Sujaoti, M. A. Amat, E. Kokkoli, O. Terasaki, R. W. Thompson, M. Tsapatsis. Microstructural optimization of a zeolite membrane for organic vapor separation. *Science* **2003**;300(5618):456-460.

7. D. Kim, M. Y. Jeon, B. L. Stottrup, M. Tsapatsis. para‐Xylene Ultra‐selective Zeolite MFI Membranes Fabricated from Nanosheet Monolayers at the Air–Water Interface. *Angewandte Chemie International Edition* **2018**;57(2):480-485.

8. S. Sorribas, P. Gorgojo, C. Téllez, J. Coronas, A. G. Livingston. High flux thin film nanocomposite membranes based on metal–organic frameworks for organic solvent nanofiltration. *Journal of the American Chemical Society* **2013**;135(40):15201-15208.

9. Y. Ma, F. Zhang, S. Yang, R. P. Lively. Evidence for entropic diffusion selection of xylene isomers in carbon molecular sieve membranes. *Journal of Membrane Science* **2018**;564:404-414.

10. G. Zhu, F. Zhang, M. P. Rivera, X. Hu, G. Zhang, C. W. Jones, R. P. Lively. Molecularly Mixed Composite Membranes for Advanced Separation Processes. *Angewandte Chemie* **2019**.

11. I. Voigt, M. Stahn, A. Junghans, J. Rost, W. Voigt. Integrated cleaning of coloured waste water by ceramic NF membranes. *Separation and Purification Technology* **2001**;25(1-3):509-512.

12. D. Fritsch, P. Merten, K. Heinrich, M. Lazar, M. Priske. High performance organic solvent nanofiltration membranes: Development and thorough testing of thin film composite membranes made of polymers of intrinsic microporosity (PIMs). *Journal of Membrane Science* **2012**;401:222-231.

13. M. F. Jimenez-Solomon, Q. Song, K. E. Jelfs, M. Munoz-Ibanez, A. G. Livingston. Polymer nanofilms with enhanced microporosity by interfacial polymerization. *Nature materials* **2016**;15(7):760.

14. M. Cook, P. R. Gaffney, L. G. Peeva, A. G. Livingston. Roll-to-roll dip coating of three different PIMs for Organic Solvent Nanofiltration. *Journal of Membrane Science* **2018**;558:52-63.

15. B. Liang, H. Wang, X. Shi, B. Shen, X. He, Z. A. Ghazi, N. A. Khan, H. Sin, A. M. Khattak, L. Li. Microporous membranes comprising conjugated polymers with rigid backbones enable ultrafast organic-solvent nanofiltration. *Nature chemistry* **2018**;10(9):961.

16. P. Marchetti, L. Peeva, A. Livingston. The selectivity challenge in organic solvent nanofiltration: membrane and process solutions. *Annual review of chemical and biomolecular engineering* **2017**;8:473-497.

17. S. Tsarkov, V. Khotimskiy, P. M. Budd, V. Volkov, J. Kukushkina, A. Volkov. Solvent nanofiltration through high permeability glassy polymers: Effect of polymer and solute nature. *Journal of Membrane Science* **2012**;423:65-72.

18. P. M. Budd, E. S. Elabas, B. S. Ghanem, S. Makhseed, N. B. McKeown, K. J. Msayib, C. E. Tattershall, D. Wang. Solution‐processed, organophilic membrane derived from a polymer of intrinsic microporosity. *Advanced Materials* **2004**;16(5):456-459.

19. D.-Y. Koh, R. P. Lively. Nanoporous graphene: Membranes at the limit. *Nat Nano* 05//print **2015**;10(5):385-386.

20. C. Z. Leng, M. D. Losego. Vapor phase infiltration (VPI) for transforming polymers into organic–inorganic hybrid materials: a critical review of current progress and future challenges. *Materials Horizons* **2017**;4(5):747-771.

21. I. Azpitarte, M. Knez. Vapor phase infiltration: from a bioinspired process to technologic application, a prospective review. *MRS Communications* **2018**;8(3):727-741.

22. A. Subramanian, N. Tiwale, C.-Y. Nam. Review of Recent Advances in Applications of Vapor-Phase Material Infiltration Based on Atomic Layer Deposition. *JOM Journal of the Minerals Metals and Materials Society* **2019**;71(1):185-196.

23. W. F. Ingram, J. S. Jur. Properties and Applications of Vapor Infiltration into Polymeric Substrates. *JOM Journal of the Minerals Metals and Materials Society* **2019**;71(1):238-245.

24. H.-C. Yang, R. Z. Waldman, Z. Chen, S. B. Darling. Atomic layer deposition for membrane interface engineering. *Nanoscale* **2018**;10(44):20505-20513.

25. G. N. Parsons, J. W. Elam, S. M. George, S. Haukka, H. Jeon, W. Kessels, M. Leskelä, P. Poodt, M. Ritala, S. M. Rossnagel. History of atomic layer deposition

and its relationship with the American Vacuum Society. *Journal of Vacuum Science & Technology A: Vacuum, Surfaces, and Films* **2013**;31(5):050818.

26. K. J. Dusoe, X. Ye, K. Kisslinger, A. Stein, S.-W. Lee, C.-Y. Nam. Ultrahigh Elastic Strain Energy Storage in Metal-Oxide-Infiltrated Patterned Hybrid Polymer Nanocomposites. *Nano Letters* **2017**;17(12):7416-7423.

27. S.-M. Lee, E. Pippel, U. Gösele, C. Dresbach, Y. Qin, C. V. Chandran, T. Bräuniger, G. Hause, M. Knez. Greatly increased toughness of infiltrated spider silk. *Science* **2009**;324(5926):488-492.

28. I. Azpitarte, A. Zuzuarregui, H. Ablat, L. Ruiz-Rubio, A. López-Ortega, S. D. Elliott, M. Knez. Suppressing the Thermal and Ultraviolet Sensitivity of Kevlar by Infiltration and Hybridization with ZnO. *Chemistry of Materials* **2017**;29(23):10068-10074.

29. B. D. Piercy, M. D. Losego. Tree-based control software for multilevel sequencing in thin film deposition applications. *Journal of Vacuum Science & Technology B* **2015**;33:043201.

30. M. L. Jue, C. S. McKay, B. A. McCool, M. Finn, R. P. Lively. Effect of Nonsolvent Treatments on the Microstructure of PIM-1. *Macromolecules* **2015**;48(16):5780-5790.

31. F. Yang, J. Brede, H. Ablat, M. Abadia, L. Zhang, C. Rogero, S. D. Elliott, M. Knez. Reversible and Irreversible Reactions of Trimethylaluminum with Common Organic Functional Groups as a Model for Molecular Layer Deposition and Vapor Phase Infiltration. *Advanced Materials Interfaces* **2017**;4(18).

32. S. Karan, S. Samitsu, X. Peng, K. Kurashima, I. Ichinose. Ultrafast viscous permeation of organic solvents through diamond-like carbon nanosheets. *Science* **2012**;335(6067):444-447.

33. K. Vanherck, S. Hermans, T. Verbiest, I. Vankelecom. Using the photothermal effect to improve membrane separations via localized heating. *Journal of Materials Chemistry* **2011**;21(16):6079-6087.

34. A. V. Volkov, V. V. Parashchuk, D. F. Stamatialis, V. S. Khotimsky, V. V. Volkov, M. Wessling. High permeable PTMSP/PAN composite membranes for solvent nanofiltration. *Journal of Membrane Science* **2009**;333(1-2):88-93.

35. K. Vanherck, T. Verbiest, I. Vankelecom. Comparison of two synthesis routes to obtain gold nanoparticles in polyimide. *Journal of Physical Chemistry C* **2011**;116(1):115-125.

36. P. Gorgojo, S. Karan, H. C. Wong, M. F. Jimenez‐Solomon, J. T. Cabral, A. G. Livingston. Ultrathin polymer films with intrinsic microporosity: anomalous

solvent permeation and high flux membranes. *Advanced Functional Materials* **2014**;24(30):4729-4737.

37. M. Sairam, X. Loh, Y. Bhole, I. Sereewatthanawut, K. Li, A. Bismarck, J. Steinke, A. Livingston. Spiral-wound polyaniline membrane modules for organic solvent nanofiltration (OSN). *Journal of Membrane Science* **2010**;349(1-2):123-129.

38. Y. S. Toh, F. Lim, A. Livingston. Polymeric membranes for nanofiltration in polar aprotic solvents. *Journal of Membrane Science* **2007**;301(1-2):3-10.

39. M. L. Jue, V. Breedveld, R. P. Lively. Defect-free PIM-1 hollow fiber membranes. *Journal of Membrane Science* **2017**;530:33-41.

APPENDIX B. ADDITION SORPTION DATA FOR POLYMER OF INTRINSIC MICROPOROSITY 1

B.1 Organic Vapor Sorption Isotherms

Organic vapor sorption isotherms were measured using a Dynamic Vapor Sorption system (DVS Vacuum, Surface Measurement Systems). PIM-1 hollow fiber membranes were placed and in situ dried at 110 ºC in the sample chamber of the DVS. The samples were then exposed to organic molecule vapors of a prescribed pressure at 25 ºC. Equilibrium criteria was set to less than 0.001 weight percent change within 10 minutes. As shown in Figure B.1, PIM-1 exhibits high uptake of large organic molecules, which suggests its potential in volatile organic compounds sorption.

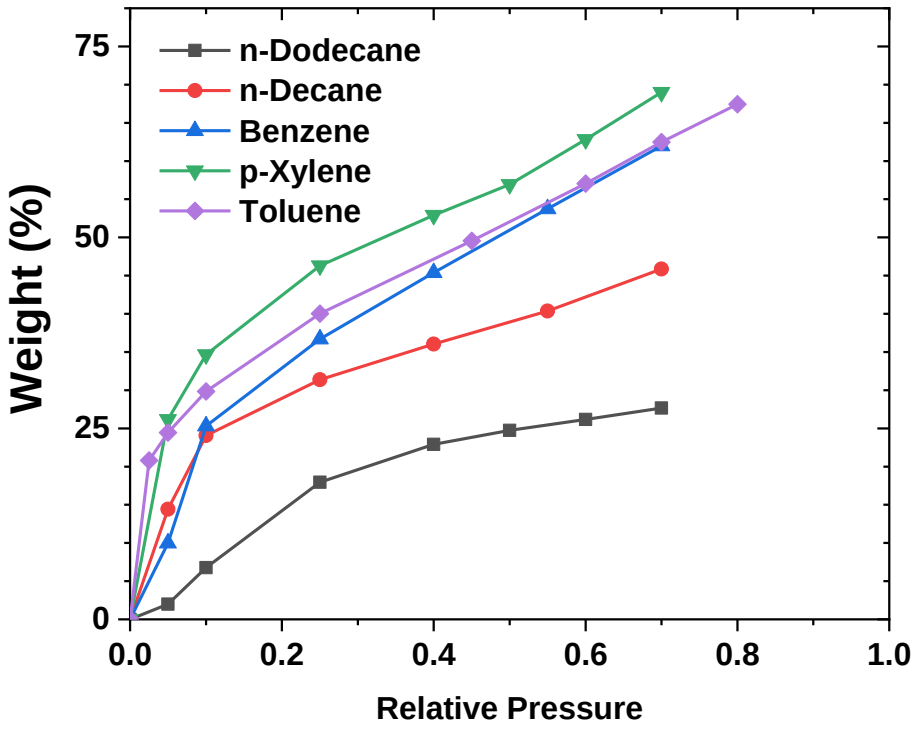

Figure B.1 25 ºC organic vapor sorption isotherms for PIM-1.

B.2 UV-Vis Spectrum of Vapor-Saturated PIM-1

The UV-vis spectrum is collected by a customized UV-vis spectrometer (Avantes). Dense transparent PIM-1 membranes with 50-μm thickness are saturated with organic vapors at 25 °C and then characterized in the transmission mode. As shown in Figure B2, organic solvent guest molecules significantly influence the absorbance of visible light with wavelength from 480 nm to 500 nm. This suggest that PIM-1 can be used as a highly sensitive sensor for organic compounds.

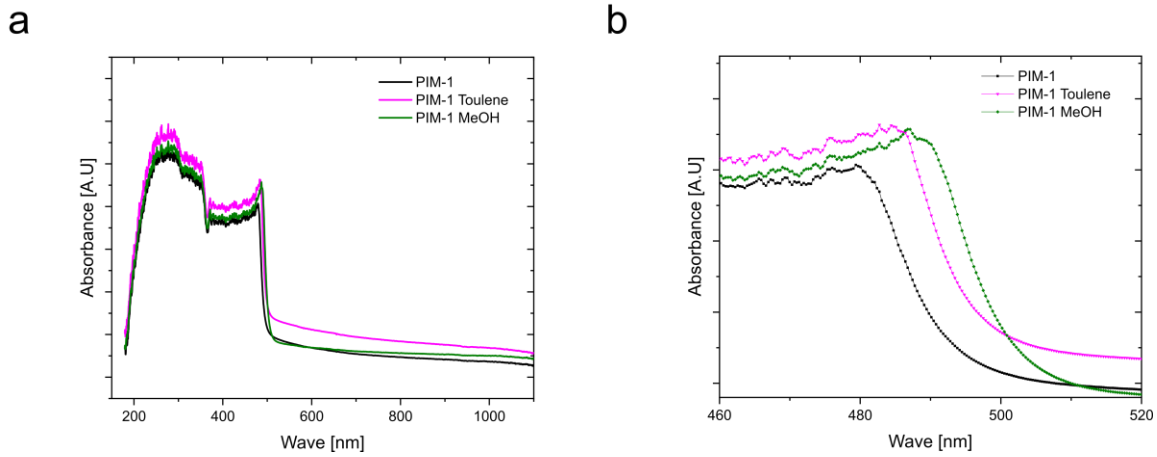

Figure B.2 (a) UV-vis spectrum for PIM-1 saturated with organic vapor. (b) The UV-vis signals significantly influenced by adsorbed organic vapors.

APPENDIX C. EXAMPLE CODE FOR 3D PRINTING

In this section, one example code that instruct the DIW 3D printer to fabricate a scaffold is presented. Owing to the periodic filament layout, this structure is compatible with parallel 3D printing. This code follows the standard of G-code commands used by RepRap firmware. Specific instructions should be tweaked for different 3D printer setups.

```
G1      X 50    Y 60    F 350
% Following the symbol "%" is the comment line for the last command;
% G1 means linear move; X 50 and Y50 specify the target position; F 350 specify the printing speed;
% The unit is defined in the 3D printer firmware, please check the manual;
% The purpose of this command is to reach the steady status of filament deposition;
G1      X0      Y0
% This command moves the nozzle back to the origin;

G1      X       32
% This command moves the nozzle to the position with X=32, Y=unchanged, Z=unchanged;
G1      Y       1
% This command moves the nozzle to the position with X= unchanged, Y=1, Z=unchanged;
G1      X       0
G1      Y       2
G1      X       32
G1      Y       3
G1      X       0
G1      Y       4
```

```
G1  X  32
G1  Y  5
G1  X  0
G1  Y  6
G1  X  32
G1  Y  7
G1  X  0
G1  Y  8
G1  X  32
G1  Y  9
G1  X  0
G1  Y  10
G1  X  32
G1  Y  11
G1  X  0
G1  Y  12
G1  X  32
G1  Y  13
G1  X  0
G1  Y  14
G1  X  32
G1  Y  15
G1  X  0
G1  Y  16
G1  X  32
```

```
G1 Y 17
G1 X 0
G1 Y 18
G1 X 32
G1 Y 19
G1 X 0
G1 Y 20
G1 X 32
G1 Y 21
G1 X 0
G1 Y 22
G1 X 32
G1 Y 23
G1 X 0
G1 Y 24
G1 X 32
G1 Y 25
G1 X 0
G1 Y 26
G1 X 32
G1 Y 27
G1 X 0
G1 Y 28
G1 X 32
G1 Y 29
```

```
G1    X    0
G1    Y    30
G1    X    32
G1    Y    31
G1    X    0
G1    Y    32
G1    X    32
```

% The commands above fabricate the first layer of the structure

```
G1    Z    1
```

% The commands move the nozzle to the position with X = uncahnged, Y = unchanged, Z = 1;

% The nozzle is elevated to print the next layer;

```
G1    Y    0
G1    X    31
G1    Y    32
G1    X    30
G1    Y    0
G1    X    29
G1    Y    32
G1    X    28
G1    Y    0
G1    X    27
G1    Y    32
G1    X    26
```

```
G1    Y    0
G1    X    25
G1    Y    32
G1    X    24
G1    Y    0
G1    X    23
G1    Y    32
G1    X    22
G1    Y    0
G1    X    21
G1    Y    32
G1    X    20
G1    Y    0
G1    X    19
G1    Y    32
G1    X    18
G1    Y    0
G1    X    17
G1    Y    32
G1    X    16
G1    Y    0
G1    X    15
G1    Y    32
G1    X    14
G1    Y    0
```

```
G1  X  13
G1  Y  32
G1  X  12
G1  Y  0
G1  X  11
G1  Y  32
G1  X  10
G1  Y  0
G1  X  9
G1  Y  32
G1  X  8
G1  Y  0
G1  X  7
G1  Y  32
G1  X  6
G1  Y  0
G1  X  5
G1  Y  32
G1  X  4
G1  Y  0
G1  X  3
G1  Y  32
G1  X  2
G1  Y  0
G1  X  1
```

```
G1      Y       32
G1      X       0
G1      Y       0
% The commands above fabricate the second layer of the structure
…
```